Laser Surface Texturing, Crystallization and Scribing of Thin Films in Solar Cell Applications

Hongliang Wang

Submitted in partial fulfillment of the
requirements for the degree of
Doctor of Philosophy
in the Graduate School of Arts and Sciences

COLUMBIA UNIVERSITY

2013

ABSTRACT

Laser Surface Texturing, Crystallization and Scribing of Thin Films in Solar Cell Applications

Hongliang Wang

Thin films have been considered for use in terrestrial solar cell applications because of their significantly reduced cost compared with bulk crystalline silicon. However, their overall efficiency and stability are less than that of their bulk crystalline counterpart. The work presented in this thesis seeks to investigate these issues via a series of experimental and numerical analysis of the influences of laser processing on microstructure, optical and electrical properties of two absorber materials, a-Si:H (hydrogenated amorphous silicon) and CdTe (cadmium telluride).

a-Si:H thin film solar cells suffer from disadvantages of low efficiencies and light induced degradation. A one-step laser processing is investigated for introducing light-trapping structure and crystallization on a-Si:H thin films, which can potentially simultaneously alleviate the two weaknesses of a-Si:H. The nanoscale conical and pillar-shaped spikes formed on the surface of a-Si:H films by irradiation of both femtosecond (fs) infrared and nanosecond (ns) excimer lasers enhanced light absorption, while the formation of a mixture of hydrogenated nanocrystalline silicon (nc-Si:H) and a-Si:H after crystallization suggests that the overall material stability can potentially improve. It is shown that growth is a more dominant spike formation mechanism in excimer laser processing, rather than ablation which is dominant during fs laser texturing. Experimental and analytical approaches are also developed revealing the effect of hydrogen on texturing behavior and crystallization during excimer laser irradiation, and a step-by-step crystallization process is proposed to prevent the hydrogen from diffusing out in order to reduce the defect density. In addition, a comparison of absorptance spectra for various surface

morphologies and crystallinity is developed and the absorptance across the solar spectrum shows that the combination of surface texturing and crystallization induced by laser processing is very promising for a-Si:H thin film solar cell applications.

CdTe thin-film solar cells are the basis of a significant technology with major commercial impact on terrestrial photovoltaic production, since CdTe leads to substantial cost reduction. Laser scribing is a key process used to increase thin-film solar panel efficiency through the formation of serial interconnections to reduce photocurrent and resistance losses. Currently, scribing is performed using glass-side laser processes which have led to increased scribe quality. Defects formed during scribing such as micro cracks, film delamination, thermal effect and tapered sidewall geometries, however, still keep solar panels from reaching their theoretical efficiencies. In this study, a ns Nd:YAG laser operating at the fundamental (1064nm) or frequency-doubled (532nm) wavelengths is employed for pattern 1 (P1) and 2 (P2) scribing on CdTe thin-film solar cells. The experimental investigation shows that film removal mechanisms for different materials are due to laser-induced ablation, thermal stress and micro-explosion processes. The formation mechanisms and mitigation techniques of the defects during micro-explosion process are studied. A fully-coupled thermal and mechanical finite element model is developed to analyze the laser-induced spatio-temporal temperature and thermal stress distribution responsible for SnO2:F film removal, and a plasma expansion model is also investigated to simulate the film removal of CdTe/Cds multilayer due to the micro-explosion process. The characterization of removal qualities will enable the process optimization and design required to enhance solar module efficiency.

Table of Contents

Chapter 1: Introduction

1.1 Applications and Opportunities of Laser Processing in Solar Cells…….……..…….. 1

1.1.1 Introduction to Solar Cells…….……..... 1

1.1.1.1 The Physics of the Solar Cell…….……..…….. 1

1.1.1.2 Characteristics of the Solar Cell……..…….……..... 4

1.1.1.3 Solar Cell Materials and their Practical and Theoretical Efficiencies..... 6

1.1.2 Laser Processing in Solar Cell Applications……...…… 10

1.2 Introduction to Laser Surface Texturing and Crystallization of a-Si:H Thin Films..... 11

1.2.1 Hydrogenated Amorphous Silicon (a-Si:H) – A Background…….……... 11

1.2.2 Laser Surface Texturing……..... 15

1.2.2.1 Femtosecond Laser Interaction with Wide-Band-Gap Materials……..... 17

1.2.2.2 Physical Description of Femtosecond Laser Surface Texturing……..... 19

1.2.2.3 Physical Description of Nanosecond Laser Surface Texturing……..... 20

1.2.2.4 Constitutive Model for Spike Formation by Excimer Laser Irradiation..... 22

1.2.3 Laser Crystallization……..... 24

1.2.3.1 Physical Description of the Melt-Mediated Process via Pulsed ns Laser..... 24

1.2.3.2 Femtosecond Laser Induced Crystallization……..... 25

1.3 Introduction to Laser Scribing of Thin-Film Solar Cells……..... 26

1.3.1 Cadmium Telluride – A Background……..... 26

1.3.2 Structure of Multilayer Thin-Film Solar Cells……..... 28

1.3.3 Laser Scribing Processes……..... 30

1.3.4 Laser Scribing Induced Defects Formation……..……..... 33

1.3.5 Influences of Laser-Induced Defects on Electrical Property Change……..... 36

1.4 Material Characterization……..... 38

1.4.1 Measurement of Film Thickness……..... 38

1.4.2 TEM Sample Preparation……..... 39

1.5 Organization of the Thesis……..... 40

Chapter 2: Femtosecond Laser-induced Simultaneous Surface Texturing and Crystallization of a-Si:H Thin Film: Morphology Study

2.1 Introduction……..……..……..... 44

2.2 Theoretical Background……..……..……..... 47

2.2.1 Femtosecond Laser Interaction with Wide-Band-Gap Materials…..…….…..... 47

2.2.2 Femtosecond Laser-Induced Surface Texturing Mechanism…..…..…..…..... 48

2.3 Experimental Setup……..……..……..…..... 50

2.4 Results and Discussion……..…..……..…..... 51

2.4.1 Absorptance Spectra of As-Received Film……..…….……..... 52

2.4.2 Study of Morphology in Air……..……..…..…..……..... 57

2.4.3 Further Study of Morphology in Water……..……..... 64

2.5 Conclusion……..…..……..... 71

Chapter 3: Femtosecond Laser-induced Simultaneous Surface Texturing and Crystallization of a-Si:H Thin Film: Absorption and Crystallinity

3.1 Introduction……..……..……..…..... 73

3.2 Background……..……..……..…… 75

3.2.1 Factors Affecting Light absorption..... 75

3.2.2 Femtosecond Laser-induced Crystallization..... 76

3.3 Experimental Setup..... 78

3.4 Results and Discussion..... 79

3.4.1 Surface Morphology after Laser Scanning..... 79

3.4.2 Effect of Laser Processing on Absorption..... 83

3.4.3 Modeling of Surface Geometry Effect on Absorption..... 86

3.4.4 Effect of Laser Processing on Crystallinity..... 93

3.4.5 Effect of Crystallinity on Absorption..... 98

3.4.6 Effect of Processing Medium on Absorption..... 100

3.5 Conclusion..... 102

Chapter 4: Effect of Hydrogen on Surface Texturing and Crystallization of a-Si:H Thin Film Irradiated by Excimer Laser

4.1 Introduction..... 104

4.2 Background..... 106

4.2.1 Hydrogen Effect on Nanosecond Laser-Induced Surface Texturing on a-Si:H..... 106

4.2.2 Hydrogen Effect on Crystallization of a-Si:H..... 107

4.3 Experimental Setup..... 108

4.4 Results and Discussion..... 110

4.4.1 Effect of Hydrogen on Surface Morphology..... 110

4.4.1.1 Surface Topography on Laser Irradiated a-Si:H..... 110

4.4.1.2 Surface Topography on Dehydrogenated a-Si..... 114

4.4.2 Effect of Hydrogen on Crystallization and Absorptance…..……..……..... 121

4.4.2.1 Hydrogen Effect on Crystallization..... 122

4.4.2.2 Hydrogen Effect of Crystallization Dependent on Pulse Duration and Pulse Number..... 126

4.4.2.3 Hydrogen Effect on bsorptance..... 129

4.4.3 Effect of Step-by-step Process on Residual Hydrogen Concentration, Crystallinity and Absorptance.....…..……..... 129

4.5 Conclusion…….....……..……..... 134

Chapter 5: Predictive Modeling for Glass-Side Laser Scribing of Thin Film Photovoltaic Cells

5.1 Introduction.....……..... 135

5.2 Background……..….....…..... 138

5.2.1 Thermal Stress and Brittle Failure Analysis..... 139

5.2.2 Micro-Explosion Analysis..... 140

5.2.3 Traction Separation Analysis..... 141

5.3 Experimental Setup..... 142

5.4 Results and Discussion..... 143

5.4.1 Simulation on SnO2:F Film Removal by Thermal Stress..... 143

5.4.2 Experiments on Laser Scribing of SnO2:F Thin Films..... 151

5.5 Simulation on CdTe Film Removal by Micro-Explosion..... 156

5.6 Conclusion..... 163

Chapter 6: Removal Mechanism and Defect Characterization for Glass-Side Laser Scribing of CdTe/CdS Multilayer in Solar Cells

6.1 Introduction..... 165

6.2 Background..... 168

6.2.1 Laser Induced Defects and Their Effects on Solar Cell..... 168

6.2.2 Dynamic Response of Brittle Materials..... 170

6.3 Experimental Setup..... 172

6.4 Results and Discussion..... 173

6.4.1 Film Removal by Single Pulse Irradiation..... 175

6.4.1.1 Scribe Geometry and Defect Characterization at a High Fluence..... 175

6.4.1.2 Scribe Geometry and Defect Characterization at a Low Fluence..... 181

6.4.2 Numerical Investigation on Film Removal and Defect Formation..... 186

6.4.3 Line Scribing and Sheet Resistance Measurement..... 192

6.5 Conclusion..... 194

Chapter 7: Conclusion

7.1 Laser Surface Texturing and Crystallization of a-Si:H Thin Films..... 196

7.1.1 Effect of Pulse Duration and Hydrogen on Spike Formation..... 196

7.1.2 Effect of Processing Medium and Pulse Duration on Crystallinity and Absorption..... 197

7.2 Laser Scribing of CdTe-Based Thin-Film Solar Cells..... 198

7.2.1 Film Removal and Defect Characterization of Glass-Side Laser Scribing..... 198

7.2.2 Numerical Investigation..... 199

7.3 Major Contributions..... 200

7.4 Further Work..... 201

References..... 203

Appendix..... 219

A1 Numerical Models..... 219

A1.1 Simulation of Light Absorption of As-Received a-Si:H Thin Film..... 219

A1.2 Simulation of Light Absorption of Laser Textured a-Si:H Thin Film..... 220

A1.3 Models for Ellipsometry Measurement..... 220

A1.4 Simulation of Spike Spacing during Excimer Laser Irradiation..... 221

A1.5 Simulation of P1 Laser Scribing of CdTe Solar Cell..... 222

A1.6 Simulation of P2 Laser Scribing of CdTe Solar Cell..... 222

A2 Peak Identification of Laser Textured a-Si:H Thin Film..... 223

A3 Programs for Laser Hardware Control..... 224

A3.1 Program of Femtosecond Laser Control..... 224

A3.2 Program of Excimer Laser Control..... 224

A4 Publications Under Candidature..... 225

List of Figures

Chapter 1

Figure 1.1	A schematic of a simple conventional solar cell. Creation of electron-hole pairs, e- and h+, respectively (Luque and Hegedus, 2003)	2
Figure 1.2	The radiation spectrum for black body at 5762 K, an AM0 spectrum and AM1.5 global spectrum (Luque and Hegedus, 2003)	3
Figure 1.3	The equivalent circuit of a solar cell	5
Figure 1.4	Current-voltage characteristic of a silicon solar cell (Luque and Hegedus, 2003)	6
Figure 1.5	Schematic of 40% multijunction solar cell (King, 2007)	7
Figure 1.6	Reported timeline of solar cell energy conversion efficiencies evolution of best research cells by technology type (Kazmerski, 2012)	8
Figure 1.7	Maximum theoretical efficiencies dependence of the band gap energy for several solar cell technologies. (Kazmerski, 2006)	9
Figure 1.8	Laser applications for solar cell and solar module production (Schulz-Ruhtenberg, 2009)	11
Figure 1.9	Spectra of the optical absorption coefficient α as a function of photon energy $h\nu$ of c-Si and a-Si:H (Luque and Hegedus, 2003 and Vanecek, et al., 1998)	12
Figure 1.10	Schematic of light absorption in direct and indirect band gap semiconductors. CB and VB represent conduction band and valence band. k is crystal momentum (k-vector) and E is energy.	13
Figure 1.11	(a) Schematic of laser surface texturing on piston ring; (b) femtosecond laser texturing of light trapping structure on the c-Si surface and schematic of light multi-reflection between textured spikes. (Etsion, 2008; Carey, 2004)	16
Figure 1.12	A side-view of a femtosecond laser (wavelength of 800nm, pulse duration of 100fs, fluence of 1J/cm^2) textured c-Si sample, cleaved through an irradiated spot. The tips of the structures are all at or below the original wafer surface, showing femtosecond laser surface texturing is a ablation-dominant process (Carey, 2004).	20

Figure 1.13	SEM images of (a) top view (b) side view of excimer laser (wavelength of 248nm, pulse duration of 30ns, fluence of 3J/cm^2) surface textured silicon surface formed in SF6, showing the growth-dominant formation via VLS mechanism (Crouch, et al., 2004).	21
Figure 1.14	Energy payback time (EPBT) of current PV technologies (First Solar, 2012)	28
Figure 1.15	Interconnection schematic of thin-film solar module (Bovatsek, et al. 2010)	29
Figure 1.16	Schematic of (a) Ablative removal in film-side laser scribing; (b) Micro-explosion-based removal in glass-side laser scribing (Wang, et al. 2010).	31
Figure 1.17	SEM images of overview and boundary of (a) film-side and (b) glass-side single pulse irradiation of SnO2:F thin film on glass substrate at 127 J/cm2.	31
Figure 1.18	Schematic of P1, P2, and P3 laser scribing of multilayer thin films. P1 removes the front contact layer. P2 removes the absorber layer while P3 removes the absorber and back contact layers simultaneously. (Dunsky, et al. 2008)	32
Figure 1.19	Schematic of the defects, such as non-vertical sidewall, thermal effect, residual material, film delamination and micro cracks, caused by laser scribing	34
Figure 1.20	(a) SEM image of P2 scribing of a-Si:H film from glass side using a 532nm ps laser, showing a-Si:H film delamination after processing; (b) SEM image of Mo film removal through 20ns-pulses at the repetition rate of 250kHz and scan speed of 5m/s. Dashed circles denote the delamination of Mo films. (Gecys, et al. 2010; Tamaoki, et al. 2010)	34
Figure 1.21	Relationship between the power loss and the number of cells cracked in the mechanical load test, showing the power loss can reach up to 10% due to the cracked cells. (Kontgers, et al. 2010)	37
Figure 1.22	Interaction of polarized light with a sample(J.A. Woollam Co. Inc., 2008)	38
Figure 1.23	(a) FIB image of TEM sample cut loose at bottom; (b) FIB image showing probe needle attached to the ear (Roberts and Otterloo, 2001)	40

Chapter 2

Figure 2.1	Comparison of measured and model fitted optical data in the ellipsometer measurement of a-Si:H layer thickness that deposited on glass substrate	52

Figure 2.2	(a) SEM image and (b) AFM image of as-received a-Si:H film surface	52
Figure 2.3	Schematic of one-dimensional absorption simulation model of as-received a-Si:H film on glass substrate, film thickness d=1.6μm, real and imaginary parts of refractive index of a-Si:H film are n and k, s and n0 are the refractive index of the substrate and air, respectively	53
Figure 2.4	Comparison of transmittance spectra for both simulation and measurement by spectrophotometer of as-received a-Si:H film on glass substrate	54
Figure 2.5	Comparison of reflectance spectra for both simulation and measurement by spectrophotometer of as-received a-Si:H film on glass substrate	54
Figure 2.6	Comparison of calculated absorptance spectra of as-received a-Si:H film on glass substrate based on both transmission and reflection simulation and measurement by spectrophotometer	55
Figure 2.7	SEM images of a-Si:H film surface after being irradiated by the following number of pulses in air at 0.4J/cm^2 (a)2, (b) 10, (c)20, (d) 60, (e)100, (f) 100. With lower magnification, (f) shows about a quarter of irradiated area and the arrow in (f) showing the spikes are becoming smaller and denser moving from center to the edge	59
Figure 2.8	Dependence of average spike height on average spike spacing after laser treatment in air, determined from an area of 50×50 μm^2 at the processing center (0.4J/cm^2, 100 pulses). The solid straight line is a linear fitting to the measurement, error bars indicate standard deviation	60
Figure 2.9	Dependence of average spike spacing on laser fluence for a fixed number of pulses (100 pulses) after treated in air, determined from an area of 50×50 μm^2 at the processing center, error bars indicate standard deviation	62
Figure 2.10	SEM images near the edge of underwater laser irradiation area on a-Si:H film for (a) 2 pulses (b) 5 pulses at the fluence of 1.4J/cm^2	65
Figure 2.11	SEM images of underwater laser irradiation of a-Si:H film for 50 pulses at fluence of 1.4J/cm^2 , the irradiation spot diameter is 150μm, the inset images in the right show the high magnification at the center (a) and edge (b)	65
Figure 2.12	SEM images of underwater laser irradiation of a-Si:H film for 50 pulses at fluence of (a) 1.2J/cm2 (b) 1.6J/cm^2	67
Figure 2.13	Schematic of peak identification of extraction data from AFM images of underwater laser irradiated a-Si:H film at different fluence and number of pulses, asterisks indicate the identified peak point, solid curves indicate the contour spectra, AFM scanning area is 5×5 μm, color bar unit: nm	67

Figure 2.14 Dependence of average spike spacing on laser fluence and number of pulses in water, error bars indicate standard error 68

Figure 2.15 Dependence of average spike height on laser fluence and number of pulses in water, error bars indicate standard error 71

Chapter 3

Figure 3.1 (a) SEM image and (b) AFM image of surface of a-Si:H film laser irradiated in air, (0.4J/cm^2, 1mm/s), showing texturing with conical spikes on the surface 80

Figure 3.2 Comparison of textured spikes made by (a) scanning (0.4 J/cm^2, 1mm/s) and (b) stationary (0.4 J/cm^2, 100 pulses) pulsing in air, showing nanoparticles distributed on the whole spike after laser scanning 81

Figure 3.3 Comparison of textured spikes made by (a) scanning (1.2J/cm^2, 2mm/s) and (b) stationary (1.2J/cm^2, 50 pulses) pulsing in water, showing similar pillar-shaped spikes textured on the both sample surfaces 81

Figure 3.4 XPS spectra of a-Si:H sample surfaces of as received, laser irradiated in air (0.4J/cm^2, 1mm/s) and in water (1.2J/cm^2, 2mm/s). The spectra have been shifted up for clarity. Note increase in oxygen and decrease in carbon after laser processing 82

Figure 3.5 Comparison of absorptance spectra of as-received and laser treated a-Si:H films at fluences of 0.4J/cm^2 (scan speed 1mm/s) and 1.2J/cm^2 (scan speed 2mm/s) in air and water by spectrophotometry, showing increase in absorptance over entire spectrum for both treated samples 85

Figure 3.6 Schematic of cross-sectional absorption simulation model for textured a-Si:H film on glass substrate, total thickness is 1.6μm, real and imaginary parts of refractive index of a-Si:H film are n and k, s and n0 are the refractive index of the substrate and air, respectively. Magnified image in the right shows the reference and local coordinate systems ($\bar{X}$, $\bar{Y}$, $\bar{Z}$) and (X, Y, Z), where S denotes the spike surface that reflects the ray passing through point $\bar{P}0$ 89

Figure 3.7 Comparison of simulated and measured absorptance spectra of the laser treated sample in air with the textured surface of conical spikes, with height of 900 nm and top angle of 90° 89

Figure 3.8 Comparison of simulated and measured absorptance spectra of the laser treated samples in water with textured surface of pillar-shaped spikes with height of 400nm height and a diameter of 100nm 90

Figure 3.9	Comparison of simulated absorptance spectra for the textured surfaces with two different densities of conical spikes, showing the surface with higher density spikes has higher absorptance	91
Figure 3.10	Comparison of simulated absorptance spectra for textured surfaces with different heights of conical spikes, showing similar absorptance over the entire wavelength range	92
Figure 3.11	X-ray diffraction spectra of as-received a-Si:H film, laser treated films at $0.4J/cm^2$, 1mm/s and $1.2J/cm^2$, 2mm/s in air and water, respectively. All the spectra show an "amorphous peak" at around $2\theta=25°$ and no signs of crystallinity for the untreated sample and that treated in water. Sample treated in air shows three different peaks for (111), (220) and (311) orientation of silicon. The spectra have been shifted for clarity	94
Figure 3.12	X-ray diffraction spectra of a-Si:H films laser treated at fluences of $0.5J/cm^2$ and $1.2J/cm^2$,and scan speeds of 2mm/s and 25 mm/s in water. An "amorphous peak" around $2\theta=25°$is observed for all samples. Sample processed at $0.5J/cm^2$ and 25mm/s shows existence of two peaks for (111) and (220) orientation of silicon, showing the effect of different laser parameters on crystallinity	97
Figure 3.13	X-ray diffraction spectrum of laser treated a-Si:H film at different fluences from $0.5J/cm^2$ to $0.8J/cm^2$ with the same scan speed of 25 mm/s in water. An "amorphous peak" around $2\theta=25°$ is observed for all samples. Existence of two overall different peaks for (111) and (220) orientation of silicon is found except for the condition at $0.8J/cm^2$, showing that the crystallinity decreases with increasing of fluence	98
Figure 3.14	(a) SEM image and (b) AFM image of surface of a-Si:H film laser irradiated in water ($0.5J/cm^2$, 25mm/s), showing texturing with randomly oriented spikes on the surface	99
Figure 3.15	Comparison of absorptance spectra measured by spectrophotometry of as-received and laser irradiated a-Si:H films with and without crystallinity at different fluences and scan speeds ($0.5J/cm^2$ at 25mm/s, $1.2J/cm^2$ at 2mm/s) in water, showing the effect of crystallinity on absorption	99
Figure 3.16	Comparison of absorptance spectra measured by spectrophotometry of as-received and laser irradiated a-Si:H film in air ($0.4J/cm^2$, 1mm/s) and water($0.5J/cm^2$, 25mm/s), showing the effect of different factors, such as surface geometry, crystallinity and processing medium on absorption	102

Chapter 4

Figure 4.1	SEM images of a-Si:H film surface after being irradiated by the following number of pulses at 0.4J/cm^2 (a) 1, (b) 5, (c) 50 pulses at the magnification of 1.5K, and (d) 50 pulses at the magnification of 30K	110
Figure 4.2	AFM image of surface morphology at the laser irradiation boundary of a-Si:H film at a fluence of 0.4J/cm^2 with 50 pulses, showing the spikes are protruded from the original surface	111
Figure 4.3	Dependence of average spike height, protrusion and spacing on number of pulses for a fixed fluence of 0.4J/cm^2, determined from an area of 50×50μm^2 at the processing center, error bars indicate standard deviation	112
Figure 4.4	Dependence of average spike height, protrusion and spacing on laser fluence for a fixed number of pulses (100 pulses), determined from an area of 50×50μm^2 at the processing center, error bars indicate standard deviation	114
Figure 4.5	Simulation results of dependence of the spike height on laser fluence for a fixed number of pulses (1 and 100 pulses)	118
Figure 4.6	Transmission infrared spectra for thermal annealed a-Si:H samples at different annealing time, showing hydrogen concentration decreases with increasing of annealing time	119
Figure 4.7	SEM images of 80-hour thermal annealed a-Si:H film surface after being irradiated at a fluence of 0.4J/cm^2 and 100 pulses, showing no sharp spikes on the surface	120
Figure 4.8	X-ray diffraction spectra of as-received a-Si:H film, laser treated films at 0.4J/cm^2 with 50 and 100 pulses, and 0.3J/cm^2 with 100 pulses. There is no signs for crystallinity for the untreated sample and are three different peaks for (111), (220) and (311) orientation of silicon for all laser treated samples. The spectra have been shifted for clarity	122
Figure 4.9	In-situ front-side transient reflectance signals of a-Si:H films irradiated at different fluences	123
Figure 4.10	Cross-sectional view TEM micrographs of a-Si:H samples irradiated at (a) 1 and 50 pulses at (b) low, (c) high magnification and (d) high-resolution TEM image with a fixed fluence of 0.4J/cm^2	125
Figure 4.11	Cross-sectional view TEM micrographs of a-Si:H samples irradiated by 130-fs laser pulses at a fluence of 0.4J/cm^2 and a scan speed of 1mm/s	127

Figure 4.12 Dependence of maximum grain sizes of laser irradiated a-Si:H films on number of pulses at a fluence of 0.4J/cm^2 127

Figure 4.13 Comparison of absorptance spectra measured by spectrophotometry of as-received and laser irradiated a-Si:H films at fluences of 0.4J/cm^2 with 50 and 100 pulses, and 0.3J/cm^2 with 100 pulses 128

Figure 4.14 Transmission infrared spectra for single-step and step-by-step laser processed a-Si:H samples, where EF, SW and # indicate ending fluence, step width and number of pulses, respectively 130

Figure 4.15 Normalized crystallinity and hydrogen concentration of step-by-step laser processed a-Si:H samples at a fixed initial fluence of 0.05J/cm^2 and final fluence of 0.3J/cm^2 with different increments and number of pulses 132

Figure 4.16 Comparison of absorptance spectra measured by spectrophotometry of single-step and step-by-step laser processed a-Si:H samples, inset shows the SEM image of surface morphology of a step-by-step laser processed a-Si:H sample with a final fluence of 0.3J/cm^2, step width of 0.05J/cm^2 and 100 pulses at each sequence 133

Chapter 5

Figure 5.1 Illustration of the glass-side laser scribing model for SnO2:F and CdTe film removal. Lasers with wavelength of 1064nm and 532nm are adopted for SnO2:F and CdTe scribing, respectively 144

Figure 5.2 Temperature distribution in the SnO2:F/glass multilayer system under laser irradiation at a fluence of 3J/cm^2. A large penetration depth of laser energy allows for a uniform temperature distribution along film thickness. Snapshot is taken at 36ns. 10X Deformation scale for viewing clarity 145

Figure 5.3 Fully coupled thermal stress analysis of SnO2:F removal by laser irradiation at a fluence of 3J/cm^2 at 38ns. Absorption of laser energy induces local thermal expansion and thermal stress. Elements experiencing a principal stresses larger than the failure strength are deleted from calculation. A 2μm opening has been generated accordingly. 10X Deformation scale for viewing clarity 146

Figure 5.4 Principal stress and heat flux history in an element at SnO2:F film center. The element deletion occurs at 38ns. Heat flux drops to zero due to instantaneous dependence between thermal and mechanical analyses 146

Figure 5.5	The result of SnO2:F removal by 3J/cm^2 laser irradiation based on the fully coupled thermal stress analysis. An 8.3μm opening is generated. The snapshot is taken at 200ns. Deformation scale is 10X for viewing clarity	147
Figure 5.6	Temperature and stress history in a deleted element at SnO2:F film center treated at a fluence of 1J/cm^2. The element is subjected to a compressive stress followed by a tensile stress. The element fails when the tensile failure stress is met at 1430ns	148
Figure 5.7	Comparison of depths and widths of the removed SnO2:F films obtained in simulation and experiments. The film is completely removed in depth for all the conditions used in the simulations	150
Figure 5.8	(a) SEM image of the film removal by single pulse processed SnO2:F samples from glass side at a fluence of 127J/cm^2; (b) Removal line profile along A measured by optical profilometry; (c) SEM image of scribe sidewall; (d) EDX line profile scanning along A	152
Figure 5.9	(a) 3D scanning of the removal film profile by optical profilometry and (b) SEM image of the sidewall of film removal by single pulse processed SnO2:F samples from film side at a fluence of 127J/cm^2	154
Figure 5.10	Dependence of removal depth and width on laser fluence. Error bars indicate standard deviation	155
Figure 5.11	Temperature distribution of CdTe/SnO2:F/glass multilayer system under laser irradiation at a fluence of 0.2J/cm^2	156
Figure 5.12	Temporal distribution of the plasma pressure at different fluences from 0.2J/cm^2 to 0.8J/cm^2	158
Figure 5.13	Micro-explosion model with a pressure input at the CdTe/SnO_2:F interface and the plasma dimension is 10μm in width. A layer of cohesive elements is defined between the CdTe layer and SnO_2:F layer. The CdTe film deforms due to the plasma expansion. The snapshot is taken at 10ns. Deformation scale is 10X for viewing clarity	158
Figure 5.14	S_{22} stress distribution of the magnified area A in Fig. 5.11 at the same moment. The cohesive elements have been deformed due to S_{22} stress. Deformation scale is 10X for viewing clarity	160
Figure 5.15	S_{22} stress distribution of the region shown in Fig. 5.12 at the later stage (20ns), showing some cohesive elements have been deleted. Deformation scale is 10X for viewing clarity	160

Figure 5.16 Stress evolution of the failed elements at the top center and bottom center of the CdTe layer. Tensile stress occurs on the top, while compressive stress occurs at the bottom. The stresses drop to zero once the Coulomb-Mohr criterion is met 161

Figure 5.17 Typical evolution of stresses and the quadratic nominal stress ratio defined in Eq. (5.7) of the removed cohesive elements. Nodal displacement of the cohesive element is also shown 162

Figure 5.18 Maximum principal stress distribution at 66ns. The film has been completely removed with an opening width of 12.5μm. Both brittle failure and film delamination contribute to the film removal. Deformation scale is 2X for viewing clarity 162

Chapter 6

Figure 6.1 Schematic of film removal of P2 laser scribing on CdTe-based solar cells under micro-explosion mechanism 174

Figure 6.2 (a) SEM image of film removal by a pulse irradiated at a fluence of 3J/cm^2; (b) magnified SEM image at square D; (c) Optical profilometry measurement along A 176

Figure 6.3 EDX line profile scanning along A in Fig. 6.2 (a), showing a clean removal at the center, and small amount of remaining material is CdS and no inter-diffusion occurs at the interface of TCO/CdS 177

Figure 6.4 Cross-sectional TEM image of as-received CdTe/CdS/TCO/Glass samples 177

Figure 6.5 Cross-sectional TEM image of scribe boundary at square B shown in Fig. 6.2 (a), showing micro-crack is formed near the top surface at the scribe sidewalls 179

Figure 6.6 Cross-sectional TEM images of (a) near scribe boundary B and (b) scribe center region C in Fig. 6.2 (a) 180

Figure 6.7 SEM image of film removal by a pulse irradiated at a fluence of 1J/cm^2, showing much more CdS remaining after processing compared to that processed at a fluence of 3J/cm^2 180

Figure 6.8 Cross-sectional TEM images of (a) scribe boundary at square B' shown in Fig. 6.7 and (b) magnified image at the delamination tip, showing dislocations formed at both between the two layers and grains which may introduce further crack initiation 182

Figure 6.9	(a) TEM images taken at region C' in Fig. 6.7 and (b) magnified TEM image at the interface between CdS and SnO_2:F layers, showing nano-bubbles formed due to the oxidation of sulfur during the laser processing	182
Figure 6.10	Dependence of scribe area and remaining CdS on laser irradiation conditions, error bars represents standard deviation	184
Figure 6.11	Simulation result of temperature distribution of CdTe/CdS/SnO_2:F/glass multilayer thermal model at a fluence of 1J/cm^2	185
Figure 6.12	Simulation results of dependence of SnO_2:F (TCO) temperature on fluence, showing the TCO layer will be damaged when the fluence reaches 5.5J/cm^2	187
Figure 6.13	Complete film removal with a fluence of 1J/cm^2 at 97.9ns, the scribe radius is 28.7μm and delamination is 2.8μm through the interface	188
Figure 6.14	Complete film removal with a fluence of 3J/cm^2 at 76.8ns, the scribe radius is 34.8μm and micro-crack with a length of 1.4μm occurs near the top surface	189
Figure 6.15	Comparison of experimental and simulation results on scribe width, error bars represents standard deviation	190
Figure 6.16	Comparison of experimental and simulation results on residual CdS, error bars represents standard deviation	190
Figure 6.17	Simulation results of micro-crack and delamination lengths after laser scribing	192
Figure 6.18	SEM images of (a) line scribing at a fluence of 3J/cm^2 and a speed of 2mm/s, (b) magnified image at scribe boundary, showing macro-cracks are removed due to the pulse overlapping	193
Figure 6.19	Dependence of sheet resistances on fluence. The high resistance at low energy range is due to the residual CdS, and high resistance at high energy range is caused by the TCO damage. Red dash line represents the sheet resistance of TCO material only and error bars represent standard deviations	194

List of Tables

Table 3.1	Chemical constituent concentrations of the a-Si:H sample surfaces for as received, laser irradiated in air and laser irradiated in water	82
Table 4.1	List of a-Si properties used in the simulation calculation	115
Table 5.1	Material properties used in simulation	144

Acknowledgements

The success of this research would undoubtedly not have been possible without the aid of a number of groups and individuals. I must of course express my deepest gratefulness and respect to my dissertation advisor Dr. Y. Lawrence Yao for his guidance and insight throughout my research, and financial support during my doctoral study. What I learned in the Manufacturing Research Laboratory led by Dr. Yao will be extremely beneficial to my future career.

Many thanks go to my dissertation committee members, Dr. Chee Wei Wong, Dr. Elon Terrell, Dr. James S. Im, and Dr. Hongqiang Chen for their valuable suggestions and comments. Additionally, I am very pleased to thank past and present colleagues, such as Dr. Sinisa Vukelic, Dr. Gen Satoh, and Panjawat Kongsuwan, from Manufacturing Research Lab for their professional support and friendship. I must appreciate Kim Kisslinger and Dr. Dmytro Nykypanchuk for their guidance and help with TEM and spectrophotometry in Brookhaven National Laboratory. Thanks are due to Drs. Marco Leona and Pablo Londero, Department of Scientific Research, the Metropolitan Museum of Art, for their assistance in access to the green laser processing equipment. A debt of gratitude is also owed to Robert Stark and Walter Khan for their supporting role.

Lastly, but in no sense the least, I express my thanks and appreciation to my parents and my wife for their great love, support and extraordinary encouragement.

This dissertation is dedicated to

my deeply-loved parents,

and

my wife Lan Yu

Chapter 1: Introduction

1.1 Applications and Opportunities of Laser Processing in Solar Cells

1.1.1 Introduction to Solar Cells

The growth of the photovoltaics (PV) industry has been dramatic in the past few years, from just 5.3 GW in 2005 to 69.7 GW in 2011, which is sufficient to generate 85 TWh (terawatt hour) per year. Cumulative installations at the end of 2012 are expected to reach from 89.9 to 109.9 GW, and from 207.9 to 342.8 GW by the end of 2016. This growth is largely driven by the demand for electricity providers to include renewable energy generation in their portfolio and the economic policies of environmental sustainability (Booth, 2010).

1.1.1.1 The Physics of the Solar Cell

A solar cell (also called a photovoltaic cell) is an electrical device that converts the energy of light into electricity through the photovoltaic effect. It is a form of photoelectric cell which, when exposed to light, can generate and support an electric current without any external voltage source. Semiconductors have the capability to absorb light and to deliver a portion of the absorbed energy to carriers of electrical current – electrons and holes. A simple conventional solar cell structure is shown in Fig. 1.1. Sunlight is incident from the top on the front of the solar cell. A metallic grid forms one of the electrical contacts of the diode and allows light to fall on the semiconductor between the grid lines and thus be absorbed and converted into electrical energy. An antireflective layer between the grid lines increases the amount of light transmitted to the semiconductor. The semiconductor diode is fashioned when an n-type semiconductor and a p-type semiconductor are brought together to form a metallurgical junction. This is typically

achieved through diffusion or implantation of specific impurities (dopants) or via a deposition process. The diode's other electrical contact is formed by a metallic layer on the back of the solar cell. All electromagnetic radiation, including sunlight, is composed of particles called photons, which carry specific amounts of energy determined by the spectral properties of their source. Photons also exhibit a wavelike character with the wavelength, λ, being related to the photon energy, $E_\lambda = hc/\lambda$, where h is Plank's constant and c is the speed of light. Only photons with sufficiency energy to create an electron-hole pair, this is, those with energy greater than the semiconductor band gap (E_g), the energy difference between valence band and conduction band of the material, will contribute to the energy conversion process (Luque and Hegedus, 2003).

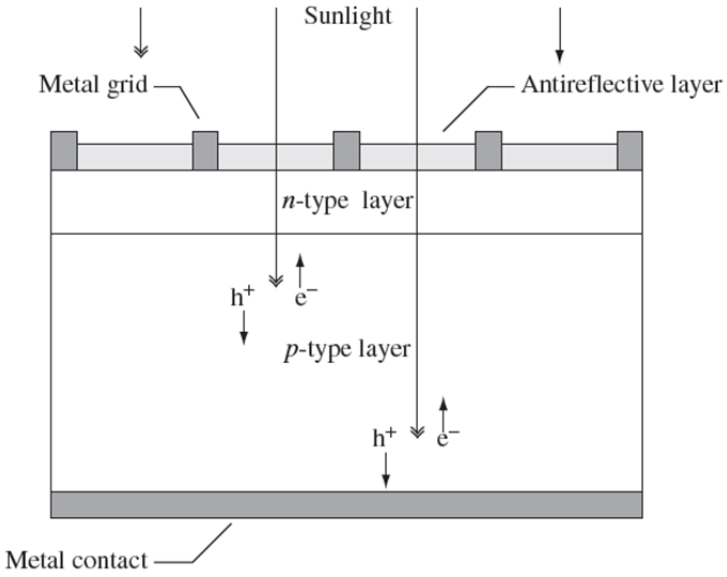

Figure 1.1 A schematic of a simple conventional solar cell. Creation of electron-hole pairs, e^- and h^+, respectively (Luque and Hegedus, 2003)

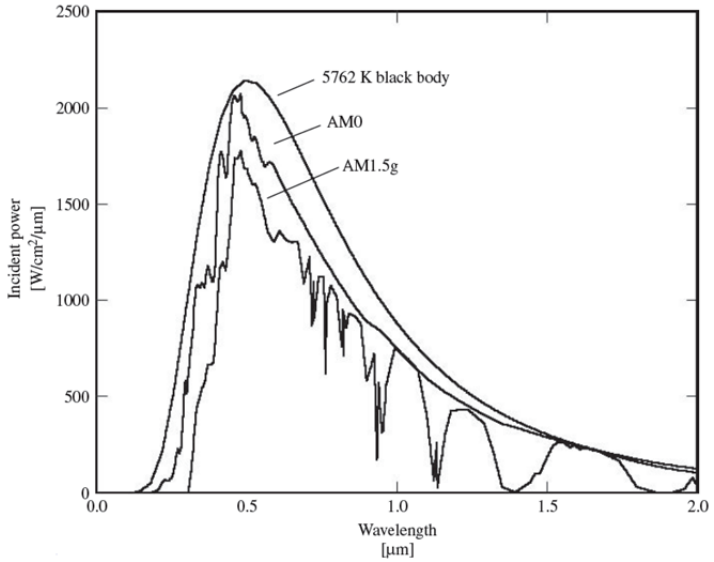

Figure 1.2 The radiation spectrum for black body at 5762 K, an AM0 spectrum and AM1.5 global spectrum (Luque and Hegedus, 2003)

The sun has a surface temperature of 5762 K and its radiation spectrum can be approximated by a black-body radiator at that temperature (Luque and Hegedus, 2003). Emission of radiation from the sun, as with all black-body radiators, is isotropic. However, the Earth's great distance from the sun (approximately 93 million miles) means that only those photons emitted directly in the direction of the Earth contribute to the solar spectrum as observed from Earth. Therefore, for practical purposes, the light falling on the Earth can be thought of as parallel streams of photons. Just above the Earth's atmosphere, the radiation intensity, or Solar Constant, is about 1.353 kW/m2 (Green, 1982) and the spectral distribution is referred to as an air mass zero (AM0) radiation spectrum. The Air Mass is a measure of how absorption in the atmosphere affects the spectral content and intensity of the solar radiation reaching the Earth's surface. The Air Mass number is given by $Air\ Mass = 1/\cos\theta$, where θ is the angle of incidence. A widely used standard for comparing solar cell performance is the AM1.5 spectrum normalized to a total power density of 1 kW/m^2. The spectral content of sunlight at the Earth's surface also has a diffuse component

owing to scattering and reflection in the atmosphere and surrounding landscape and can account for up to 20% of the light incident on a solar cell. Black body (T=5762 K), AM0, and AM1.5g (terrestrial) radiation spectra are shown in Fig. 1.2.

The most commonly known solar cell is configured as a large-area p-n junction made from silicon. As a simplification, one can imagine bringing a layer of n-type silicon into direct contact with a layer of p-type silicon. In practice, p-n junctions of silicon solar cells are not made in this way, but rather by diffusing an n-type dopant into one side of a p-type wafer (or vice versa). If a piece of p-type silicon is placed in intimate contact with a piece of n-type silicon, then a diffusion of electrons occurs from the region of high electron concentration (the n-type side of the junction) into the region of low electron concentration (p-type side of the junction). When the electrons diffuse across the p-n junction, they recombine with holes on the p-type side. The diffusion of carriers does not happen indefinitely, however, because charges build up on either side of the junction and create an electric field. The electric field creates a diode that promotes charge flow, known as drift current that opposes and eventually balances out the diffusion of electrons and holes. This region where electrons and holes have diffused across the junction is called the depletion region because it no longer contains any mobile charge carriers.

1.1.1.2 Characteristics of the Solar Cell

To understand the electronic behavior of a solar cell, it is useful to create a model which is electrically equivalent, and is based on discrete electrical components whose behavior is well known. An ideal solar cell may be modeled by a current source in parallel with a diode; in

practice no solar cell is ideal, so a shunt resistance and a series resistance component are added to the model (Lorenzo, 1994). The resulting equivalent circuit of a solar cell is shown in Fig. 1.3.

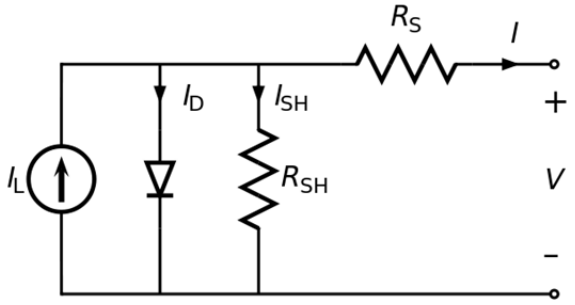

Figure 1.3 The equivalent circuit of a solar cell

From the equivalent circuit, it is evident that the current produced by the solar cell, I, can be expressed as

$$I = I_L - I_D - I_{SH} = I_L - I_0 \left\{ \exp\left[\frac{q(V + IR_S)}{nkT} \right] - 1 \right\} - \frac{V + IR_S}{R_{SH}} \tag{1.1}$$

where I, I_L, I_D, I_{SH} and I_0 are output current, photocurrent, diode current, shunt current and reverse saturation current. q is elementary charge, n is diode ideality factor, k is Boltzmann's constant, T is absolute temperature, V is voltage output, R_S is series resistance and R_{SH} is shunt resistance.

In principle, given a particular operating voltage, V, Eq. (1.1) may be solved to determine the operating current, I, at that voltage. However, because Eq. (1.1) involves the current on both sides in a transcendental function, the equation has no general analytical solution. Instead, it is easily solved using numerical methods. Since the parameters I_0, n, R_S, and R_{SH} cannot be measured directly, the most common application of the characteristic equation is nonlinear regression to extract the values of these parameters on the basis of their combined effect on the solar cell behavior – I-V characteristic. Figure 1.4 shows the current-voltage characteristic of a

typical silicon solar cell. It illustrates several important figures of merit for solar cells – the short-circuit current, I_{SC}, open-circuit voltage, V_{OC}, and fill factor, FF, where fill factor is the available power at the maximum power (P_{max}) divided by I_{SC} and V_{OC}. The energy conversion efficiency, η, of a solar cell, the percentage of the solar energy to which the cell is exposed that is converted into electrical energy, can be obtained as

$$\eta = (V_{MP} \cdot I_{MP} / E \cdot S) \cdot 100\% = (FF \cdot V_{OC} \cdot I_{SC} / E \cdot S) \cdot 100\% \quad (1.2)$$

where E is irradiation intensity and S is cell area.

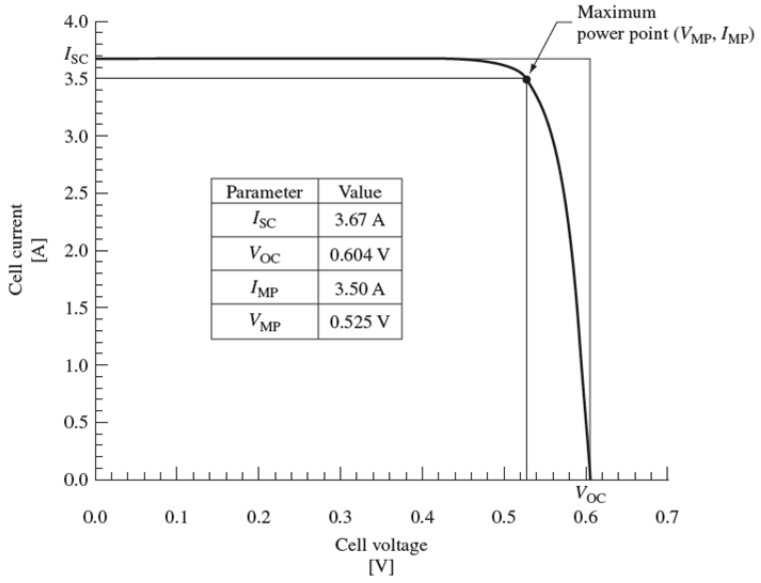

Figure 1.4 Current-voltage characteristic of a silicon solar cell (Luque and Hegedus, 2003)

1.1.1.3 Solar Cell Materials and their Practical and Theoretical Efficiencies

Solar cell can be fabricated from a number of semiconductor materials, and various materials display varying efficiencies and costs. Many current available terrestrial solar cells are made from bulk materials, including monocrystalline silicon and polycrystalline silicon, which are cut

into wafers between 180 to 240 micrometers thick. In contrast, some materials are made as thin film layers, such as amorphous silicon (a-Si), cadmium telluride (CdTe) and copper indium gallium selenide (CIGS), which are deposited on supporting substrates. Thin film solar cells are of interest for researchers nowadays, since thin films can significantly reduce the material cost and be available to structure as multi-junction cells that can reach efficiency up to 44%. Multijunction solar cells contain multiple different tandem p-n junctions. These p-n junctions have semiconducting band gaps spread out over the spectral distribution of the sun, arranged in decreasing order as shown in Fig 1.5. This allows the sunlight to be automatically filtered as it passes though the cell ensuring that the light is absorbed in the most efficient junction. Unfortunately the high production costs of multijunction cells make them only be used in space applications.

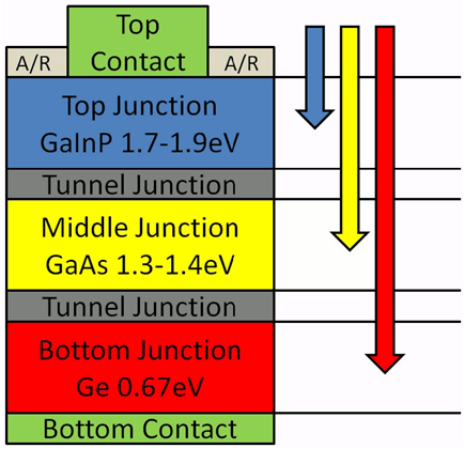

Figure 1.5 Schematic of 40% multijunction solar cell (King, 2007)

Figure 1.6 shows the efficiency evolution of best research cells by technology type. Those cells have been measured under standard conditions and confirmed at one of the world's accepted

centers, such as National Renewable Energy Laboratory (NREL), for standard solar-cell measurements.

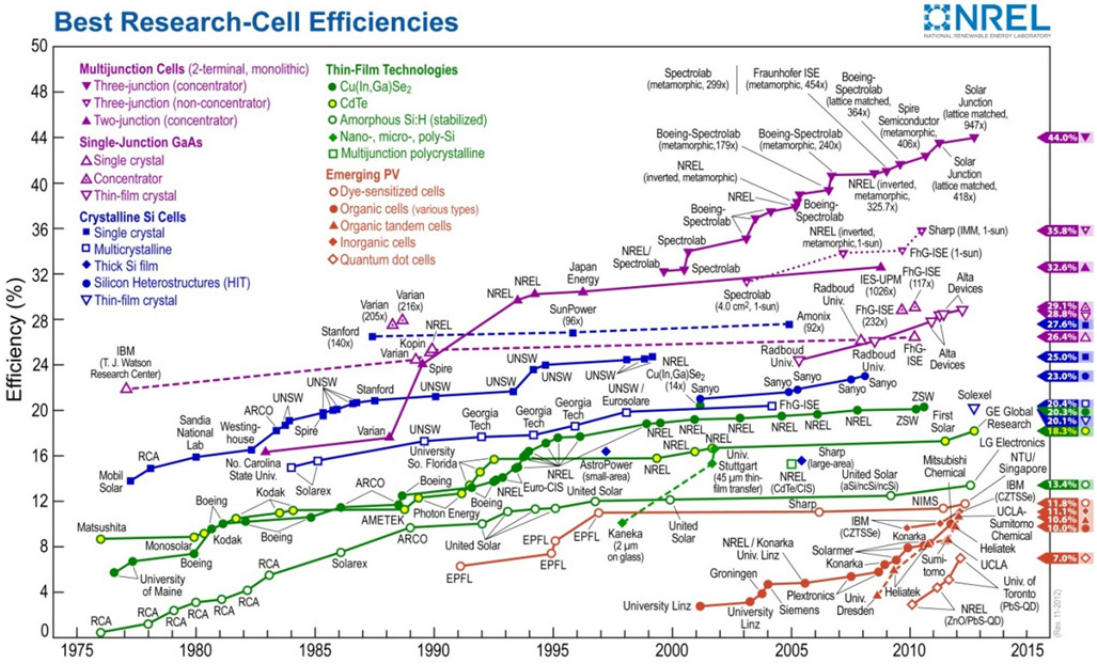

Figure 1.6 Reported timeline of solar cell energy conversion efficiencies evolution of best research cells by technology type (Kazmerski, 2012)

There are some quite fundamental investigations of the efficiency upper limit of a solar cell (Shockley and Queisser, 1961; Baruch, 1995). Based on the Eq. (1.2), the solar efficiency is proportional to the product of open circuit voltage V_{OC} and short circuit current I_{SC}. For the estimation of the photocurrent, it is known that the photon energy lower than the band gap cannot be absorbed by the semiconductor. Assuming there is an ideal cell with no optical losses, and the attainable current density for a given band-gap semiconductor is then obtained by integrating the solar spectral distribution. Starting value is the band gap energy and the integration runs over all shorter wavelengths.

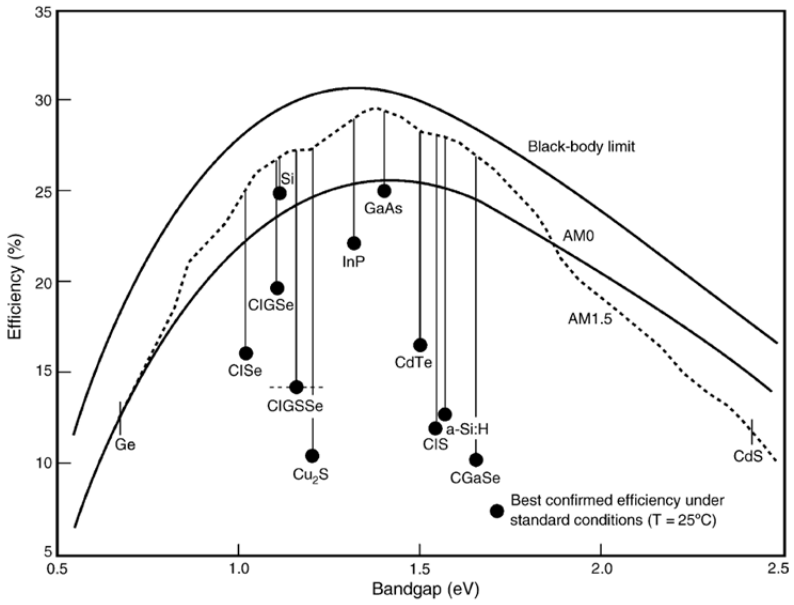

Figure 1.7 Maximum theoretical efficiencies dependence of the band gap energy for several solar cell technologies (Kazmerski, 2006)

Therefore, lower-band-gap semiconductors yield higher currents because they absorb larger parts of the spectrum. Photons are absorbed by exciting electrons from the valence band to the conduction band through the process of electron–hole pair generation. However, as required by the detailed balance (Shockley and Queisser, 1961), a radiative recombination process is also produced so that a free electron can decay from the conduction band to the valence band which is responsible for luminescent light emission. In fact, many of such luminescent photons with the energy slightly above the band gap can be reabsorbed, leading to new electron–hole pair generations and balancing out the recombinations. Assume that the charge transport is purely through diffusion of minority carriers. The relationship between current and voltage yields the following approximate expression:

$$V_{OC} = \frac{kT}{q} \ln\left(\frac{I_{SC}}{I_{00}}\right) \tag{1. 3}$$

where k is Boltzman constant, T is temperature, q is electrical charge of the electron, and I_{00} is the diffusion current of minority carriers in a p-type absorber. Therefore, lower-band-gap semiconductors yield lower voltage, however, higher current. The combined effect of the band gap on upper limits of a solar cell is shown in Fig. 1.7. The material properties of a-Si:H and CdTe will be discussed in detail later.

1.1.2 Laser Processing in Solar Cell Applications

The use of lasers in the processing of solar cell structures has been known for many years both for crystalline silicon (c-Si) and thin-film solar technologies. The maturity of the laser technology, the increase in scale of solar module production and the pressures to drive down cost of ownership and increase cell efficiencies have all contributed to the adoption of laser processes in industrial manufacturing. Part of the laser application for solar cell and solar module production is shown in Fig. 1.8. For c-Si solar cells the primary laser application is edge isolation and this is well-established in industrial production of most types of wafer-based cells. Other laser processes are used in the production of high-efficiency c-Si solar cells such as laser grooved buried contacts, emitter wrap through and laser fired contacts. To date, laser systems are also the tool of choice in thin-film module manufacturing both for scribing the cell interconnects and for the module edge isolation (Booth, 2010).

Although laser has been found many applications in solar cells, further investigations for those manufacturing process, including better understanding the process mechanisms and development of predictive capabilities, are still ongoing to improve the throughput and qualities of fabrications. In addition, more investigations in process innovation, such as one-step laser

process of surface texturing and crystallization, and pulsed laser film deposition, are also needed, although these laser processes for photovoltaics that have not entered the commercialization stage due to cost-effective processes or technical immaturity (Dunsky, 2007).

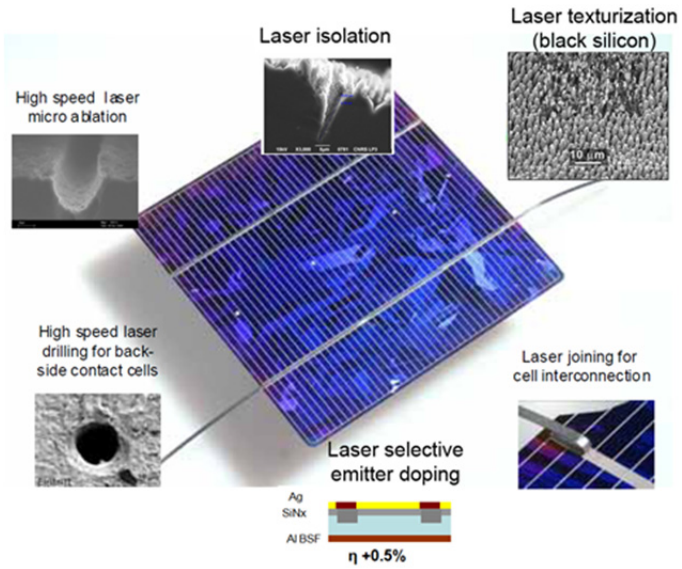

Figure 1.8 Laser applications for solar cell and solar module production
(Schulz-Ruhtenberg, 2009)

1.2 Introduction to Laser Surface Texturing and Crystallization of a-Si:H Thin Films

1.2.1 Hydrogenated Amorphous Silicon (a-Si:H) – A Background

Silicon (Si) is a fourfold coordinated atom which is usually tetrahedrally bonded to four neighboring Si atoms. In crystalline silicon (c-Si), this tetrahedral structure continues over a large range, generating a well-ordered crystal lattice. In contrast, this long range order does not exist in amorphous silicon (a-Si). Instead, the atoms form a continuous random network. In addition, due to the disordered nature of the material, some atoms have a dangling bond since not all the atoms within a-Si are fourfold coordinated. Physically, these dangling bonds represent defects in the continuous random network, acting as recombination centers that may cause a low

electron-hole density in solar cells. In order to decrease the density of dangling bonds, it is found that the plasma-deposited a-Si contained a significant percentage of hydrogen atoms bonded into the a-Si structure which reduces the dangling bond density by several orders of magnitude. This hydrogen atoms induced dangling bond passivation is essential to the improvement of the electronic properties, which indicates that hydrogenated amorphous silicon (a-Si:H) has a sufficiently low amount of defects to be used within solar cell devices.

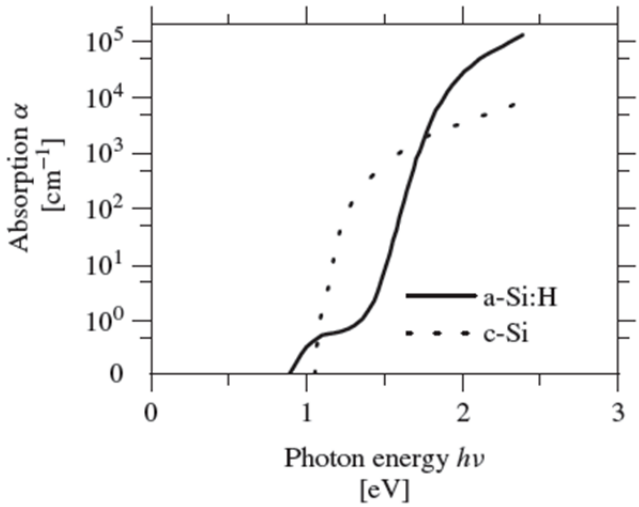

Figure 1.9 Spectra of the optical absorption coefficient α as a function of photon energy $h\nu$ of c-Si and a-Si:H (Luque and Hegedus, 2003 and Vanecek et al., 1998)

a-Si:H has two advantages compared to crystalline silicon (c-Si): First, the technology involved is relatively simple and inexpensive compared to that of crystal growth. For example, a-Si can be deposited to very inexpensive substrates, such as glass, for fabrication of large-area panels. The deposition method is now often termed plasma chemical vapor deposition (PECVD). Second, the optical properties of a-Si are very promising for collecting solar energy. Figure 1.9 shows the spectrum for the optical absorption coefficients α for a-Si:H and c-Si. It can be observed that when the photon energy is larger than the absorption energy threshold (band gap of a-Si:H ~1.7eV), the absorption coefficients of a-Si:H can achieve up to two orders of magnitude as that

of c-Si. This indicates that an a-Si:H film with a thickness of 500nm can absorb essentially all photons with the energies greater its band gap, however, c-Si material needs a few hundred micrometer thickness to achieve the same amount of absorption. The reason is because c-Si is an indirect-band-gap semiconductor and a-Si:H has a direct band gap. A schematic of light absorption in both direct and indirect band gap semiconductors is shown in Fig. 1.10.

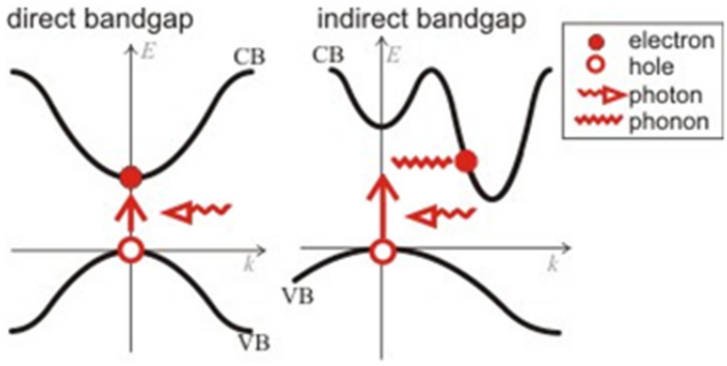

Figure 1.10 Schematic of light absorption in direct and indirect band gap semiconductors. CB and VB represent conduction band and valence band. *k* is crystal momentum (*k*-vector) and *E* is energy

The band gap called “direct” indicates that the momentums of the electrons and holes are the same in both the conduction band and the valence band, and an electron can directly absorb a photon and move from valence band to conduction band. In an “indirect” gap, a photon cannot be directly absorbed, because the electron must pass through an intermediate state and absorb or emit of a phonon where the phonon momentum equals the difference between the momentums of the electron and the hole. Therefore, light with photon energy close to the band gap can penetrate much farther before being absorbed in an indirect-band-gap material than a direct band gap material, so that c-Si does not absorb light very well.

However, a-Si:H also suffers two disadvantages: First, the cell efficiency of a-Si:H is relatively low compared to other thin film technologies as shown in Fig. 1.5; Second, the material hydrogenation is unfortunately associated with light induced degradation of the material, termed the Staebler-Wronski Effect (SWE), which induced an additional 50% reduction of the initial efficiency when exposed to sunlight over a period of several months (Staebler and Wronski, 1980). The most important material properties that play a role in the SWE are the high disorder in the Si network and high concentration of impurities, which cause some atoms to have dangling bonds that act as defects. Although these dangling bonds can be passivated by hydrogen, light exposure generates electron-hole pairs that will combine. The released energy can break the Si-H bond and promote H to a transport state. The diffusing H-atom successively breaks Si-Si bonds creating Si-H bonds and a neighboring dangling bond. This increasing defect density caused by the so-called SWE can further reduce the cell efficiency. In a thermal annealing process, the hydrogen atoms will revert back to their original positions. This process can reverse the SWE; however, the same degradation process will happen again when the material is exposed to sunlight (Kolodziej, 2004).

Due to their low efficiency and instability, a-Si:H thin-film solar cells require a highly efficient light-trapping design to absorb a significant fraction of the incident sunlight and material property changes to increase stability against the SWE. Antireflection (AR) coatings (Fig. 1.1) and front-side texturing through the use of alkaline-based solutions, such as KOH and NaOH etching, have been used on crystalline silicon solar cells, and pulsed laser irradiation has been used to enhance light trapping on both amorphous and crystalline materials (Martirosyan et al., 2007; Hylton et al., 2004; Crouch et al., 2004; Nayak and Gupta, 2007), however, AR coating

requires additional material and anisotropic wet chemical etching is not applicable for amorphous materials or thin films. In order to reduce the SWE, hybrid a-Si:H/nc-Si:H (hydrogenated nanocrystalline silicon) tandem modules have been developed and are able to achieve both higher efficiency and stability compared with single junction a-Si:H (Yamamoto et al., 2004). a-Si:H with reduced thickness will contain less defects, and the nc-Si:H is more stable and has wider spectral absorption compared to a-Si:H. To eliminate the need for two deposition steps, laser-induced crystallization of a-Si:H has been proposed to produce a mixture of nc-Si:H and a-Si:H and simultaneously form a light trapping texture on the surface of the material. Therefore, laser-based treatment of a-Si:H may solve the efficiency and stability issues in a one-step process, which is a promising methodology for thin film solar cell fabrication.

1.2.2 Laser Surface Texturing

Surface texturing can be induced by reactive ion etching (RIE), chemical etching and laser processing. Compared with other methods, laser can introduce sharper surface geometries which lead to a better light trap. In addition, laser surface texturing leads to a lower manufacturing cost than that of RIE, and can be widely used for amorphous and crystalline materials; however, chemical etching is only applicable to crystalline material. Laser surface texturing can be used for enhancing tribological properties of mechanical components, such as piston rings and seals, and modification the cell response of polymeric material in biological applications. Laser surface texturing also can be utilized to fabricate light trapping structure of semiconductors in order to improve their optical properties. Figure 1.11 shows two examples of laser surface texturing on piston ring and c-Si.

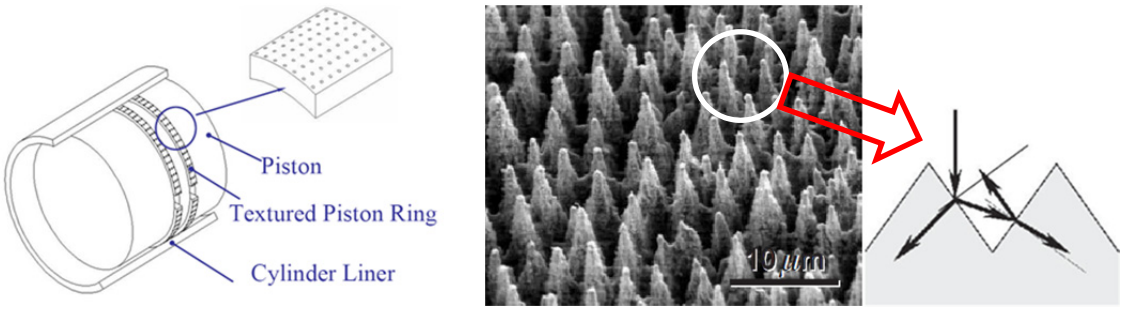

(a) (b)

Figure 1.11 (a) Schematic of laser surface texturing on piston ring; (b) femtosecond laser texturing of light trapping structure on the c-Si surface and schematic of light multi-reflection between textured spikes. (Etsion, 2008; Carey, 2004)

For bulk c-Si, the light trapping structure can be achieved by laser surface textured V-groove shaped, patterned and micro-spiked structures, which is more widely applied than that of chemical surface etching. Under a more restrict processing window than c-Si, laser surface texturing can be also applicable for thin films, especially for unstable amorphous cells, such as a-Si:H, which will be partially crystallized during the laser processing that may potentially increase the stability simultaneously. In order to manufacture pattern surface structures, the laser used needs to be suitable for the workpiece material and capable of either melting or ablating the material. In practice, based on the pulse duration, there are two main types of laser utilized in laser surface texturing – femtosecond (fs) lasers, such as Ti:sapphire laser, and nanosecond (ns) lasers, including Nd:YAG laser and excimer lasers. Regarding to the wavelength, ultraviolet (UV) is preferred for ns lasers, since the large photo energy compared to the band gap of semiconductor could lead to a deep absorption. However, the wavelength of an fs laser does not need to be absorptive to the target material, because its unique property – nonlinear absorption enables the laser-material interaction.

1.2.2.1 Femtosecond Laser Interaction with Wide-Band-Gap Materials

Surface texturing can be achieved by both femtosecond and long-pulse lasers, however, femtosecond lasers are better suited for precise micromachining due to their extremely high peak power and ultrashort pulse duration, which leads to greatly reduced thermal energy diffusion and heat-affected-zone and allows for precise control over the texturing process. Keldysh, 1965, shows that the non-linear absorption is triggered by photoionization and it occurs on a much shorter time scale than that required for energy transfer from electrons to the lattice. The energy absorption leads to excitation of the electrons which become freely from the valence band. When the intensity of the femtosecond laser pulse reaches $10^{13} - 10^{15}$ W/cm^2 or more, multiphoton or tunneling ionization will occur within a few to tens of femtoseconds. When the intensity drops below 10^{12} W/cm^2, avalanche ionization is triggered by the seed electrons supplied by multiphoton ionization. Some researchers refer to this type of ionization as multiphoton impact ionization (Jiang and Tsai, 2003). Excited free electrons are heated by the laser pulse, and subsequently collide with the electrons constrained in the valence band resulting in the generation of multiple free electrons. The process keeps producing the free electrons necessary for the plasma formation. According to the Stuart et al., 1995, the free electron density is governed via Fokker-Planck equation:

$$\frac{\partial n(E_K,t)}{\partial t}+\frac{\partial}{\partial E_K}\left[R_J(E_K,t)n(E_K,t)-\alpha(E_K)E_P n(E_K,t)-D(E_K,t)\frac{\partial n(E_K,t)}{\partial E_K}\right]=S(E_K,t) \quad (1.4)$$

where n is electron density distribution, E_K is electron kinetic energy, E_P is the phonon energy, t is the time, α is the electron–phonon energy transfer to the lattice, R_J is the electron heating rate, D is the diffusion coefficient and S represents sources and sinks of electrons. The three terms of $R_J(E_K,t)n(E_K,t)$, $\alpha(E_K)E_P n(E_K,t)$ and $D(E_K,t)\frac{\partial n(E_K,t)}{\partial E_K}$ represent the rate of electron

distribution and have the following physical meanings: the first term represents Joule heating, the second is because of the inelastic scattering of phonons and the third is the electron energy diffusion. Joule heating rate can be given as:

$$R_J\left(E_K,t\right)=\frac{1}{3}\frac{e^2\tau_m\left(E_K\right)}{m^*\left(1+\omega^2\tau_m\left(E_K\right)^2\right)}\varepsilon^2 \tag{1.5}$$

where $1/\tau_m$ is the energy-dependent, electron-phonon transport scattering rate, m^* is the effective mass of an electron, and ω is the laser frequency. The energy diffusion term is expressed as:

$$D(E_K,t)=2E_K R_J\left(E_K,t\right) \tag{1.6}$$

The term of $S(E_K, t)$ in Eq. (1.4) consists of a photoionization component and an impact ionization component:

$$S\left(E_K,t\right)=S_{Pi}\left(t\right)+4R_I\left(2E_K+U_{IP}\right)n\left(2E_K+U_{IP},t\right)-R_I\left(E_K\right)n\left(E_K,t\right) \tag{1.7}$$

where $S_{Pi}\left(t\right)$ is the multiphoton ionization component, U_{IP} is the ionization potential and $R_I\left(E_K\right)$ is impact ionization rate described by the Keldysh impact formula (Keldysh, 1965):

$$R_I\left(E_K\right)=\delta\left(\frac{E_K}{U_I}-1\right)^2 \tag{1.8}$$

where δ is the proportionality constant.

After the laser pulse, the energy absorbed by the electrons is transferred back to the material over a picosecond time scale, which can be expressed as:

$$E\cong n_e\left(2\frac{m_e}{m_i}v_{ei}+\frac{1}{2}m_i u_i^2+\frac{\upsilon_e^2}{3\eta}\right) \tag{1.9}$$

The first term in Eq. (1.9) represents the electron-ion energy exchange rate, where m_e and m_i are the masses of electrons and ions, respectively, and v_{ei} is the momentum exchange rate. The total energy transferred is a function of the Maxwellian distribution functions of collision between

ions and electrons and their initial and final momenta (Polishchuk and Meyer-Ter-Vehn, 1994), simplified by assuming that the material is initially cold. The second term is due to ion acceleration by the gradient of the electron pressure, and it assumes that ions are initially cold and electronic pressure, $P_e=n_eT_e$, where T_e is temperature of electrons. Kinetic velocity of ions can be estimated by the Newton's equation: $\frac{\partial(m_i n_i u_i)}{\partial t} \cong -\nabla P_e$ as $u \cong ZT_e t / m_i l_{abs}$ where Z is the average ion charge and t is energy transfer time which is in the order of a few picoseconds. The last term means the contribution from the nonlinear electronic heat conduction, driven by the heat wave which emerges as a precursor to the shock wave. η is thermal conduction coefficient and v_e is the velocity of electrons. Within a few microseconds, the thermal energy of the plasma that diffuses out from the focal volume can cause thermal melting or vaporization and can leave behind permanent structural damage for sufficiently high laser intensities (Gattass and Mazur, 2008; Sundaram and Mazur, 2002).

1.2.2.2 Physical Description of Femtosecond Laser Surface Texturing

Extensive work has been performed on femtosecond laser induced surface texturing of semiconductors, such as silicon, and the corresponding two-stage texture formation mechanism has been described by Tull et al., 2006. During the early stage of formation, there are three important patterns occurring at different pulse numbers. A ripple pattern at the wavelength of the laser forms after the second pulse, with the ripples' long axis perpendicular to the laser polarization, which is called light-induced periodic surface structure (LIPSS). After irradiation of five pulses, the ripple pattern coarsens significantly and beads begin to form along the ripples at a spacing larger than the laser wavelength. At the tenth pulse, the beads become more pronounced with certain spacing for both the vertical and horizontal directions. The spacing and

size of beads strongly depend on capillary waves and surface tension, which are influenced by impurities, molten depth, and temperature. This bead-like pattern remains in essentially the same arrangement throughout the entire late stage of the formation. The beads act to concentrate subsequent laser light into the valleys between them through reflection off the sides of the beads. This causes the ablation rate to be higher inside the valleys than on the bead tips, which leads to sharpening of the beads into spikes after hundreds of laser pulse assisted texturing steps (Fig. 1.11b). Figure 1.12 shows that the tips of all microstructures are at or below the surface of the original silicon wafer, which indicates that those conical structures are ablation-dominant formed rather than grown (Carey, 2004).

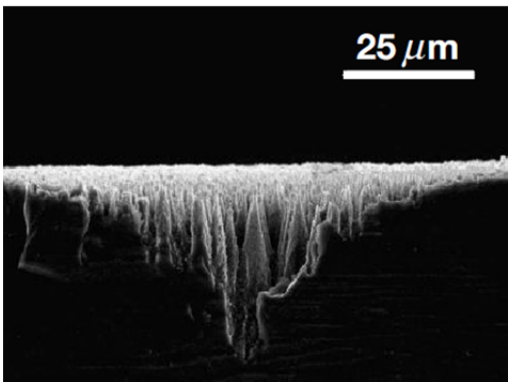

Figure 1.12 A side-view of a femtosecond laser (wavelength of 800nm, pulse duration of 100fs, fluence of 1J/cm^2) textured c-Si sample, cleaved through an irradiated spot. The tips of the structures are all at or below the original wafer surface, showing femtosecond laser surface texturing is a ablation-dominant process (Carey, 2004)

1.2.2.3 Physical Description of Nanosecond Laser Surface Texturing

Nanosecond laser can produce micro-conical/column spikes on semiconductor surfaces, for instance, silicon or germanium (Ge), after a few hundred to thousands of pulses. Compared to DPSS (diode-pumped solid-state) lasers, excimer laser can deliver a larger spot size with

spatially uniformly distributed pulse energy through the mask-projection and beam homogenization system. The spike formation mechanism can be divided into two steps: spike initialization and growth. Dehghanpour et al., 2009, indicated that the sharp spikes are initially caused by the generation of capillary waves due to the micro-fluid mechanics of the molten layer, and then the periodic bead-like structure is formed as the seed of the final spikes. The development of the spikes is explained based on the formation of preferential removal of the material through Vapor-liquid-solid (VLS) mechanism (Lowndes et al., 2000). The silicon-rich vapor generated between the spikes preferentially redeposits on the molten tip of the microcolumns due to high accommodation coefficient of liquid, while the vapor prefers to dissolve into the liquid rather than solid, so that those spikes grow uniformly with the increasing of laser pulses. At the sides of the columns, because the increased reflectivity with increasing incident angle, they are not melted or ablated. Figure 1.13 shows both the top- and side-view SEM images of excimer laser textured silicon sample. In contrast to femtosecond laser, the tips of spikes textured by nanosecond pulses protrude well above the original surface, suggesting that growth is a more dominant formation mechanism rather than ablation.

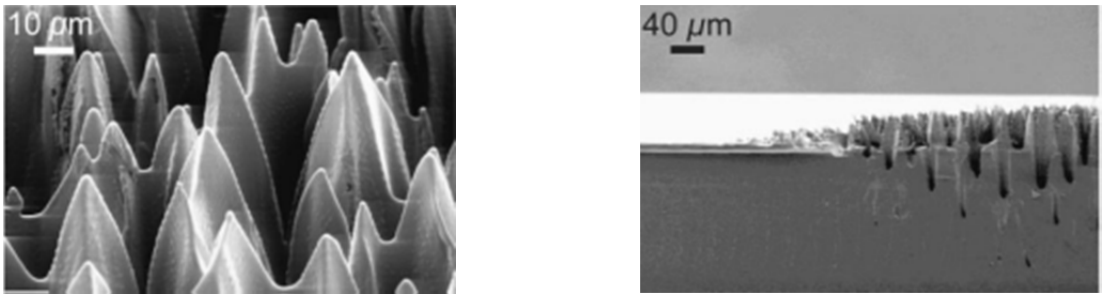

(a) (b)

Figure 1.13 SEM images of (a) top view (b) side view of excimer laser (wavelength of 248nm, pulse duration of 30ns, fluence of 3J/cm^2) surface textured silicon surface formed in SF_6, showing the growth-dominant formation via VLS mechanism (Crouch et al., 2004)

Regarding to the surface texturing on a-Si:H thin films, Mathe et al., 1992, showed that the surface roughness caused by single-nanosecond-pulse irradiation on a-Si:H could be almost two orders of magnitude larger than that of non-hydrogenated a-Si, and mentioned that the movement of H_2 gas bubbles generated by the combination of H atoms and molecules in the ambient medium are responsible for the surface roughness. Therefore, the mechanism of the spike formation on a-Si:H thin films is likely the combination of surface texturing on silicon and the effect of hydrogen movement which improves the texturing behavior. However, hydrogen effect only exists in nanosecond-pulse irradiation due to the deep molten pool and high temperature gradient, and no influence is investigated for femtosecond laser texturing behavior since it is an ablation-dominant process.

1.2.2.4 Constitutive Model for Spike Formation by Excimer Laser Irradiation

In order to explain the formation of surface structures of a-Si film irradiated by an excimer laser, it is assumed that the formation of a molten pool is formed as superficial waves of thermo-capillary nature. To quantify these two phenomena, two problems have been solved: first, the absorption of the laser energy and heat transfer into the irradiated sample; second, propagation and freezing of superficial waves on the surface of molten pool. The heat transfer phenomenon can be modeled by the combination of the conservation of energy principle and the Fourier´s law, obtaining the equation as follow (Carslaw and Jaeger, 1958)

$$\rho(T)C_P(T)\frac{\partial T(\vec{r},t)}{\partial t} - \nabla[\kappa(T)\nabla(T(\vec{r},t))] = 0 \tag{1.10}$$

where, ρ, C_P, κ, T, r and t are density, specific heat, thermal conductivity, temperature, radius and time, respectively.

The geometry of the irradiated sample can be considered as semi-infinite, since the thermal penetration depth is lower than the thickness of the sample (Bejan, 1993). Assume the material is isotropic and uniform, the spatial pulse energy distribution is uniform and the dimension of the irradiated area is bigger than the thermal penetration depth. The problem can be considered as unidimensional and the temperature field will depend exclusively on the depth (Prokhorov et al., 1990). Finally, the thermo-physical parameters, such as density, specific heat and thermal conductivity, of the a-Si film are assumed to be constants. A numerical approach based on the finite element method is used to solve the differential equation (1.10) with the initial and boundary conditions as discussed. A one-dimensional thermal filed of the laser irradiated sample is obtained for different laser fluences, and values of the depth and lifetime of the molten pool, thermal gradient and the solidification velocity are derived.

The thermal gradient in the molten pool drives the motion of the liquid material provoking the deformation of the surface and generating capillary waves that propagates at the surface. This convective motion can be attributed to the thermal variation of the surface tension, and the pressure differences created at a curved interface support the evolution of the deformations in the liquid surface. In order to obtain the amplitude of the thermo-capillary waves, the Navier-Stokes equation has been solved for a stationary and incompressible fluid. The solution integrated in z-direction provides the change in height at different locations in the molten pool induced by the motion of the waves, which reflects the final formation of the spikes (Schwarz-Selinger et al., 2001).

1.2.3 Laser Crystallization

1.2.3.1 Physical Description of the Melt-Mediated Process via Pulsed ns Laser

Pulsed laser annealing has received enduring interest as a means for crystallizing amorphous and polycrystalline silicon films for thin film transistor (TFT) fabrication. In addition to its practical applications, it is also a powerful tool for studying the fundamental characteristics of rapid solidification of a wide array of semiconductor, ceramic and metallic systems. Excimer laser systems are typically preferred as they operate at UV wavelengths with an enhanced optical absorption enabling efficient laser-material energy coupling. The process proceeds as follows: the film surface is pulse irradiated (pulse duration ~ 30 ns) where most of the laser energy is absorbed over a very near surface layer causing a rapid increase in surface temperature. When the incident energy is high enough, surface melting occurs and forms a liquid-solid interface that will then propagate toward the underlying substrate as thermal diffusion takes place. The ultimate depth of melting is typically proportional to the incident laser energy, however, the laser fluence may or may not be sufficient for melting the film through the entire thickness.

Hydrogen may have some effects on the crystallization of a-Si:H thin films. Im et al., 1993, showed hydrogen could play a role in triggering explosive crystallization. When the incident laser energy density is only sufficient to induce partial melting of a-Si layer, explosive crystallization can be observed and converts a-Si into fine-grained polycrystalline Si via a melt-meditated mechanism (Polman et al., 1991). The buried liquid layer is at a temperature higher than the melting point of a-Si but lower than the melting point of c-Si, and propagates into the a-Si layer by simultaneously melting of a-Si and solidifying into c-Si. Due to latent heat difference between c-Si and a-Si, the propagation is self-sustaining. In addition, hydrogen may slow down

the crystallization process because more energy density is needed to crystallize a given depth when hydrogen is present (Mathe et al., 1992). Large-grained polycrystallites are generated at the hydrogen depletion region near the surface, and fine-grained ones are located at hydrogen contained area underneath. Therefore, hydrogen could cause fine-grained polycrystallites by explosive crystallization and spend part of the laser energy that slows down the crystallization process.

1.2.3.2 Femtosecond Laser Induced Crystallization

In contrast with nanosecond pulse induced melt-mediated crystallization, femtosecond laser excitation of semiconductors is assumed to initiate ultrafast phase transition via the plasma annealing mechanism. A high level of electronic excitation will severely weaken interatomic bonds which lead to disordering of the lattice through "cold" atomic motion. The conservation equation for electrons excited by multiphoton absorption can be written as (Choi et al., 2003)

$$\frac{\partial N(x,t)}{\partial t} = \frac{(1-R)\alpha I(x,t)}{h\nu} + \frac{(1-R)^2 \beta I^2(x,t)}{2h\nu} \tag{1.11}$$

where N is electron density, R is reflectivity, α is linear absorption coefficient, $h\nu$ is the photon energy of the laser beam, β is the two photon absorption coefficient, and $I(x,t)$ is the laser intensity expressed as follows (Choi et al., 2003),

$$\frac{\partial I(x,t)}{\partial t} = -(\alpha + \Theta N) I \tag{1.12}$$

where Θ is the free carrier absorption cross section. If the critical density of electrons, which is estimated to be 10^{22} cm^{-3}, is exceeded, they are excited out of the bonding states of the valence band into the conduction band, and a non-thermal ultrafast phase transition will occur. Due to the removal of a significant number of electrons from the material, the bond charge will be so weak

that the material structure will no longer be stable and will collapse caused by the atoms' enhanced mobility. Thus the phase changes to liquid without thermal effects, which is called the plasma annealing mechanism. As the plasma becomes less dense due to expansion and energy transfer, the material will pass back through the phase transition and covalent bonding will gradually reappear (Vechten et al. 1979; Linde and Fabricius, 1982). Choi et al., 2003, considered that the non-thermally melted layer vanishes in a few picoseconds during which time a portion of the covalent bonds start to reappear due to relaxation of electrons back to the valence band. Within a nanosecond, the surface starts to be melted due to thermal diffusion after the transfer of energy from the excited electrons to the material. Resolidification of this thermal melting layer causes the final crystallization which is the same as melt-mediated crystallization. Callan et al., 2001, also suggests that the ultrafast non-thermal phase transition described above does not lead to a thermodynamically stable crystalline phase, but to a nonequilibrium disordered phase, and this disorder-to-disorder phase transition can cause defect formation which is considered to be the driving force for subsequent rapid nucleation (Choi et al., 2003). This process which includes non-thermal and thermal melting leading to solidification describes femtosecond laser-induced crystallization, which is different from nanosecond laser crystallization where only a rapid thermal melting and solidification process occurs.

1.3 Introduction to Laser Scribing of Thin-Film Solar Cells

1.3.1 Cadmium Telluride – A Background

Cadmium Telluride (CdTe) is a direct-band-gap (1.5eV) II-VI semiconductor with a high absorption coefficient, $>5\times10^{5}cm^{-1}$. As shown in Fig. 1.7, the dependence of ideal solar cell conversion efficiency on band gap shows that CdTe is nearly optimally matched to the solar

spectrum. CdTe can absorb 99% of the absorbable AM1.5 photons within 2μm of film thickness. CdTe appeared as a new electronic material in 1947 when Frerichs synthesize CdTe crystals by the reaction of Cd and Te vapors in a hydrogen atmosphere and measured their photoconductivity (Frerichs, 1947). Superstrate polycrystalline CdTe/CdS heterojunction thin-film solar cells were first demonstrate by Adironvich et al., 1969, with evaporated CdTe on a CdS/SnO_2/glass substrate, yielding an efficiency >2%.

To date, thin-film CdTe solar cells are the basis of a significant technology with major commercial impact on terrestrial photovoltaic production. Large-area monolithic CdTe thin-film modules demonstrate long-term stability, competitive performance, and the fast payback time in current PV technologies as shown in Fig. 1.14. The maximum experimentally observed efficiency of a single CdTe mini-module has been certified by the National Renewable Energy Laboratory (NREL) to reach 17.3%, whereas the theoretical value is ~28%. The efficiency if further reduced to only 11.7% for a large-area panel after scribing. Nonetheless, the efficiency potential of CdTe panels has spurred significant industry interest and investment into their use. General Electric Company announced plans in 2011 to build the largest CdTe-based thin-film solar cell manufacturing plant in the US by 2013, capable of producing 400MW worth of solar panels a year with average module efficiencies of 14%. The largest manufacturer of CdTe thin-film panels, First Solar, plans to achieve production module efficiency of 13.5% to 14.5% by the end of 2014 (Burger, 2011). The ability to reach these efficiency goals and to approach the efficiency of a single mini-module requires significant improvements in the manufacturing processes.

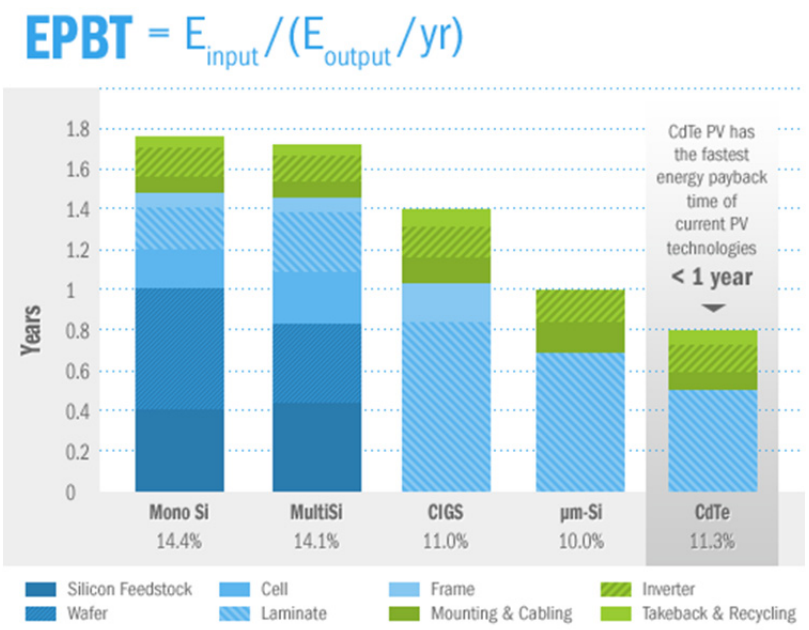

Figure 1.14 Energy payback time (EPBT) of current PV technologies (First Solar, 2012)

1.3.2 Structure of Multilayer Thin-Film Solar Cells

Thin film solar cells are a promising technology for terrestrial and space photovoltaic (PV) applications due to their lower material cost compared to crystalline silicon (Chopra et al. 2004). Typical thin-film solar cells used in terrestrial PV applications consist of back contact, absorber and front contact films deposited on inexpensive substrates, such as glass. The 400-500nm thick front and back contact layers are used to collect the current produced in the 2 to 3µm thick absorber layer. This represents a significant reduction in material volume compared to bulk crystalline silicon panels which are hundreds of microns thick. Absorber materials used in thin film cells include a-Si:H, a-Si:H/µc(microcrystalline)-Si:H tandems, CdTe and CI(G)S. Transparent conducting oxide (TCO) materials such as SnO_2 (tin dioxide), ITO (indium tin oxide) and ZnO (zinc oxide) are used for the front contact layer so that light can reach the absorber while the back contact layer can be TCO or metal, such as nickel or aluminum.

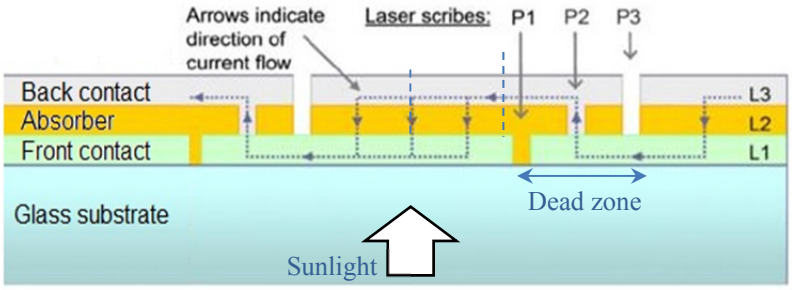

Figure 1.15 Interconnection schematic of thin-film solar module (Bovatsek et al. 2010)

The first step to power generation with a solar panel is the photoelectric generation of free electrons within the absorber layer after exposure to sunlight. Current is produced by the movement of carriers, electrons and holes, to the back and front contact layers, respectively. The efficiency of solar panels, however, is hampered by resistive losses in the module which are proportional to the square of this current. In practice, photocurrent is decreased by sectioning (scribing) the module into a large number (100 to 200) of mini-modules and connecting them in series to create a high-voltage, low-current device (Booth, 2010). Since each layer in the solar module must be scribed after deposition, scribing is performed in 3 steps – Patterns 1, 2 and 3 (P1, P2, P3). P1 denotes scribing of the front contact layer. P2 and P3 denote selective removal of the absorber layer and simultaneous removal of the absorber and back contact layers, respectively. The resultant cell interconnections and structure are depicted in Fig. 1.15. The photo-excited current flows between the back and front contact layers in every mini-module and between mini-modules through the P2 scribing slot which is filled with conductive back contact material.

1.3.3 Laser Scribing Processes

Compared to mechanical scribing, key advantage of laser scribing is able to enable much smaller line width (50μm Vs. 500μm), so the "dead zone" can be much smaller with higher efficiency. In addition, it is currently only industrial standard process for high speed mass production (scribing speed around 1 m/s Vs. 0.05~0.1 m/s). Laser scribing can be performed under two configurations: film- and glass-side scribing. The dominant removal mechanism of film-side laser scribing is thermal ablation as shown in Fig. 1.16a which has been shown to leave a large heat-affected zone around the scribe, can cause poor isolation between cells and low shunt resistance. This process also leaves non-vertical sidewalls as depicted in Fig. 1.17a and high positive ridges along the edge of the scribe line, which act as electrical shorts (Compaan et al. 2000). In contrast, glass-side laser scribing, which is applicable to brittle layers such as absorber and TCO materials, is a thermo-mechanical process which involves stress induced material failure and removal, commonly referred to as micro-explosion processing (Matylitsky et al. 2011). In this process, localized laser energy absorption causes the formation and expansion of a high pressure plasma at the film/substrate interface which expands resulting in mechanical removal of the solid film above (Fig. 1.16b). As shown in Fig. 1.17b, the sidewalls formed with this method are steep and no protrusions are detected at the edges. While glass-side scribing has significant advantages over film-side scribing, the HAZ, imperfect sidewall geometry, and microcracks have yet to be eliminated.

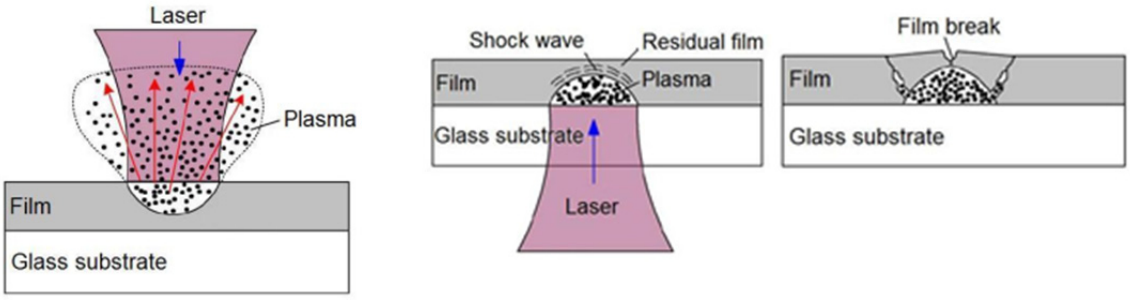

(a) film-side laser scribing (b) glass-side laser scribing

Figure 1.16 Schematic of (a) Ablative removal in film-side laser scribing; (b) Micro-explosion-based removal in glass-side laser scribing (Wang et al. 2010)

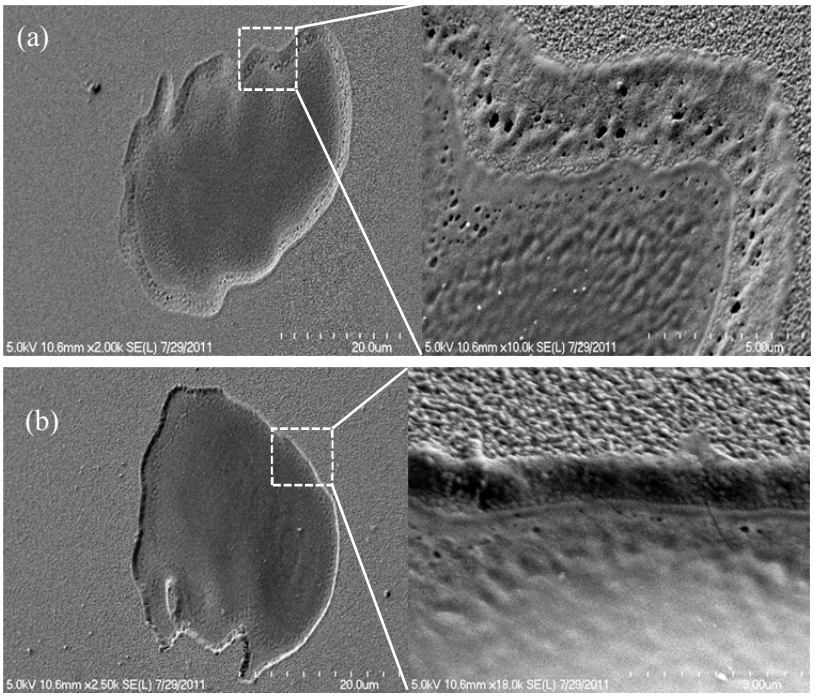

Figure 1.17 SEM images of overview and boundary of (a) film-side and (b) glass-side single pulse irradiation of SnO_2:F thin film on glass substrate at 127 J/cm^2

Processing steps typical of glass-side laser scribing are shown in Fig. 1.18. Due to the large optical absorption depth in TCO materials, the P1 process is dominated by thermal ablation, typically by 1064nm laser irradiation. In contrast, the P2 and P3 processes, which are both initiated by removal of the absorber layer, utilize 532nm laser irradiation due to the large

difference in damage thresholds between the absorber and TCO materials at this wavelength and occurs through a micro-explosion mechanism due to the localized absorption by the absorber layer. First Solar currently uses 1064nm laser irradiation for P2 and P3 patterning due to the longer laser lifetime which enables cost-effective manufacturing despite the lower scribing quality (Bohland et al. 2000, 2004). The deposition of each layer between scribing steps is performed to cover the surface of the previous layer and fill any previously formed scribe slots. While the majority of scribing operations are performed following the process described above, P2 and P3 scribes for CIGS-based solar cells are performed using film-side laser scribing since the contact layer deposited on the substrate is not transparent to laser irradiation (Murison et al. 2010).

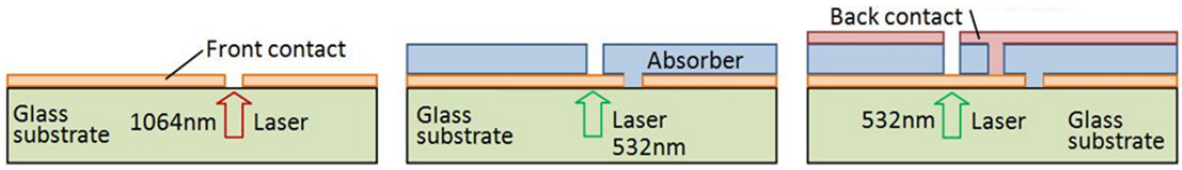

(a) Pattern 1 (b) Pattern 2 (c) Pattern 3 (P3)

Figure 1.18 Schematic of P1, P2, and P3 laser scribing of multilayer thin films. P1 removes the front contact layer. P2 removes the absorber layer while P3 removes the absorber and back contact layers simultaneously. (Dunsky et al. 2008)

Further improvements in scribing quality have been achieved by reducing thermal effects through the use of ultrashort pulse-duration lasers. Scribing slots with steep sidewalls and low thermal effect have been produced by picosecond (ps) pulse-duration lasers (Hu et al. 2010) while Bian et al. showed nearly nonthermal ablation of ITO-coated glass by femtosecond pulse-duration laser processing (Bian et al. 2010). While important for certain applications, ultrashort pulse-duration lasers are complex and expensive which results in increased production costs for solar cell panels. Femtosecond lasers are further limited by their low output frequency which

eliminates the possibility for high speed processing. In addition to temporal pulse-duration effects, it has shown that the greater uniformity of energy deposition from flat top spatial beam profiles can lead to higher scribing quality with reduced thermal effect and steeper sidewalls compared to Gaussian pulses (Patel, 2010 and Laskin et al. 2010).

1.3.4 Laser Scribing Induced Defects Formation

While scribing reduces resistive losses in the module by decreasing photocurrent, it also forms dead zones between the P1 and P3 slots, which contribute to reductions in module efficiency. The direct connection between the front and back contact layers in these zones causes them to not be able to generate voltage. The width of the dead zones is determined by the offset between scribe slots and the scribe widths. Non-vertical side-wall geometries can increase the effective scribe width, while thermal effects can cause adjacent material to experience microstructural changes increasing the density of defects which act as recombination centers for free electron-hole pairs. In addition, the formation of micro-cracks, delamination, and residual film material after scribing can lead to further reductions in module efficiency due to increased electrical resistance between layers or decreased isolation across the scribe slot as shown in Fig. 1.19. Next generation products are projected to reduce the scribe width from 25-50μm to 25-30 μm resulting in dead zones widths of less than 200μm (Dunsky et al. 2008).

Due to the unique mechanical fracture caused by the micro-explosion process, defects as sidewall definition, micro cracks, film delamination, residue materials and dislocations are induced resulting in poor photocurrent and inactive cells. Lauzurica, 2011, reported the formation of irregular scribe boundaries and observed film peeling after ns-pulsed, P3 laser

scribing of a-Si-based thin film solar cells. Even with the use of ultra-short pulse-duration lasers, defects such as film delamination, as presented in Fig. 1.20a (Gecys et al. 2010). Tamaoki et al., 2010, investigated the formation of micro-cracks and film delamination after scribing of Mo (molybdenum) metallic film on glass substrate as shown in Fig. 1.20b. Wang et al., 2013, have shown that the residue material of CdS are observed in the scribe slots during ns-pulsed, P2 laser scribing of CdTe-based, multilayer thin films. In addition, through dislocations and micro-twins are also detected at the crack tips which can affect the long-term stability of solar cells.

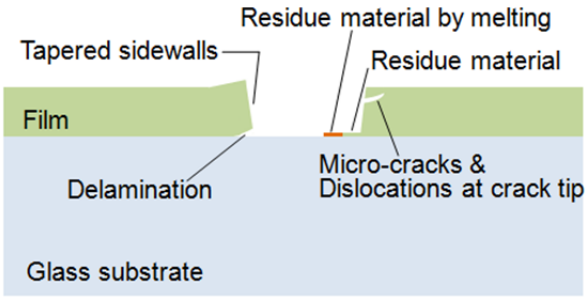

Figure 1.19 Schematic of the defects, such as non-vertical sidewall, thermal effect, residual material, film delamination and micro cracks, caused by laser scribing

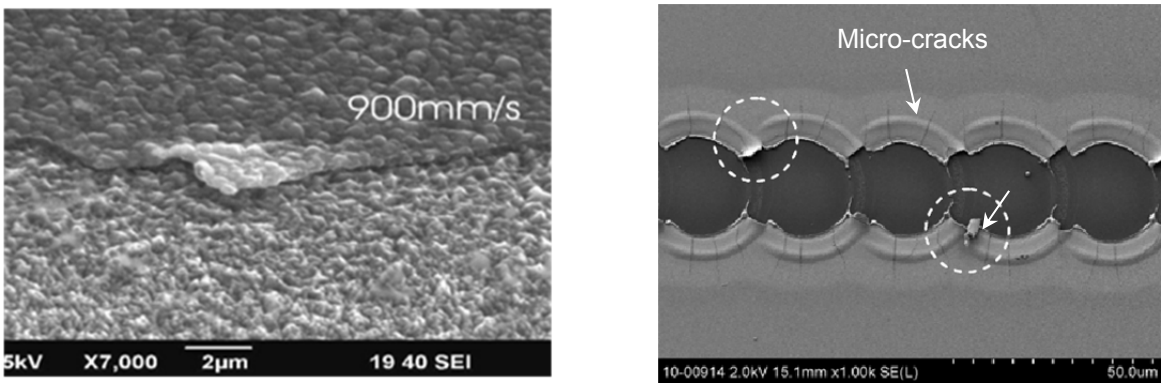

(a) (b)

Figure 1.20 (a) SEM image of P2 scribing of a-Si:H film from glass side using a 532nm ps laser, showing a-Si:H film delamination after processing; (b) SEM image of Mo film removal through 20ns-pulses at the repetition rate of 250kHz and scan speed of 5m/s. Dashed circles denote the delamination of Mo films. (Gecys et al. 2010; Tamaoki et al. 2010)

Defects generation can also be introduced by laser-induced thermal effect during micro-explosion. Luque et al., 2003, showed that laser induced high temperature can cause thermal damage of TCO material underneath and interdiffusion of sulfur into TCO layers. Wang et al., 2013, showed that partial of the residue CdS had been melted and recrystallized after P2 scribing. In addition, when the laser photon energy is higher than the band gap of semiconductors, defect formation of vacancies (Schottky defects) can be introduced even at low laser fluences (less than the melting threshold). Emel'yanov et al. 1992, showed that the fraction of the energy of the photo-excited electron-hole pairs is transferred in the process of electron-phonon relaxation and heat the lattice. The strong rise in temperature T (up to melting point) leads to the generation of defects by thermo-fluctuation, which are frozen in after the end of the pulse due to the very rapid cooling process. The density of the thermo-fluctuation defects reaches its stationary value

$$N_d = const \cdot \exp\left[-\frac{E_A}{K(T_0 + \Delta T)} \right] \tag{1.13}$$

where T_0 is the initial temperature, ΔT is the temperature rise due to laser heating, E_A is the defect formation energy, K is Boltzmann constant. The lattice deformation caused by the heating reduces the value of the defect activation energy in Eq. (1.13). The defect formation energy can also be reduced due to the localization of the electronic energy in some point of the crystal, which will decrease the potential barrier of the defect transition to a new equilibrium position. Thus, the localization of the electronic excitation on some initial defect can introduce new recombination centers due to the process of defect multiplication.

1.3.5 Influences of Laser-Induced Defects on Electrical Property Change

In order to mitigate the defect formation and optimize the scribing processes, it is important to understand the correlations between those defects and electrical property change, such as contact resistance, current and voltage (power) output and efficiencies, of solar cells. Golovan, 1996, showed significant decreases of photoluminescence of CdTe after the laser condition reaches the melting threshold ($40mJ/cm^2$) and explained the reason is because the generation of Schottky defects acting as recombination centers caused by laser-induced melting and recrystallization. Kontgers, 2010, have investigated the risk of power loss, up to 10% as shown in Fig. 1.21, in photovoltaic modules due to micro cracks induced inactive cells, and pointed out that the micro cracks can be continually opened up subjected to the mechanical and thermal stress. Acciani, 2010, have examined the abnormal heating in the restricted area of solar cells due to the presence of defects, such as voids, causes hot-spots, and the increased temperature will introduce dead cells in the solar panel. In addition, a dead zone between the P1 and P3 slots shown in Fig. 1.15 contributes to reductions in solar module efficiency. The width of dead zones is determined by the offset between scribe slots and the scribe widths. The scribe width can be affected by many factors, such as the laser pulse shape/duration and spot size, formation of film delamination and micro-cracks as well as non-vertical side-wall geometries.

While various defects exist at the same time and the correlation between those defects and laser scribing conditions is not straightforward. How to pick and drop multi-existing defects is a key process for defect mitigation process. These defects can be divided into four levels through their effects on solar cell performance. First, film delamination, macro/micro cracks and sidewall definition responsible for the dead zones, and residue material and TCO damage related to

contact resistance; Second, melting/recrystallization of CdS responsible for density of Schottky defects acting as recombination centers, and diffusion of sulfur into TCO layer related to contact resistance; Third, micro-bubbles/voids responsible for abnormal heating; Fourth, formation of dislocations and micro-twins at crack tips responsible for crack initiation (long-term stability).

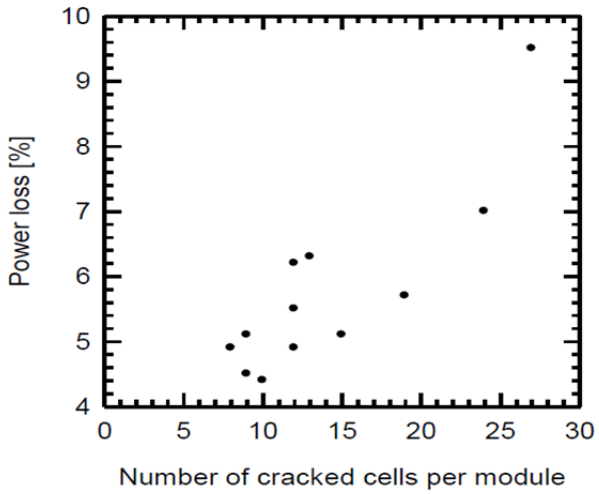

Figure 1.21 Relationship between the power loss and the number of cells cracked in the mechanical load test, showing the power loss can reach up to 10% due to the cracked cells (Kontgers et al. 2010)

A number of conditions, including laser fluence, repetition rate and scribing speed, will be tested through design of experiment. A working window for complete film removal without TCO layer damage needs to be investigated at the first place. This will help for further narrow down of the initial working window. While the rest defects may not be eliminated, a weight function can be applied to each defect based on those four categories of influence mentioned above. A mitigation of major defects will be followed up based on their importance and final justification can be approached through the measurements of solar cell efficiencies.

1.4. Material Characterization

Film thickness is measured via ellipsometry. The methods for characterizing the surface morphology are through SEM (scanning electron microscopy), AFM (atomic force microscopy), optical profilometry and optical microscopy. Crystallinity is characterized by XRD (x-ray diffractometry) and TEM (transmission electron microscopy), and the TEM samples are prepared using FIB (focused ion beam). Transmittance and reflectance spectra are measured by spectrophotometry and material chemical composition is analyzed by XPS (X-ray photoelectron spectroscopy) and DEX (energy dispersive x-ray spectroscopy). Here, the working principles of ellipsometry and FIB are described as follow.

1.4.1 Measurement of Film Thickness

Sample thickness is measured through ellipsometry, which is a non-destructive optical technique for investigation of complex refractive index of thin films as shown in Fig. 1.22.

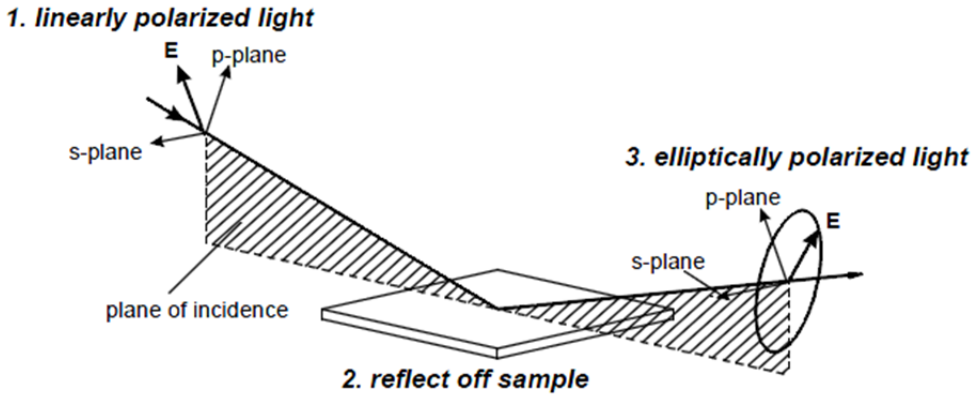

Figure 1.22 Interaction of polarized light with a sample (J.A. Woollam Co. Inc., 2008)

Ellipsometry measures the complex reflectance ratio, ρ, of a system, which may be expressed by the amplitude component Ψ and the phase difference Δ. The polarization state of the incident

light can be decomposed into an *s*- and a *p*-component (the *s* component is oscillating perpendicular to the plane of incidence and parallel to the sample surface, and the *p* component is oscillating parallel to the plane of incidence). The amplitudes of the *s* and *p* components, after reflection and normalized to their initial value, are denoted by γ_s and γ_p, respectively. The change in polarization state is commonly characterized by (J.A. Woollam Co. Inc., 2008)

$$\rho = \frac{\gamma_p}{\gamma_s} = \tan(\Psi)e^{i\Delta} \tag{1.14}$$

Thus, *tan(Ψ)* is the amplitude ratio via reflection. The material optical constants n and k can be calculated through (J.A. Woollam Co. Inc., 2008)

$$\langle \tilde{n} \rangle^2 = \left(\langle n \rangle + i \langle k \rangle \right)^2 = \sin^2 \phi \left[1 + \tan^2 \phi \left(\frac{1-\rho}{1+\rho} \right)^2 \right] \tag{1.15}$$

Since ellipsometry measures the ratio of two values rather than the absolute value of either, it is very robust, accurate, and reproducible.

1.4.2 TEM Sample Preparation

Due to the limit spike size and the specific location needed, samples cannot be prepared by the polishing and ion milling. Instead, a "lift-out" method using focused ion beam will be utilized to fabricate TEM samples from bulk materials. Sample will be first deposited a layer of gold and followed by platinum to the area of interest, in order to prevent material amorphization by ion beam. Using a large beam current for fast ion milling, two trenches are milled on either side that has been deposited above the area of interest, leaving a wall of material in the center that is approximately two microns thick. The trenches themselves are approximately twenty-micron wide, fourteen microns long and ten to fifteen microns deep. A smaller beam current is used to further thin the central membrane between the two trenches to a thickness of approximately 1

micrometer, as indicated in Fig.1.23a. The specimen is then attached to probe needle using platinum deposition capability in the FIB as shown in Fig. 1.23b. The sample is then cut away, manipulated to a TEM grid in the vacuum system and micro-welded to the grid using platinum deposition. The probe is then cut away from the specimen and further thinning is followed in the FIB. The last thinning step, again reducing the beam current, brings the membrane to a thickness of between 50 and 120 nanometers. At these thicknesses, the membrane is electron transparent, and will clearly display the cross-section of the area of interest in a TEM.

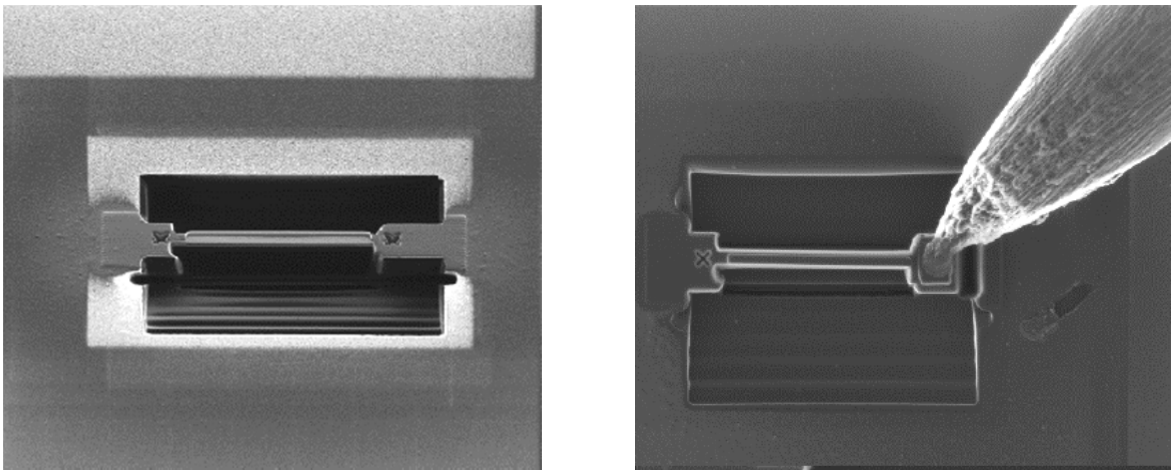

(a) (b)

Figure 1.23 (a) FIB image of TEM sample cut loose at bottom; (b) FIB image showing probe needle attached to the ear (Roberts and Otterloo, 2001)

1.5 Organization of the Thesis

In Chapter 1, the general background of the solar cell, including working principle, absorber materials, characteristics, limit of efficiencies and laser applications, is overviewed. The different mechanisms of spike formation through surface texturing and crystallization induced by pulse duration (femtosecond and nanosecond) are introduced. The physics of thin-film solar cells and the key manufacturing process of laser scribing are also reviewed. The numerical methods for

predictions of absorption on surface geometry, spike formation of excimer laser irradiation on a-Si:H thin films and film removal of P1 and P2 scribing, are described. At the end, the motivations of this work and organization of the thesis are given.

In Chapter 2, submicrometer conical and pillar-shaped spikes are fabricated by irradiating a-Si:H thin films deposited on glass substrates with hundreds of 800 nm-wavelength, 130 fs-duration laser pulses in air, and water environments, respectively. The formation mechanisms for the surface spikes are discussed, and the differences in the surface feature characteristics are also presented and explained within the context of the different processing environments.

In Chapter 3, both surface texturing and crystallization on a-Si:H thin film are achieved through one-step femtosecond laser processing. The nanoscale conical and pillar-shaped spikes formed on the surface of a-Si:H films by femtosecond laser irradiation in both air and water are presented and enhanced light absorption is observed due to light trapping based on surface geometry changes, while the formation of a mixture of hydrogenated nanocrystalline silicon (nc-Si:H) and a-Si:H after crystallization suggests that the overall material stability can potentially be increased. The relationship among crystallinity, fluence, and scan speed is also discussed. Furthermore, a comparison of absorptance spectra for various surface morphologies is developed. Finally, the absorptance measurement across the solar spectrum shows that the combination of surface texturing and crystallization induced by femtosecond laser processing is very promising for a-Si:H thin film solar cell applications.

In Chapter 4, hydrogenated and dehydrogenated amorphous silicon thin films deposited on glass substrates were irradiated by KrF excimer laser pulses and the effect of hydrogen on surface

morphologies and microstructures is discussed. Sharp spikes are focused only on hydrogenated films, and the large-grained and fine-grained regions caused by two crystallization processes are also induced by presence of hydrogen. Enhanced light absorptance is observed due to light trapping based on surface geometry changes of a-Si:H films, while the formation of a mixture of nanocrystalline silicon and original amorphous silicon after crystallization suggests that the overall material stability can potentially improve. The relationship between crystallinity, fluence and number of pulses is also investigated. Furthermore, a step-by-step crystallization process is introduced to prevent the hydrogen from diffusing out in order to reduce the defect density, and the relationship between residue hydrogen concentration, fluence and step width is discussed. Finally, the combined effects show that the single-step process of surface texturing and step-by-step crystallization induced by excimer laser processing are also promising for a-Si:H thin-film solar cell applications.

In Chapter 5, a fully-coupled multilayer thermal and mechanical finite element model is developed to analyze the laser-induced spatio-temporal temperature and thermal stress responsible for SnO2:F film removal. A plasma expansion induced pressure model is also investigated to simulate the non-thermal film removal of CdTe due to the micro-explosion process. Corresponding experiments of SnO_2:F films on glass substrates by 1064nm ns laser irradiation show a similar removal process to that predicted in the simulation. Differences between the model and experimental results are discussed and future model refinements are proposed. Both simulation and experimental results from glass-side laser scribing show clean film removal with minimum thermal effects indicating minimal changes to material electrical properties.

In Chapter 6, a nanosecond (ns) laser with a wavelength at 532nm is employed for pattern 2 (P2) scribing on CdTe based thin-film solar cells. The film removal mechanism and defects caused by laser-induced micro-explosion process are studied. The relationship between those defects, removal geometry, laser fluences and scribing speeds are also investigated. In addition, thermal and mechanical numerical models are developed to analyze the laser-induced spatio-temporal temperature and pressure responsible for film removal, and an improvement on strain-rate-dependent fracture criterion is implemented in the model. The simulation can well-predict the film removal geometries, TCO (transparent conducting oxide) layer thermal damage, generation of micro cracks, film delamination, and residual materials. The characterization of removal qualities will enable the process optimization and design required to enhance solar module efficiency.

In chapter 7, major findings and contributions based on this dissertation are briefly summarized.

Chapter 2: Femtosecond Laser-induced Simultaneous Surface Texturing and Crystallization of a-Si:H Thin Film: Morphology Study

2.1 Introduction

Many industrial solar cells in use today use bulk materials as absorbers with crystalline silicon (c-Si) being the most prevalent. Crystalline silicon, however, suffers from the disadvantage of high material cost since relatively large thicknesses are required primarily due to its low absorption coefficient. Recently, thin film absorbers are becoming more attractive based on their potential for low-cost modules, tandem junctions, and large-scale manufacturability (Luque and Hegedus, 2003; Chopra et al., 2004; Kazmerski, 2006). a-Si:H is the most popular material for use in thin film form due to its low energy econom et al.y (cost/watt). The main issue with a-Si:H is the high order of dangling bonds which act as recombination centers that severely reduce the carrier lifetime which results in the efficiency being below 10%. Additionally, this initial efficiency will decrease by 50% or more when exposed to sunlight over a period of several months which is known as the Staebler-Wronski effect or SWE (Miles, 2005; Staebler and Wronski, 1980).

Due to their low efficiency and instability, thin-film a-Si:H solar cells require a highly efficient light-trapping design to absorb a significant fraction of the incident sunlight and material property changes to increase stability against the SWE. Antireflection (AR) coatings and front-side texturing through the use of alkaline-based solutions, such as KOH and NaOH etching have been used on crystalline silicon solar cells, and pulsed laser irradiation has been used to enhance light trapping on both amorphous and crystalline materials (Martirosyan et al., 2007; Hylton, et

al., 2004; Crouch et al., 2004; Nayak and Gupta, 2007), however, AR coating requires additional material and anisotropic wet chemical etching is not applicable for amorphous materials or thin films. In addition, in order to reduce the SWE, hybrid a-Si/nc-Si (nanocrystalline silicon) tandem modules have been developed and are able to achieve both higher efficiency and stability compared with single junction a-Si:H (Yamamoto et al., 2004) due to the use of a thinner a-Si layer and the wider spectral absorption of nc-Si. To eliminate the need for two separate deposition steps which are required to form these tandem cells, laser-induced crystallization of a-Si:H has been proposed to produce a mixture of nc-Si:H and a-Si:H and simultaneously form a light trapping texture on the surface of the material (Nayak and Gupta, 2007). Therefore, laser-based treatment of a-Si:H may solve its efficiency and stability issues in a one-step process, which is a promising methodology for thin-film solar cell fabrication.

Surface texturing can be achieved by both femtosecond and long-pulse lasers, however, femtosecond lasers are better suited for precise micromachining due to their extremely high peak power and ultrashort pulse duration, which leads to greatly reduced thermal energy diffusion and heat-affected-zone and allows for precise control over the texturing process (Zheng and Jiang, 2010; Jiang and Tsai, 2003). Therefore, for texturing films with limited thickness, femtosecond laser processing is more desirable. A number of different techniques have been reported for forming microstructures on silicon surfaces using femtosecond lasers. Younkin et al., 2003, and Sheehy et al., 2005, showed micron-size conical spikes formed on crystalline bulk silicon when irradiated with hundreds of femtosecond laser pulses in different background gases, such as SF_6, N_2, and air. The formation of submicron spikes and ripples with periodicity in the nano-scale on crystalline silicon has also been investigated after femtosecond laser irradiation in water, and has

been shown to produce much denser spikes than when processed in a gas environment (Shen et al., 2004; Daminelli et al., 2004). Compared to the successful light trapping enhancement achieved on bulk c-Si, limited work has been performed on a-Si:H thin films. Nayak and Gupta, 2007, reported the observation of crystallization and simultaneous formation of randomly distributed irregular spikes on a-Si:H thin films through femtosecond laser processing in air. However, the surface geometry created on a-Si:H films is not as regular as that generated on c-Si, and the effects of different processing environments, such as background gases and water, are not well understood. Furthermore, comparing thin film and bulk samples, the processing conditions should be more critical for thin films since the entire film must not be removed during the process. Additionally, based on the difference in thermal properties between amorphous and crystalline materials, the periodicity of the final texture on a-Si:H should be different, especially for underwater treatment.

In this study, a-Si:H thin films deposited on glass substrates are irradiated with different numbers of femtosecond laser pulses at various fluences in air and water, and the formation of conical and pillar-shape spiked surface structure is observed. The feature characteristics are studied through scanning electron microscopy (SEM) and atomic force microscopy (AFM) for different processing environments. The generated surface structure on a-Si:H films shows potential capability of enhancing the efficiency of thin film solar cells, and the effect of laser processing on absorption and crystallinity is investigated in the later work (Wang et al., 2012).

2.2 Theoretical Background

2.2.1 Femtosecond Laser Interaction with Wide-Band-Gap Materials

In this study, the wavelength of the femtosecond laser is 800nm, which cannot be directly absorbed by a-Si:H (band gap of a-Si:H is 1.7eV or 730nm). Therefore, nonlinear absorption is the main laser-material interacting mechanism. When the intensity of the femtosecond laser pulse reaches $10^{13} – 10^{15}$ W/cm^2 or more, multiphoton or tunneling ionization will occur within a few to tens of femtoseconds. When the intensity drops below 10^{12} W/cm^2, avalanche (or collisional) ionization which is described by the Fokker-Planck equation occurs (Jiang and Tsai, 2003):

$$\frac{\partial N(E_K,t)}{\partial t}+\frac{\partial}{\partial E_K}\left[R_J(E_K,t)N(E_K,t)-\alpha(E_K)E_P N(E_K,t)-D(E_K,t)\frac{\partial N(E_K,t)}{\partial E_K}\right]=S(E_K,t) \quad (2.1)$$

where N is the electron density distribution, E_K is the electron kinetic energy, E_P is the phonon energy, t is the time, R_J is the heating rate of electrons, α is the electron–phonon energy transfer to the material, D is the diffusion coefficient and S indicates sources and sinks of electrons. More details of avalanche ionization can be found in Jiang and Tsai, 2003.

As the excited electron density increases, the material is first transformed into a plasma that reflects and absorbs the remaining pulse energy. “Gentle ablation”, which is caused by ions being pulled out of the material, can then occur if the electric field formed by the excited electrons is strong enough. This critical electron density can be estimated by (Jiang and Tsai, 2003),

$$n_{cr}=\frac{\pi m_e c^2}{e^2\lambda^2} \quad (2.2)$$

where m_e is the electron mass, c is the speed of light, e is the electron charge, and λ is the laser wavelength.

After the laser pulse, the energy absorbed by the electrons is transferred to the material over a picosecond time scale. Within a few microseconds, the thermal energy of the plasma that diffuses out from the focal volume can cause thermal melting or vaporization and can leave behind permanent structural damage for sufficiently high laser intensities (Gattass and Mazur, 2008; Sundaram and Mazur, 2002).

2.2.2 Femtosecond Laser-Induced Surface Texturing Mechanism

Most micromachining work under the ablation regime is performed by removing the material within the irradiated area and generating a crater. However, under some certain conditions, the laser can induce periodic surface structures with periodicity much smaller than the spot size. Extensive work has been performed on femtosecond laser induced surface texturing of crystalline bulk silicon, and the corresponding two-stage texture formation mechanism has been described by Shen et al., 2004 and Tull et al., 2006. During the first stage of processing in a gas environment, straight wavelength-dependent ripple structures are first formed on the silicon surface which is called light-induced periodic surface structure (LIPSS). The ripples are mainly orientated perpendicular to the electric field vector of the incident laser beam and the period can be predicted by (Tan and Venkatakrishnan, 2006):

$$\Lambda \approx \frac{\lambda}{1 \pm \sin\theta_i} \quad \text{for s-polarized light} \tag{2.3}$$

$$\Lambda \approx \frac{\lambda}{\cos\theta_i} \quad \text{for p-polarized light} \tag{2.4}$$

where, Λ is the spacing between adjacent ripples, λ is laser wavelength, and θ_i is the incident angle. After the formation of LIPSS, micron-scale ridges are generated on the top of and perpendicular to the ripples. The coarsened layer breaks up into micron-size beads which is suggested to be caused by surface tension effects (Sundaram and Mazur, 2002). For a water environment, in the first stage, most of the light is absorbed by a silicon layer tens of nanometers thick near the silicon–water interface which creates a plasma. Due to the high temperature of the plasma, micro-size bubbles are generated by the decomposition of water. Diffraction of the laser beam by these bubbles produces ripple-like structures on the silicon surface due to the existence of high and low intensity fringes. The separation between adjacent rings is found to be close to the wavelength of the laser. Roughness on the silicon surface causes the laser pulse energy to be non-uniformly absorbed across the surface, which results in a random arrangement of bubbles. The superposition of ripple structures generated by multiple laser pulses causes bead-like structures to be randomly distributed on the surface of the material.

The second stage of surface structure formation is similar for processing in both gas and water environments. The beads that formed in the first stage act to concentrate subsequent laser light into the valleys between them through reflection off the sides of the beads. This causes the ablation rate to be higher inside the valleys than on the bead tips, which leads to sharpening of the beads into spikes after hundreds of laser pulse assisted texturing steps. It is noted that, in water, the spikes are generated with submicron heights and wavelength-dependent spacing and are much shorter and denser than those formed in gas environments.

2.3 Experimental Setup

Amorphous silicon films were deposited on 0.525mm-thick Corning 1747 glass substrates using plasma enhanced chemical vapor deposition (PECVD). The a-Si:H film was deposited at a rate of 60 Å/s in an hydrogen diluted silane environment at 380°C with a hydrogen atomic concentration of around 20 at %.

Femtosecond laser texturing was carried out using a commercial Ti:sapphire oscillator and regenerative amplifier system. The system delivered 130-fs pulses of linearly polarized light at a 1 kHz repetition rate, and a central wavelength of 800 nm. The a-Si:H films were cleaned with acetone in an ultrasonic cleaner for 5 minutes and then rinsed with methanol and distilled water prior to processing.

The sample was mounted on a three-axis translation stage and irradiated by laser pulses focused by a 60 mm focal-length lens. When changing the environment to water, the sample was placed in a plastic container, the laser beam was focused by the same lens and traveled through 5 mm of distilled water before striking the surface, and the focal plane was positioned below the sample surface in order to obtain the desired spot size of 150μm. For both air and underwater cases, the laser beam was acting normally to the sample surface and the beam spot on the sample surface was circular. For the morphology study, the samples were held stationary and irradiated at various fluences (0.2J/cm^2 to 0.45J/cm^2) in air and at higher fluences (1J/cm^2 to 1.8J/cm^2) in water with different numbers of pulses (2-100). At each condition, the experiment had been repeated three times for reliability examination.

The a-Si:H film thickness was measured by ellipsometry at three different locations of each sample wafer, in order to check the uniformity of the PECVD-deposited film. The untreated and treated samples were observed through scanning electron microscopy (SEM). Surface roughness and the distribution of spikes in the treated samples were also examined using an atomic force microscope (AFM). The optical transmittance and reflectance of as received a-Si:H films were measured by a spectrophotometer over a wavelength range of 250nm-2500nm which corresponds to the main spectral range of solar irradiation (Goetzberger et al., 1998). The reflectance (R in %) and transmittance (T in %) are then used to calculate the absorptance (A in %) of the film: $A=100-R-T$.

2.4 Results and Discussion

The measured and fitted Psi (Ψ) and Delta (Δ) curves from ellipsometer measurements of the as-received a-Si:H films are shown in Fig. 2.1. The thickness is determined to be 1578.6±2.28 nm with a surface roughness of 2.62±0.28 nm, where the variation represents standard deviation. These curves were fitted by a numerical model, also shown in Fig. 2.1, and it is observed that the model generated data matches experimental data well for both number of oscillations and spectral locations.

Figure 2.2 shows the SEM and AFM images of the initial surface of the a-Si:H film. The surface appears smooth from SEM image, and the surface average roughness measured by AFM is 2.08 nm, which is close to that measured by the ellipsometer. Therefore, the surface of the as-received a-Si:H film is relatively flat with very little initial texture.

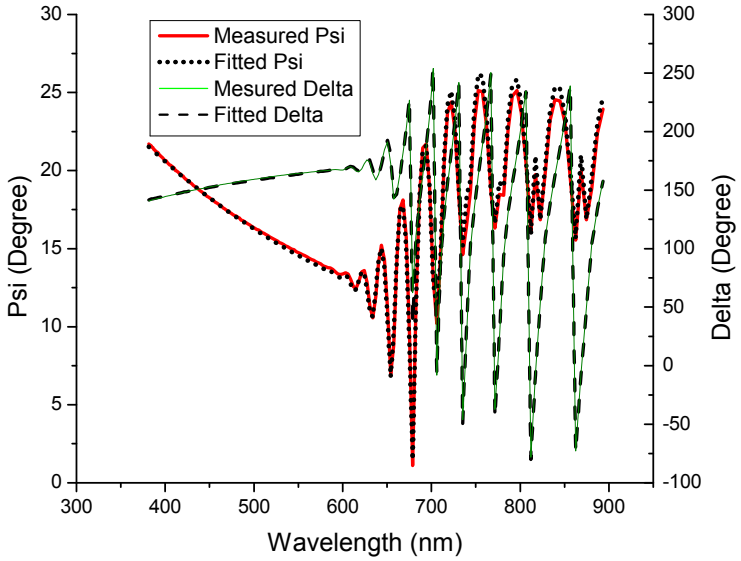

Figure 2.1 Comparison of measured and model fitted optical data in the ellipsometer measurement of a-Si:H layer thickness that deposited on glass substrate

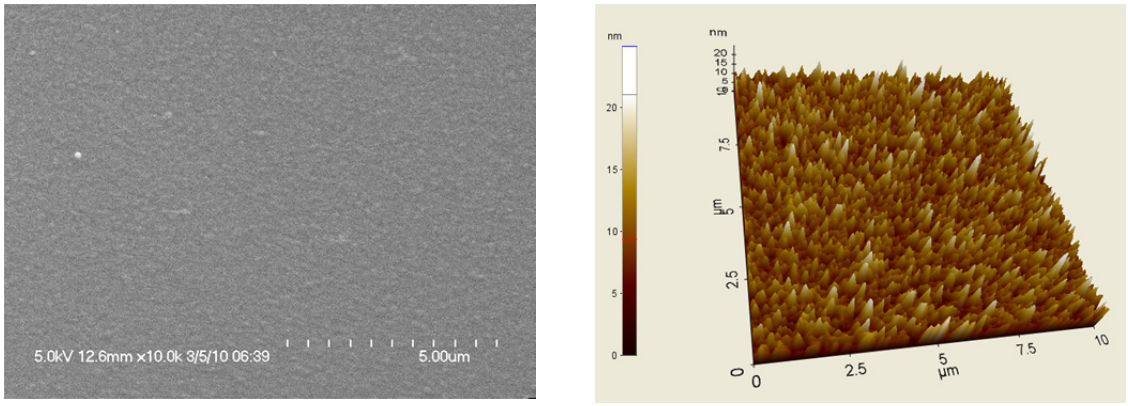

(a) (b)

Figure 2.2 (a) SEM image and (b) AFM image of as-received a-Si:H film surface, average roughness R_a is around 2nm as measured by AFM

2.4.1 Absorptance Spectra of As-Received Film

The light transmittance and reflectance of a-Si:H thin films are measured by a spectrophotometer, and absorptance can be calculated based on the above two measurements. In

this study, a numerical model is also developed to predict the absorptance spectrum of a-Si:H films with planar interfaces, which is used for determining the optical constants, a function of wavelength, of the as-received a-Si:H film, and the determined parameter is helpful for the further-step absorption simulation with a certain periodic surface structures (Wang et al., 2012). The model can be also potentially used as a guideline for absorber thickness selection of a-Si:H or other materials if specific optical properties are known. The model configuration consisting of an a-Si:H thin film on a glass substrate as shown in Fig. 2.3. Since the film thickness is much larger than the surface roughness, surface roughness is ignored in the model. This is further justified by the fact that internal interference induced oscillation is observed in the measured transmittance spectrum shown in Fig. 2.4, which indicates that the thickness of the film is uniform. The light transmittance and reflectance of the a-Si:H thin film are also measured by a spectrophotometer in the solar spectrum of 250nm to 2500nm, and absorptance is calculated based on the above two measurements as shown in Fig. 2.4 through Fig. 2.6.

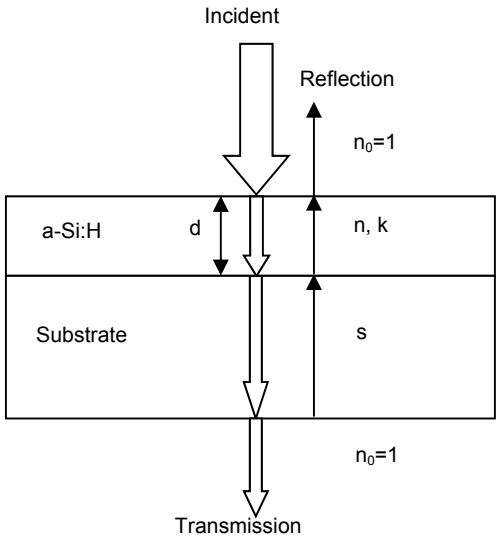

Figure 2.3 Schematic of one-dimensional absorption simulation model of as-received a-Si:H film on glass substrate, film thickness d=1.6μm, real and imaginary parts of refractive index of a-Si:H film are n and k, s and n_0 are the refractive index of the substrate and air, respectively

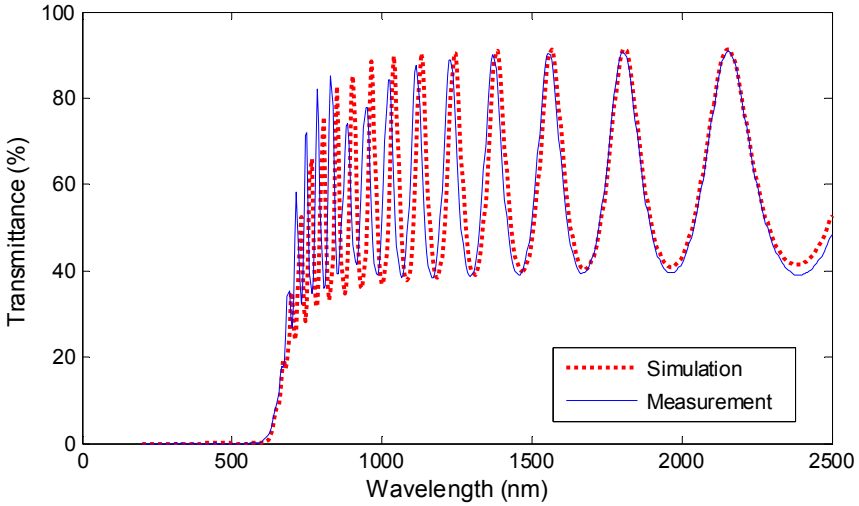

Figure 2.4 Comparison of transmittance spectra for both simulation and measurement by spectrophotometer of as-received a-Si:H film on glass substrate, film thickness is 1.6μm

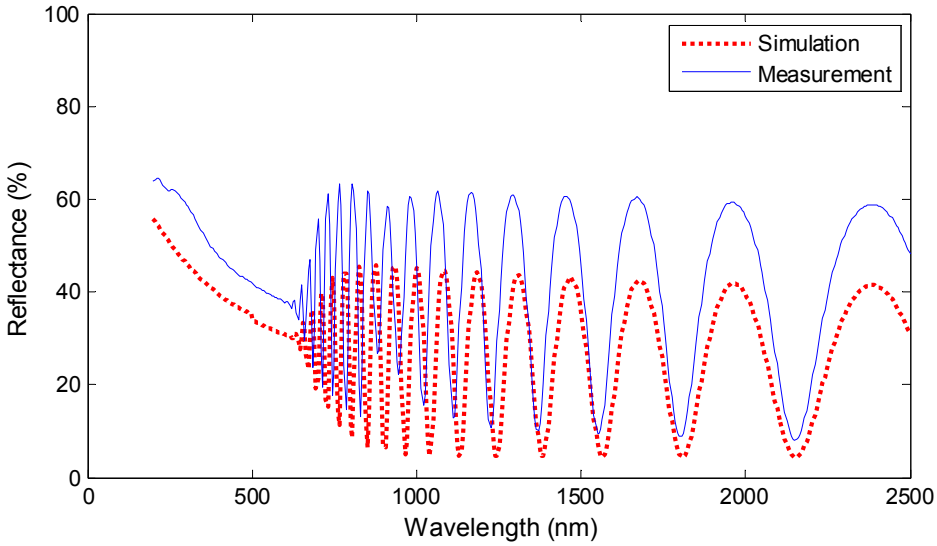

Figure 2.5 Comparison of reflectance spectra for both simulation and measurement by spectrophotometer of as-received a-Si:H film on glass substrate, film thickness is 1.6μm

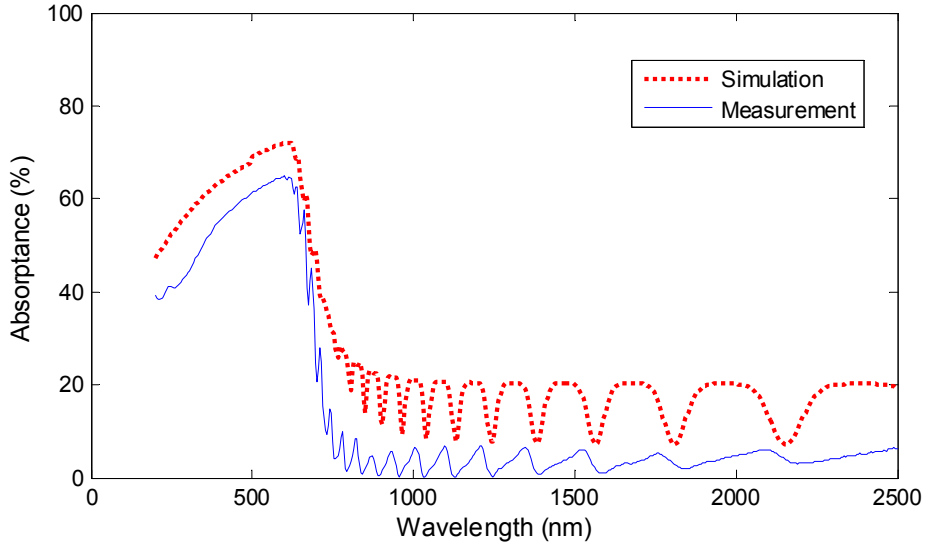

Figure 2.6 Comparison of calculated absorptance spectra ($A=100-T-R$) of as-received a-Si:H film on glass substrate based on both transmission and reflection simulation and measurement by spectrophotometer, film thickness is 1.6μm

The transmittance through the film/substrate pair can be estimated by considering the light reflection and refraction at the interface between different mediums and the absorption inside the a-Si:H film as below (Swanepoel, 1983),

$$T = \frac{Ax}{B - Cx + Dx^2} \tag{2.5}$$

where, $A=16n(s^2+k^2)$, $B = [(n+1)^2+k^2][(n+1)(n+s^2)+k^2]$,

$C=[(n^2-1+k^2)(n^2-s^2+k^2)-2k^2(s^2+1)]2\cos\varphi-k[2(n^2-s^2+k^2)-(s^2+1)(n^2-1+k^2)]2\sin\varphi$,

$D=2(n-1)^3(n-s^2)$, $\varphi=4\pi nd/\lambda$, and $x=e^{-4\pi k/\lambda}$.

In order to determine optical constants, the method described by Swanepoel, 1983, is followed which uses the transmittance measurement to determine the optical constants from the interference fringes.

In Fig. 2.4, within the transparent region, the interference fringes of the model can be written as the maximum and minimum transmittance values for Eq. (2.5) for k=0 (Swanepoel, 1983),

$$T_{peak} = \frac{A'x}{B' - C'x + D'x^2}, \quad T_{valley} = \frac{A'x}{B' + C'x + D'x^2} \tag{2.6}$$

where, $A'=16ns^2$, $B' = (n+1)^3(n+s^2)$, $C'=2(n^2-1)(n^2-s^2)$, and $D'=2(n-1)^3(n-s^2)$

The optical constants can be calculated using Eq.(2.6) at the corresponding wavelengths that cause peaks and valleys, and a polynomial curve fitting of those values gives the optical constants over the solar spectrum. The reflectance can be estimated by the correlation between the light reflection, transmission, a-Si:H absorption coefficient and film thickness (Shaaban, 2008),

$$\alpha = \frac{1}{d}\ln\left[\frac{(1-R)^2 + \sqrt{(1-R)^4 + 4R^2T^2}}{2T}\right] \tag{2.7}$$

The simulation parameters used in the calculation are, substrate refractive index s=1.5 and film thickness d=1600nm. As seen in Fig. 2.4, the transmittance simulation results show good agreement with the measurement in both periodicity and magnitude. Reflectance curves for both experimental and numerical results in Fig. 2.5 show that the simulation has the same periodicity as the measurement, however, the simulation values are 10 to 15% lower than those measured experimentally. The underestimation could be caused by ignoring the complicated a-Si:H network structure which introduces internal reflections within the film, while the film structure is considered as homogeneous in the model. In addition, ignoring the interface between the glass substrate and the surrounding air in Eq. (2.7) can also result in a lower reflectance. As a result, the simulated absorptance ($A=100-R-T$) is higher than measured experimentally as shown in Fig. 2.6, however the overall wavelength dependence is accurately captured by the model.

2.4.2 Study of Morphology in Air

The majority of the published work on femtosecond laser texturing has focused on bulk crystalline silicon, and the texture formation mechanism has been suggested to be quite similar to that of a-Si:H, since both of them occur under the ablation regime. However, in order not to damage the entire film, thin film samples have a much narrower window of suitable texturing fluences and number of pulses than that of bulk materials. Also, for the creation of tandem cells for enhanced stability while maintaining the absorption characteristics of amorphous silicon, crystallization of the entire film must be avoided. This is challenging due to the high absorption coefficient of amorphous silicon and the relatively thin material. Also, the difference morphologies between c-Si and a-Si:H due to the effects on thermal properties and existence of hydrogen are not well studied. Therefore, understand the texturing process of a-Si:H thin films is essential for enabling their widespread use in solar cell applications.

The conditions used to texture crystalline bulk silicon ($0.8J/cm^2$ and 500 pulses) (Tull et al., 2006) easily damage the thin film samples. In order to texture the films without removing them entirely, the amorphous samples are irradiated at stationary locations with lower fluences ($0.2J/cm^2$ to $0.45J/cm^2$) and numbers of pulses (2 to 100). A typical result achieved using a fluence of $0.4J/cm^2$ is shown in Fig. 2.7. The circular surface defects after 2 pulses as shown in Fig. 2.7 (a) are suggested to be generated from burst bubbles that are frozen in place on resolidification of the molten silicon. These bubbles are attributed to a local increase in vaporization of the silicon melt due to defects or impurities at the surface (Tull et al., 2006). The periodic ripples are suggested to be formed by the interference between the incident beam and light scattered by those surface defects which results in a non-uniform energy distribution on the

sample surface, which creates capillary waves with periodicity close to the laser wavelength (Sipe et al., 1983). Figure 2.7 (b) shows how the periodic ripples disappear after 10 pulses, and instead, perpendicular ridges are formed. The transition could be caused by a surface instability, since the periodic ripples will become long, liquid half-cylinders on the surface after melting. Due to the surface tension effect, the atoms at the liquid surface do not have neighboring atoms at all directions and therefore are pulled inwards. This creates an internal pressure and forces the liquid silicon to minimize its surface area. With the same volume, sphere always has the minimal surface area; therefore, those long liquid cylinders will not be stable and break up into many spherical shape droplets. Some irregular morphology on the surface may be caused by the ultrashort pulse duration, which indicates some liquid silicon has been solidified before the surface becomes stable. After 20 pulses, bead-like ripples are formed by breaking those long ridges as shown in Fig. 2.7 (c), which is caused by the surface tension effect that is responsible for the shape of liquid droplets. The above steps are part of the first stage of texture formation. The following stage is the formation of the conical spikes. Figure 2.7 (d) and (e) show how the conical spikes become sharper and deeper with increasing number of pulses. This is due to the beads formed on the surface concentrating the laser beam into the valleys between them, causing the material around the tips to be preferentially removed and sharp conical spikes to be formed. Figure 2.7 (f) presents the distribution of the spikes in one quarter of the irradiated area. It can be seen that the spikes are wider, taller and more widely spaced at the center of the laser spot, while they are narrower, shorter, and more closely packed toward the exterior. At the boundary, wavelength-dependent periodic ripples are formed instead of spikes. This may due to a difference in surface tension, which mainly depends on temperature and Gaussian spatial distribution of the laser light. The surface tension of liquid silicon is inversely proportional to the

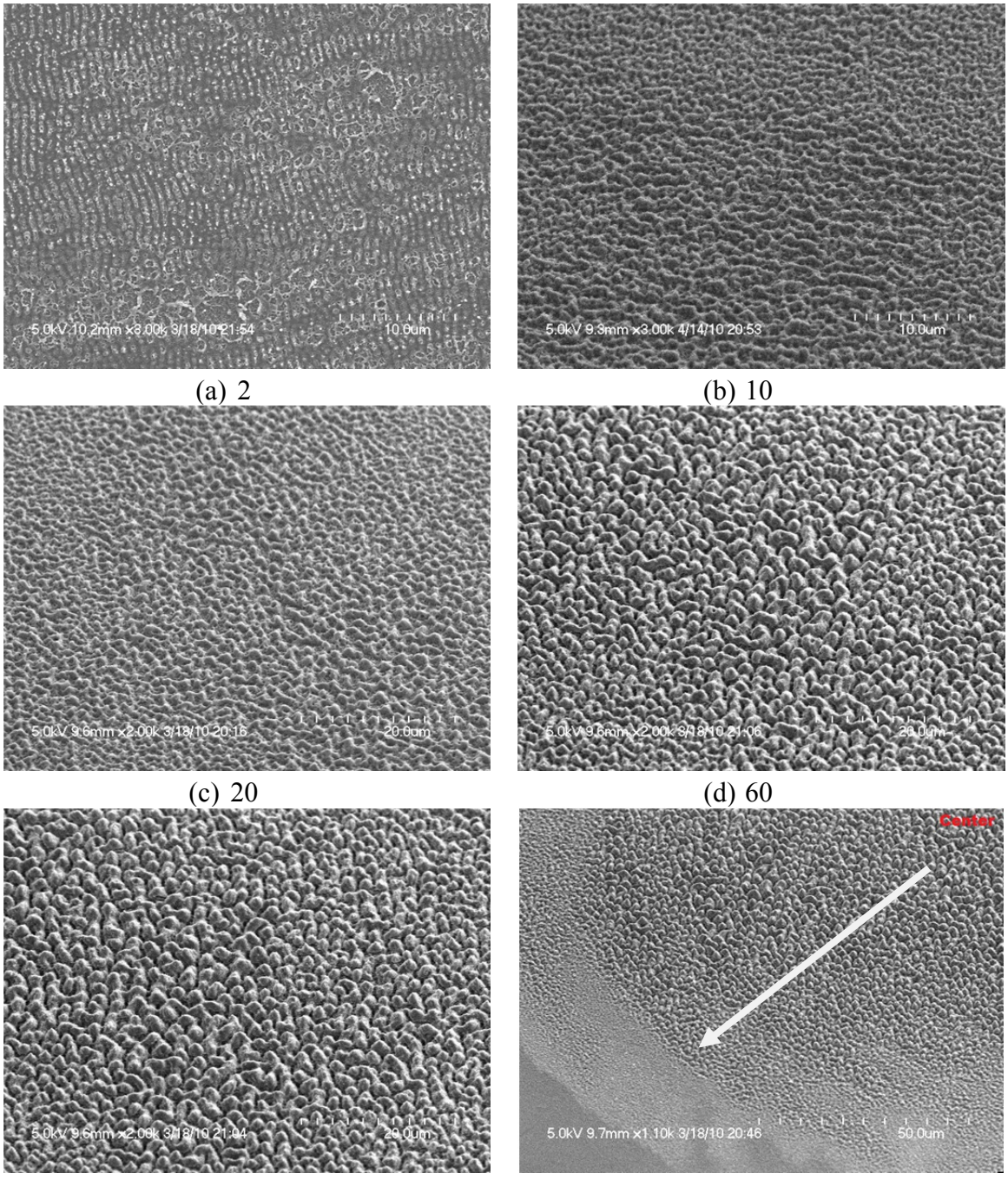

(a) 2 (b) 10

(c) 20 (d) 60

(e) 100 (f) 100

Figure 2.7 SEM images of a-Si:H film surface after being irradiated by the following number of pulses in air at 0.4J/cm^2 (a)2, (b) 10, (c)20, (d) 60, (e)100, (f) 100. With lower magnification, (f) shows about a quarter of irradiated area and the arrow in (f) showing the spikes are becoming smaller and denser moving from center to the edge

temperature (Shen et al., 2004), thus the liquid silicon at the center has a lower surface tension which leads to a larger surface area after breakup process, and then leaves more sparsely spaced beads after resolidification. When moving to the edge, the increased surface tension will make the beads more compact. Due to the Gaussian distribution of laser energy, the material removal between the beads at the central irradiated area will be more than that of exterior. Therefore, the spikes generated at the center will be higher and less dense than the spikes to the exterior. At the edge, the energy is so small that no further damage can be caused after formation of wavelength-dependent periodic ripples.

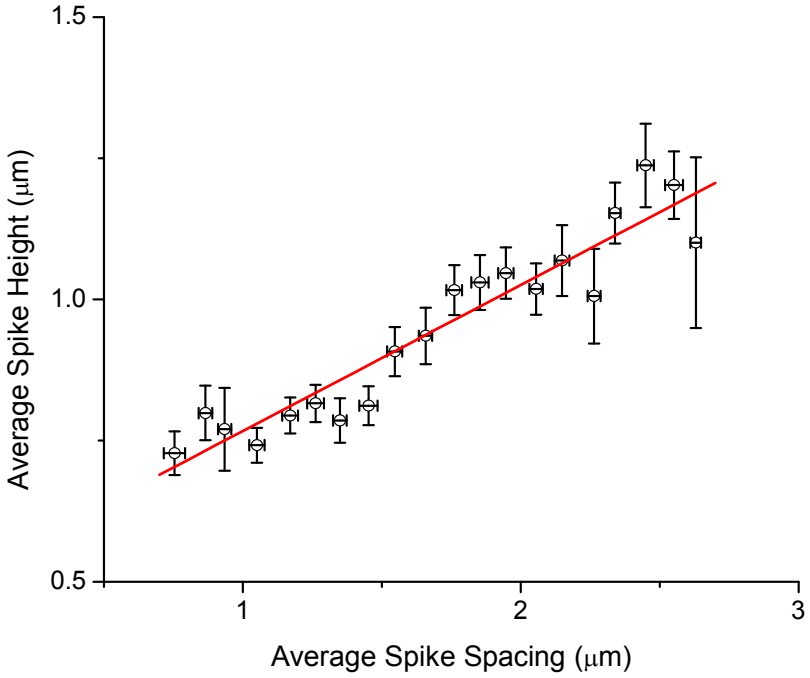

Figure 2.8 Dependence of average spike height on average spike spacing after laser treatment in air, determined from an area of 50×50 μm^2 at the processing center (0.4J/cm^2, 100 pulses). The solid straight line is a linear fitting to the measurement, error bars indicate standard deviation

In order to study the quantitative characteristics of the feature, AFM measurements are performed. The average spike height and average spike spacing are determined by measuring each spike height above the undamaged material surface, *h,* and the average distance, *d,* to the four closest neighboring spikes. A typical condition is 100 pulses at a fluence of 0.4J/cm^2. The average spike height and spacing are measured from within an area of 50×50 μm^2. Figure 2.8 shows the average spike height correlated with the average spike spacing, and the variation represents standard deviation. The solid line is a curve fit to the data, yielding a linear relation between the two parameters. When the spacing drops to below 1 μm, the surface is corrugated with no spikes. Fig. 2.9 shows the average spike spacing within the 50×50 μm^2 area as a function of fluence when irradiated by 100 pulses, and the variation represents standard deviation. It indicates that higher fluences will lead to an almost linear increase in average spike spacing; therefore, both average spike spacing and height are linearly proportional to the laser fluence, which is different from the nonlinear correlations found for bulk crystalline silicon with the condition variation from 0.5J/cm^2 to 1J/cm^2 and irradiated at 500 pulses (Her et al., 2000). The reason could be the chemical etching caused by the background gas (SF_6) during the laser irradiation on c-Si. The etching process can be described as: (1) SF_6 reacts with liquid silicon and form SiF_2 compounds; (2) SiF_2 compounds are desorbed by the laser, volatile species leave the surface (Wu, 2000):

$$3Si + SF_6 \rightarrow 3SiF_2 \text{ (solid)} + S \tag{2.8}$$

$$2SiF_2 \rightarrow SiF_4 \text{ (gas)} + Si \tag{2.9}$$

When the spikes start generating, the multi-reflection effect between the spikes introduces more intense laser energy into the valley. More silicon fluoride compounds desorb from the silicon matrix, which leads to a higher ablation rate. Thus the higher the fluence, the more chemical

reaction happened between the silicon and SF_6. Therefore, beyond the dependence on the laser fluence, the chemical reaction also plays an important role of the spike formation, which may cause the nonlinear relationship between the average spike height and spacing and the laser fluence.

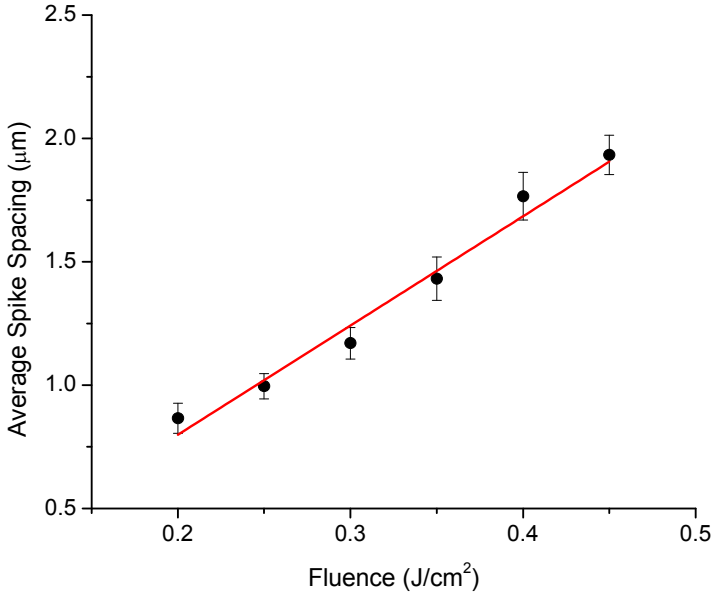

Figure 2.9 Dependence of average spike spacing on laser fluence for a fixed number of pulses (100 pulses) after treated in air, determined from an area of 50×50 μm^2 at the processing center, error bars indicate standard deviation

As shown in Carey et al., 2004, when irradiating on c-Si with a fluence of 0.4J/cm^2 and 500 pulses, the c-Si surface cannot generate sharp spikes, but only bead-like structures with an average spacing of 3.5 - 4μm. However, under the same fluence but 100 pulses, the average spacing is 1.8 μm on a-Si:H surface. Bases on the interaction mechanism of femtosecond laser, the material starts being ablated, and then thermal vaporization occurs when the energy transfers back from free electrons to the material. Finally, the remaining energy induces thermal melting underneath the ablation layer. Although the melting temperature of dehydrogenated amorphous

silicon (a-Si) is around 250˚C below that of c-Si (Kuo et al., 2006), the existence of hydrogen can significantly decrease the vaporization temperature (the energy of evaporation of H is 4 orders of magnitude lower than that of Si). Therefore, the energy absorbed by a-Si:H for melting will be less than that of c-Si, so that under the same fluence, the temperature of liquid silicon in a-Si:H sample is lower. As discussed in Fig. 2.7(f), the higher the temperature, the lower the surface tension, and the larger the spike spacing. That is why the average spike spacing of a-Si:H is smaller than that of c-Si. Her et al., 2000, also shows that, for c-Si sample processed at a higher fluence (1J/cm^2) and number of pulses (500), when the spike spacing is around 2 μm, the average spike height is 0.8-0.9 μm, which is close to that of a-Si:H sample (Fig.2.8). This may be also caused by the influence of hydrogen. Elliq et al., 1990, shows that, under the same condition, the surface roughness of a-Si:H can be several times as that of a-Si sample. The reason is that the hydrogen atoms can be aggregated together by absorbing laser energy, and finally, the hydrogen is formed as gaseous phase and diffused out from the silicon matrix. Since the ablation thresholds of both a-Si and c-Si are around 0.2J/cm^2 (Kruger and Kautek, 1995), under the same fluence, the ablation rate of a-Si:H could be more than that of c-Si. Therefore, with a smaller fluence (0.4J/cm^2) and number of pulses (100), a-Si:H sample can generate similar spike height to that of c-Si. Actually, the surface morphology can also be affected by other factors, such as melt depth, cooling rate and pressure. However, based on the formation process shown in Fig. 2.7, the average spike spacing is mainly caused by thermal effect of the melting layer at the first stage when bead-like structure is formed. The average spike height mainly depends on the ablation rate of the material and the influence of background gases. Similar to c-Si (Her et al., 2000), the laser textured spikes on a-Si:H should be at or below the original surface since it is ablation-based laser processing. In opposite, the spikes are protruded from the original surface

using a nanosecond laser where thermal effect is dominant during the spike formation (Tull et al., 2006). Although the remaining energy can cause a thin layer of molten material, the molten layer has a relative minor effect on spike height.

Compared to Nayak et al., 2007, this study can generate much more regular conical spikes, which are similar as those achieved on bulk c-Si. Therefore, with a better periodic structure, the potential of absorption could be also better than that of Nayak et al., 2007.

2.4.3 Further Study of Morphology in Water

After laser processing, the top layer of the material will become oxidized, which has a larger band gap than a-Si:H and is not desirable for solar cell absorbers; the use of a water layer, however, may be introduced to reduce the surface oxidation and eliminate debris redeposition. The difference in surface stability between liquid silicon and water compared to air may also allow for different spike geometries. During laser processing, the plasma generated at the silicon/water interface due to the high temperature can vaporize and decompose the water, since some of the large bubbles can still be observed after irradiation when the temperature goes down to room temperature, so that they must consist primarily of gaseous hydrogen and oxygen rather than water vapor. The energy absorbed by the bubbles and the scattering effects induced by these bubbles and suspended ablated material will cause part of the incident energy to be lost before it reaches the target. Daminelli et al., 2004, shows the ablation threshold for 100 femtosecond laser pulses of c-Si in water is around 1.5 times that in air, and also that periodic ripples are formed in water when irradiated at fluences of 1.5-1.6J/cm^2, which indicates that the incident energy in water needs to be higher in order to get similar energy on the target. Therefore, for the a-Si:H

surface processed in water, the sample is irradiated at stationary locations with higher fluences (1J/cm^2 to 1.8J/cm^2) than that in air and the same number of pulses (2 to 100).

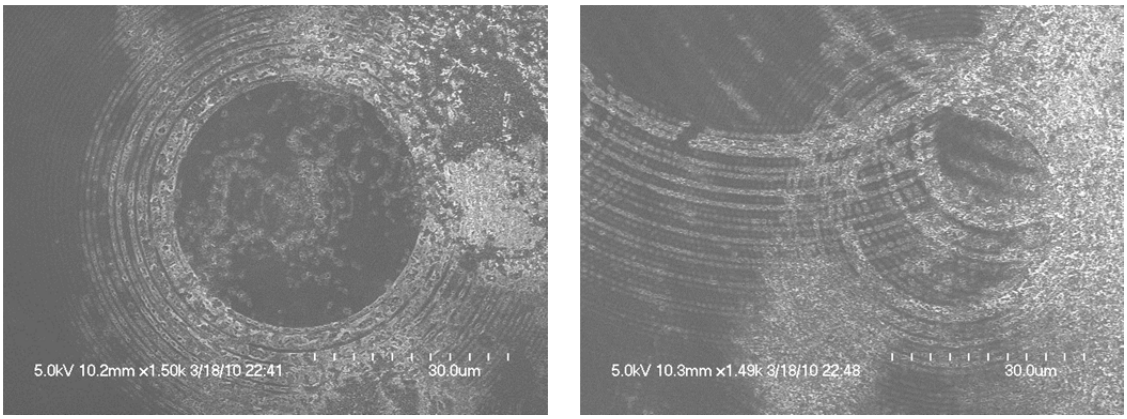

(a) 2 pulses (b) 5 pulses

Figure 2.10 SEM images near the edge of underwater laser irradiation area on a-Si:H film for (a) 2 pulses (b) 5 pulses at the fluence of 1.4J/cm^2

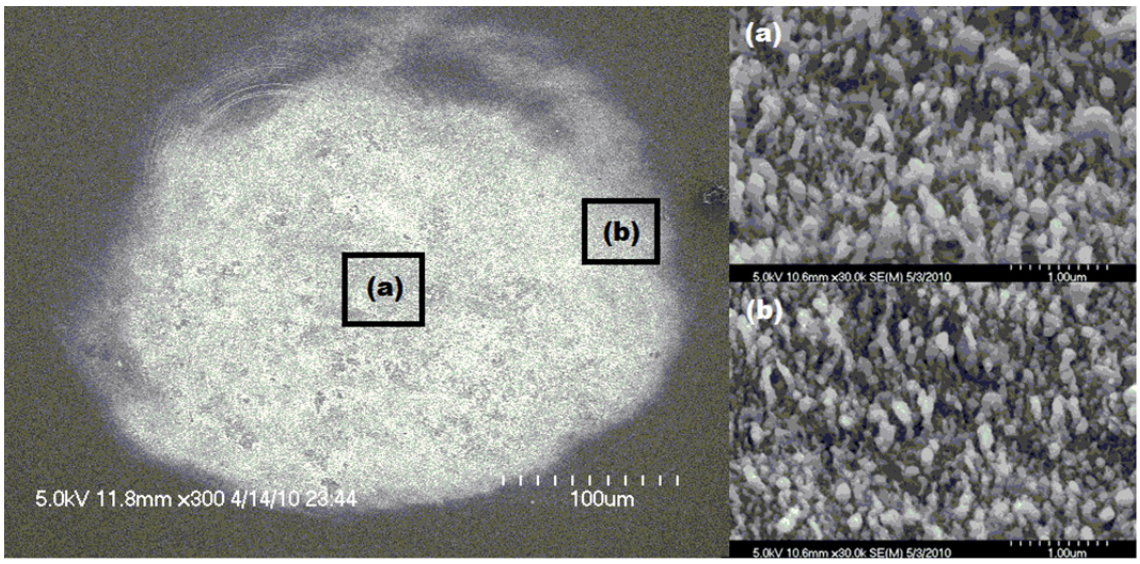

Figure 2.11 SEM images of underwater laser irradiation of a-Si:H film for 50 pulses at fluence of 1.4J/cm^2 , the irradiation spot diameter is 150μm, the inset images in the right show the high magnification at the center (a) and edge (b)

Figure 2.10 (a) and (b) show SEM images taken near the edges of the laser irradiated spot on an a-Si:H film surface after 2 and 5 pulses respectively with a fluence of 1.4J/cm^2, and the spot diameter is 150 μm. It can be seen that a ripple-like structure is generated on the surface after 2 pulses due to diffraction of the laser light by the micro-bubbles and that the spacing between the adjacent rings is closely matched to the laser wavelength (800nm). The first pulse cannot bring the ripple formation (not shown) is because no bubbles existence at the beginning. The laser energy is absorbed by the plasma at the silicon/water interface, and the heat of generated vapor and decomposed bubbles required may cool the silicon surface locally and leave the damage on the surface. After 5 pulses, at the edge of the irradiation area, it can be seen that ripples diffracted by separated bubbles start overlapping and generate a wavelength-dependent bead-like structure. When moving to the center of the area, the surface consisting of small spikes which are similar to those shown in Fig. 2.11 (a) suggests that more ripples are overlapping near the center of the beam, due to higher intensity in the center of the Gaussian beam that causes more decomposition of water and a greater number of bubbles to form. Fig. 2.11 shows the entire 50-pulse irradiated spot processed at a fluence of 1.4J/cm^2. The inset images (a) and (b) show that the spikes formed at the center and the edge are very similar, which indicates that after 50 pulses, the entire irradiated area looks more uniform and the ripples have disappeared. Instead, nano-sized pillar-shaped spikes are formed on the surface, which look less regular and denser but are more uniformly distributed than those formed in air shown in Fig. 2.7. Figure 2.12 (a) and (b) show SEM images of the surfaces irradiated by 50 pulses at fluences of 1.2J/cm^2 and 1.6J/cm^2, respectively. Compared to Fig. 2.11, the spikes formed in water at different fluences look quite similar. This is due to the surface instability effect influenced by water confinement that will be discussed later.

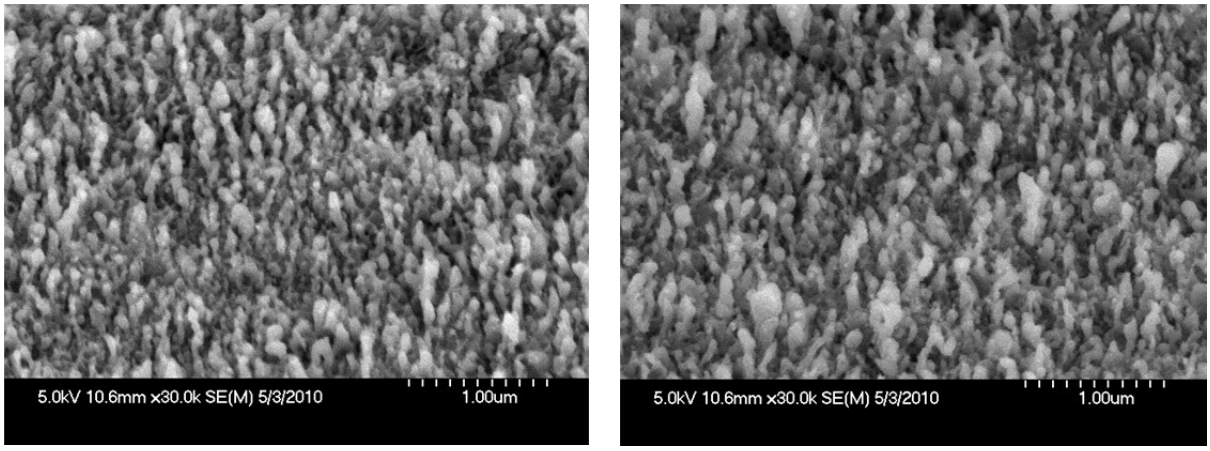

(a) 1.2 J/cm^2 (b) 1.6 J/cm^2

Figure 2.12 SEM images of underwater laser irradiation of a-Si:H film for 50 pulses at fluence of (a) 1.2J/cm^2 (b) 1.6J/cm^2

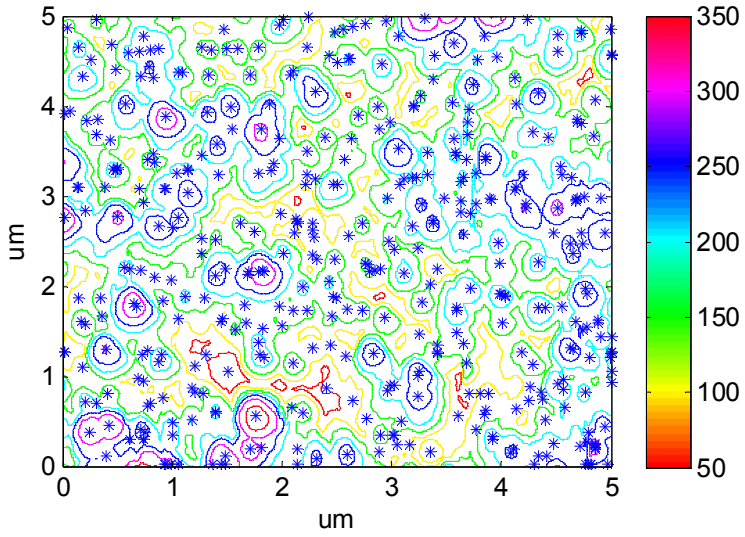

Figure 2.13 Schematic of peak identification of extraction data from AFM images of underwater laser irradiated a-Si:H film at different fluence and number of pulses, asterisks indicate the identified peak point, solid curves indicate the contour spectra, AFM scanning area is 5×5 μm, color bar unit: nm

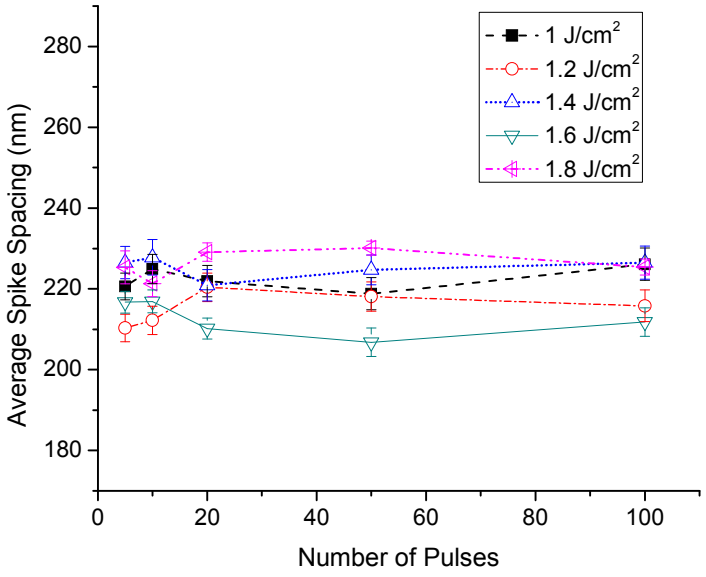

Figure 2.14 Dependence of average spike spacing on laser fluence and number of pulses in water, error bars indicate standard error

In order to further understand the correlation between spike formation and fluence, AFM images were taken at the center ($5\times5\mu m^2$) of samples irradiated by different fluences and numbers of pulses, and then the average spike height and spacing were calculated. In order to obtain reasonable estimate for the non-uniform spike morphology, peak identification from the AFM data was performed by first applying a smoothing filter in order to eliminate the labeling of small height fluctuations as peaks. The peak positions were determined by finding points where the first order derivative is zero and second order derivative less than zero. A typical result is shown in Fig. 2.13, where asterisks indicate peak positions. The average distance to the 4 closest peaks is determined for each peak and the average spacing between the peaks can then be estimated. Figure 2.14 shows that the average spike spacing is nearly constant for different fluences and number of pulses. Considering the imperfect spike distribution, this small variation range of 210-

230 nm suggests that the separation between the spikes is stable at around 200 nm, and it is much smaller than the wavelength-dependent ripples formed at the beginning of irradiation. A similar phenomenon has been shown by Daminelli et al., 2004, the ripples generated on crystalline bulk silicon with both wavelength-dependent and much smaller (~100 nm) spacing are observed after 100 pulses irradiation at a fluence of 1.5-1.6 J/cm^2, and only 100 nm periodicity structures left after 1000 pulses. They suggested that this smaller spacing could be due to surface energy effects between the molten silicon and water which stabilizes more tightly spaced ripples. This may indicate that the a-Si:H surface will be unstable after superposition of the wavelength-dependent ripples and further self-assembly processes make the surface stabilize at much smaller-spaced spikes. The larger spacing of 200 nm compared to the crystalline samples textured in water may be caused by differences in the physico-chemical properties (Kautek et al., 2005) between a-Si:H and c-Si, which indicates that a-Si:H may have a larger surface energy during processing such that the larger-spacing spikes are formed by a larger driving force. It is noted that Shen et al., 2004, showed regular spikes with wavelength-dependent spacing generated on a c-Si surface by irradiating hundreds of pulses at a fluence of 0.76 J/cm^2. This shows that the surface can be stable after superposition of different diffracted ripples if the fluence is low enough and the self-assembly process does not occur. It may suggest that the self-assembly process has a “threshold”, such that at a fluence lower than the “threshold” the smaller-spaced surface structures will not be formed. As discussed above, this threshold is much lower for a-Si:H than for c-Si, which could be caused by different optical properties between the different materials. Since the molten surface of both a-Si:H and c-Si are the same, i.e. liquid silicon, the surface temperatures at this “threshold” of both materials must be equal. a-Si:H will absorb more energy than c-Si after the same number of laser pulses at the same fluence, and the higher temperature distribution on the

a-Si:H surface causes it to have a lower threshold to re-assemble the molten surface during solidification.

In Fig. 2.15, it can be seen that for the fluences of 1J/cm^2, 1.2J/cm^2 and 1.4J/cm^2, the average spike heights linearly increase with increasing fluence and number of pulses up to about 50 pulses. Due to the bead-like structure concentrating the light and causing the ablation rate beside the beads to be higher than that on the tips, the spikes are formed increasingly higher. After a few tens of pulses, the average height goes to a maximum which means that material between the spikes has been completely removed, therefore, the subsequent laser pulses start reducing the height of the spikes because the pulses only remove the material at the tips and the energy is not high enough to damage the substrate. This causes the average height of spikes after 100 pulses to be lower than that at 50 pulses. The tallest spikes after 100 pulses are formed for the lowest fluence of 1J/cm^2 since the ablation rate is proportional to fluence, resulting in the least spike tip ablation. At the higher fluences of 1.6 J/cm^2 and 1.8 J/cm^2, the average peak heights follow the same overall trend with number of pulses as the lower fluences. However, the spike height after 50 pulses at 1.6 J/cm^2 is less than that when processed at 1.4J/cm^2, which means the spike height has already started decreasing by 50 pulses at 1.6 J/cm^2. For an even higher fluence of 1.8 J/cm^2, the point at which full-film-depth ablation occurs is after only 10 pulses, and the significantly reduction in peak height after 20 pulses indicates that nearly the whole film has been removed. The reason why the substrate between the spikes cannot be clearly seen in Fig. 2.12 (b) may be due to the re-deposition of ablated material. However, if the sample is irradiated by hundreds of pulses, it will be clear that the film has been fully removed at the center of the irradiated area (not shown).

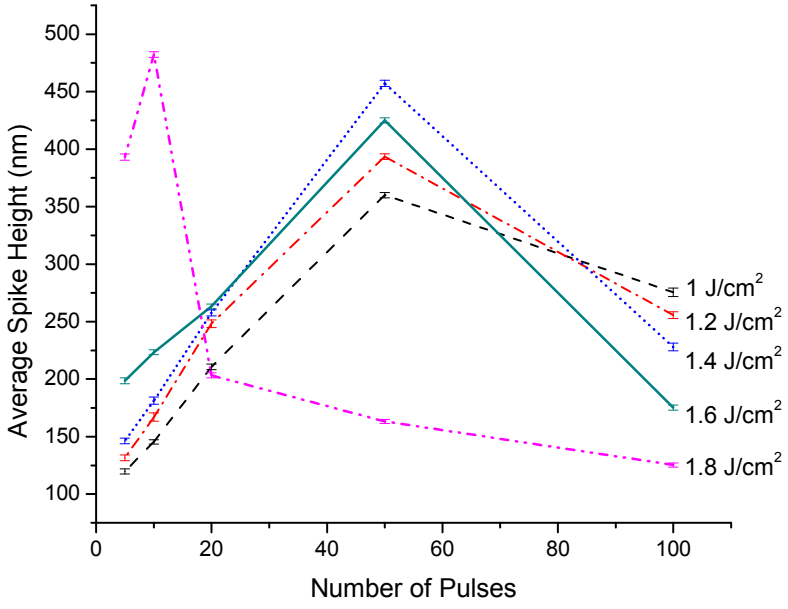

Figure 2.15 Dependence of average spike height on laser fluence and number of pulses in water, error bars indicate standard error

2.5 Conclusion

In conclusion, it has been demonstrated that the surface texturing of a-Si:H thin films is able to be achieved by irradiation by multiple femtosecond laser pulses in both air and water environments. Furthermore, the formation of spikes on laser irradiated a-Si:H surfaces in air follows a similar mechanism to crystalline bulk silicon, however, compared to bulk silicon, a-Si:H thin film have a narrower processing window for suitable texturing fluences in order to not damage or crystallize the entire film. The average spike spacing and height is proportional to the laser fluence, and the spikes are taller, wider and more sparsely distributed at the center than those at the exterior due to the spatial Gaussian distribution of the laser pulses. In water treatment, unlike the formation of wavelength dependent spikes or 100nm-spacing periodic ripples on crystalline bulk silicon, pillar-shaped spikes are generated on a-Si:H film surfaces with

an average spike spacing of around 200nm. This has been suggested to be caused by the presence of water that influences the interface and the stabilization of more tightly spaced ripples. The average spike height formed in water increases linearly with laser fluence and number of pulses until the material between the spikes is completely removed, after which the opposite trend is observed. Finally, the surface texturing is suggested to improve the absorptance over the entire solar radiation spectrum, which indicates that femtosecond laser processing may allow for the fabrication of more efficient and economical a-Si:H thin film absorbers than currently achievable through crystalline bulk silicon for solar cells applications.

Chapter 3: Femtosecond Laser-induced Simultaneous Surface Texturing and Crystallization of a-Si:H Thin Film: Absorption and Crystallinity

3.1 Introduction

Many industrial solar cells in use today use bulk materials as absorbers with crystalline silicon being the most prevalent. However, crystalline silicon suffers from the disadvantage of high material cost since relatively large thicknesses are required primarily due to its low absorption coefficient. Recently, thin film absorbers are becoming more and more attractive based on their potential for low-cost modules, possibility to create tandem junctions and large-scale manufacturability (Luque and Hegedus, 2003; Chopra et al., 2004; Kazmerski, 2006). a-Si:H is the most popular material for use in thin film form due to its low energy economy (cost/watt). The main issue with a-Si:H is the high order of dangling bonds which act as recombination centers that severely reduce the carrier lifetime which results in the solar cell efficiency being below 10%. Additionally, this initial efficiency will decrease by 50% or more when exposed to sunlight over a period of months which is known as the Staebler-Wronski effect or SWE (Miles, 2005; Staebler and Wronski, 1980).

Surface texturing by laser processing is a way to improve efficiency, but the SWE remains. The most important material properties that play a role in the SWE are the high disorder in the Si network and high concentration of impurities, which cause some atoms to have dangling bonds that act as defects. Although these dangling bonds can be passivated by hydrogen, light exposure generates electron hole pairs that will combine. The released energy can break the Si-H bond and promote H to a transport state. The diffusing H-atom successively breaks Si-Si bonds creating Si-H bonds and a neighboring dangling bond. This increasing defect density caused by the so-

called SWE can further reduce the cell efficiency. In a thermal annealing process, the hydrogen atoms will revert back to their original positions. This process can reverse the SWE; however, the same degradation process will happen again when the material is exposed to sunlight (Staebler and Wronski, 1980; Kolodziej, 2004). In order to reduce the SWE, hybrid a-Si:H/nc-Si:H tandem modules have been developed and are able to achieve both higher efficiency and stability compared with single junction a-Si:H (Yamamoto et al., 2004). a-Si:H with reduced thickness will contain less defects, and the nanocrystalline silicon (nc-Si:H) is more stable and has wider spectral absorption compared to a-Si:H. To eliminate the need for two deposition steps, laser-induced crystallization of a-Si:H has been proposed to produce a mixture of nc-Si:H and a-Si:H and simultaneously form a light trapping texture on the surface of the material. Therefore, laser-based treatment of a-Si:H may solve the efficiency and stability issues in a one-step process, which is a promising methodology for thin-film solar cell fabrication.

While both nanosecond and femtosecond pulsed lasers are useful tools for a-Si:H crystallization (Gosain et al., 2003; Shieh et al., 2004), the femtosecond laser-induced crystallization includes an non-thermal ultrafast phase transition, followed by a thermal process which is different from rapid thermal melting and resolidification caused by a nanosecond laser (Choi et al., 2003). However, due to the much smaller thermal diffusion and heat-affected-zones, femtosecond laser processing is more desirable for texturing the limited thickness of thin films. Extensive work on surface texturing of crystalline bulk silicon had been reported by Mazur et al. (Younkin et al., 2003; Sheehy et al., 2005). Micron-size conical spikes have been generated on crystalline silicon a few hundred-micrometers thick when irradiated with a femtosecond laser in different background gases, such as SF_6, N_2, and air, and a significant enhancement in light absorptance is

achieved after texturing. However, limited work is presented for a-Si:H thin films. Nayak et al., 2007, showed the observation of crystallization and simultaneous formation of surface structures on roughly 2μm-thick a-Si:H thin films through femtosecond laser processing in air, and showed that the nano-sizes spikes resulted in similar absorption enhancement to that of laser processed crystalline bulk silicon. However, the light absorption for different surface geometries on a-Si:H surfaces has not been characterized after laser irradiation in different processing environments, such as background gases and water.

In the previous study (Wang et al., 2010, 2011, 2012), the formation of nano-scale conical and pillar-shaped spikes on a-Si:H surfaces has been studied through scanning electron microscopy (SEM) and atomic force microscopy (AFM) for femtosecond laser irradiation in both air and water. Base on the parametric study of the relationship between the surface morphologies and processing conditions, the dependence of light absorptance on typical surface structure is studied by spectrophotometry while the effect of laser processing on crystallinity is investigated by x-ray diffractometry (XRD). The combined effects of light trapping surface structure and crystallization on a-Si:H suggests a one-step process for potentially enhancing the efficiency and stability of thin film solar cells.

3.2 Background

3.2.1 Factors Affecting Light absorption

The light absorption capabilities of a material depend on its optical properties (refractive index, absorption coefficient), film thickness, and surface roughness. This paper mainly focuses on a-Si:H, and thus the optical properties are considered to be consistent between samples. As known,

the thicker the film, the higher the light absorption. However, a thick a-Si:H layer increases the number of recombination centers. As a result, the stability performance deteriorates and the cost increases. Anti-reflection coating is also a way to improve absorption, but additional costs for the material and deposition process are also introduced. Therefore, changing the surface geometry is the most economical and efficient way for enhancing the light absorptance.

Yagi et al., 2006, showed a significant reduction in the reflectance of crystalline silicon with a pyramidal textured surface by anisotropic etching, and also found that the reflectance of silicon deposited on V-shaped glass substrates increases with increasing angle of the V-shape. Halbwax et al., 2008, investigated the dependence of absorption on different shape surface structures and showed conical spikes had the best absorption, followed by pillars and pyramids. Hua et al., 2010, showed the absorption caused by different surface geometries, and found that surface structures with higher density, smaller top angle, and a spike shape that can introduce a greater number of reflections within the periodic structures, will absorb a larger fraction of the incoming light.

3.2.2 Femtosecond Laser-induced Crystallization

During femtosecond laser irradiation, the conservation equation for electrons excited by multiphoton absorption can be written as (Choi et al., 2003),

$$\frac{\partial N(x,t)}{\partial t} = \frac{(1-R)\alpha I(x,t)}{h\nu} + \frac{(1-R)^2 \beta I^2(x,t)}{2h\nu} \tag{2.1}$$

where N is electron density, R is reflectivity, α is linear absorption coefficient, $h\nu$ is the photon energy of the laser beam, β is the two photon absorption coefficient, and $I(x,t)$ is the laser intensity expressed as follows (Choi et al., 2003),

$$\frac{\partial I(x,t)}{\partial t} = -(\alpha + \Theta N)I \tag{3.2}$$

where Θ is the free carrier absorption cross section.

If the critical density of electrons, which is estimated to be 10^{22} cm^{-3} (Choi et al., 2003), is exceeded, they are excited out of the bonding states of the valence band into the conduction band, and a non-thermal ultrafast phase transition will occur. Due to the removal of a significant number of electrons from the material, the bond charge will be so weak that the material structure will no longer be stable and will collapse caused by the atoms' enhanced mobility. Thus the phase changes to liquid without thermal effects (Vechten et al., 1979; Linde and Fabricius, 1982). This ultrafast phase transition caused by a high density photo-excited plasma without increasing the materials thermal energy is called the plasma annealing mechanism. Van Vechten et al., 1979, showed that, as the plasma becomes less dense due to expansion and energy transfer to the material, the material will pass back through the phase transition and covalent bonding will gradually reappear. Crystallization of the material can occur if this solidification process does not occur too quickly. Choi et al., 2003, considered that the non-thermally melted layer vanishes in a few picoseconds during which time a portion of the covalent bonds start to reappear due to relaxation of electrons back to the valence band. Within a nanosecond, the surface starts to be melted due to thermal diffusion after the transfer of energy from the excited electrons to the material. Resolidification of this thermal melting layer causes the final crystallization. Callan et al., 2001, also suggests that the ultrafast non-thermal phase transition described above does not lead to a thermodynamically stable crystalline phase, but to a nonequilibrium disordered phase, and this disorder-to-disorder phase transition can cause defect formation which is considered to be the driving force for subsequent rapid nucleation (Choi et al., 2003). This process which includes non-thermal and thermal melting leading to solidification describes femtosecond laser-

induced crystallization, which is different from nanosecond laser crystallization where only a rapid thermal melting and solidification process occurs.

3.3 Experimental Setup

1.6μm-thick amorphous silicon films were deposited on 0.525mm-thick glass substrate using plasma enhanced chemical vapor deposition. The films were deposited at a rate of 60 Å/s in a hydrogen diluted silane environment at 380°C with a hydrogen atomic concentration of around 20 at %. Femtosecond laser texturing was carried out using a commercial Ti:sapphire oscillator and regenerative amplifier system. The system delivered 130-fs pulses of linearly polarized light at a 1 kHz repetition rate, and a central wavelength of 800 nm. The sample is mounted on a three-axis translation stage and irradiated by laser pulses focused by a 60 mm focal-length lens. When changing the environment to water, the sample is placed in a plastic container, and the laser beam focused by the same lens travels through 5 mm of distilled water before striking the sample surface. The focal plane of the laser is moved below the sample surface in order to adjust the beam spot size. For both air and water cases the beam spot on the sample surface was circular with a diameter of 150μm. The spikes generated at different fluences in water have a similar geometry, which suggests that they will have similar absorptance. Therefore, a fluence of 1.2J/cm^2 is selected to produce typical results for underwater treatment. In order to reproduce the surface morphology observed for stationary processing at a fluence of 0.4J/cm^2 with 100 pulses in air and at a fluence of 1.2J/cm^2 with 50 pulses in water, 10×15 mm^2 areas were processed at specific scan speeds. The scan speed, v, is set by the Full width at half maximum (FWHM) of the Gaussian beam profile, d, the number of pulses, N, and the repetition rate of the laser, f, through the relation $v=df/N$ (Crouch et al., 2004).

The untreated and treated samples were also observed through scanning electron microscopy (SEM). Surface roughness and the distribution of spikes in the treated samples were examined using an atomic force microscope (AFM). The optical transmittance and reflectance of both untreated and treated samples were measured by a spectrophotometer over a wavelength range of 250nm-2500nm which corresponds to the main spectral range of solar irradiation (Goetzberger et al., 1998). The reflectance (R in %) and transmittance (T in %) are then used to calculate the absorptance (A in %) of the film: $A=100-R-T$. X-ray diffraction (Cu K_α-line) was used for crystallinity estimation. X-ray photoelectron spectroscopy is used for composition analysis.

3.4 Results and Discussion

3.4.1 Surface Morphology after Laser Scanning

When observed optically, the surface of the processed a-Si:H film is much darker than the original shiny reddish gray color which shows that the textured surface has the capability to trap light which greatly reduced the visible light reflection. Since the relationship of the formation of the spikes and number of pulses under different laser fluences is investigated in the previous studies (Wang et al., 2010, 2011, 2012), typical conditions, 0.4J/cm^2 and 1.2J/cm^2 in air and water, respectively, are selected to study the surface morphology via laser scanning. Figure 3.1 (a) shows the SEM images of the surface processed at a fluence of 0.4J/cm^2 and a speed of 1mm/s in air, and the spikes look similar to those formed during stationary spot irradiation (Wang et al., 2010, 2012). The AFM measurement in Fig.3.1 (b) shows that conical spikes are formed on the sample surface with an average height of 0.922±0.0487μm and an average spike spacing of 1.886±0.0824μm where the variation represents standard deviation. Figure 3.2 (a) and (b) show high magnification SEM images of scanned and stationary processed sample surfaces; there are

two visible differences between these two samples. First, the spikes on the stationary sample have a smooth conical shape at the tips while those on the scanned sample look blunter and lack this smooth conical shape. Second, the scanned sample has a larger amount of nanoscale particles spread across the spike surfaces. The nanoscale particles on the scanned sample are made of redeposited material from the ejected plasma plume and can lead to light scattering. On a stationary sample, most of this debris lies away from the area where the surface morphology forms, and deposits as a ring around the irradiation spot (Carey, 2004). The conical tips at the a-Si:H surface can be caused by resolidified droplets of redeposited molten silicon. The droplets at the tips are flowing around the spike surface towards the bottom due to gravity and a conical tip is formed after resolidification.

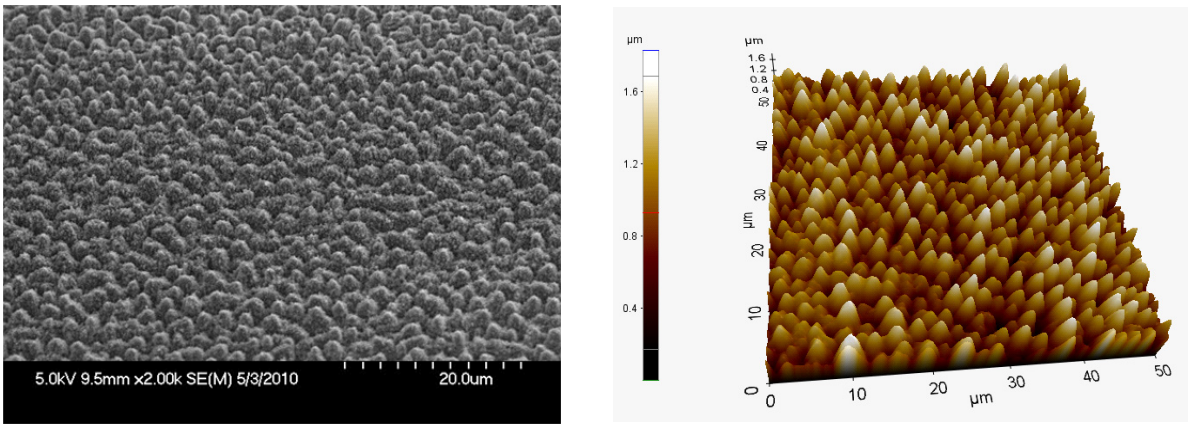

(a) (b)

Figure 3.1 (a) SEM image and (b) AFM image of surface of a-Si:H film laser irradiated in air, (0.4J/cm^2, 1mm/s), showing texturing with conical spikes on the surface

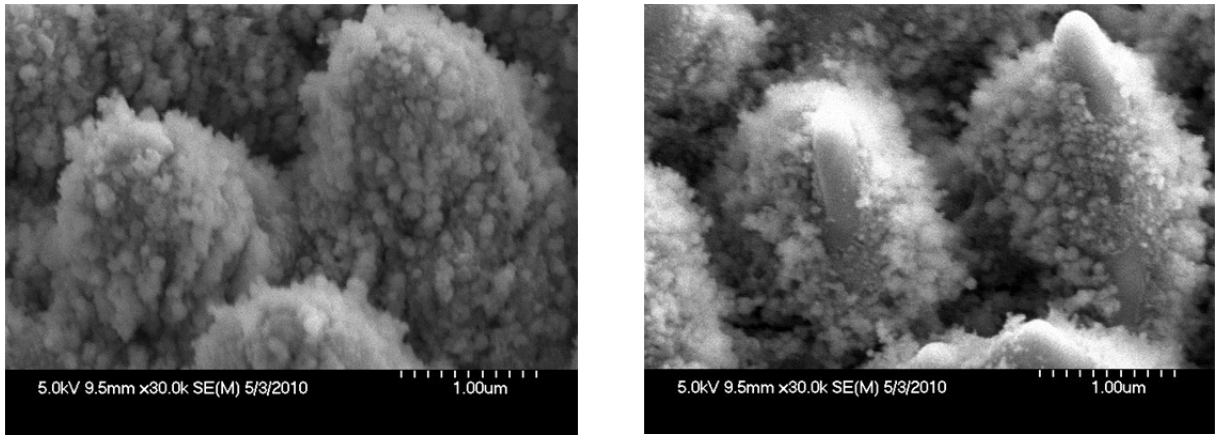

(a) (b)

Figure 3.2 Comparison of textured spikes made by (a) scanning (0.4 J/cm^2, 1mm/s) and (b) stationary (0.4 J/cm^2, 100 pulses) pulsing in air, showing nanoparticles distributed on the whole spike after laser scanning

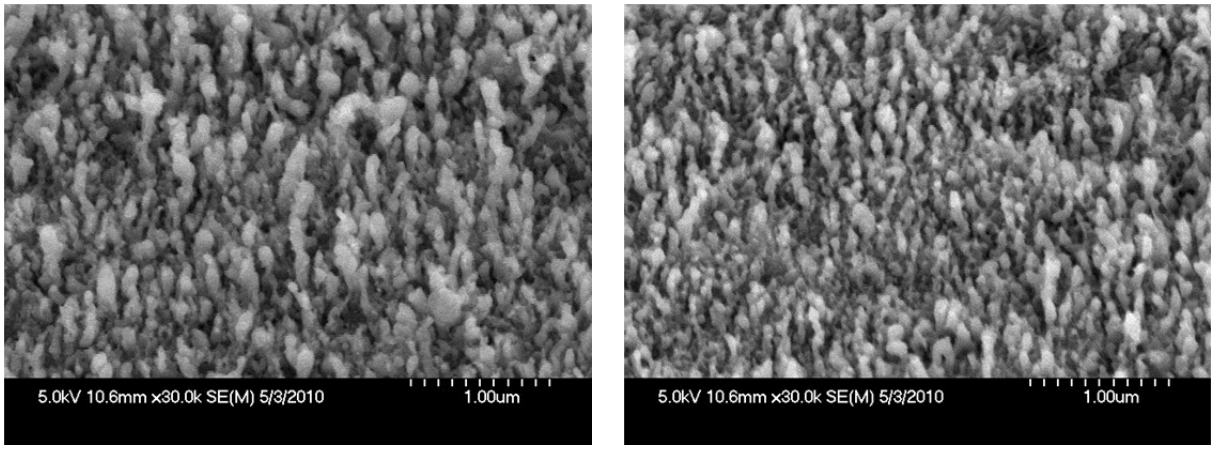

(a) (b)

Figure 3.3 Comparison of textured spikes made by (a) scanning (1.2J/cm^2, 2mm/s) and (b) stationary (1.2J/cm^2, 50 pulses) pulsing in water, showing similar pillar-shaped spikes textured on the both sample surfaces

Figure 3.3 shows the SEM images of both a scanned sample surface treated at a fluence of 1.2 J/cm^2 at 2mm/s and a stationary sample treated at 1.2J/cm^2 at 50 pulses in water and similar spike formations are observed. The reason is that water convection and the motion of decomposed bubbles contribute to the reduction of debris redeposition. Therefore, the spike surfaces in both

samples are smooth. The average spike height and spacing of scanned sample measured by AFM are 391.75±2.612 nm and 218.63±3.867 nm, respectively, which are close to those measured on stationary samples (Wang et al., 2012); the variation represents standard error.

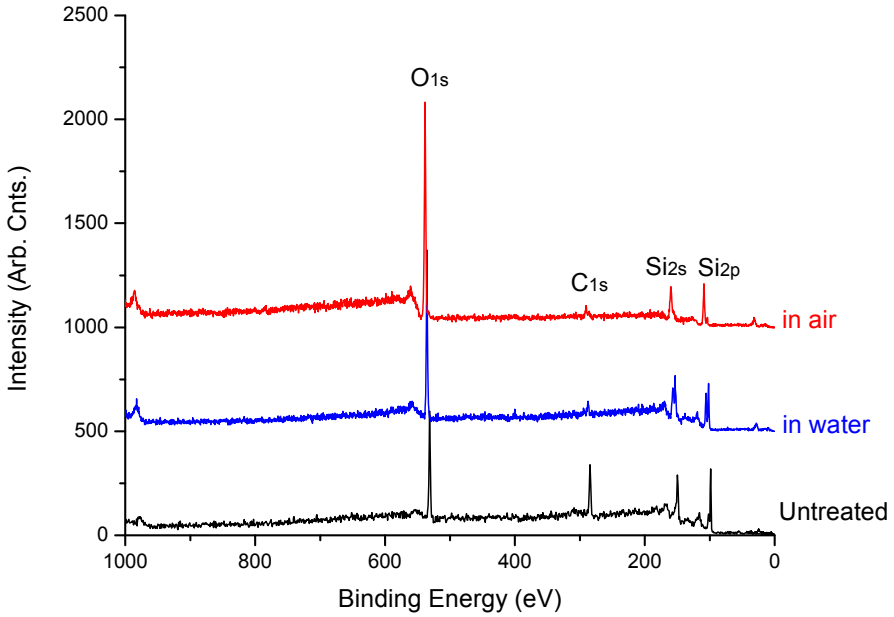

Figure 3.4 XPS spectra of a-Si:H sample surfaces of as received, laser irradiated in air (0.4J/cm2, 1mm/s) and in water (1.2J/cm^2, 2mm/s). The spectra have been shifted up for clarity. Note increase in oxygen and decrease in carbon after laser processing

Table 3.1 Chemical constituent concentrations of the a-Si:H sample surfaces for as received, laser irradiated in air and laser irradiated in water

Elements / Samples	O_{1s}	C_{1s}	Si_{2s}	Si_{2p}
Untreated a-Si:H	22.1%	23.6%	21.6%	32.6%
Treated in water	32.01%	3.44%	31.26%	33.29%
Treated in air	47.4%	4.28%	22.86%	25.46%

In order to analyze the chemical constituent on the spike surfaces, XPS measurements are carried out for untreated and treated samples in air and water. The results are shown in Fig. 3.4 and Table 3.1. The XPS survey results in Fig. 3.4 have been shifted vertically and superposed for clarity. The concentration of oxygen increases to almost 50% after laser treatment in air, which indicates that the nanoparticles attached on the spikes are silicon oxide (SiO_x). The 10% increase in oxygen concentration after underwater treatment is considered to be caused by the existence of a thicker oxidation layer on the surface compared to the as received a-Si:H films. The oxidization layer is not desirable for absorption because it is an isolator, however, due to the smaller refractive index than that of a-Si:H, the reflectivity of silicon oxide layer is smaller. Based on Nayak et al., 2007, the oxygen concentration decreases to less than 10% at the depth of 30 nm after laser processing, therefore, compared to the film thickness, the oxidization layer is so thin that cannot affect the final absorption. The carbon peaks for both cases decrease almost to zero, this is due to the formation of carbon oxide (CO_x) during the processing, so that the solid-phase carbon changes to gas-phase carbon oxide and is released into the air environment or forms bubbles which are suspended in the water.

3.4.2 Effect of Laser Processing on Absorption

Based on the spike formation by laser scanning, an area of 10×15 mm^2 is treated in order to investigated the effect of morphology change on absorption. Figure 3.5 shows the comparison of absorptance measurements of untreated and treated samples with surface texture consisting of low-density conical spikes formed in air and high-density pillar-shaped spikes formed in water. A dramatic increase in the absorptance can be seen for the treated a-Si:H films over the entire spectrum. The absorptance spectra for both treated samples go up to more than 90% from UV

wavelengths to the band gap of a-Si:H (730nm) due to multiple reflections enabled by the surface texture, and decrease to around 45% and 30% in the below-band-gap region, for the air and water treated samples respectively. The laser induced oxidization layer can be also helpful for absorption enhancement, because it causes a reflection decrease at the surface due to the refractive index change. In the above-band-gap range, the absorptions for the samples processed under different conditions as a function of wavelength show different trends. The increase in absorptance for the untreated sample from UV wavelengths to the band gap is mainly caused by the material's optical properties, which indicates that the absorption coefficient increases with increasing wavelength. However, the opposite trend is observed in the sample treated in air which may be caused by light scattering by the nanoparticles attached to the surface of the conical spikes (Fig. 3.2). According to Rayleigh scattering theory, when the radius of the particle is much smaller than the wavelength of the incident light, the intensity of scattered light is inversely proportional to the fourth power of the wavelength (Steen, 2003)

$$I(\lambda)_{scattering} \propto \frac{I(\lambda)_{incident}}{\lambda^4} \tag{3.3}$$

where I and λ are intensity and wavelength, respectively. Therefore, at shorter wavelengths, a larger fraction of the incident light is scattered by the nanoparticles, which causes the highest absorptance to occur at the shortest wavelength. The absorptance spectrum of the sample treated in water is almost flat, which can be caused by much fewer nanoparticles being generated on the spikes due to the influence of water, thus a smaller fraction of light is scattered.

The differences in the below-band-gap absorptance of the treated a-Si:H samples could be attributed to different levels of crystallinity (band gap of nc-Si:H is 1.1eV) (Meillaud et al., 2009) which broadens the absorption range to 1100nm while the textured surface introduces light

trapping through multiple reflections as well as scattering by the nanoparticles. Moreover, the water environment may introduce less impurities and defects during processing which can cause fewer sub-band gaps to form, which causes the material to absorb a smaller fraction of light with longer wavelengths compared to the sample treated in air. The reason why the absorptance starts decreasing at 730nm rather than 1100nm is due to the material remaining primarily amorphous with a band-gap of 730nm. In the below-band-gap range, unlike for untreated a-Si:H, the absorptance curves for the treated films do not oscillate. The multiple reflections caused by the textured surface change the transmitted light paths through the film such that rays are not reflected back along their original paths, eliminating internal interference.

Overall, it is shown that the absorption can depend on the surface geometry, such as spike shape, density and attached nanoparticles, as well as crystallinity and impurity concentrations.

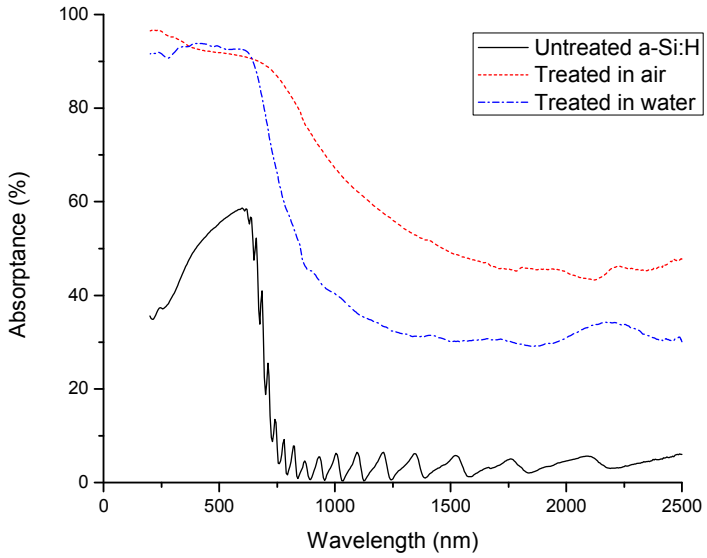

Figure 3.5 Comparison of absorptance spectra of as-received and laser treated a-Si:H films at fluences of 0.4J/cm^2 (scan speed 1mm/s) and 1.2J/cm^2 (scan speed 2mm/s) in air and water by spectrophotometry, showing increase in absorptance over entire spectrum for both treated samples

3.4.3 Modeling of Surface Geometry Effect on Absorption

In order to analyze the effect of surface geometry, a ray tracing method (Hua et al., 2010; Spencer et al., 1962) is used for calculating the path of waves through a system with regions of varying propagation velocity and absorption characteristics, based on geometrical optics. A solution is achieved by repeatedly advancing idealized narrow beams called rays through a medium by discrete amounts. A given ray is specified at a point, $\overline{P_0}$, as shown in Fig. 3.6, in a reference coordinate system $(\overline{X},\overline{Y},\overline{Z})$ with origin $\overline{O}$ $(\overline{x_0},\overline{y_0},\overline{z_0})$, and has a certain wavelength, intensity and a direction of travel, $(\overline{k},\overline{l},\overline{m})$. An absorbing material with a surface, *S,* that is specified by an equation *F(X,Y,Z)=0* is defined in coordinate system *(X,Y,Z)* having its origin at point *O*.

The first step is to transform the ray coordinates and direction cosine into their values in the *(X,Y,Z)* coordinate system. If the rotation angles between the *(X,Y,Z)* system and the $(\overline{X},\overline{Y},\overline{Z})$ system are (α,β,γ), the transformation matrix can be written as (Spencer et al., 1962)

$$Q=\begin{bmatrix}(\cos\alpha\cos\gamma+\sin\alpha\sin\beta\sin\gamma) & -\cos\beta\sin\gamma & (-\sin\alpha\cos\gamma+\cos\alpha\sin\beta\sin\gamma)\\ (\cos\alpha\sin\gamma-\sin\alpha\sin\beta\cos\gamma) & \cos\beta\cos\gamma & (-\sin\alpha\sin\gamma+\cos\alpha\sin\beta\cos\gamma)\\ \sin\alpha\cos\beta & \sin\beta & \cos\alpha\cos\beta\end{bmatrix} \quad (3.4)$$

If $\overline{P_0}$ in coordinate *(X,Y,Z)* is $(\overline{X_0},\overline{Y_0},\overline{Z_0})$,The transformation equations for $\overline{P_0}$ and the ray direction vector are

$$\begin{bmatrix}X_0\\ Y_0\\ Z_0\end{bmatrix}=Q\begin{bmatrix}\overline{X_0}-\overline{x_0}\\ \overline{Y_0}-\overline{y_0}\\ \overline{Z_0}-\overline{z_0}\end{bmatrix} \text{ and } \begin{bmatrix}k\\ l\\ m\end{bmatrix}=Q\begin{bmatrix}\overline{k}\\ \overline{l}\\ \overline{m}\end{bmatrix} \quad (3.5)$$

Second, the point of intersection of the ray with the surface *S* is found. The parametric equations of the given ray may be written as (Spencer et al., 1962)

$$X=X_0+ks,\ Y=Y_0+ls,\ Z=Z_0+ms \tag{3.6}$$

where s is the distance along the ray measured from ($X_0,\ Y_0,\ Z_0$). s is determined by satisfying the equation $F(X,Y,Z)=0$, which can be calculated by a numerical method such as the Newton-Raphson iteration technique as follows (Spencer et al., 1962)

$$s_{j+1}=s_j-F(X_j,Y_j,Z_j)/F'(X_j,Y_j,Z_j) \tag{3.7}$$

where, $X_j=X_0+ks_j,\ Y_j=Y_0+ls_j,\ Z_j=Z_0+ms_j$, and

$$F'(X_j,Y_j,Z_j)=dF/ds(s=s_j)=\frac{\partial F}{\partial X_j}k+\frac{\partial F}{\partial Y_j}l+\frac{\partial F}{\partial Z_j}m \tag{3.8}$$

This process starts from a first approximation, $s_1=0$, and is terminated with the value s_f for which $\left|s_f-s_{f-1}\right|<\varepsilon$, where ε is a small pre-assigned tolerance.

Third, the change in direction at the intersection point of the ray and the surface is found. Reflection is based on Snell's law and the intensity change is determined by Fresnel's equations. Fourth, the second and third steps are repeated to find the subsequent points of intersection of the reflected ray with the surface, and the absorption caused by the ray traveling through the material is calculated based on Beer Lambert's law, until the intensity of the ray decreases to a negligible amount, e.g., 0.1% of the original intensity. The absorptance, $A(\lambda,i)$, reflectance, $R(\lambda,i)$, and transmittance, $T(\lambda,i)$ of a given ray i at wavelength λ are the total absorbed, reflected and transmitted intensities, respectively, divided by the initial ray intensity $I(\lambda,i)$.

Lastly, if the light source is defined by a spectrum from λ_1 to λ_2, and for each wavelength it can be divided into a discrete number of rays, p, at different initial points $\overline{P_0}$ and propagation directions $(\overline{k},\overline{l},\overline{m})$, the relationship between absorptance, reflectance, transmittance, and source intensity can be described as

$$\sum_{\lambda_1}^{\lambda_2}\sum_{i=1}^{i=p}[A(\lambda,i)+R(\lambda,i)+T(\lambda,i)]I(\lambda,i)=I_{lightsource} \tag{3.9}$$

In this paper, the model is realized by a ray-tracing software TracePro (Hua et al., 2010). The Monte Carlo method is used to sample the distribution of rays emanating from light sources and each ray with a certain intensity, direction and wavelength is traced through the model structure. Consequently, portions of the ray are reflected or refracted at every interface and absorbed through the film, with the fraction being calculated by the angle of incidence and the optical properties. The model configuration consisting of an a-Si:H thin film on a glass substrate is shown in Fig. 3.6. Since the absorption coefficient of crystalline silicon is two orders of magnitude less than that of a-Si:H, and the amount of crystalline silicon after crystallization is much smaller than that of a-Si:H, the model does not consider the effect of crystallization on the thin film absorptance. The model also assumes that the entire structure is uniform and no nanoparticles are attached on the spikes; therefore internal defects and Rayleigh scattering are not simulated. The surface structures are designed with dimensions similar to the conical and pillar-shaped spikes formed in air and water, respectively. The simulated area is 300×300 μm^2, and the diameter of the circular light source is 200μm with a wavelength range between 250nm and 2500nm. The wavelength step is 10nm, and a set of 60,000 rays are randomly generated with a total intensity of 1 watt. The light is normally incident to the textured surface with conical spikes, and has a 45° incident angle to the surface with pillar-shaped spikes.

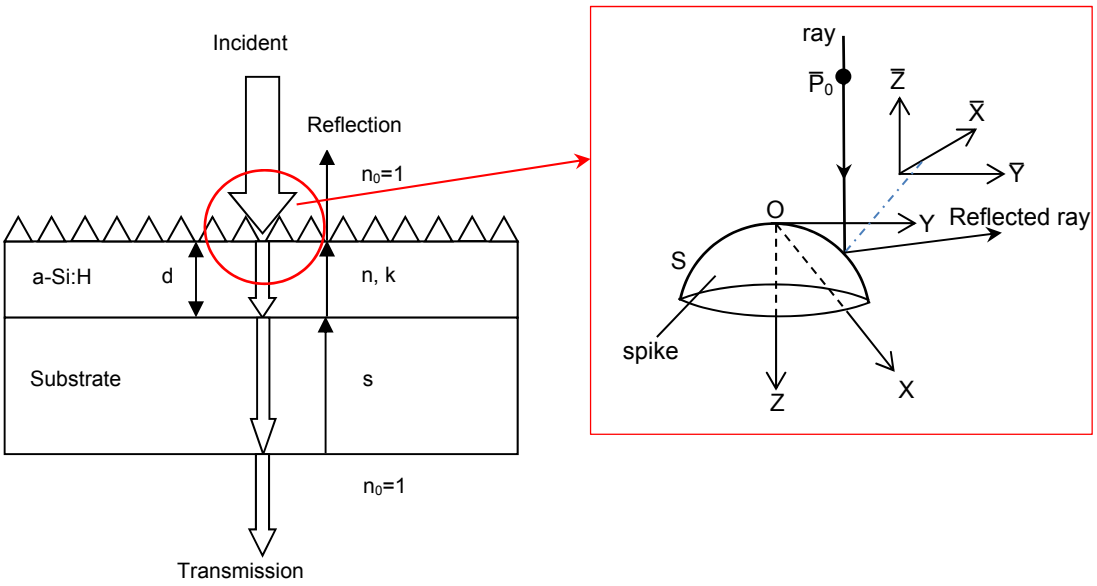

Figure 3.6 Schematic of cross-sectional absorption simulation model for textured a-Si:H film on glass substrate, total thickness is 1.6μm, real and imaginary parts of refractive index of a-Si:H film are n and k, s and n_0 are the refractive index of the substrate and air, respectively. Magnified image in the right shows the reference and local coordinate systems ($\bar{X}$, $\bar{Y}$, $\bar{Z}$) and (X, Y, Z), where S denotes the spike surface that reflects the ray passing through point $\bar{P}_0$

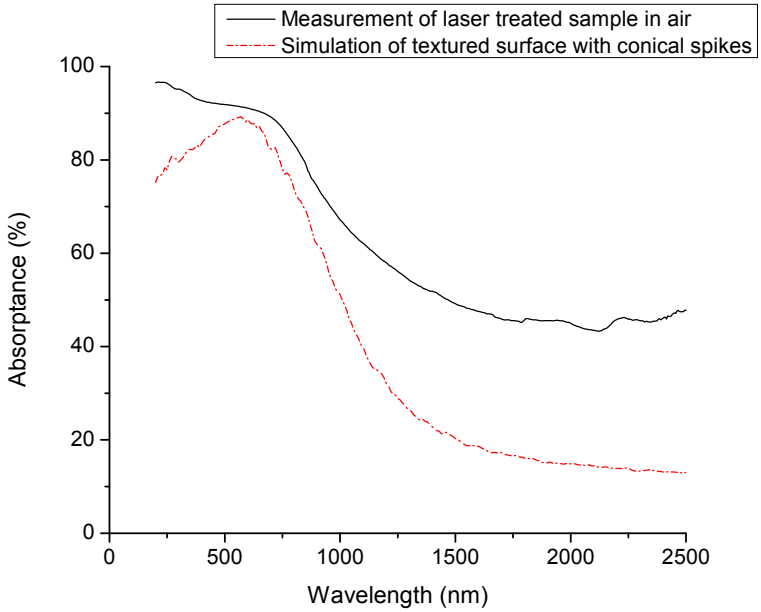

Figure 3.7 Comparison of simulated and measured absorptance spectra of the laser treated sample in air with the textured surface of conical spikes, with height of 900 nm and top angle of 90°

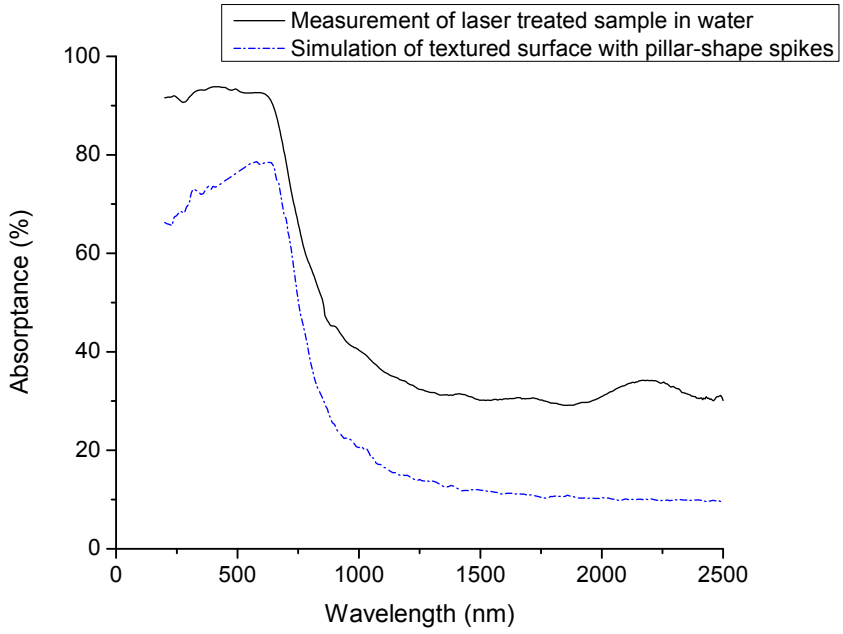

Figure 3.8 Comparison of simulated and measured absorptance spectra of the laser treated samples in water with textured surface of pillar-shaped spikes with height of 400nm height and a diameter of 100nm

Figure 3.7 and 3.8 show the comparison between the simulated and measured absorptance spectra of the samples treated in air and water, respectively. The overall trends of the simulation curves are similar to the measurement spectra except in the above-band-gap range. All of the simulated results show a similar trend to the untreated sample in this wavelength range (Fig. 3.5), which suggests that the difference is neglect of the Rayleigh scattering effect by the nanoparticles as discussed above. The underestimate in the below-band-gap region can be caused by neglecting the scattering effect. Moreover, ignoring the crystallization effect, defects, and impurities generated after laser processing could be another reason of under-prediction. As known, the defects can act as recombination centers for electron-hole pairs, and the impurities may introduce sub-band gaps that absorb light with longer wavelengths. Furthermore, the simplification of periodic surface structure in the model differs from the exact spikes generated

after laser processing, especially since the pillar-shaped spikes formed in water are pointed in different directions and are more irregular than the simulated model geometry. Therefore, the real spike shape and distribution can obtain a greater number of reflections at the surface than the regular pillar-shaped surface simulation, which causes underestimation of the absorptance over the entire spectrum. However, most of the characteristics of the measurement are captured by the simulated curves, so that the model can be used for estimating the effect of different surface geometries on the absorptance. During the comparison, it can be seen that the conical spikes have better absorption performance than pillar-shape spikes.

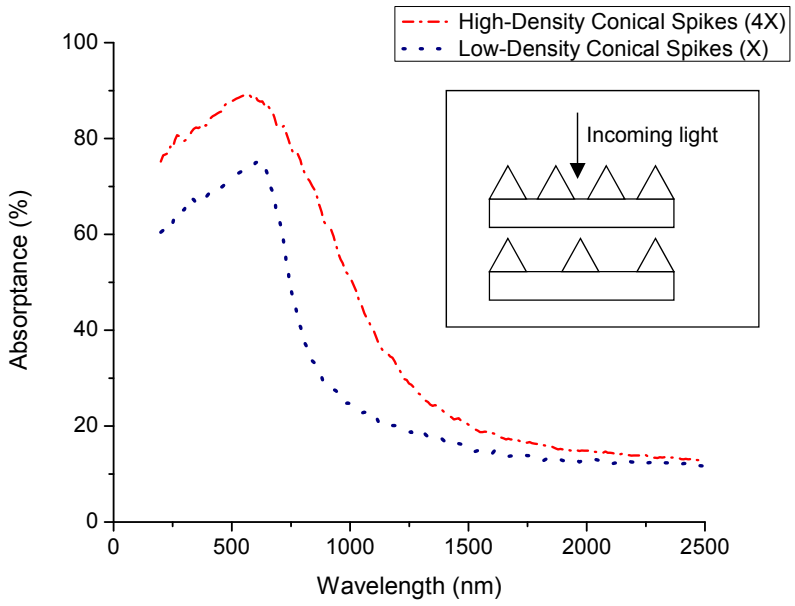

Figure 3.9 Comparison of simulated absorptance spectra for the textured surfaces with two different densities of conical spikes, showing the surface with higher density spikes has higher absorptance

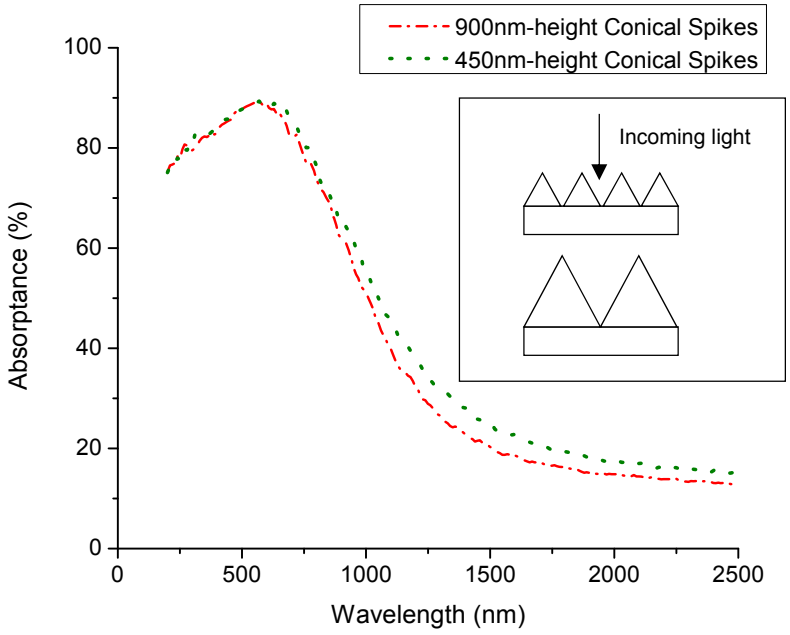

Figure 3.10 Comparison of simulated absorptance spectra for textured surfaces with different heights of conical spikes, showing similar absorptance over the entire wavelength range

In order to further understand the effect of different geometric factors, two models with different spike densities and heights are investigated. Figure 3.9 shows the simulated absorptance spectra of textured surfaces with conical spikes of different densities. The inset image shows the schematic of the spike distribution on the surface. It is assumed that the spike geometric parameters, such as height (900nm) and top angle (90˚), are the same, and the only difference is the density, one is 4 times as the other. During the spike formation process, when the surface shows a bead-like structure as seeds of the spikes, the average bead spacing, which is similar to the final average spike spacing, is different under different fluences. And then using different number of pulses under those fluence conditions can generate similar geometries of the spikes with different distances between the adjacent spike bases. In order to simplify the problem, it is treated as a flat area in between the spike bases during the simulation.

The results indicate that the surface with higher-density spikes has better absorption performance. This is because the sample with higher density has less open space in between the spike bases, which cannot cause multiple reflections. The reflectance on a unit surface with higher density spikes will be much less so that the absorptance is higher. However, in the below-band-gap region, the absorption performance deteriorates when the wavelength increases. The light with longer wavelength is more difficult to be absorbed due to the low photon energy, although the multiple reflections still occur. This can also explain why the difference between the absorptance spectra becomes smaller and smaller. According to the better absorption performance by the surface with high-density conical spikes, it can be seen that the factor of spike shape plays a more important role in absorption. The simulated absorptance spectra of textured surfaces with different height of conical spikes are shown in Fig. 3.10, and the inset image shows the schematic of the spike distribution on the surface. It is assumed that the spikes are closed-packed (spikes are connected together) and the shape and top angle are the same, and one sample has a twice height texturing as the other. It shows that the absorptance performances for different height spikes are almost the same. The reason is that for those closed-packed spikes with the same top angle, no matter how the spike height and density are, the number of times a ray is reflected between spikes is the same, so that the distance traveled by the rays inside the two samples are very similar, and the total absorptance is similar.

3.4.4 Effect of Laser Processing on Crystallinity

In order to study the crystallization of the treated films, x-ray diffraction patterns were taken for the untreated and treated a-Si:H films in air and water and are shown in Fig. 3.11. The spectra have been shifted vertically for clarity. All the spectra show an amorphous peak around $2\theta=25°$,

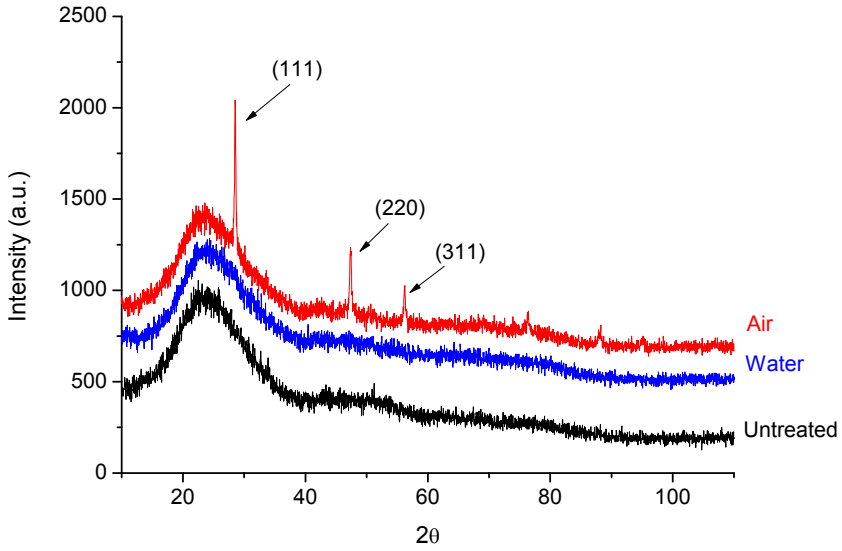

Figure 3.11 X-ray diffraction spectra of as-received a-Si:H film, laser treated films at 0.4J/cm^2, 1mm/s and 1.2J/cm^2, 2mm/s in air and water, respectively. All the spectra show an "amorphous peak" at around 2θ=25° and no signs of crystallinity for the untreated sample and that treated in water. Sample treated in air shows three different peaks for (111), (220) and (311) orientation of silicon. The spectra have been shifted for clarity

which is caused by the internal constructive interference of the amorphous Si network. Three peaks at around 2θ=29°, 47° and 56° emerge after processing in air which indicate a structural change after laser irradiation and can be indexed to the (111), (220) and (311) crystalline orientations of silicon. During femtosecond laser processing an ultrafast non-thermal disorder-to-disorder phase transition occurs within a few picoseconds of the laser pulse which cannot lead to crystallization. The material is then partially melted due to thermal diffusion after energy transfer from the excited electrons to the material. The resolidification of the melted layer proceeds via vertical growth from the remaining un-melted material and results in random crystal orientations due to the amorphous structure of the film. According to the silicon powder diffraction file, the highest three intensities of x-ray diffraction are for the (111), (220) and (311) orientations and are the same as observed in Fig. 3.11. The crystallization is considered to be under the partial

melting regime, resulting in no preferential orientation during solidification. This suggests that the laser irradiated film becomes a mixture of nc-Si:H and a-Si:H with most of the nc-Si:H believed to be contained within the top melted surface. However, the XRD pattern also shows that the sample treated in water at 1.2J/cm^2 with a scan speed of 2mm/s has no crystallinity.

In order to further understand the laser processing parameters, fluence and scan speed, effect on crystallinity in water, a film was treated with a lower fluence (0.5J/cm^2) at 2 mm/s and at a higher scan speed (25mm/s). The XRD patterns are shown in Fig. 3.12. Only the sample treated at 0.5J/cm^2 with scan speed of 25mm/s has two small peaks that can be indexed to the (111) and (220) orientations of silicon. The reason is due to the higher cooling rate in a water environment than in air; the melted silicon resolidifies so quickly that much less material is able to crystallize. The sample processed at the same fluence, 0.5J/cm^2, but lower scan speed of 2mm/s has no crystallinity; the reason could be the higher pulse overlap during processing. Daminelli et al., 2004, showed that the ablation threshold of silicon decreases with increasing number of pulses due to modification of the absorption behavior of the film such that subsequent surface texturing occurs at fluence levels lower than for previous pulses. Processing with this decreased threshold caused by higher overlap can be considered to be equivalent to processing at a higher fluence and lower overlap. The femtosecond laser-induced crystallization is ablation-dominant process rather than that of nanosecond laser which crystallinity is proportional to the laser energy since it is a melting-dominant process. Therefore, more material will be removed by a higher energy input, resulting in a deeper buried melting thin layer underneath. This deeper melting layer will cause larger temperature gradients through thickness direction compared to that of lower energy input. Therefore, a higher cooling rate is induced during the solidification process and the liquid layer

does not have enough time to be crystallized. Similarly, Fig. 3.13 shows the XRD pattern of samples treated at the same scan speed, 25mm/s, but different fluences from 0.5 to 0.8J/cm^2. It can be seen that the crystallinity decreases with increasing fluence, and fluences larger than 0.7J/cm^2 do not introduce crystallinity. The femtosecond laser induced crystallization has a non-thermal melting process within 1 about picosecond; however, it will not affect the crystallization. The crystallization happened at nanosecond scale when the energy transferred back from free electrons to material and started melting the material. Therefore, Eq. (3.1) is no longer valid for analyzing the temperature distribution at this point. It is assumed that the process can be separated by two models – nonlinear absorption (free electron excitation) and linear thermal diffusion (energy transferred back to material). Therefore, for the crystallization process, it can be assumed that the heat source is from those free electrons rather than the laser and the energy loss during the electron movement is negligible. The thermal effects of laser processing on crystallization can be described using a model that is based on one-dimensional heat flow given by (Palani et al., 2008),

$$c_s(T)\rho_s(T)\frac{\partial T(x,t)}{\partial t} = \frac{\partial}{\partial x}\left[\kappa(T)\frac{\partial T(x,t)}{\partial x}\right] + S(x,t) \tag{3.10}$$

where $T(x,t)$ is the temperature distribution, $c_s(T)$ is the specific heat, $\rho_s(T)$ is the density, $\kappa(T)$ is the thermal conductivity and $S(x,t)$ is the source which is proportional to the energy absorbed by the surface layer estimated by,

$$S(x,t) = \alpha(t)I(x,t) \quad \text{and} \quad I(x,t) = I_0(t)\left[1 - R(T)\right]e^{-\alpha(T)x} \tag{3.11}$$

where $R(T)$ is the reflectivity, $\alpha(t)$ is absorption coefficient and $I_0(t)$ is the intensity that absorbed by free electrons which is proportional to the laser pulse intensity.

As discussed in section 3.2.2, thermal melting occurs underneath the ablated layer and is caused by thermal diffusion, thus the higher the fluence, the thicker the ablated layer, and the deeper the thermally melted layer will be. Based on Eq. (3.10), the influence of laser fluence on the temperature distribution along the depth of the film is shown in (Palani et al., 2008); it can be seen that the temperature gradient increases with increasing fluence and depth into the film. Thus the thermal melting caused by higher fluences introduces steeper temperature gradients compared to lower fluence treated samples and can be solidified quicker. Thus the higher fluence can cause a higher cooling rate, which accelerates the cooling/resolidification process and reduces crystallinity.

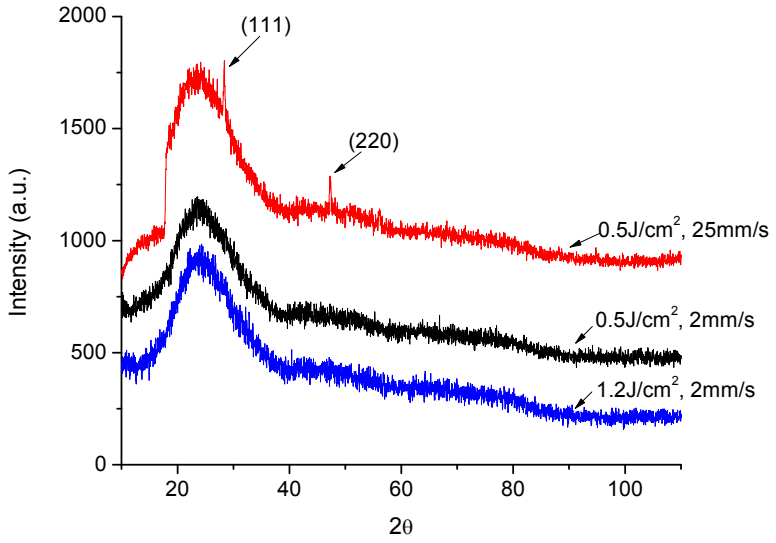

Figure 3.12 X-ray diffraction spectra of a-Si:H films laser treated at fluences of 0.5J/cm^2 and 1.2J/cm^2,and scan speeds of 2mm/s and 25 mm/s in water. An "amorphous peak" around 2θ=25°is observed for all samples. Sample processed at 0.5J/cm^2 and 25mm/s shows existence of two peaks for (111) and (220) orientation of silicon, showing the effect of different laser parameters on crystallinity

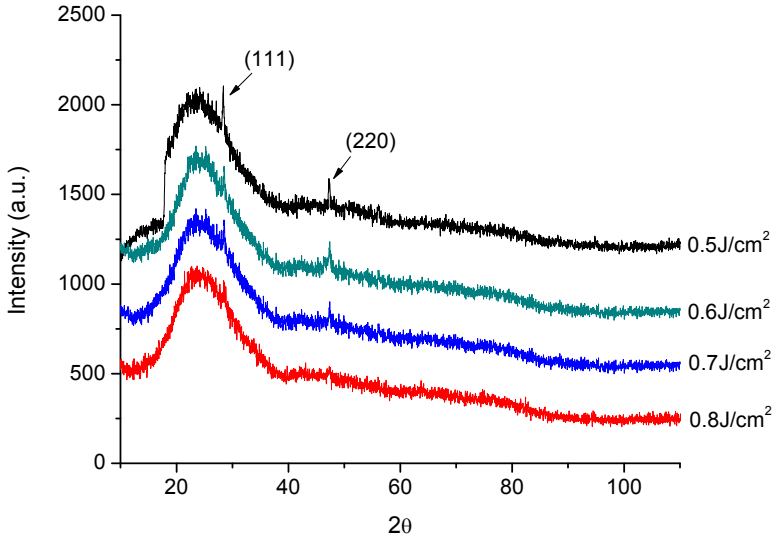

Figure 3.13 X-ray diffraction spectrum of laser treated a-Si:H film at different fluences from 0.5J/cm^2 to 0.8J/cm^2 with the same scan speed of 25 mm/s in water. An "amorphous peak" around 2θ=25° is observed for all samples. Existence of two overall different peaks for (111) and (220) orientation of silicon is found except for the condition at 0.8J/cm^2, showing that the crystallinity decreases with increasing of fluence

3.4.5 Effect of Crystallinity on Absorption

Figure 3.14 (a) shows an SEM image of an a-Si:H film surface laser treated at a fluence of 0.5J/cm^2 with a scan speed of 25mm/s in water. The small nano-size spikes with blunt tips are randomly orientated and irregularly distributed on the surface after laser treatment. The surface roughness and spike distribution is further observed in the AFM image in Fig.3.14 (b), which shows an average spike height of 138±2.58 nm and an average spike spacing of 216±6.77 nm where the variation represents standard error. Visually, the surface texture is similar to that of samples treated at a higher fluence of 1.2J/cm^2 at a scan speed of 2mm/s (Fig. 3.3), moreover, the spike spacing measured through AFM of the two samples are also close, and spike heights are 138nm and 391nm, respectively. Therefore, the absorptance of these two samples should be similar if both are not crystallized, since the spike height does not affect the result as discussed

above. In fact, the sample processed at 25mm/s is partially crystalline while the sample processed at 2mm/s is not. The comparison of these two samples can show the effect of crystallization on absorption.

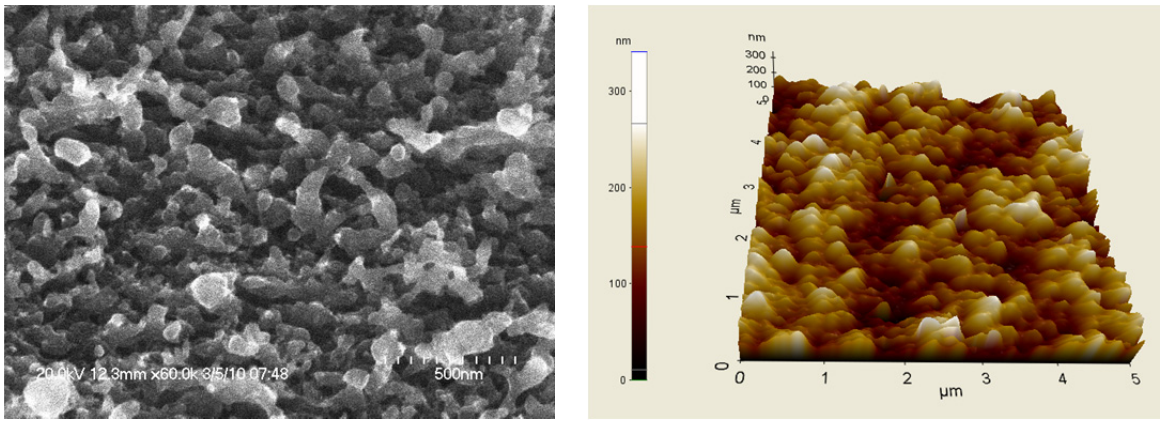

(a) (b)

Figure 3.14 (a) SEM image and (b) AFM image of surface of a-Si:H film laser irradiated in water (0.5J/cm^2, 25mm/s), showing texturing with randomly oriented spikes on the surface

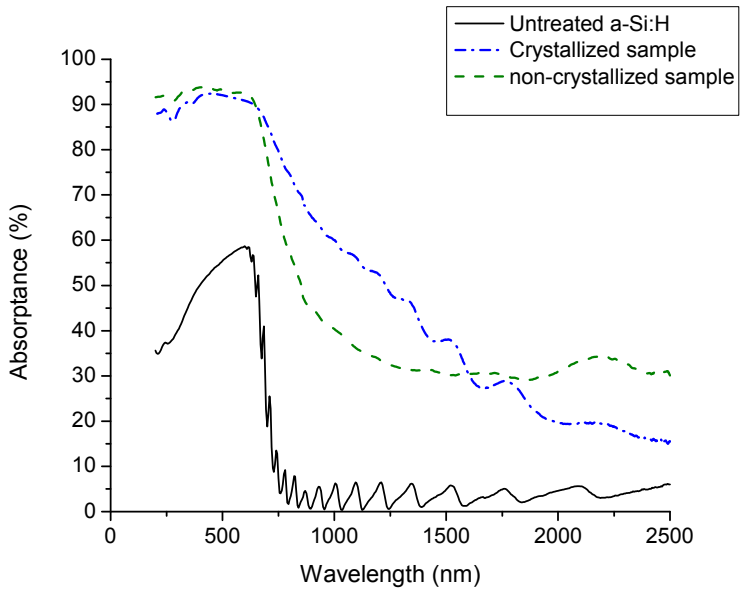

Figure 3.15 Comparison of absorptance spectra measured by spectrophotometry of as-received and laser irradiated a-Si:H films with and without crystallinity at different fluences and scan speeds (0.5J/cm^2 at 25mm/s, 1.2J/cm^2 at 2mm/s) in water, showing the effect of crystallinity on absorption

Figure 3.15 shows the absorptance versus wavelength for both the crystallized and non-crystallized samples, and the untreated sample is also included for comparison. As seen, due to the similar surface texture, in the above-band-gap region, the absorptance spectra of both laser treated samples are almost the same, no matter how deep the spikes are. The change in crystallinity is not significant here since the majority of the material is still a-Si:H after processing. The highest absorptance from the band gap to around 1600nm is for the crystallized sample processed at 0.5J/cm^2, followed by the non-crystallized sample treated at 1.2J/cm^2; the reason could be that the crystallized portion of the sample has a band gap of 1.1 eV, which helps to absorb light with wavelengths up to 1100nm. Moreover, the crystallized sample has a thicker a-Si:H layer due to the formation of shorter spikes and the resulting higher defect and impurity concentrations could also cause higher absorption. The reason that the crystallized sample has lower absorption for wavelengths above 1600nm is not well understood. However, based on the solar radiation spectrum, the radiation intensity in this range is a very small portion of the total intensity (Goetzberger et al., 1998), which suggests that lower absorption at these higher wavelengths will only have a small effect on the total energy absorption. Therefore, over the entire range of the spectrum, it can be concluded that with similar surface structure, a crystallized sample has better absorption performance due to the combination of both surface texturing and crystallization.

3.4.6 Effect of Processing Medium on Absorption

In order to compare the effect on different factors, such as surface geometry and crystallinity, absorptance spectra for samples treated in air (0.4J/cm^2 and 1mm/s) and in water (0.5J/cm^2 and 25mm/s) are shown in Fig. 3.16. It shows that the sample treated in air has better absorptance

performance over the entire spectrum. In the above-band-gap region, the conical spikes and attached nano-particles formed on the sample treated in air can induce greater light reflection and scattering between the spikes, which play a more important role in absorptance than spike density, which is higher for the water treated sample. The conical spikes, greater crystallinity, as well as the defects and impurities formed during the laser processing in air introduce greater numbers of reflections, a wider absorption spectrum, and sub-band gaps for the sample treated in air. These effects all work to increase the absorptance in the below-band-gap region to above that achieved by the sample treated in water. Therefore, with a sufficient thickness of a-Si:H left after laser processing for absorption, a treated sample surface having regular spike shapes with sharper angles, attached nano-particles, more crystallinity, greater defect and impurity concentrations, and larger spike densities will have better absorptance. Compared to the absorptance spectra of the crystalline silicon wafers laser treated in different background gas environments as show by Younkin et al., 2003, it can be seen that both textured crystalline bulk silicon and a-Si:H thin films in air have similar absorptance performance in the above-band-gap region. In the below-band-gap range, the absorptance of crystalline silicon drops quickly to almost zero, but for the a-Si:H film, the absorptance only drops to around 45% and remains more or less constant with increasing wavelength. Therefore, comparing the thicknesses of a few hundred microns for crystalline silicon and 1.6μm for a-Si:H, it can be concluded that a-Si:H thin films have greater absorptance while being more economical than c-Si and may be ideal for solar cell fabrication.

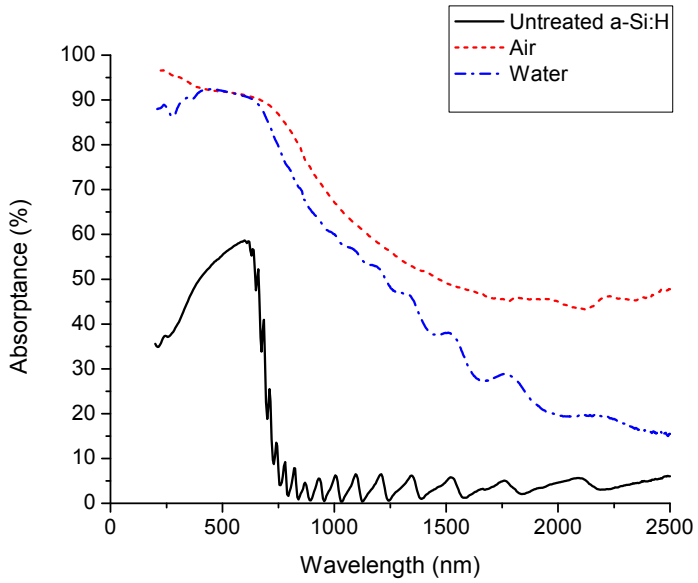

Figure 3.16 Comparison of absorptance spectra measured by spectrophotometry of as-received and laser irradiated a-Si:H film in air (0.4J/cm^2, 1mm/s) and water(0.5J/cm^2, 25mm/s), showing the effect of different factors, such as surface geometry, crystallinity and processing medium on absorption

3.5 Conclusion

In conclusion, it has been demonstrated that simultaneously improving the absorptance of sunlight and the stability against the SWE of a-Si:H thin films is possible through femtosecond laser irradiation in both air and water. Absorptance enhancement is caused by light trapping based on the surface geometry changes, as well as increased defect and impurity concentrations caused by laser processing. The change in crystallinity after processing reduces the thickness of the a-Si:H layer but may allow for greater stability in a-Si:H-based solar cells and broadens the absorptance range to 1100nm. Furthermore, the correlation between the crystallinity, scan speed and fluence when treated in water have been investigated; the crystallinity decreases with increasing laser fluence and decreasing scan speed, which may be due to the increased cooling rate caused by the higher surface temperature and temperature gradient. Finally, the absorptance

spectra indicate that the samples treated in air with regular conical spikes, crystallization and high defect and impurity concentration have the best absorption performance over the solar radiation spectrum. Compared with the absorptance of laser textured crystalline bulk silicon, it can be concluded that femtosecond laser processing of a-Si:H thin films may allow for more efficient and economical solar cell applications.

Chapter 4: Effect of Hydrogen on Surface Texturing and Crystallization of a-Si:H Thin Film Irradiated by Excimer Laser

4.1 Introduction

Many industrial solar cells in use today use bulk materials as absorbers with crystalline silicon being the most prevalent. However, crystalline silicon suffers from the disadvantage of high material cost since relatively large thicknesses are required primarily due to its low absorption coefficient. Recently, thin film absorbers are becoming more attractive based on their potential for low-cost modules, possibility to create tandem junctions and large-scale manufacturability (Luque and Hegedus, 2003; Chopra et al., 2004; Kazmerski, 2006). a-Si:H is the most popular material for use in thin film form due to its low energy economy (cost/watt). The main issue with a-Si:H is the high order of dangling bonds which act as recombination centers that severely reduce the carrier lifetime which results in the solar cell efficiency being below 10%. Additionally, this initial efficiency will decrease by 50% or more when exposed to sunlight over a period of months which is known as the Staebler-Wronski effect or SWE (Miles, 2005; Staebler and Wronski, 1980).

Due to their low efficiency and instability, thin-film a-Si:H solar cells require a highly efficient light-trapping design to absorb a significant fraction of the incident sunlight and techniques to increase stability against the SWE. Antireflection (AR) coatings and front-side texturing through the use of alkaline-based solutions, such as KOH and NaOH etching have been used on crystalline silicon solar cells, and pulsed laser irradiation has been used to enhance light trapping on both amorphous and crystalline materials (Martirosyan et al., 2007; Hylton et al., 2004;

Crouch et al., 2004; Nayak and Gupta, 2007). However, AR coating requires additional material and anisotropic wet chemical etching is not applicable for amorphous materials or thin films. In addition, in order to reduce the SWE, hybrid a-Si/nc-Si (nanocrystalline silicon) tandem modules have been developed and are able to achieve both higher efficiency and stability compared with single junction a-Si:H[10] due to the use of a thinner a-Si layer and the wider spectral absorption of nc-Si. To eliminate the need for two separate deposition steps which are required to form these tandem cells, laser-induced crystallization of a-Si:H has been proposed to produce a mixture of nc-Si:H and a-Si:H and simultaneously form a light trapping texture on the surface of the material (Nayak and Gupta, 2007). Therefore, laser-based treatment of a-Si:H may solve its efficiency and stability issues in a one-step process, which is a promising methodology for thin-film solar cell fabrication.

Extensive work on surface texturing of crystalline bulk silicon had been reported by using both femtosecond and nanosecond laser (Tull et al., 2006; Lowndes, 2000). Wang et al., 2012a, 2012b and Nayak et al., 2007, also achieved both surface texturing and crystallization on a-Si:H thin films by using femtosecond laser. Compared to the femtosecond laser, nanosecond laser can induce more crystallinity due to the longer pulse duration and more thermal effect, which can potentially improve the stability. Therefore, the feasibility of nanosecond laser-induced surface texturing and crystallization of a-Si:H becomes of interest. Many research group focused on excimer laser induced crystallization on non- or low-hydrogen a-Si thin films (Im et al., 1993; Miyasaka and Stoemenos, 1999), and Mathe et al., 1992, reported the effect of hydrogen on surface roughness and crystallization of a-Si:H thin films by single-pulse irradiation of excimer laser. However, there is no work showing a sharp spiked surface on the a-Si:H thin film after

multiple excimer laser pulses irradiation, and how hydrogen plays a role in the laser-induced surface texturing and crystallization is still not clear.

In this study, the formation of a densely packed, spiked surface structure has been studied through scanning electron microscopy (SEM) and atomic force microscopy (AFM) for excimer laser irradiation of a-Si:H thin films, and light absorptance dependence of surface structure is studied by spectrophotometry. The time-resolved analysis of melting and solidification of a-Si:H sample was analyzed by *in-situ* front-side transient reflectance measurement. The effect of laser processing on crystallinity and microstructure are investigated by x-ray diffractometry (XRD) and transmission electron microscopy (TEM), and the hydrogen concentration is measured by Fourier transform infrared spectroscopy (FTIR). The experimental results show that the hydrogen is necessary for fabricating sharp spikes on a-Si:H thin films, and the combined effects of light trapping by surface structuring and crystallization illustrate a one-step process for potentially enhancing the efficiency and stability of a-Si:H thin film solar cells.

4.2. Background

4.2.1 Hydrogen Effect on Nanosecond Laser-Induced Surface Texturing on a-Si:H

Mathe et al., 1992, showed that the surface roughness caused by single-pulse irradiation on a-Si:H could be almost two orders of magnitude larger than that of non-hydrogenated a-Si, and mentioned that the movement of H_2 gas bubbles generated by the combination of H atoms and molecules in the ambient medium are responsible for the surface roughness. Since there is no literature showing sharp spikes formed on a-Si:H surface by multiple nanosecond pulses, the mechanism of the spike formation on a-Si:H is likely the combination of surface texturing on

non-hydrogenated Si and hydrogen movement which improves the texturing behavior. Therefore, it is necessary to understand the formation mechanism of surface texturing on non-hydrogenated Si before studying that on a-Si:H.

Nanosecond laser can produce micro-conical/column spikes on bulk crystalline silicon (c-Si) surface at the fluence of 1-5J/cm^2 after a few hundred to thousands of pulses. The mechanism can be divided into two steps: spike initialization and growth. Dehghanpour et al., 2009, indicated that the sharp spikes are initially caused by the generation of capillary waves due to the micro-fluid mechanics of the molten layer, and then the periodic bead-like structure is formed as the seed of the final spikes. The development of the spikes is explained based on the formation of preferential removal of the material through Vapor-liquid-solid (VLS) mechanism (Lowndes, 2000). The silicon-rich vapor generated between the spikes preferentially redeposits on the molten tip of the microcolumns due to high accommodation coefficient of liquid, while the vapor prefers to dissolve into the liquid rather than solid, so that those spikes grow uniformly with the increasing of laser pulses. At the sides of the columns, because the increased reflectivity with increasing incident angle, they are not melted or ablated.

4.2.2 Hydrogen Effect on Crystallization of a-Si:H

Partial crystallization of a-Si:H is helpful to improve the stability, and larger grains with less grain boundaries are more desirable microstructures since defects and impurities are always located at grain boundaries. Hydrogen may have some drawbacks on the crystallization effect. First, hydrogen could trigger explosive crystallization (Im et al., 1993). When the incident laser energy density is only sufficient to induce partial melting of a-Si layer, explosive crystallization

can be observed and converts a-Si into fine-grained polycrystalline Si via a melt-meditated mechanism (Polman et al., 1991). The buried liquid layer is at a temperature higher than the melting point of a-Si but lower than the melting point of c-Si, and propagates into the a-Si layer by simultaneously melting of a-Si and solidifying into c-Si. Due to latent heat difference between c-Si and a-Si, the propagation is self-sustaining. Two different nucleation scenarios, a moving liquid/solid Si interface can be unstable with respect to nucleation of c-Si (Tsao and Peercy, 1987) and small crystallites can nucleate in a-Si during heating phase prior to melting (Roorda and Sinke, 1989), had been made to explain why explosive crystallization occurs. Second, an observation by Mathe et al., 1992, showed that hydrogen slows down the crystallization process because more energy density is needed to crystallize a given depth when hydrogen is present. Large-grained polycrystallites are generated at the hydrogen depletion region near the surface, and fine-grained ones are located at hydrogen contained area underneath. Therefore, hydrogen could cause fine-grained polycrystallites by explosive crystallization and spend part of the laser energy that slows down the crystallization process. However, these effects may be alleviated by multiple-pulse radiation which will be discussed later.

4.3 Experimental Setup

Amorphous silicon films were deposited on 0.525mm-thick Corning 1747 glass substrates using plasma enhanced chemical vapor deposition (PECVD). The a-Si:H film was deposited at a rate of 60 Å/s in an hydrogen diluted silane environment at 380°C with a hydrogen atomic concentration of around 20 at %. Film thickness was found to be roughly 1.6 μm through ellisometry measurements (Wang et al., 2012a). The a-Si:H films were cleaned with acetone in

an ultrasonic cleaner for 5 minutes and then rinsed with methanol and distilled water prior to processing.

Surface texturing and crystallization was carried out using an unpolarized KrF excimer laser with a wavelength of 248 nm and pulse duration of 30 ns. After passing through an attenuator, the laser beam is homogenized by a multi-lens homogenizer system and then further shaped as it passes through a photomask. This shape is then demagnified (5X) and focused onto the sample through a projection lens. This results in a homogeneous 1mm×1mm square irradiated spot at the sample surface. The samples were mounted on a three-axis translation stage and irradiated by one to a hundred laser pulses with various fluence (0.15J/cm^2 to 0.5J/cm^2) at a stationary spot, and moved to an adjacent point for the next irradiation until an area of 10mm by 10mm is treated. For the step-by-step process, the condition starts at 0.05 J/cm^2 and ends at the desired final laser fluences (0.3J/cm^2 and 0.4J/cm^2) using step widths from 0.01J/cm^2 to 0.08J/cm^2 and 50 or 100 pulses at each step.

The untreated and treated samples were observed through SEM. Surface roughness and the distribution of spikes in the treated samples were also examined using an AFM. Crystallinity and material microstructure after laser irradiation are analyzed by XRD and TEM, and the hydrogen concentration is investigated by FTIR. The time-resolved analysis of melting and solidification of a-Si:H sample was analyzed by *in-situ* front-side transient reflectance measurement. The optical transmittance and reflectance of as received and laser treated a-Si:H films were measured by a spectrophotometer over a wavelength range of 250nm-2500nm which corresponds to the main spectral range of solar irradiation (Goetzberger et al., 1998). The reflectance (*R* in %) and

transmittance (*T* in %) are then used to calculate the absorptance (*A* in %) of the film: *A=100-R-T*.

4.4 Results and Discussion

4.4.1 Effect of Hydrogen on Surface Morphology

4.4.1.1 Surface Topography on Laser Irradiated a-Si:H

Lowndes et al., 2000, showed that in the polarized pulsed-laser irradiation on c-Si, two different phenomena may be seen: at lower fluence (<1J/cm^2), laser-induced periodic surface structures (LIPSS) occurs on the silicon surface; at higher fluence (1 to 5J/cm^2), columnar or conical spikes of a few tens of micrometers in height are generated. However, in texturing a-Si:H thin films, a much lower and narrower processing window is tested in order to not damage or crystallize the entire film. In this study, the amorphous samples are irradiated at stationary locations with lower fluences (0.15 J/cm^2 to 0.5 J/cm^2) and numbers of pulses (1 to 100). A typical result achieved using a fluence of 0.4 J/cm^2 is shown in Fig. 4.1.

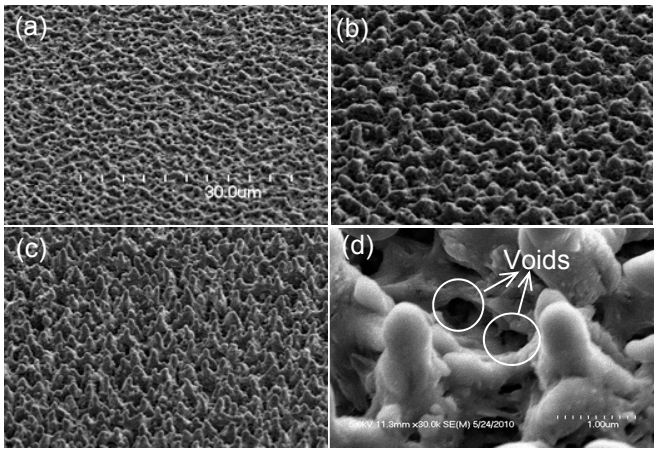

Figure 4.1 SEM images of a-Si:H film surface after being irradiated by the following number of pulses at 0.4J/cm^2 (a) 1, (b) 5, (c) 50 pulses at the magnification of 1.5K, and (d) 50 pulses at the magnification of 30K

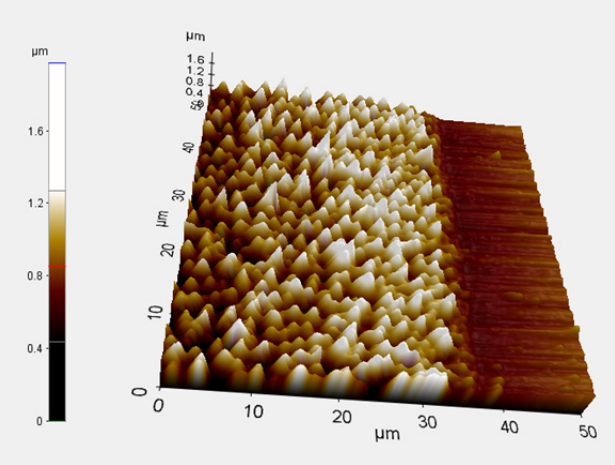

Figure 4.2 AFM image of surface morphology at the laser irradiation boundary of a-Si:H film at a fluence of 0.4J/cm2 with 50 pulses, showing the spikes are protruded from the original surface

The average spike height and spacing after 1 pulse measured by AFM (Wang et al., 2012a) are 460.8±10.6 nm and 1.637±0.037 µm, respectively, where the variation represents standard deviation. As discussed in 4.2.1, beyond the capillary waves formed by solidifying of the molten layer, hydrogen should play an important role in formation of the spikes. It is showed that the hydrogen atoms combine to form H_2 gas, and then diffuse into the ambient medium and leave the blister regions after laser processing (Mathe et al., 1992). However, a more complex process could occur, i.e., the combined hydrogen molecules may explode when the laser energy is high enough; subsequently, the released pressure drives the upper liquid silicon layer to move upward while the surrounding liquid silicon flows to the explosion position. The liquid silicon solidifies before it achieves equilibrium, which forms much higher spikes compared to the dehydrogenated a-Si samples. It is noted that no LIPSS structure is observed after 1 pules based on SEM image of surface morphology shown in Fig. 4.1 (a). The reason is that the laser beam is unpolarized, and no interference occurs because of the random phase change between the incident beam and scattered light. After 5 pulses shown in Fig. 4.1 (b), the spikes are distributed more uniformly and sparsely. This is because the remelting layer cannot be stable after the first pulse, and

hydrogen effect may not be dominant due to the hydrogen depletion at the surface, therefore, the liquid silicon stabilizes at different surface geometry due to the surface tension effect and the spike spacing becomes around 2µm. After that, the sharp conical spikes are developed on the formation of preferential removal of the material through VLS mechanism as shown in Fig. 4.1 (c) of surface morphology after 50 pulses, and the average spike height and spacing are 1.837 ± 0.0317µm and 2.121 ± 0.035µm, respectively. Figure 4.1 (d) shows the high magnification SEM image of the spikes formed after 50 pulses, it can be seen that voids are generated underneath the solidified silicon, which indicates the existence of hydrogen explosion. The spikes are partially protruded 1.426 ± 0.059µm from the original surface which is proved by the AFM measurement at the boundary of the irradiation area in Fig. 4.2. It is suggested that growth is a dominant spike formation mechanism under nanosecond laser while ablation dominant for femtosecond pulses (Tull et al., 2006).

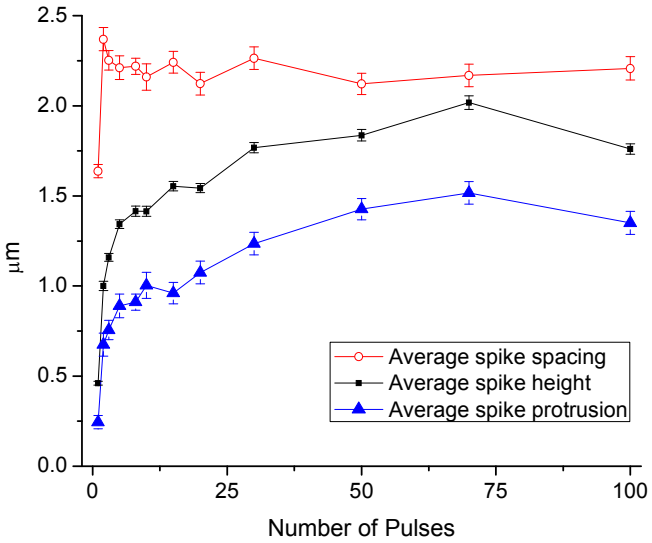

Figure 4.3 Dependence of average spike height, protrusion and spacing on number of pulses for a fixed fluence of 0.4J/cm^2, determined from an area of 50×50µm^2 at the processing center, error bars indicate standard deviation

In order to study the quantitative characteristics of the feature, AFM measurements are performed. The average spike height, protrusion and spacing are measured within an area of 50×50 μm^2. Figure 4.3 shows the average spike height, protrusion and spacing correlated with the number of pulses at a fluence of 0.4J/cm^2, and the error bars represent standard deviation. It can be divided into 3 regions: first, for the first 10 pulses or so, the spike height and protrusion are increased rapidly due to both effects of hydrogen explosion and VLS caused by multiple reflection in between the spikes; second, from 10 pulses to about 70 pulses, the hydrogen are mostly depleted so that the VLS mechanism is dominant, therefore, the average spike height increase rate slows down; third, after 70 pulses, the average spike height increases to around 2μm, and the silicon-rich ablated material in between the spikes is difficult to reach to the tips so that VLS cannot happen. As a result, the average spike height and protrusion start decreasing. The average spacing remains a constant of around 2.2 μm after the first pulse. This is because the molten layer solidifies before reaching equilibrium at the first pulse and forms a higher tightened surface structure due to the presence of hydrogen, so that the remelting layer by the second pulse cannot be stable. The liquid silicon will be re-distributed due to the surface tension effect and is stabilized until the spike bases are connected together before solidification. After that, the spikes spacing already initially formed cannot be affected by subsequent pulses. The average spike height, protrusion and spacing dependent on different fluences at 100 pulses are investigated in Fig. 4.4. It shows that the average spike spacing remains the same under different fluences and the average spike height and protrusion increase with the increasing of the fluence until it reaches around 2μm. As discussed above, when the spikes are high enough, VLS mechanism is not dominant so that the spike height starts decreasing, that is why the average spike height becomes lower at 0.5J/cm^2 than that of 0.45J/cm^2. However, the spike protrusion still remains the

highest at 0.5J/cm^2, which indicates that the depth between the undamaged material and original surface is lower. The reason is that more material can be ablated under a higher fluence, however, when the spike height is high enough, the ablated material cannot reach the tips of the spikes. Therefore, the material could only be redeposited back to the valley between the spikes which cause a shallower depth. The average spike spacing is around 1.6 μm at 0.15J/cm^2 and remains between 2 to 2.2 μm at higher fluences, which may be due to the surface stabilization during the initial spike base formation. The exception at 0.15J/cm^2 is because no spike formed at this point and the surface structure is formed more tightened similar to the first pulse effect.

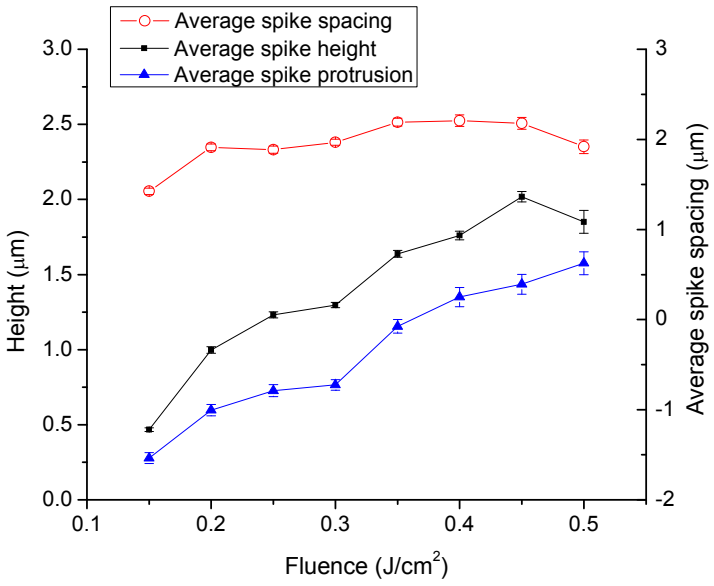

Figure 4.4 Dependence of average spike height, protrusion and spacing on laser fluence for a fixed number of pulses (100 pulses), determined from an area of 50×50μm^2 at the processing center, error bars indicate standard deviation

4.4.1.2 Surface Topography on Dehydrogenated a-Si

In order to study the effect of hydrogen on surface morphology, a numerical simulation and experiments of spike formation on laser irradiated dehydrogenated a-Si are investigated to compare with that of a-Si:H samples.

For the first pulse, the heat transfer phenomenon can be obtained by (Carslaw and Jaeger, 1958),

$$\rho(T)C_P(T)\frac{\partial T(\vec{r},t)}{\partial t}-\nabla[\kappa(T)\nabla(T(\vec{r},t))]=0 \tag{4.1}$$

where, ρ, C_P, κ, T, r and t are density, specific heat, thermal conductivity, temperature, radius and time, respectively. The properties of a-Si used in the simulation are listed in Table 4.1.

Table 4.1 List of a-Si properties used in the simulation calculation

a-Si property	Units	Value	Literature source
ρ	g/cm^3	2.2	Unamuno and Fogarassy, 1989
C_p	J/gK	0.952	Unamuno and Fogarassy, 1989
K	$W/m^{-1}K^{-1}$	0.007	Unamuno and Fogarassy, 1989
R		0.54	Ong et al., 1986a
η	$mPas^{-1}$	0.7-0.8	Kolasinski. 2007
T_m	K	1423	Unamuno and Fogarassy, 1989
T_v	K	3538	Unamuno and Fogarassy, 1989
$\partial\sigma/\partial T$	N/mK	7.4×10^{-5}	Kolasinski. 2007
α	cm^{-1}	1.5×10^{6}	Bäuerle, 2000; Ong et al., 1986b
L_f	Cal/g	315	Bäuerle, 2000
σ	mN/m	850	Kolasinski, 2007

The geometry of the irradiated sample can be considered as semi-infinite, because the thermal penetration depth (Eq. 4.2) is lower than the thickness of the sample (Bejan, 1993),

$$L_T=2\sqrt{\delta\tau_l} \tag{4.2}$$

where, δ the thermal diffusivity and τ_l the laser pulse duration.

Assuming the sample material is isotropic and uniform, the laser radiation is approximately uniform and the transversal dimension of the irradiated area is larger than the thermal penetration depth, the problem can be considered as a unidimensional model and the temperature field will depend exclusively on the depth (z-axis) (Prokhorov et al., 1990). The variation of the thermo-physical parameters (ρ, C_P, κ) of the a-Si film with the temperature is not big enough to be considered, and average values of these parameters are taken into account. The convection and radiation losses at temperatures between 1000K and 2000K hardly exceed 1-3 W/cm^2 (Bäuerle, 2000), so that they are negligible during the simulation.

With these hypotheses, Eq. (4.1) with the initial and boundary conditions can be written as follows:

$$\rho C_P \frac{\partial T(z,t)}{\partial t} - \kappa \nabla^2 [T(z,t)] = 0 \tag{4.3}$$

$$T(z, t=0) = T_{ambient} \tag{4.4}$$

$$\kappa \left[\frac{\partial T(z,t)}{\partial z} \right]_{z=0} = Q_{laser} - Q_{ambient} - Q_{radiation} \tag{4.5}$$

$$\kappa \left[\frac{\partial T(z,t)}{\partial z} \right]_{z=\infty} = 0 \tag{4.6}$$

where, $Q_{laser} = I(x,y,t)(1-R)q(t)$, and $I(x,y,t)$ is the laser intensity, R is the reflectance and $q(t)$ is the temporal dependence of the laser pulse.

The thermal gradient in the molten pool drives the motion of the liquid silicon provoking the deformation of the surface, and the pressure differences created at a curved interface support the evolution of the deformations on the liquid surface, which is known as capillary waves with the

dispersion relationship between the wave-vector k and the angular frequency ω given by (Kolasinski, 2007),

$$\omega^2 = \frac{\alpha k^3}{\rho}\tanh(kh) \tag{4.7}$$

where, α is the surface tension of the liquid and h is the depth of the molten pool.

In order to obtain the amplitude of the thermo-capillary waves, the Navier-Stokes equation has been solved for a stationary and incompressible fluid stated by the Eq. (4.8) with the boundary conditions of Eq. (4.9) and (4.10),

$$\nabla\vec{v} = 0\,, \qquad \nabla^2\vec{v} = 0 \tag{4.8}$$

$$\vec{v} = 0 \text{ at } z = -h \tag{4.9}$$

$$\eta\left(\frac{\partial v_r}{\partial z} + \frac{\partial v_z}{\partial r}\right) = \frac{\partial \alpha}{\partial r} = \frac{\partial \alpha}{\partial T}\frac{\partial T}{\partial r} \text{ at } z = 0 \tag{4.10}$$

where $\vec{v}$ is fluid velocity, η is the dynamic viscosity, and the subscripts r and z label the radial and normal components of the velocity, respectively.

Eq. (4.8) is integrated in z-direction (Schwarz-Selinger et al., 2001) that provides the change in the morphology of the fluid Δz due to the motion of the wave.

$$\Delta z = -\frac{1}{2\eta r}\frac{\partial \alpha}{\partial T}\frac{\partial}{\partial r}\left[r < h^2 > \frac{\partial I}{\partial r}\right] \tag{4.11}$$

with $I = \int_{T_S > T_m}(T_s - T_m)dt$ and $< h^2 > I = \int_{T_S > T_m} h^2(T_s - T_m)dt$, T_s the surface temperature and T_m the melting temperature of a-Si.

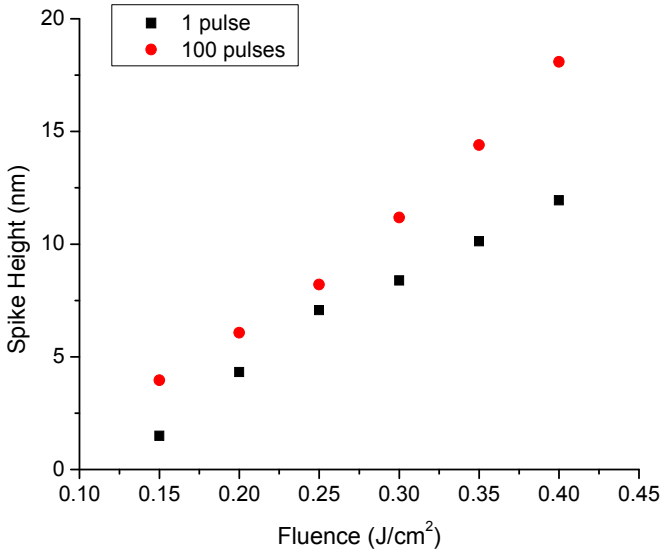

Figure 4.5 Simulation results of dependence of the spike height on laser fluence for a fixed number of pulses (1 and 100 pulses)

For multiple pulses, the following hypotheses are established: first, the influence of the phase transformation after the pulses on the thermal and optical properties is negligible; second, the reflectance is only affected by the change of surface roughness. The simulated spike heights at different fluence and number of pulses are shown in Fig. 4.5. The spike height at 1 or 100 pulses almost linearly increase with increasing of fluence. According to Mathe et al., 1992, the spike heights at 1 pulse are close to the experimental results. The average spike height of laser irradiated dehydrogenated a-Si thin films (prepared by thermal annealing at 80 hours) at 0.4J/cm^2 and 100 pulses is around 58nm. Although this is in the same order of magnitude as the simulation result, the numerical predictions underestimated the spike height. The reason could firstly be that the reflectance is not a constant spatially, i.e. the light absorption inside the valleys is more than that in the peaks. Therefore, more material is actually ablated and redeposited on the tips. Secondly, the material in the simulation is uniform, but in reality, a-Si has defects and

impurities, such as residual hydrogen, these imperfect properties could intensify the light absorption and increase the spike height.

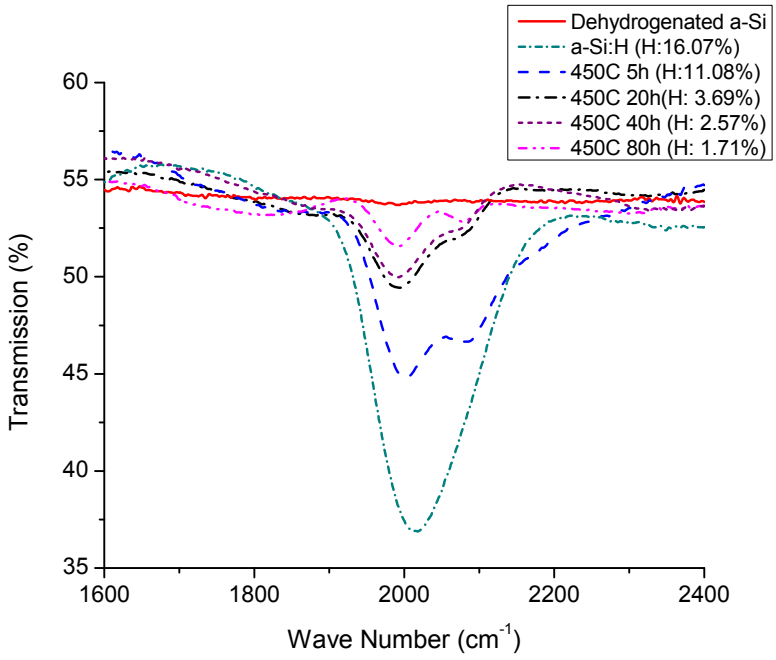

Figure 4.6 Transmission infrared spectra for thermal annealed a-Si:H samples at different annealing time, showing hydrogen concentration decreases with increasing of annealing time

In order to show the effect of hydrogen on surface morphology experimentally, the a-Si:H samples are annealed in a vacuum furnace at 450˚C (Heya et al., 2008) for different amounts of time to diffuse out hydrogen as much as possible. Figure 4.6 shows the FTIR spectra measured for different annealing time. The non-hydrogen a-Si sample (100nm thick a-Si on SiO_2 coated glass) is introduced as a reference spectrum. The hydrogen concentration can be estimated from peaks caused by the stretching mode of Si-H at 2000cm^{-1} and SiH_2 at 2100cm^{-1} using equation (Heya et al., 2008)

$$N = A\int \frac{\alpha}{\omega} d\omega = A\frac{S}{t\omega_0} \tag{4.12}$$

where N, A, α, ω, t, ω_0, and S are the hydrogen density, the conversion factor (9×10^{9} cm^{-2} at 2000 cm^{-1} and 2.2×10^{10} cm^{-2} at 2100 cm^{-1}), the absorbance, the frequency, the film thickness, the peak frequency, and the peak area, respectively.

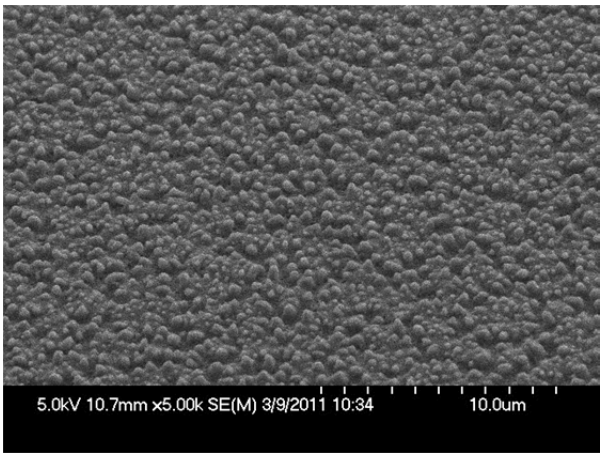

Figure 4.7 SEM image of 80-hour thermal annealed a-Si:H film surface after being irradiated at a fluence of 0.4J/cm^2 and 100 pulses, showing no sharp spikes on the surface

Based on Eq. (4.12), the initial H concentration of 16.07% is significantly reduced to 1.71% after thermal annealing of 80 hours, and the XRD measurement shows that the thermal annealed sample still remains amorphous (not shown). The SEM image of laser processed 80-hour-annealed sample at a fluence of 0.4J/cm^2 with 100 pulses is shown in Fig. 4.7, and the average spike height is 57.8 ± 2.15nm. It can be seen that no sharp spikes are formed without the presence of hydrogen. As discussed above, the molten layer can form capillary waves after solidification, however, the amplitude of the wave is too small to introduce the light multiple reflection towards the valleys. Therefore, when the next pulse comes, the irradiated area will be melted again similarly as the first pulse does and no spikes are formed after multiple pulses. This is different from the femtosecond laser experiments, where ablation is dominant, the sharp spikes can be fabricated due to the different ablation rate when the periodic surface structure is formed.

Moreover, dehydrogenate a-Si thin films cannot stand the higher fluences used for c-Si, since it is easy to damage the entire film. Therefore, from both the simulation and experiment results, the hydrogen is necessary for forming sharp spikes on a-Si:H thin films by a nanosecond laser.

4.4.2 Effect of Hydrogen on Crystallization and Absorptance

In order to study the crystallization of the treated films, x-ray diffraction patterns taken for the untreated and treated a-Si:H films are shown in Fig. 4.8. The spectra have been shifted vertically for clarity. All the spectra show an amorphous peak around $2\theta=25°$, which is caused by the internal constructive interference of the amorphous Si and glass network. Three peaks at around $2\theta=29°$, 47° and 56° emerge after processing which indicate a structural change after laser irradiation and can be indexed to the (111), (220) and (311) crystalline orientations of silicon. The normalized crystallinity is estimated by the calculated area differences of the measured spectra between the laser processed and untreated samples. The largest area at the condition of $0.4J/cm^2$ and 100 pulses is defined as a crystallinity of 100%, and the other conditions are calculated by dividing it. The normalized crystallinity at conditions of $0.4J/cm^2$ with 50 pulses, and $0.3J/cm^2$ with 100 pulses are 98.98% and 57.38%, respectively. It is understood that under partial melting regime, the higher the fluence, the higher the crystallinity. However, under the same fluence, when the number of pulses achieves a certain number, the crystallinity levels off. This is because the spikes can reach a certain height to avoid the ablated material redepositing to the tips, so that there will no more amorphous material can be melted underneath the crystallized layer.

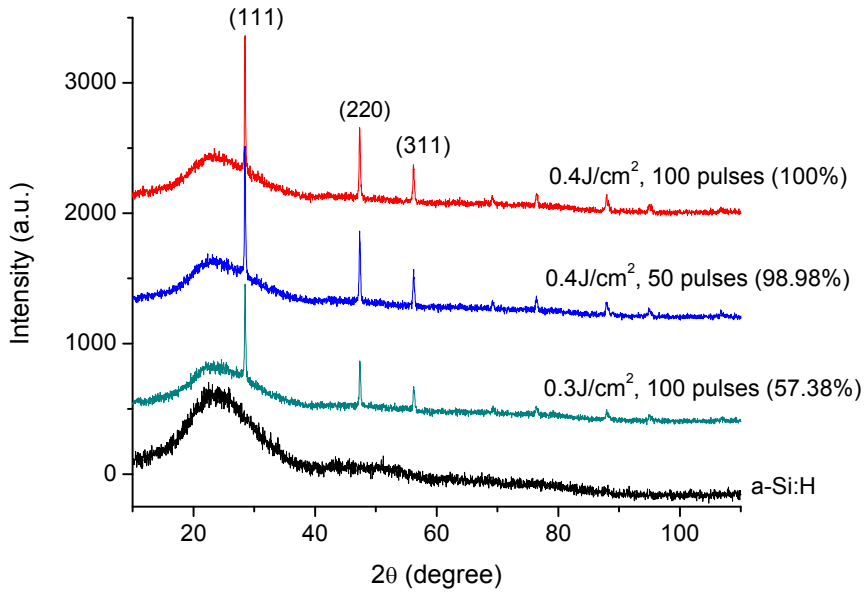

Figure 4.8 X-ray diffraction spectra of as-received a-Si:H film, laser treated films at 0.4J/cm^2 with 50 and 100 pulses, and 0.3J/cm^2 with 100 pulses. There is no signs for crystallinity for the untreated sample and are three different peaks for (111), (220) and (311) orientation of silicon for all laser treated samples. The spectra have been shifted for clarity

4.4.2.1 Hydrogen Effect on Crystallization

Single-pulse laser irradiation as well as *in situ* front-side transient reflectance (FTR) measurement are performed for analyzing the dynamics of melting and solidification of a-Si:H thin films. Figure 4.9 shows the FTR signals correlation with different fluences (0.1J/cm^2 to 0.5J/cm^2). It can be seen that no damage or phase change at 0.1J/cm^2. The signal intensity decrease at 0.15J/cm^2 indicates that the material starts being crystallized since the reflectivity of c-Si is lower than that of a-Si. When the fluence is higher than 0.15J/cm^2, the signal oscillation, due to the interference effect resulting from the fast-moving melting buried layer, shows that explosive crystallization occurs at the beginning (Im et al., 1993). The following plateau means that the solidified surface has been re-melted by the rest of the pulse, and it can be seen that

higher fluence always has a longer lifetime of the molten pool, which may cause larger grains after crystallization. Hu, 2010, showed that no explosive crystallization occurs for excimer laser irradiated dehydrogenated a-Si deposited by PECVD. Therefore, hydrogen must play a role for triggering explosive crystallization. However, the reason is not clear at this point. It is suggested that the H atom moving may absorb or release the energy and change the temperature in the local area. At some point, nucleation could occur due to the heating or change of the molten Si cooling rate locally, and these nuclei will be the seeds triggering the explosive crystallization.

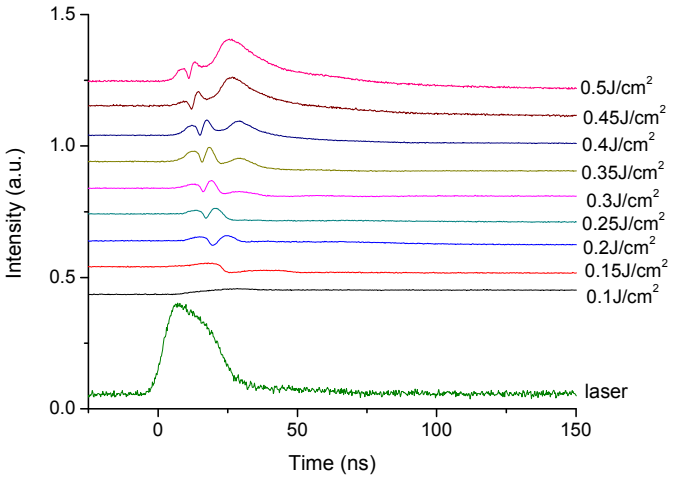

Figure 4.9 *in-situ* front-side transient reflectance signals of a-Si:H films irradiated at different fluences

Figure 4.10 shows the cross-sectional TEM images at the fluence of 0.4J/cm^2 with different number of pulses. It can be seen that after the first pulse, microstructure of the material can be divided into two regions – large- and fine-grained regions. The FTR signal shows that explosive crystallization occurs within 20ns which forms the fine-grained region, and after that, the top layer has been melted again because of the heat accumulation by the rest of the pulse. The hydrogen atoms inside the material start moving by absorbing the laser energy and aggregating at

the interface between the solid and liquid silicon. Those hydrogen atoms combine as molecules and form as bubbles, and those bubbles keep dilating and explode when the internal pressure inside the bubbles becomes higher than the outside. The bubble explosion at the liquid/solid silicon interface drives the liquid silicon to move up and the surrounding liquid flows towards it. Before the liquid silicon reaches equilibrium, the material has solidified and formed as spikes with a height of ~350nm and left large bubbles at the interface as shown in Fig. 4.10 (a). Because the molten layer at the surface can last for almost 20ns, the crystallized material can form much larger grains of ~140nm than that of explosive crystallization. Figure 4.10 (b) shows the cross sectional TEM image of a-Si:H sample irradiated at 50 pulses under low magnification. It can be seen that the spike height and spacing are around 1.5μm and 2 μm, respectively. Since TEM samples cannot be prepared to be exactly at the center of the spike, this is why the spike height measured by TEM is always lower than that measured by AFM, but the spike spacing measurements are similar. The connected open cavities underneath the spikes are caused by the hydrogen bubble explosions. Because the melting temperature of c-Si is around 225K higher than that of a-Si (Polman et al., 1991) and a broad disorder zone exists at the interface between the large- and fine-grained regions after first pulse, the excited hydrogen atoms during multiple-pulse processing will preferentially move to this interface. Therefore, more and more bubbles explode at the same location and form connected open cavities. In order to estimate the grain size after 50 pulses, one of the spikes is focused at during TEM measurement and the sample was tilted with a step of 0.1˚ in both x and y directions to avoid the effect of band contours. Since different grains will have different band contours at a certain direction, the moving region of the same contour shows the grain region. As shown in Fig. 4.10 (c), the large-grained region is only located on the spike and the largest grain size is around 400nm. Figure 4.10 (d) shows the high-

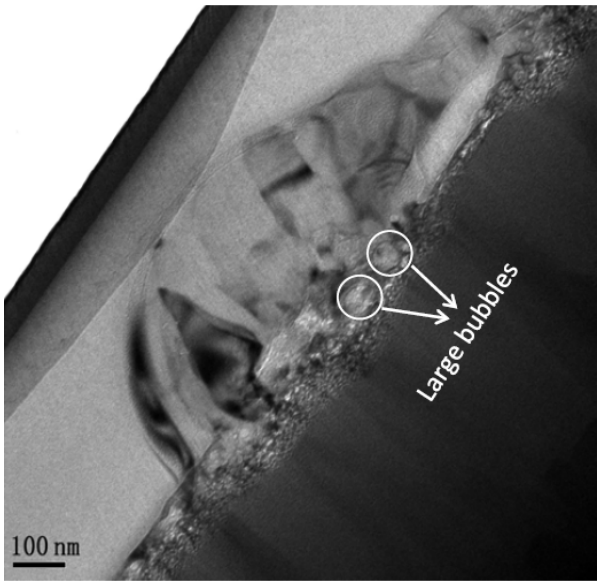

(a) 1 pulse

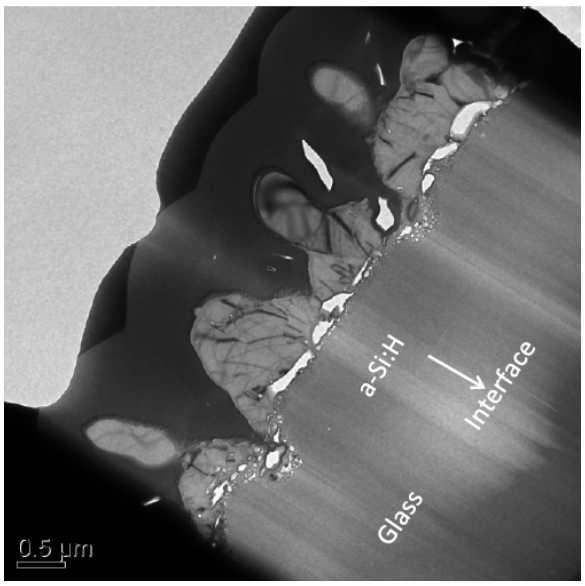

(b) 50 pulse

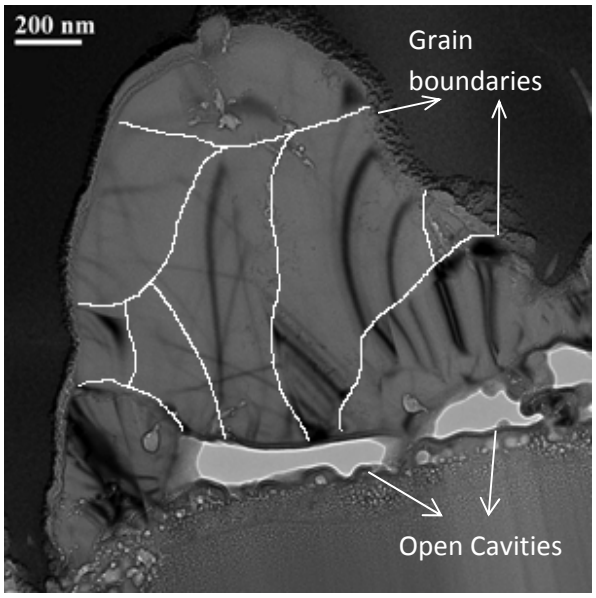

(c) 50 pulses

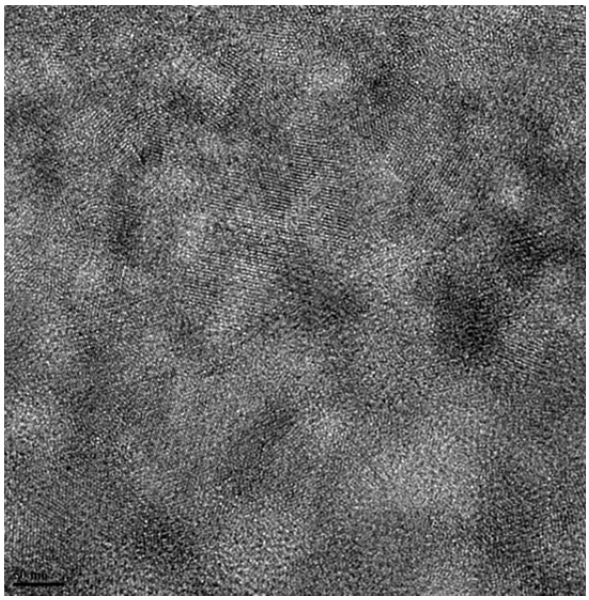

(d) HR-TEM at the bottom of the spike

Figure 4.10 Cross-sectional view TEM micrographs of a-Si:H samples irradiated at (a) 1 and 50 pulses at (b) low, (c) high magnification and (d) high-resolution TEM image with a fixed fluence of 0.4J/cm^2

resolution TEM image taken at the interface of large- and fine-grained regions, and the grain sizes is around 40nm. When moving to even deeper to the substrate, the grain size becomes smaller and smaller until reaching the amorphous region. This can also prove that the presence of explosive crystallization after the first pulse, since the buried liquid layer of explosive crystallization is only a-few-nanometers thick and very small grains are formed, and those tiny bubbles are formed by hydrogen effect during the explosive crystallization process.

4.4.2.2 Hydrogen Effect of Crystallization Dependent on Pulse Duration and Pulse Number

The effect of hydrogen during the laser processing depends on the pulse duration. As shown in Fig. 4.11, the a-Si:H sample is irradiated by a femtosecond laser with a pulse duration of 130fs and a condition of 0.4J/cm^2 at a scan speed of 1mm/s. Much less bubbles and void area are observed from the image, which may be caused by a different crystallization process induced by femtosecond laser. Wang et al., 2012b, shows that a non-thermal melting occurs within a picosecond and material start being ablated or thermally vaporized afterwards due to the energy transfer back from electrons to the material, at last, a very thin layer underneath can be thermally melted and crystallized after solidification. Therefore, the thermal effect which can cause hydrogen explosion inside the material is only a less dominant process, so that hydrogen effect is much less during femtosecond laser process. Another difference between the two different laser processes is that the large-grained layer is covered over a conical spike with fine grains on an amorphous matrix. This is because the ablation dominant formation mechanism by the femtosecond laser. When the spikes are formed after a certain number of pulses, the crystallized top layer on the spikes will protect the underneath material from being ablated, and the ablated material around the spikes will deposit preferentially to the tips to form a thicker and thicker

crystallized layer. Compared to Fig. 4.10 (c), much more defects are observed in the large-grained region in femtosecond laser irradiated a-Si:H films, which could act as a combination center of the photo-excited electron-hole pairs, therefore, the cell efficiency and stability could be better by excimer laser processed samples rather than femtosecond laser.

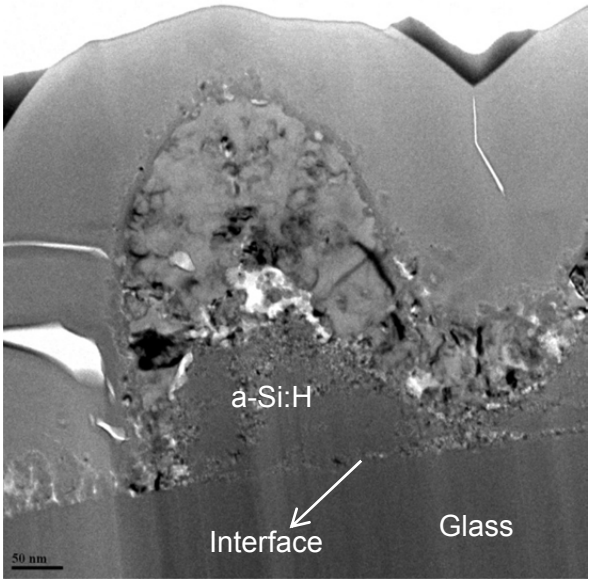

Figure 4.11 Cross-sectional view TEM micrograph of a-Si:H samples irradiated by 130-fs laser pulses at a fluence of 0.4J/cm^2 and a scan speed of 1mm/s

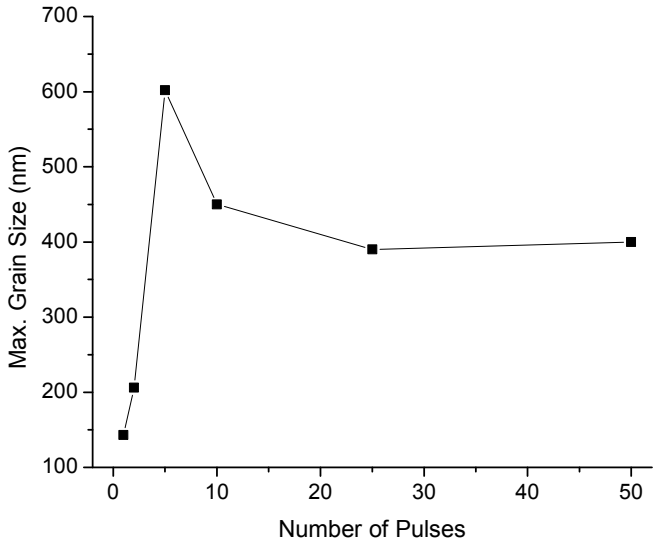

Figure 4.12 Dependence of maximum grain sizes of laser irradiated a-Si:H films on number of pulses at a fluence of 0.4J/cm^2

Figure 4.12 shows the maximum grain size at a fluence of 0.4J/cm^2 with different number of pulses. An observation of maximum grain is achieved at 5 pulses. For the first two pulses, due to the hydrogen effect, part of the pulse energy is absorbed by hydrogen and used for generating fine-grained crystallites caused by explosive crystallization. So that the grain size increases when the number of pulses increases while the hydrogen concentration decreases. After 5 pulses, the hydrogen is almost depleted, and the spikes are formed. It is noticed that the diameter of the spikes becomes smaller and smaller due to the light multi-reflection between the spikes, and the material around the spike has been ablated, deposits on the tips and crystallizes to a random orientation. Therefore, the grain size starts decreasing since the large grains are only located at the spikes. When the spikes are sharp enough after 25 pulses, no more material can be ablated from the side of the spikes, and the grain size remains unchanged.

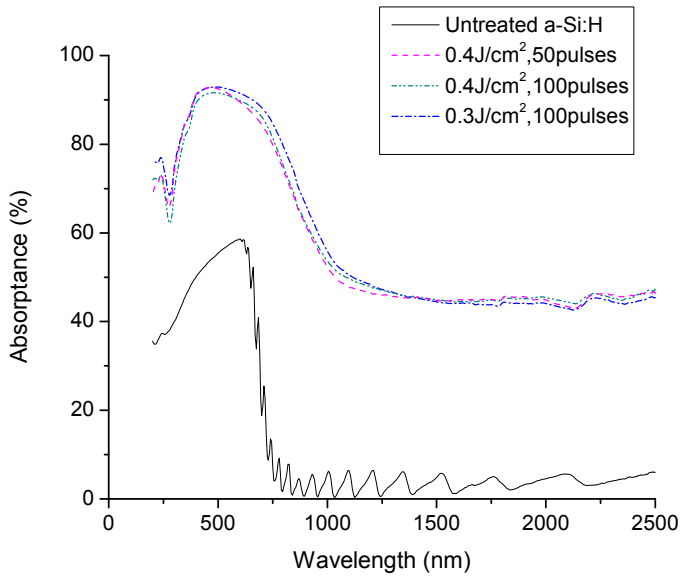

Figure 4.13 Comparison of absorptance spectra measured by spectrophotometry of as-received and laser irradiated a-Si:H films at fluences of 0.4J/cm^2 with 50 and 100 pulses, and 0.3J/cm^2 with 100 pulses

4.4.2.3 Hydrogen Effect on Absorptance

The absorptance spectra of untreated and laser treated samples are shown in Fig. 4.13. It can be seen that the absorptance increases over the entire spectrum. The absorptance spectra of the laser processed samples under different conditions are similar due to the similar light-trapping surface geometries, and the absorptance at the below-band-gap region could be caused by the impurities and defects generated during the laser processing. It is noted that the absorptance decreases rapidly at the wavelength of ~300nm, which may be caused by the interference at the open cavities. As shown in Fig. 4.10 (c), the depth of the open cavity is around 150nm, and based on the constructive interference equation $2nd = m\lambda$, where n, d, m and λ are refractive index, cavity depth, integer and wavelength. Here, n=1 and d=150nm, therefore, the corresponding wavelengths can introduce constructive interference for light reflection are 300nm, 150nm, 100nm, etc. This explains why the absorptance spectra get the lowest value at around the wavelength of 300nm.

4.4.3 Effect of Step-by-step Process on Residual Hydrogen Concentration, Crystallinity and Absorptance

Hydrogen is used for passivation of the defects in the Si network and grain boundaries in order to increase the efficiency of the solar cell. However, from Fig. 4.14, the FTIR spectra show that there is no hydrogen left after laser processing at the conditions of 0.3J/cm^2 and 0.4J/cm^2 with 100 pulses. Therefore, leaving as much hydrogen as possible after processing is another criterion. Lengsfeld et al., 2000, shows that a residual hydrogen concentration of ~5% was observed after step-by-step excimer laser induced crystallization of a-Si:H with an initial hydrogen content of 10%.

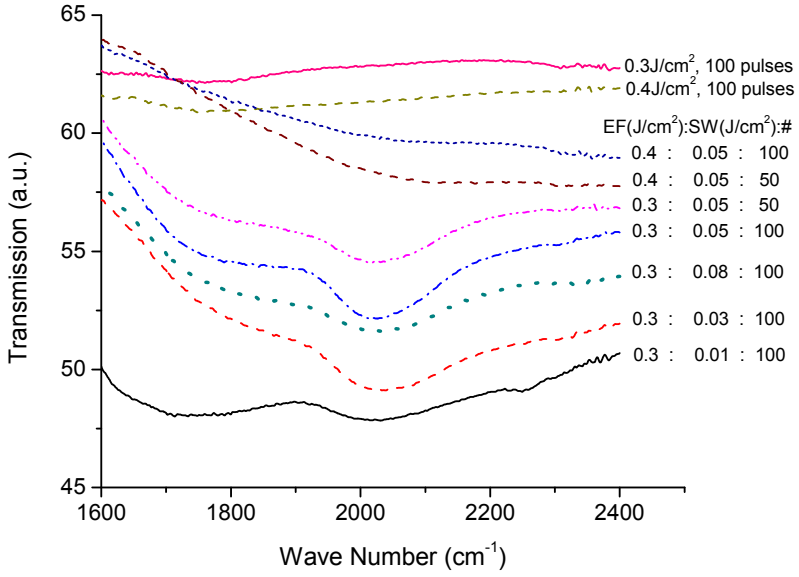

Figure 4.14 Transmission infrared spectra for single-step and step-by-step laser processed a-Si:H samples, where EF, SW and # indicate ending fluence, step width and number of pulses, respectively

In this study, step-by-step processes starting at a fluence of 0.05J/cm^2 and ending at 0.3J/cm^2 and 0.4J/cm^2 with increment of 0.05J/cm^2 are carried out. As shown in Fig. 4.14, the samples with an ending fluence of 0.4J/cm^2 have no hydrogen left after processing, whether 50 or 100 pulses are applied for each step. In order to understand the effect of the increment on residual hydrogen concentration, step-by-step processes with a desired final fluence of 0.3J/cm^2 and different increments from 0.01J/cm^2 to 0.08J/cm^2 are taken, and 100 pulses are used for each process sequence. It can be seen that the hydrogen concentration varies with different increment. The quantitative characteristics of hydrogen concentration and normalized crystallinity based on Eq. (4.12) and XRD measurement are performed with the conditions that have residual hydrogen left, and the results are shown in Fig. 4.15. For 100 pulses at each step, a maximum hydrogen concentration is achieved at 3.25% with a step width of 0.03J/cm^2. Based on the FTR

measurement, the a-Si:H sample starts to be crystallized at 0.15J/cm^2. At the step of 0.01J/cm^2, there are almost 10 steps before the structure phase change. However, the hydrogen inside the material will be diffused out due to the laser-induced thermal effect, which is more than 450˚C shown in Fig. 4.6, during those undamaged steps. Therefore, the hydrogen concentration at the step of 0.01J/cm^2 is smaller than that of 0.03J/cm^2. When the step goes to 0.05J/cm^2, thermal annealing by lower fluences is less dominant since only 2 to 3 steps before the crystallization threshold. However, the fluence at each step plays a more important role. Since the crystallized material performs as a protection layer for hydrogen from diffusing out, at the step of 0.03J/cm^2, after the crystallization threshold, the laser pulse at each step is less energetic compared to that of 0.05J/cm^2, which indicates that less energy is transferred underneath the crystallized layer to diffuse out the hydrogen at each step. Although more steps are taken, the final residual hydrogen is still less for the smaller-step process. Likewise, an even lower hydrogen concentration is detected at a step of 0.08J/cm^2. It is also noted that, at the step of 0.05J/cm^2, higher hydrogen concentration is achieved by 100 pulses at each step than that caused by 50 pulses at each step. The reason is that with the same increment, more pulses could cause a thicker crystallized layer at the crystallization threshold, and this layer can prevent too much hydrogen being diffused out from the next step. Therefore, at the same step, more pulses applied each step will retain more residual hydrogen. For crystallinity, it can be observed that crystallinity increases with increasing of increment until it reaches 0.05J/cm^2 and remains at around 50% afterwards. The reason is that with a smaller step, the laser process at each step can only melt a shallower layer compared to that caused by a higher step; therefore, less material can be crystallized after each step. The final crystallinity will become in samples processed in small increment although more steps are taken. When the increment is higher than 0.05J/cm^2, the crystallinity remains at around 50%. This is

because the spikes are grown to the saturated height (around 2μm) at some point during the processing, and the ablated material cannot reach to the tips of the spikes. Therefore, beyond this point, only remelting and recrystallizing of the crystallized material occur at each step, but no effect on crystallinity. Likewise, at the step of 0.05J/cm^2, the crystallinity is also unchanged at both 50 and 100 pulses at each step. Overall, the condition at the increment of 0.05J/cm^2 and 100 pulses exhibits a relatively good performance at both cell efficiency and stability.

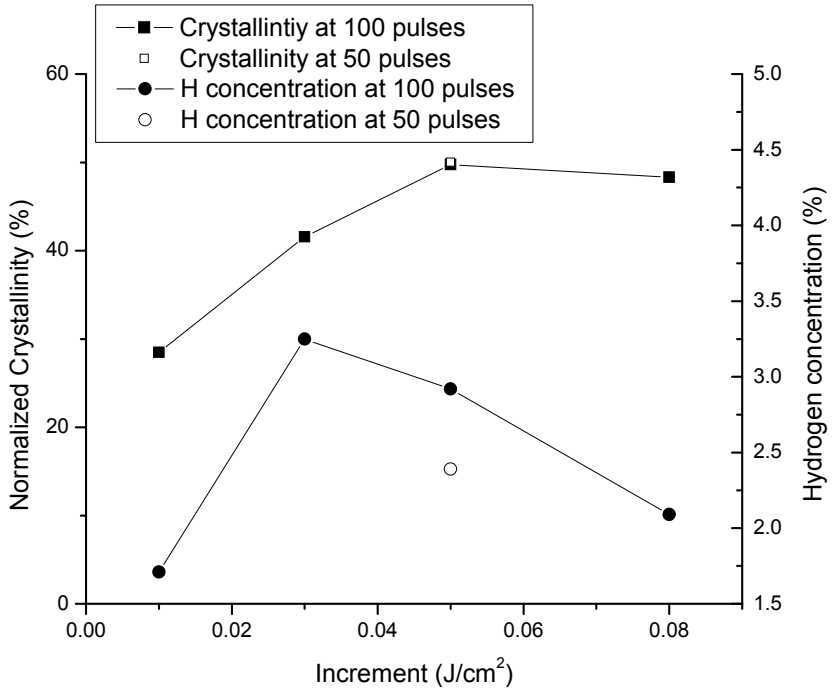

Figure 4.15 Normalized crystallinity and hydrogen concentration of step-by-step laser processed a-Si:H samples at a fixed initial fluence of 0.05J/cm^2 and final fluence of 0.3J/cm^2 with different increments and number of pulses

Figure 4.16 shows the comparison of absorptance between single-step and step-by-step processed a-Si:H samples. It can be seen that all the laser processed samples perform similarly. The inset shows the SEM image of a step-by-step processed a-Si:H sample at a final fluence of 0.3J/cm^2 with a step of 0.05J/cm^2 and 100 pulses at each sequence. A similar formation of spikes

is observed compared to the single-step processed sample shown in Fig. 4.1, which explains the similar absorptance due to a similar change of surface geometry. It is also noted that the interference at around 300nm is not eliminated by the step-by-step processes, which means the open cavities are still formed as shown in Fig. 4.10 (c). Further work is in progress to avoid those cavities for improvement of the light absorption. Overall, the combined effects of surface texturing, crystallization and residual hydrogen by excimer laser-induced step-by-step process (condition: a final fluence of 0.3J/cm^2, a step of 0.05J/cm^2 and 100 pulses at each sequence) of a-Si:H thin films yield the most desirable performance.

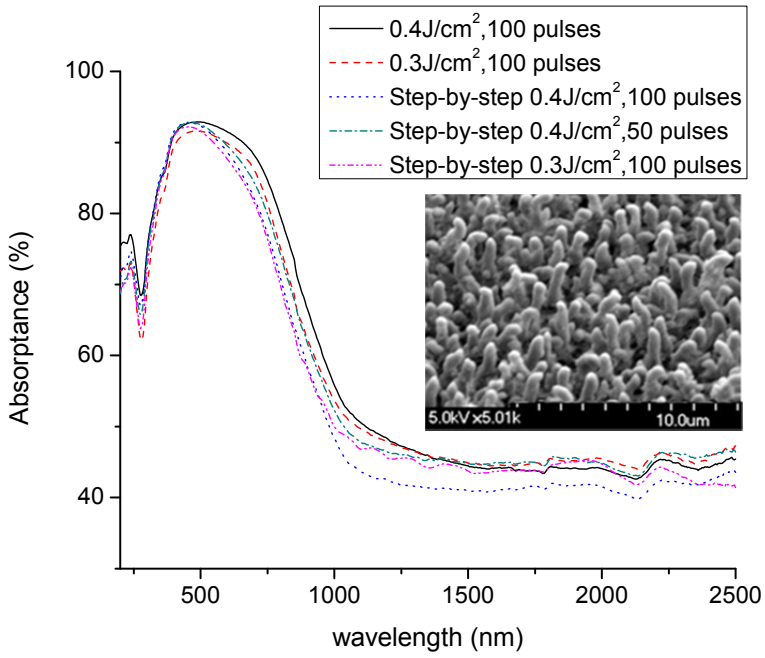

Figure 4.16 Comparison of absorptance spectra measured by spectrophotometry of single-step and step-by-step laser processed a-Si:H samples, inset shows the SEM image of surface morphology of a step-by-step laser processed a-Si:H sample with a final fluence of 0.3J/cm^2, step width of 0.05J/cm^2 and 100 pulses at each sequence

4.5 Conclusion

In conclusion, it has been demonstrated that hydrogen is necessary for the formation of sharp spikes on the surface of a-Si:H thin films irradiated by multiple excimer laser pulses. Hydrogen can also trigger explosive crystallization at the first 15-20ns, and then crystallized Si on the top will be re-melted in the next tens of nanosecond if the laser energy is high enough. The released pressure by H_2 gas bubble explosion at the interface between liquid Si and solid Si will drive the liquid Si to move up and form as spikes after solidification. Subsequently, the spikes are grown by VLS mechanism until they reach a certain height (~2μm) and the crystallinity also saturates at this point because no more amorphous material underneath the crystallized layer can be melted. The large-grain polycrystallites are located on the spikes and fine-grain ones are distributed underneath, with open cavities caused by hydrogen explosion at the interface. Furthermore, a step-by-step process is taken in order to retain hydrogen as much as possible after processing. It is shown that the residual hydrogen concentration depends on the final fluence, the increment and the number of pulses, and a maximum hydrogen concentration of 3.25% is obtained at a final fluence of 0.3J/cm^2 with steps of 0.03J/cm^2 and 100 pulses for each step. Finally, both single-step and step-by-step processed samples exhibit a similar absorption capability due to the similar surface geometries obtained after different laser processes. It can be concluded that excimer laser step-by-step processing of a-Si:H thin films may allow for more efficient and stable solar cells.

Chapter 5: Predictive Modeling for Glass-Side Laser Scribing of Thin Film Photovoltaic Cells

5.1 Introduction

Thin-film solar cell technology promises to achieve a significant cost reduction in materials, by adopting large area deposition capability, and the use of cheap and flexible substrates. Typical thin film solar cells used in terrestrial PV (photovoltaic) applications consist of back contact, absorber and front contact films. CdTe (Cadmium telluride) is the dominant absorber material in recent years because of its attractive price and stable performance at high temperatures (Dhere et al., 2011; Luque and Hegedus, 2003). The efficiency of thin-film solar panels, however, is hampered by resistive losses in the module proportional to the square of the photocurrent. In practice, photocurrent is decreased by scribing the solar module into a large number (between 100 and 200) mini-modules and connecting them in series to create high-voltage, low-current devices (Booth, 2010). Since each layer in the solar module must be scribed after deposition, scribing is performed in 3 steps – Patterns 1, 2 and 3 (P1, P2 and P3) processes, which are also used in the commercial production of a-Si:H (hydrogenated amorphous silicon) and CI(G)S (copper indium gallium selenide) based thin film solar cell fabrications (Compaan and Matulionis, 2000; Murison et al., 2010; Bovatsek et al., 2010). Compared to mechanical scribing, key advantage of laser scribing is able to enable much smaller line width (50μm Vs. 500μm) so the "dead zone" can be much smaller with higher efficiency. Also it is currently only industrial standard process for high speed mass production (scribing speed around 1 m/s Vs. 0.05~0.1 m/s). However, laser scribing has been shown to leave a heat-affected zone around the scribe, which causes undesirably poor isolation between cells and low shunt resistance. Laser scribing has also

been shown to leave high protruded ridges along the edge of the scribe line, contributing to electrical shorts (Compaan and Matulionis, 2000). While scribing reduces resistive losses by decreasing photocurrent, it also forms dead zones between P1 and P3 slots, which contribute to reductions in module efficiency (Gecys and Raciukaitis, 2010).

In order to decrease the thermal effect of laser irradiation during processing, the use of ultrashort pulsed lasers, such as picosecond and femtosecond lasers, are being investigation for scribing processes (Dunsky and Colville, 2008; Wang et al., 2010). These lasers are complex and expensive, and regardless of pulse duration, material melting cannot be totally eliminated (Murison et al., 2010). Glass side laser processing (Beyer et al., 2003; Sano et al., 2002) has been shown to be more efficient than film side processing with reduced thermal effect. Film side laser scribing is governed by heating, melting and vaporizing of selective films, while glass side laser scribing is a thermal-mechanical process which involves stress induced material failure and removal rather than vaporization. The mechanical fracture and removal of film material during glass side scribing is commonly referred to as lift off or micro-explosion processing. During micro-explosion processing, the laser irradiates through the transparent substrate and is fully absorbed in a very thin layer of film at the interface. High pressure plasma is generated and expanded in the film. The plasma punches through the solid film above and the material is removed mechanically (Matylitsky et al., 2011). Micro-explosion processing is pronounced when the laser material penetration depth is much shallower than the film thickness. One example is that of CdTe irradiated with a green laser at a wavelength of 532nm. Laser energy is mainly absorbed at the CdTe/substrate interface. High pressure plasma is generated and lifts off the solid film above. For front contact films made by transparent conducting oxide (TCO)

materials, such as ITO (indium tin oxide) and SnO_2:F (fluorine-doped tin dioxide), penetration depths exceed that of the film thicknesses, and the micro-explosion process cannot occur during laser scribing. Because of this effect it is difficult to scribe the TCO layers with low thermal effects using nanosecond (ns) lasers.

While glass-side laser scribing has led to improved scribe quality over competing methods, defects such as irregular scribe geometry, heat-affected zones and micro cracks that lead to decreased module efficiency are still introduced (Shinohara et al., 2006; Kontgers et al., 2010). The physical phenomena responsible for film removal during laser scribing and their effect on scribe quality are not well known. In order to be cost competitive to other PV technologies like crystalline silicon based cell, major thin-film solar players such as General Electric are pushing hard to develop next generation of cell with significantly higher efficiency and lower manufacturing cost. Developing modeling and better understanding for laser scribing process on thin-film PV is becoming a critical task for both industry and academy. It will help reduce the "dead zone" by predicting scribing width and improve the cell efficiency with optimization of process window. Furthermore, it will enable innovative new cell/structure design which can be better fit into current laser scribing process. To date, only rudimentary modeling efforts have been made, offering no predictive or optimization capabilities. Bovatsek et al., 2010, developed a simple, one-dimensional thermal model to estimate the through thickness temperature variation of a-Si:H based thin film solar cells by ns laser pulse irradiated from the glass side, and estimated the thermal stress as that of an expanding plate with fixed edges heated by a laser. While this model shows the formation of thermal stresses, caused by the laser fluence lower than the melting threshold, can exceed the material's compressive yield stress, it offers no predictive

capabilities of the scribe geometry due to the lack of spatial and temporal resolution. There is also limited simulation effort on micro-explosion processes.

Based on the current thin-film solar cell technology, a 1% increase in efficiency from improved scribe quality equates to roughly a 10% reduction cost. Therefore, numerical models of laser scribing processes that predict scribing width, cleanliness and thermal effect are important for the cost reduction of thin film solar cells. In this paper, two-dimensional numerical models are developed to simulate SnO_2:F and CdTe film removal via a fully-coupled thermo-mechanical stress analysis and micro-explosion processes, respectively. Brittle material failure and traction stresses at the film/substrate interface are incorporated to determine film fracture and delamination. Simulation results of SnO_2:F film removal from glass substrate are experimentally validated by glass side laser scribing. The scribe geometry and quality are characterized and studied by scanning electron microscopy (SEM), optical profilometry, and energy-dispersive x-ray spectroscopy (EDX).

5.2 Background

Because the entire layer of SnO_2:F can absorb the laser energy uniformly due to its high optical penetration depth compared to its thickness (400nm), SnO_2:F is usually removed by laser ablation which results in a heat-affected zone. Here, a film removal process of SnO_2:F with low laser fluences (less than melting threshold) is investigated. It is found that the SnO_2:F film is removed by the thermal-induced stress. CdTe, which has a lower optical penetration depth than its thickness (2μm), it is commonly removed by micro-explosion process. Because the CdTe film is thicker than the SnO_2:F film, it is difficult to thermally ablate with a single pulse. High-

pressure plasma is generated at the film/substrate interface while applying laser from the glass side, and the solid film above is lifted off during plasma expansion. CdTe film undergoes brittle material cracking during the plasma expansion, and the material at the plasma boundaries is delaminated simultaneously. Film delamination is analyzed by the traction separation mechanism at the interface, which is implemented using cohesive elements in the simulation.

5.2.1 Thermal Stress and Brittle Failure Analysis

During laser irradiation, the spatial and temporal distribution of temperature is governed by the heat equation

$$\rho C_P \left(\partial T / \partial t\right) = \nabla \cdot \left(k \nabla T\right) + q\left(r, z, t\right) \tag{5.1}$$

where ρ, C_p, T, t and k are density, specific heat, temperature, time and thermal conductivity; r and z are the radial distance to the laser beam center and film thickness, respectively; laser power density $q\left(r, z, t\right)$ represented temporal and spatial distribution within the film is given as

$$q\left(r, z, t\right) = q_0 \cdot exp(-\kappa z) \cdot exp\left[-2r^2 / R_0^2\right] \cdot exp\left[-4ln2(t / t_p - 1)^2\right] \tag{5.2}$$

where q_0, κ, R_0 and t_p are the peak power density, absorption coefficient, beam radius and pulse width. When a structure is mechanically constrained, thermal stresses are induced by thermal expansion, as determined by the Hooke's Law, $\boldsymbol{\varepsilon} = \boldsymbol{\alpha} \Delta T$, where $\boldsymbol{\alpha}$ is thermal expansion coefficient and ΔT is the temperature change. Because the thermal and mechanical response of the material is interpedent, a fully-coupled thermo-mechanical analysis, is implemented.

SnO_2:F and CdTe are considered as brittle materials and a precise failure criterion, which captures failure of a brittle material by both tensile and compressive stresses, can be provided by the Coulomb-Mohr criterion, written as (Seica and Packer, 2004)

$$\begin{cases} \sigma_1 > R_r \, or \, \sigma_2 > R_r, \, if \;\; \sigma_1 \; and \; \sigma_2 > 0; & \sigma_1 < -R_c \, or \, \sigma_2 < -R_c, \, if \;\; \sigma_1 \; and \; \sigma_2 < 0 \\ \sigma_1 / R_r + \sigma_2 / -R_c > 1, \, if \;\; \sigma_1 > 0 \; and \; \sigma_2 < 0; & \sigma_1 / -R_c + \sigma_2 / R_r > 1, \, if \;\; \sigma_1 < 0 \; and \; \sigma_2 > 0 \end{cases} \quad (5.3)$$

where σ_1 and σ_2 are the principal stresses, and R_t and R_c are the tensile and compressive failure strengths, respectively. When the principal stress of the brittle material elements exceed the Coulomb-Mohr criterion, the elements fail and cannot carry stresses any longer, and are removed from the calculation.

5.2.2 Micro-Explosion Analysis

When a target, i.e. CdTe, is irradiated by an intense laser pulse, due to its small optical penetration depth, the laser energy absorbed at the CdTe/substrate interface ionizes the material into plasma. Since the plasma is confined by the film and substrate, the solid CdTe film is lifted off during the plasma expansion, this process is known as the micro-explosion or lift-off mechanism (Matylitsky et al., 2011). The confined pressure induced by laser-produced plasma is estimated by Fabbro et al., 1990, which assumes a constant fraction α of internal energy goes into the thermal energy of the plasma while the rest (1- α) is used for ionization of the gas. The relationship between plasma pressure *P(t)* and plasma thickness *L(t)* can be derived from (Zhang and Yao, 2002)

$$\frac{dL(t)}{dt} = \frac{2P(t)}{Z} \quad (5.4)$$

$$\left(\frac{Z}{2} + \frac{3Z}{4\alpha}\right)\left(\frac{dL(t)}{dt}\right)^2 + \frac{3Z}{4\alpha} L(t) \frac{d^2L(t)}{dt^2} = AI(t) \quad (5.5)$$

where Z is the impedance of shock wave caused by the plasma expansion, t is time, *I(t)* is the incident laser intensity and A is absorption coefficient of plasma. It is also assumed that plasma pressure follows a Gaussian spatial distribution with its $1/e^2$ radius proportional to the $1/e^2$ radius

of the laser beam. The pressure is expressed as a function of space and time as $P(r,t) = P(t) \cdot exp\left[-r^2 / 2R_0^2\right]$, where R_0 is the laser beam radius.

5.2.3 Traction Separation Analysis

Because laser induced plasma expansion at the CdTe film/substrate interface can delaminate the film from the substrate, traction separation behaviors at the interface are considered using cohesive elements. The traction stress vector, $\boldsymbol{t}$, consists of two components t_u and t_v, which represent the normal and shear tractions. Corresponding displacements are δ_u and δ_v, and the strains are obtained by $\varepsilon_u = \delta_u / T_0$, $\varepsilon_v = \delta_v / T_0$, where T_0 is the original thickness of the interfacial elements. Before interface damage occurs, the relationship between the traction stress and strain is written as

$$\boldsymbol{t} = \begin{Bmatrix} t_u \\ t_v \end{Bmatrix} = \begin{bmatrix} K_{uu} & K_{uv} \\ K_{uv} & K_{vv} \end{bmatrix} \begin{Bmatrix} \varepsilon_u \\ \varepsilon_v \end{Bmatrix} = \boldsymbol{K}\varepsilon \tag{5.6}$$

where K_{uu} and K_{vv} are the stiffness in the principal directions, while K_{uv} is the stiffness in the shear direction. The CdTe/substrate traction separation law states that the traction stress depends linearly on the strain, but starts decreasing once the quadratic nominal stress ratio reaches one (Carlomagno and Brebbia, 2011),

$$\left\{\frac{\langle t_u \rangle}{t_u^0}\right\}^2 + \left\{\frac{t_v}{t_v^0}\right\}^2 = 1 \tag{5.7}$$

where material constants t_u^0 and t_v^0 are the critical values in the normal and shear directions, where the interface damage initiates. The value of $\langle t_u \rangle$ is 0 if $t_u < 0$ and t_u if $t_u > 0$, because a purely compressive stress does not initiate damage. When the stress criterion is reached, the traction stresses decrease as (Camanho and Dávila, 2002)

$$\overline{t_u} = \begin{cases} (1-D)t_u, & t_u > 0 \\ t_u, & t_u \le 0 \end{cases}, \ \overline{t_v} = (1-D)t_v \tag{5.8}$$

where the scalar damage variable, D, increases from 0 to 1 upon further loading after the initiation of damage. $\overline{t_u}$ and $\overline{t_v}$ are the stress components as a result of damage evolution. The scalar damage variable D is given as (Camanho and Dávila, 2002)

$$D = \frac{\delta_m^f \left(\delta_m^{max} - \delta_m^o\right)}{\delta_m^{max} \left(\delta_m^f - \delta_m^o\right)} \tag{5.9}$$

where δ_m is the effective displacement defined as $\delta_m = \sqrt{\langle \delta_u \rangle^2 + \delta_v^2}$, and the superscripts *max*, *o*, and *f* denote the maximum, initiation, and failure points. Eqs. (5.7) to (5.9) describe the failure behavior of the cohesive elements used in simulation and film delamination occurs when the effective displacement of the material at the interface reaches the critical value, δ_m^f.

The above analyses are carried out through a finite element method. Explicit time-stepping scheme is used for modeling this laser-induced highly dynamic process. A user-defined material property subroutine VUMAT is developed for identification of the material removal based on the criteria mentioned above.

5.3. Experimental Setup

The front contact layers, Polycrystalline TCO (SnO_2:F) material, were deposited on 3.2mm-thick soda-lime glass substrates using the chemical vapor deposition method at 1100ºF. The deposited SnO_2:F film thickness was measured to be 400nm by ellipsometry.

Laser scribing was carried out on the multilayer thin-film samples with a Q-switched Nd:YAG laser. The laser system delivered 50 ns pulses with a wavelength of 1064nm and a repetition rate of 1kHz. The SnO_2:F films were cleaned with acetone in an ultrasonic cleaner for 5 minutes and then rinsed with methanol and distilled water prior to laser processing. The sample, mounted on a three-axis translation stage, was irradiated by laser pulses focused by a 20mm effective-focal-length objective lens. The laser focal plane was placed at the SnO_2:F/glass interface with a circular 10μm in diameter beam spot. Both glass side-scribing and film-side scribing were conducted.

Laser treated samples were observed through SEM, and scribe profiles were measured by optical profilometry. The chemical components of laser processed samples were investigated by EDX to estimate the scribing quality.

5.4. Results and Discussion

5.4.1 Simulation on SnO_2:F Film Removal by Thermal Stress

The schematic of glass-side laser scribing of SnO_2:F and CdTe in both simulation and experiments is illustrated in Fig. 5.1. The SnO_2:F film thickness is 400nm, the glass substrate is 50μm thick, and the width of the model is 100μm in the simulation. A 50-ns pulse duration laser with a wavelength of 1064nm is used for SnO_2:F film scribing, a wavelength of 532nm is used for CdTe film scribing. The material properties of SnO_2:F, CdTe, and the soda-lime glass substrate used in the simulation are listed in Table 5.1.

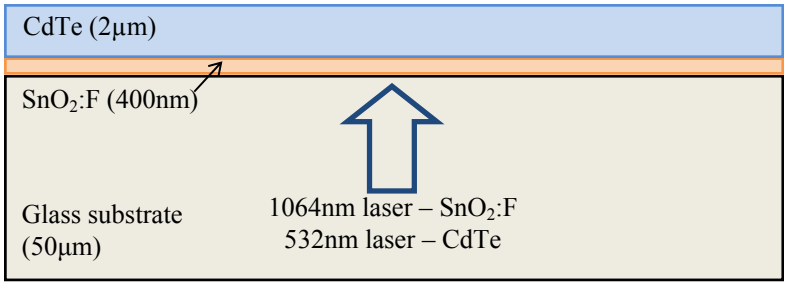

Figure 5.1 Illustration of glass-side laser scribing model for SnO_2:F and CdTe film removal. Lasers with wavelength of 1064nm and 532nm are adopted for SnO_2:F and CdTe scribing, respectively

Table 5.1 Material properties used in simulation

Properties	Unit	CdTe	SnO_2:F	Glass
Density, ρ	g/cm^3	5.85	6.95	2.52
Conductivity, k	W/mK	6.2	3.2	1
Latent Heat, L	10^5J/kg	2.092	3.17	--
Spec. Heat, C_P	J/kgK	210	353	800
Exp. Coef., κ	10^{-6}/K	5.9	4	8.6
Modulus, E	GPa	52	401	72
Poisson ratio, v		0.41	0.291	0.22
Refractive index @1064nm		--	1.6+i0.05	$1.51+i5.0\times10^{-6}$
Refractive index @532nm		2.72+i0.286	1.98+i0.01	$1.53+i1.8\times10^{-7}$
Melt. Temp., T_m	K	1370	1903	1873
Vap. Temp., T_v	K	1403	2123	--
Impedance, Z	$10^7 kg/m^2 s$	1.8	--	1.21
Tensile failure strength	MPa	40	500	--
References		Peter, 1994; Luque and Hegedus, 2011; Assay and Shahipoor, 1992	Gecys, and Raciukaitis, 2010; Luque and Hegedus, 2011	Gecys, and Raciukaitis, 2010; Luque and Hegedus, 2011; Assay and Shahipoor, 1992; Rubin, 1985

SnO_2:F is usually scribed through thermal ablation, however, a large area of heat-affected zone is always introduced. Here, in order to minimize the thermal effect, a simulation investigation of SnO_2:F film removal with a laser fluence lower than the melting threshold is carried out. By considering the energy loss due to the absorption and reflection by the glass substrate as well as the reflection by SnO_2:F/glass interface, the laser energy source in the SnO_2:F layer is written as (Bovatsek et al., 2010)

$$E(r,z,t) = \alpha_f (1-R_f)(1-R_g-A_g) I(r,z,t) e^{-\alpha_f (z-T_g)} \tag{5.10}$$

where $I(r,z,t)$ is the incident laser pulse energy. R_f and α_f are the reflectivity and absorption coefficient of SnO_2:F. R_g, A_g and T_g are the reflectivity, absorption and thickness of glass substrate. The results of thermal analysis are shown in Fig. 5.2. In the simulation, the SnO_2:F film is treated under a fluence of 3J/cm^2, which is less than the melting threshold (~4J/cm^2 for 1064nm @ 70ns) (Compaan and Matulionis, 2000), and laser is irradiated from the glass side. The highest temperature of SnO_2:F during the simulation history is 1848K, which is less than the melting point of 1903K. The large penetration depth in SnO_2:F, around 2μm at 1064nm, causes a uniform temperature distribution along the film's thickness.

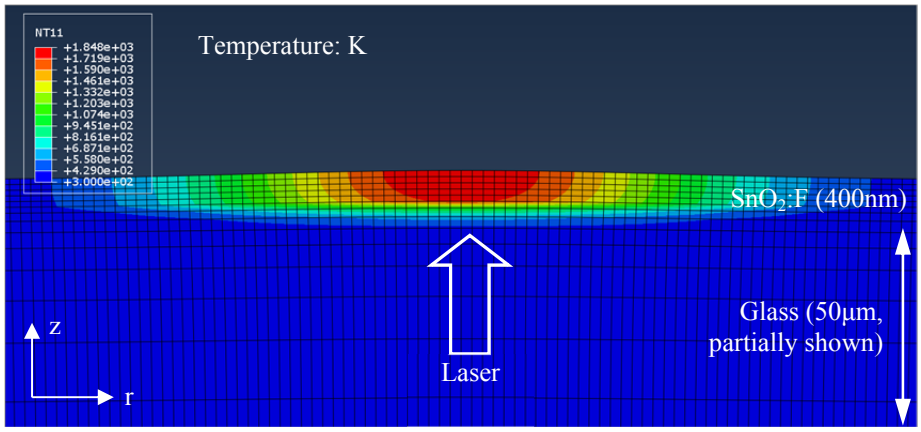

Figure 5.2 Temperature distribution in the SnO_2:F/glass multilayer system under laser irradiation at a fluence of 3J/cm^2. A large penetration depth of laser energy allows for a uniform temperature distribution along film thickness. Snapshot is taken at 36ns. 10X Deformation scale for viewing clarity

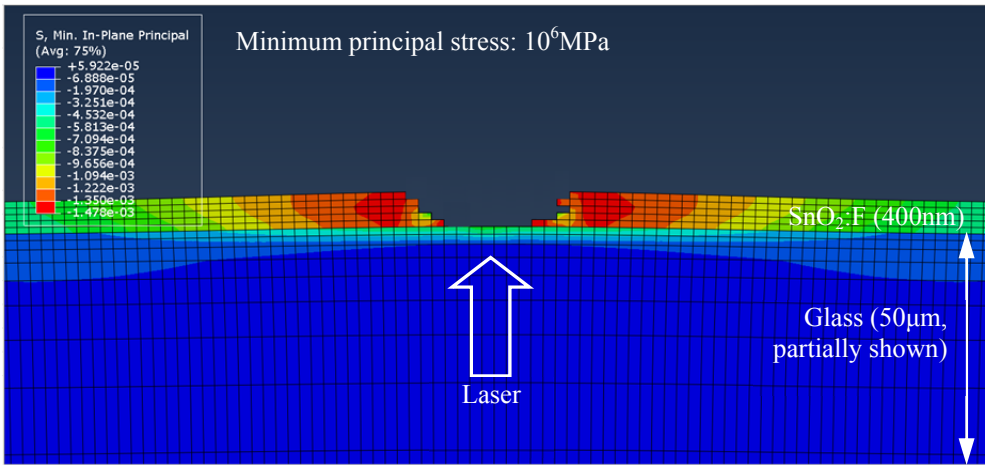

Figure 5.3 Fully coupled thermal stress analysis of SnO_2:F removal by laser irradiation at a fluence of 3J/cm^2 at 38ns. Absorption of laser energy induces local thermal expansion and thermal stress. Elements experiencing a principal stresses larger than the failure strength are deleted from calculation. A 2µm opening has been generated accordingly. 10X Deformation scale for viewing clarity

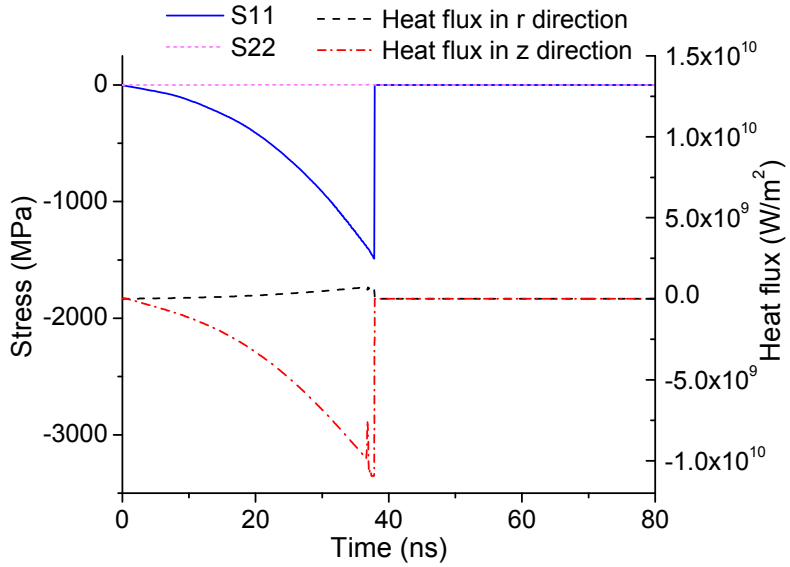

Figure 5.4 Stress and heat flux history in an element at SnO_2:F film center. The element deletion occurs at 38ns. Heat flux drops to zero due to instantaneous dependence between thermal and mechanical analyses

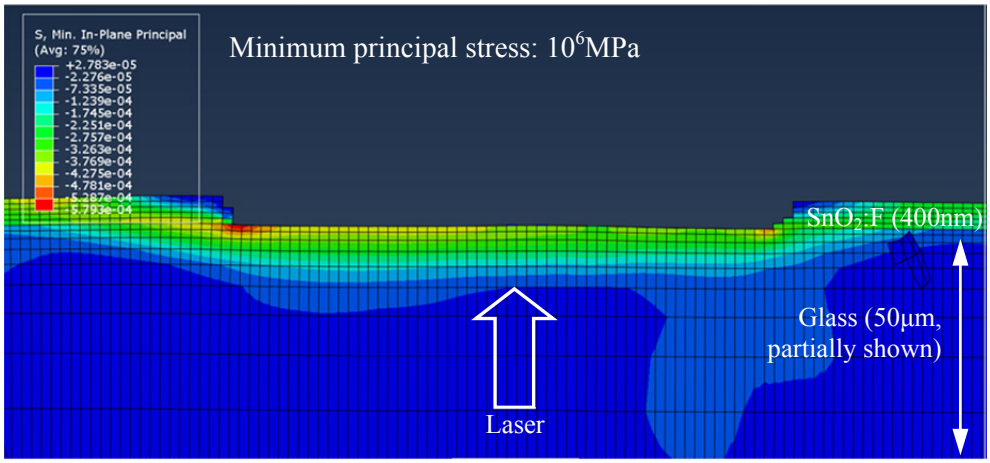

Figure 5.5 The result of SnO_2:F removal by 3J/cm^2 laser irradiation based on the fully coupled thermal stress analysis. An 8.3μm opening is generated. The snapshot is taken at 200ns. Deformation scale is 10X for viewing clarity

The fully-coupled analysis considers the simultaneous dependence between the variations of temperature, thermal stress and film deformation. In addition, the brittle failure analysis is implemented in order to simulate the film removal caused by the thermal stress. Fig. 5.3 shows a snapshot of the film removal process at 38ns. It can be seen that a 2μm opening has been generated at this moment since the elements have experienced the compressive principal stresses that are adequate to meet the Coulomb-Mohr criterion. While the absorption coefficient of SnO_2:F is much larger than that of glass, during the 50ns laser heating time, the SnO_2:F film expands much faster than that of glass, which results in a compressive stress in the film due to the confinement of the substrate. Elements are removed when the compressive stresses meet Coulomb-Mohr criterion. The evolution of the principal stress and the heat flux in an element at the center of SnO_2:F film are shown in Fig. 5.4. It can be observed that compressive stress is dominant in S_{11}, due to the discrepancy of the thermal expansions between the SnO_2:F film and glass substrate. Before element failure occurs, the compressive principal stress keeps increasing. Once the material fails, the element loses its ability to carry stress or heat which affects the

subsequent simulation step in the fully-coupled analysis. Fig. 5.5 shows the final results of complete SnO_2:F film removal irradiated at a fluence 3J/cm^2 at 200ns. A clean film removal is obtained with an opening of 8.3μm. Since phase change is not considered in the simulation, thermally induced compressive stress in the film is dominant during the film removal process.

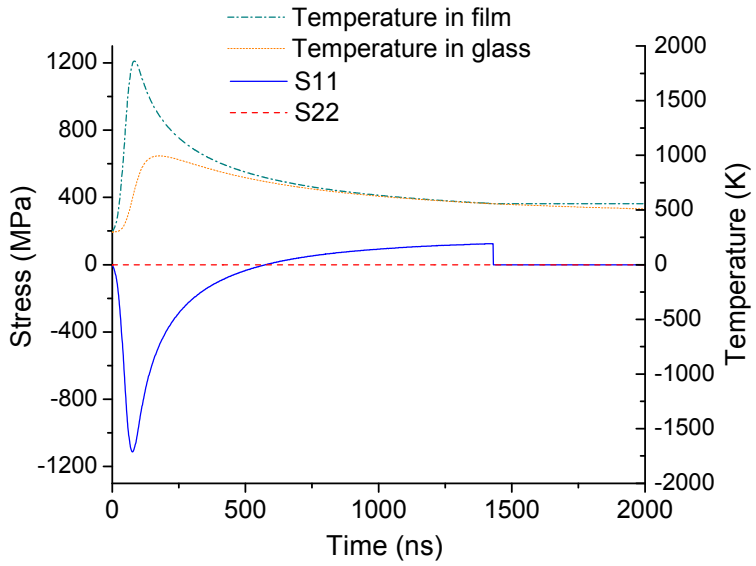

Figure 5.6 Temperature and stress history in a deleted element at SnO_2:F film center treated at a fluence of 1J/cm^2. The element is subjected to a compressive stress followed by a tensile stress. The element fails when the tensile failure stress is met at 1430ns

When the film is irradiated at a lower fluence, 1J/cm^2, the compressive stress inside the film is not adequate enough to cause the film fracture. Tension needs to be considered. In Fig. 5.6, the temperature history output shows that the glass temperature increase has a time delay compared with that of SnO_2:F. This indicates that part of the heat transfers to the glass after the fast laser heating of the film, which leads to the transition from compression to tension in the film. The expansion coefficient of glass is twice of that of SnO_2:F. The temperature change of glass is greater than SnO_2:F for a unit energy input. Thus, glass expands more than the film while heat is conducted from the film to the substrate. This leads to the decrease of compressive stress, and a

transition to tensile stress when the glass expansion exceeds that of the film. The time history evolution of principal stress in a deleted element under a laser irradiation with a fluence of $1J/cm^2$ is shown in Fig. 5.6. A clear transition between compressive and tensile stresses (S_{11}) is observed and the element is removed when the Coulomb-Mohr criterion is met. The effect of tension is neglected when the film is removed by compressive stress at higher fluences. The reason is because the elements around the scribe removed during the laser irradiation are free of confinement in r direction, which eliminates the subsequent dominant tensile stress (S_{11}). Because the film removal occurs during the laser heating time when compressive stress is dominant, the heated film is removed from the calculation before transferring the heat to the substrate; therefore, the glass thermal expansion will be much smaller and the tension is too small to fracture the rest solid film. At low fluences where compressive stress cannot lead to film removal, tensile stresses can be dominant for the removal.

A comparison of experimental and simulation results are shown in Fig. 5.7. It is observed that the scribe widths obtained from the simulation are close to the experimental results and both show a linearly increasing relationship between scribe width and laser fluence. Simulation results show that film removal is complete for all conditions; however, the experimental results depict that the films are partially removed in depth and the removal depths vary linearly with increasing laser fluence. Discrepancies between the simulation and experimental results are caused by neglecting the effect of the interface. As shown in the simulation, the temperature and stress distributions along the thickness direction are uniform due to the large laser penetration depth. However, the impurities or defects induced during the deposition process can absorb a fraction of laser energy and less energy is absorbed by the film than that in the simulation, thus the

simulation over- estimates the scribe width. Additionally, micro cracking and fracture driven mechanical interactions along the substrate film interface may play a significant role in the energy release process. Such mechanisms are not considered in the current model and may result in the partial removal of SnO_2:F film observed in experiments. Lastly, material properties, such as thermal capacity, conductivity and absorption coefficient are assumed constant, non-temperature dependent and homogeneous. The effect of fluorine doping and other impurities are also not considered in the model. These reasons may cause the over-estimation of the simulation results.

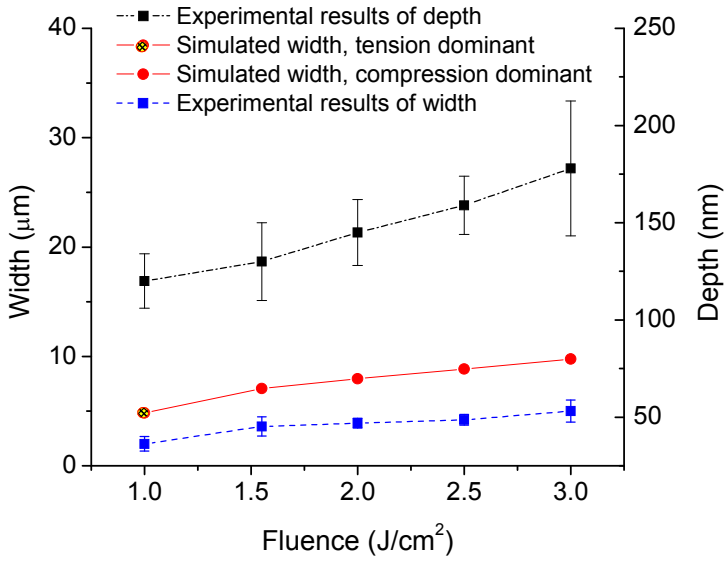

Figure 5.7 Comparison of depths and widths of the removed SnO_2:F films obtained in simulation and experiments. The film is completely removed in depth for all the conditions used in the simulations

The current model is capable of capturing the film removal process. The model shows that the film expands more at the top surface and larger stress is induced due to the different thermal expansion, so that the film starts breaking from top to the bottom, and under a certain condition,

partial removal occurs. Moreover, the width of the film removal predicted by the model is close as the experimental result. Both show the trend of decreasing width with decreasing fluence.

5.4.2 Experiments on Laser Scribing of SnO2:F Thin Films

Glass side laser scribing results are shown in Fig. 5.8 for a film processed at 127J/cm^2. Optical profilometry results, given in Fig. 5.8(b), show that the sidewall of the removed area is steep and the scribe is 35μm in width with no positive ridges. It is observed that the scribe depth is slightly greater than the film thickness (400nm) at some locations. This suggests that substrate damage occurs at this fluence. SEM cross-sectional images (Fig. 5.8(c)), show that the sidewall possesses similar granular structures as the surface of the film. This suggests that no melt material attached on the sidewalls and the entire scribe boundary is removed mechanically rather than through thermal ablation. Brittle crack propagation, caused by laser-induced plasma, along the transverse direction makes the scribe width much larger than the beam spot size, and the non-thermal-affected sidewalls is formed by the thermal stress. Film removal quality is estimated by atomic density measurement at the removal area via EDX shown in Fig. 5.8(d). Line scanning EDX shows that there is a little residual tin after one laser pulse irradiation, which may be removed during laser scribing with a certain pulse overlap. Silicon is detected at the undamaged surface because the electron penetration depth of SnO_2:F is ~1.3μ is estimated by (Potts, 1987)

$$X\,(\mu m)=0.1E^{1.5}/\rho \tag{5.11}$$

where E is accelerating voltage (keV) and ρ is density (g/cm^3). This observation shows a promising manufacturing process – mechanical dominant removal at the boundary, clean scribe with steep sidewalls. Further simulation investigations will consider higher fluence processing regimes with coexisting ablation and thermal stress film removal mechanisms.

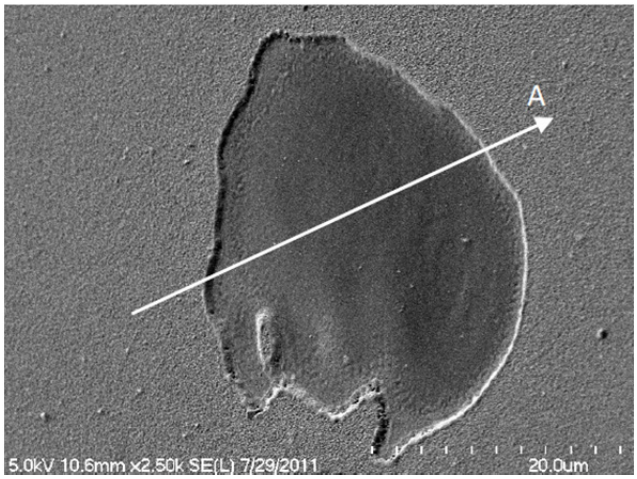

(a) Overview of film removal

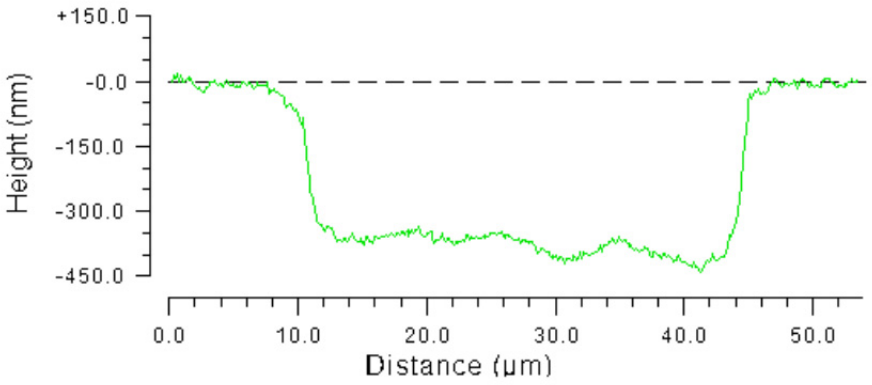

(b) Optical profilometry measurement

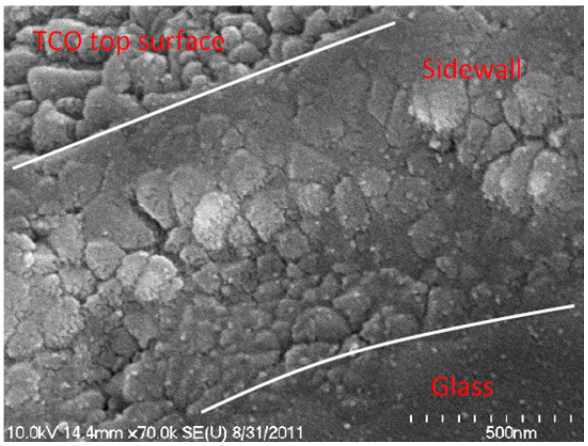

(c) Sidewall of the film removal

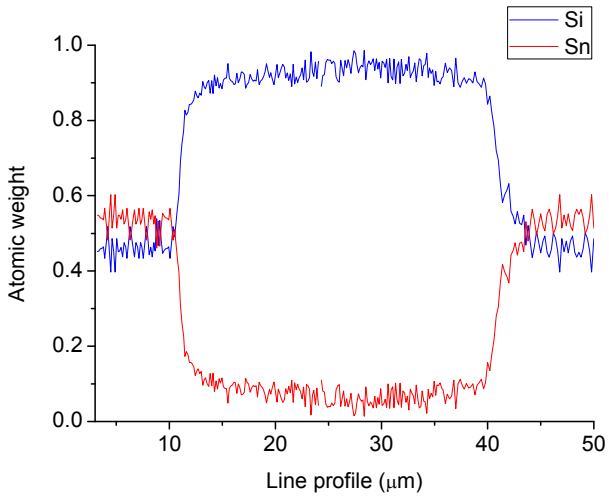

(d) EDX line scan profile

Figure 5.8 (a) SEM image of the film removal by single pulse processed SnO_2:F samples from glass side at a fluence of 127J/cm^2; (b) Removal line profile along A measured by optical profilometry; (c) SEM image of scribe sidewall; (d) EDX line profile scanning along A

As a comparison of the glass-side laser treatment, the film-side laser scribing with a fluence of 127J/cm^2 is carried out. Fig. 5.9(a) gives the 3D profile of the scribe area. The film is completely removed with a diameter of 50μm. A positive ridge exists around the scribe boundary due to SnO_2:F vapor redeposition. Thermal ablation based film removal process is driven by the thermodynamical phase transition of the film material. During the ablation process, the material is vaporized, and the vapor moves away from the target due to the high pressure. Some vaporized material redeposits on high-temperature areas, specifically the melted material at the scribe boundary, via the vapor-liquid-solid mechanism (Lowndes et al., 2000). Vapor redeposit is characterized by the protruding material around the boundary of the scribe. The sidewall of a scribed processed from the film side is captured in Fig. 5.9(b). It is seen that the granular structure disappears on the entire sidewall, which covered with the resolidified material instead.

The combined effects of the protruded ridge and residual solidified molten layer on the sidewalls indicate that film-side laser scribing can lead to undesired electrical properties.

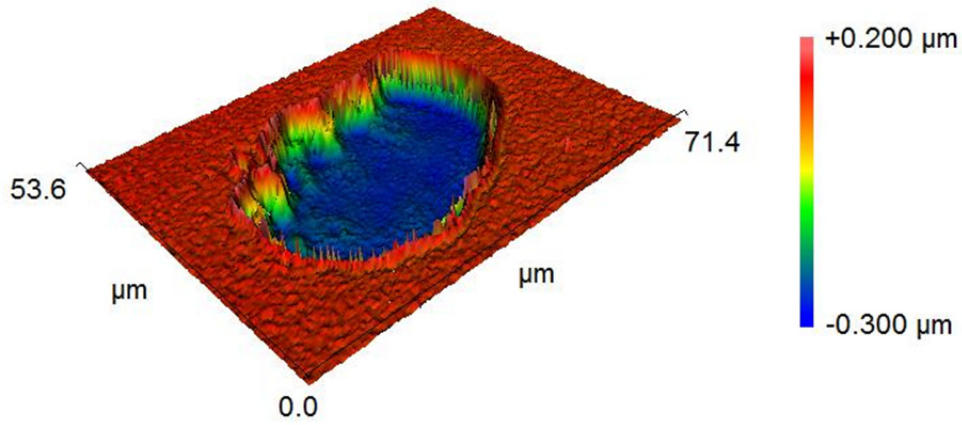

(a) 3D scan profile by optical profilometry

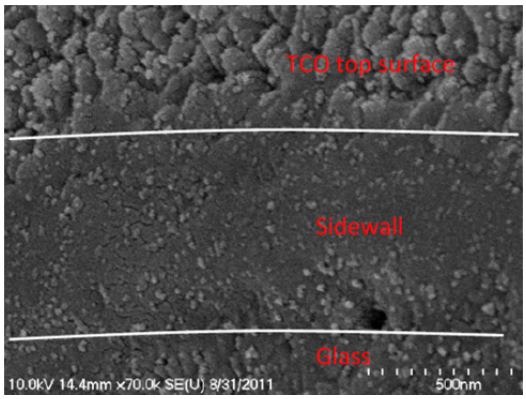

(b) Sidewall of the film removal

Figure 5.9 (a) 3D scanning of the removal film profile by optical profilometry and (b) SEM image of the sidewall of film removal by single pulse processed SnO_2:F samples from film side at a fluence of 127J/cm^2

A parametric study on glass-side laser scribing is carried out to fully understand the mechanisms under different laser treatment conditions. The scribe width and depth under different laser fluences are shown in Fig. 5.10. It is observed that the scribe depth increases with increasing fluence until the film is completely removed. This near-linear trend is not observed in the scribe

width. Width increases with fluence when treated by the fluences below 20J/cm^2 and above 60J/cm^2. When the fluence is between 20J/cm^2 and 60J/cm^2, the width remains constant. This observation indicates that a mechanism transition occurs under different fluences. At fluences below 20J/cm^2, the removal mechanism is mechanically dominant. The thermal stress is induced by the increasing temperature, and thus the scribe depth and width increase with increased fluence. At fluences between 20 and 60J/cm^2, thermal ablation removal becomes dominant. An area close to the spot size is thermally removed and part of the film is mechanically removed due to thermal stress. At fluences greater than 60J/cm^2, film surrounding the high-pressure plasma is removed by crack propagation, and the sidewalls are formed mainly by mechanical removal.

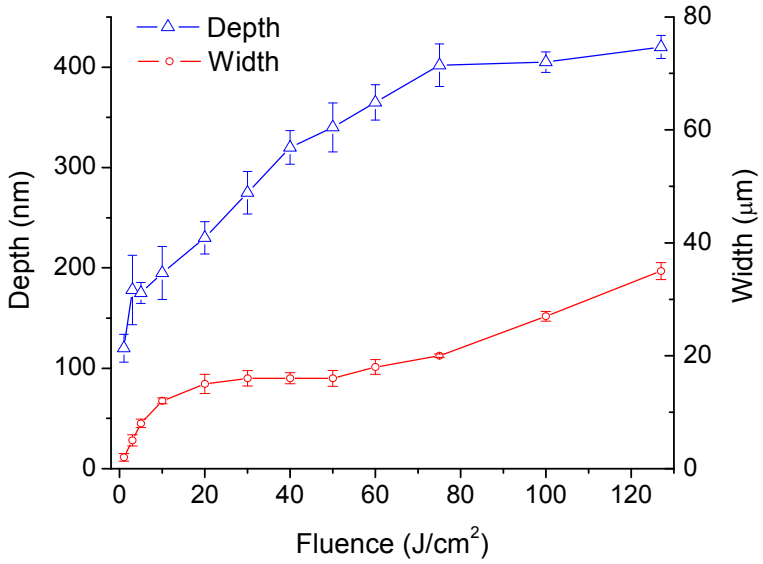

Figure 5.10 Dependence of removal depth and width on laser fluence. Error bars indicate standard deviation

Both simulation and experimental show that SnO_2:F film can be removed before the temperature reaches the melting temperature, therefore, if the scribe quality, such as thermal effect and scribe width, is more important than the manufacturing throughput, this thermal-stress dominant film

removal can be considered. Otherwise, a mechanical dominant film removal at higher fluences may be used resulting in clean scribe boundaries and larger scribe widths.

5.5 Simulation on CdTe Film Removal by Micro-Explosion

Selective scribing of a 2µm thick CdTe film is performed with a green laser at a wavelength of 532nm. A green laser is used because the melting threshold of SnO_2:F is much larger than that of CdTe at this wavelength. Therefore, laser energy can be highly transmitted though the SnO_2:F film, and fully absorbed by the CdTe film within a very thin layer near the CdTe/SnO_2:F interface. The penetration depth of CdTe at 532nm wavelength is around 167nm, which is thinner than the CdTe film thickness (2µm) by one order of magnitude. The high energy density absorbed within the thin CdTe layer increases local temperature above vaporization temperature and induces material ionization, resulting in plasma generation. The plasma is confined by the solid CdTe and SnO_2:F and is under high pressure, which lifts off the solid CdTe film above, resulting in film removal and delamination. This film removal mechanism is known as the micro-explosion process.

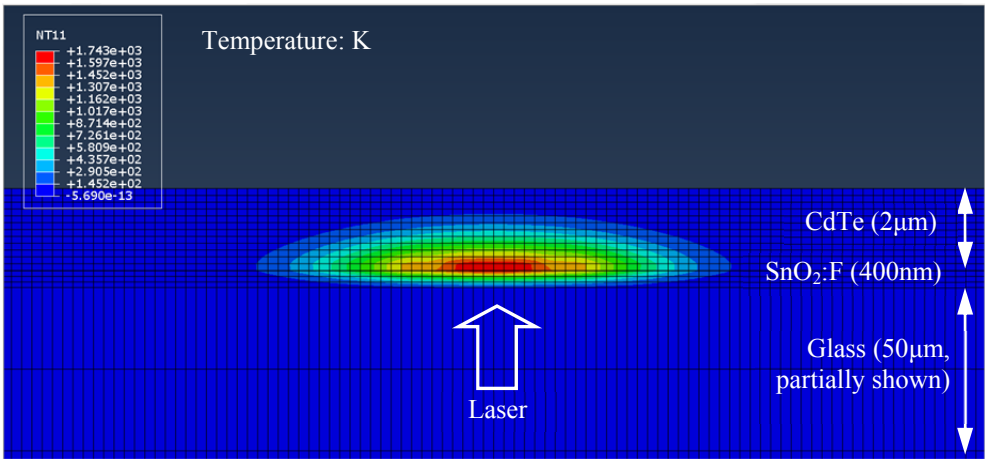

Figure 5.11 Temperature distribution of CdTe/SnO_2:F/glass multilayer system under laser irradiation at a fluence of 0.2J/cm^2

As shown in Fig. 5.11, the model is composed of a 2μm thick CdTe layer is on the top of the 400nm thick SnO_2:F layer and 50μm thick glass substrate. To consider the traction stresses at the CdTe/SnO_2:F interface, a 10nm thick layer of cohesive elements is also implemented at the interface. The cohesive layer is governed by the traction separation law described in Sec. 5.2.3, and serves the purpose of simulating the process in which the CdTe film lifts up and delaminates from the SnO_2:F layer caused by the plasma expansion. The thermal analysis is carried out with the consideration of energy loss due to the reflection at the interfaces of SnO_2:F/CdTe and glass/ SnO_2:F, as well as the absorption by the glass substrate and SnO_2:F layer. Material properties are shown in Table 5.1. The laser pulse duration is 50ns and wavelength is 532nm. The laser energy is given by (Bovatsek et al., 2010)

$$E(r,z,t) = (1-R_g-A_g)(1-R_t)(1-R_c)\alpha_c I(r,z,t)e^{-\alpha_t T_t}e^{-\alpha_c(z-T_t-T_g)} \tag{5.12}$$

where R_c and α_c are the reflectivity and absorption coefficient of CdTe, and T_t is the thickness of SnO_2:F. Fig. 5.11 shows the temperature distribution as a result of the glass-side laser irradiation at a fluence of 0.2Jcm^2. It can be observed that the absorbing volume in the CdTe layer is confined near the CdTe/SnO_2:F interface, rather than uniformly distributed in the SnO_2:F layer as shown in Fig. 5.2. This highly confined energy increases temperature higher than the vaporization temperature of CdTe (1400K), generating plasma. Figure 5.12 shows the temporal distribution of plasma pressure under the fluences from 0.2J/cm^2 to 0.8J/cm^2 as generally used in experiments. The plasma pressure achieves several hundred Mega Pascal which is much larger than the CdTe failure strength.

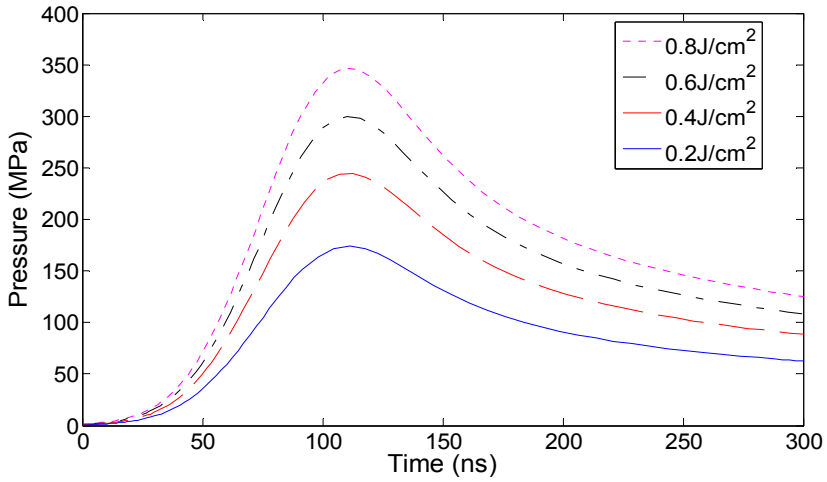

Figure 5.12 Temporal distribution of the plasma pressure at different fluences from 0.2J/cm^2 to 0.8J/cm^2

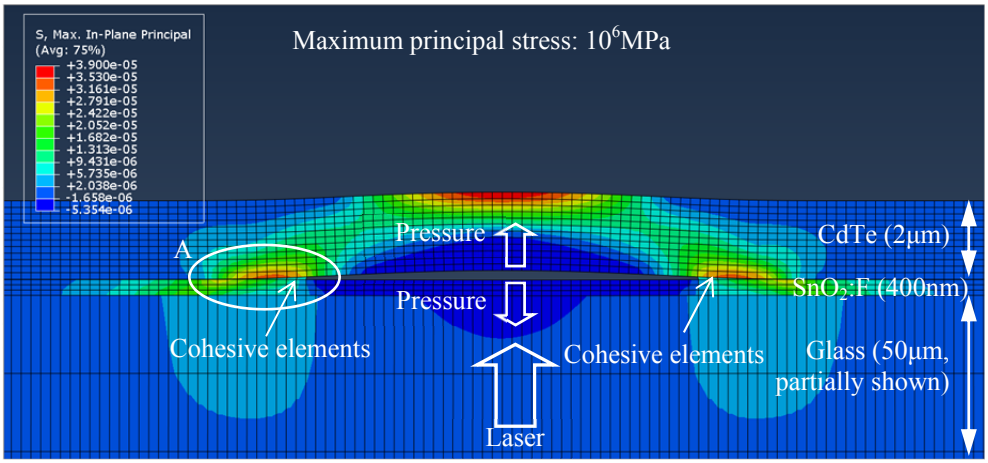

Figure 5.13 Micro-explosion model with a pressure input at the CdTe/SnO_2:F interface and the plasma dimension is 10μm in width. A layer of cohesive elements is defined between the CdTe layer and SnO_2:F layer. The CdTe film deforms due to the plasma expansion. The snapshot is taken at 10ns. Deformation scale is 10X for viewing clarity

The pressure with the temporal and spatial pressure distributions described in Sec. 5.2.2 and Fig. 5.12 are incorporated and exerted on both CdTe and SnO_2:F layers at the interface. The width of plasma is assumed to be the same as the beam spot size – 10μm. A snapshot of stress distribution in the film and substrate at 10ns after the onset of laser pulse is given in Fig. 5.13. The CdTe film

is pushed upward due to the plasma expansion. This deformation expands the top center of the film in the r direction, generating a S_{11} tensile stress. Stress in the z direction (S_{22}) is much smaller. Therefore, the principal stress on the top center of the film is mainly contributed from the S_{11} tensile stress, as shown in Fig. 5.13. Similarly, a compressive principal stress exists at the lower part of film center due to CdTe film deformation. At the edge of the plasma, a large principal tensile stress is observed at the CdTe/SnO_2:F interface. This principal tensile stress comes from the traction stress between the SnO_2:F and the deforming CdTe layers. The traction at the interface is considered in more detail in Fig. 5.14, in which Region A in Fig. 5.13 is magnified. It can be seen that large S_{22} stress in the CdTe layer, SnO_2:F layer, and the cohesive elements near the plasma boundary. This S_{22} stress is induced by the deformation of CdTe layer caused by the plasma expansion. The deforming CdTe layer in turn pulls the cohesive elements upwards. Deformed cohesive elements carry a tensile stress governed by the traction separation law, binding the CdTe film to the SnO2:F substrate, and the surrounding CdTe and SnO2:F elements also experience a tensile S_{22} stress. It is observed that S_{22} tensile stress in the film is smaller than S_{11} tensile stress; therefore, S_{11} tensile stress is dominant for the CdTe material removal. As the film deforms, the S_{11} tensile stresses at the top center and plasma boundaries in the film increases, and the film starts breaking at these locations when the principal stress satisfies the Coulomb-Mohr criterion.

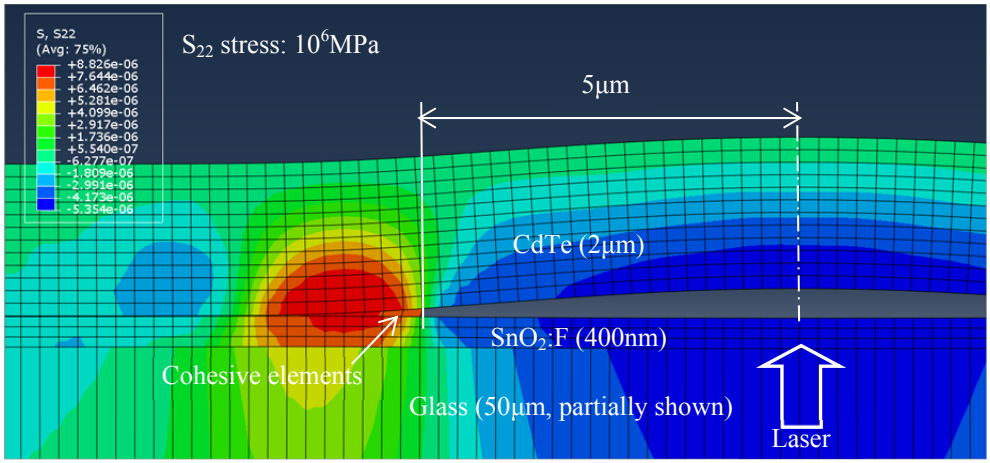

Figure 5.14 S_{22} stress distribution of the magnified area A in Fig. 5.13 at the same moment. The cohesive elements have been deformed due to S_{22} stress. Deformation scale is 10X for viewing clarity

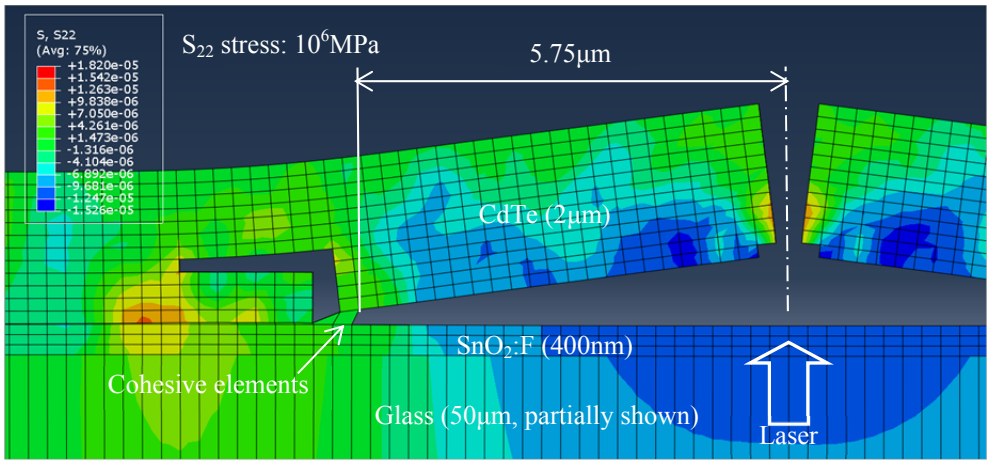

Figure 5.15 S_{22} stress distribution of the region shown in Fig. 5.14 at the later stage (20ns), showing some cohesive elements have been deleted. Deformation scale is 10X for viewing clarity

A snapshot at the early stage of the film breaking taken at 20ns is given in Fig. 5.15, which shows that material failure initiates at the center. The removal of the CdTe elements on the top center of the film is the tensile stresses dominant removal, while removal of the elements on the bottom center is dominant by the compressive stresses. Some elements near the plasma boundaries are removed due to the large S_{22} tensile stress caused by the confinement between the

cohesive elements and CdTe material. Cohesive elements failed and are deleted from the calculation based on the traction separation analysis, initiating film delamination. Material failure and film delamination both contribute to the film removal at this stage. In order to capture the processes of film breaking, the stress evolution of the failed elements at the top center and bottom center of the CdTe layer is shown in Fig. 5.16. The element at the top center undergoes tensile stress (maximum principal stress) during the simulation and is responsible for the film removal. The element at the bottom center sees compressive stress (minimum principal stress). Stresses carried in both elements increase with simulation time before failure. Once the Coulomb-Mohr criterion is met, the element fails and no longer carries stresses. The greater compressive failure strength causes the delay of material failure at the bottom center, which indicates that film breaking initiates from the top center to the bottom.

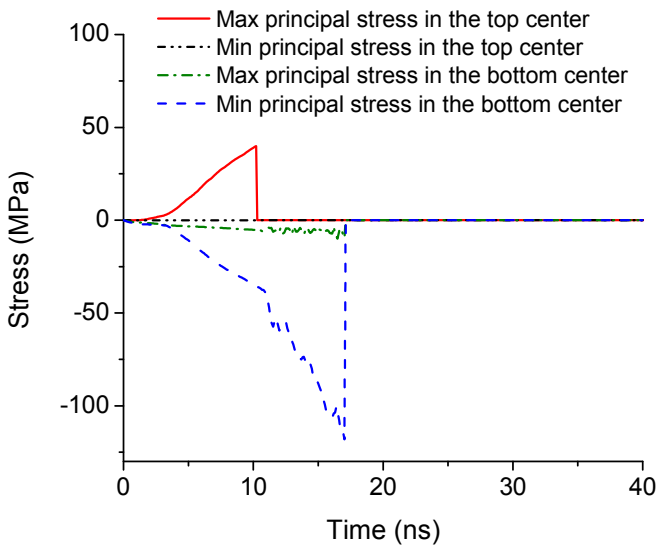

Figure 5.16 Stress evolutions of the failed elements at the top center and bottom center of the CdTe layer. Tensile stress occurs on the top, while compressive stress occurs at the bottom. The stresses drop to zero once the Coulomb-Mohr criterion is met

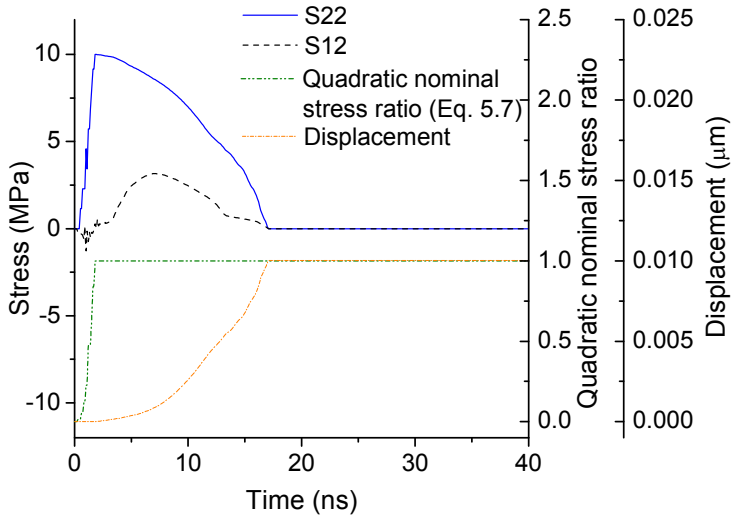

Figure 5.17 Typical evolution of stresses and the quadratic nominal stress ratio defined in Eq. (5.7) of the removed cohesive elements. Nodal displacement of the cohesive element is also shown

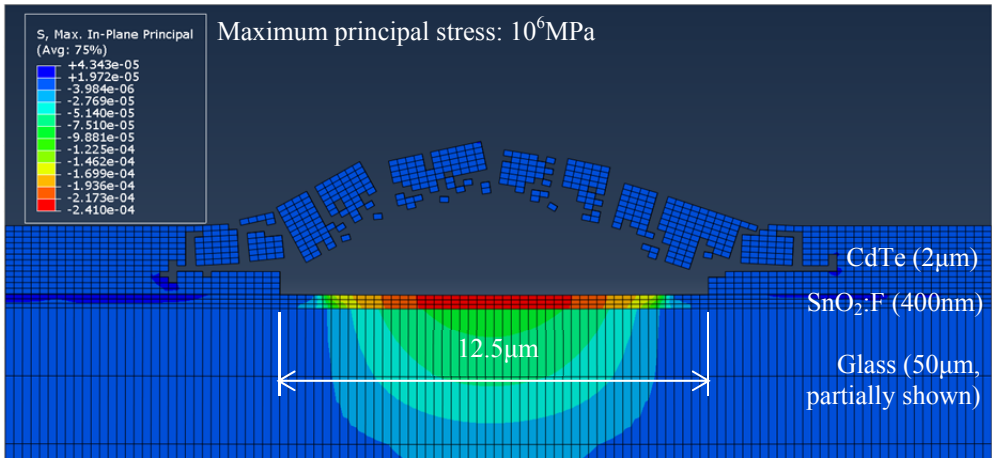

Figure 5.18 Maximum principal stress distributions at 66ns. The film has been completely removed with an opening width of 12.5μm. Both brittle failure and film delamination contribute to the film removal. Deformation scale is 2X for viewing clarity

Figure 5.17 gives the typical evolution of stresses and the quadratic nominal stress ratio defined in Eq. (5.7) of a removed cohesive element. The nodal displacement of the cohesive element, which represents the displacement of the deforming film before element failure, is also shown. In

the early stage the plasma pressure lifts the CdTe film upwards, and the cohesive element experiences S_{22} tensile stress, while the shear stress S_{12} is less dominant. The quadratic nominal stress ratio is the criterion to determine the initiation of cohesive element damage. Once the ratio reaches 1, damage initiates and the stress to be carried begins to reduce. The cohesive element then undergoes a large deformation, mainly in the z direction. Once the nodal displacement reaches a predefined value, traction stress becomes zero and the cohesive element is removed from the calculation. This suggests no confinement between the film and substrate; film delamination then occurs. The late stage of the micro-explosion process is shown in Fig. 5.18. As CdTe layer keeps deforming, it also begins breaking into multiple segments due to brittle failure. At the same time, the width of the removed film keeps enlarging from 10μm (assumed initiated size of the plasma) to 12.5μm. The enlarged opening shows a scribe width of 12.5μm. Complete film removal is achieved. The simulation shows that the film removal process via the micro-explosion mechanism is contributed from both brittle failure and film delamination processes without thermal effects. A similar observation of laser scribing of ZnO film on glass substrate is presented by Matylitsky et al., 2011. The micro-explosion model is capable of predicting the film removal quality of low-penetration-depth materials (compared to the film thickness).

5.6 Conclusion

Predictive numerical finite element models are demonstrated for glass-side laser scribing of SnO_2:F and CdTe films. A fully-coupled thermal-mechanical model is implemented, showing that SnO_2:F film is removed at a laser fluence below the damage threshold due to thermal stresses. The scribe size is predicted by simulation and is on the same order of magnitude as experimental results. Experimental results also show that SnO_2:F film removal starts from the

top, as predicted by the simulation. The micro-explosion model is developed for glass-side laser scribing of CdTe films, with the stress loading estimated by the laser-induced plasma pressure. A CdTe removal process dominated by both brittle failure and delamination with reduced thermal effects, as captured by the numerical model, is desired for reducing scribing dead zones and interlaminar shorts. Such a process is highly desirable for improved scribe quality and greater process efficiency. Numerical models investigated in this work are capable of predicting the material removal dynamics and fracture behavior of SnO_2:F and CdTe. Further numerical developments are aimed at predictively modeling the scribing line profile by taking account of the laser pulse overlapping.

Chapter 6: Removal Mechanism and Defect Characterization for Glass-Side Laser Scribing of CdTe/CdS Multilayer in Solar Cells

6.1 Introduction

Thin-film solar cell technology promises to achieve a significant cost reduction in materials, by adopting large area deposition capability, and the use of cheap and flexible substrates. Typical thin film solar cells used in terrestrial PV (photovoltaic) applications consist of back contact, absorber and front contact films. CdTe is the dominant absorber material in recent years because of its attractive price and stable performance at high temperatures (Dhere et al., 2011; Luque and Hegedus, 2003). The efficiency of thin-film solar panels, however, is hampered by resistive losses in the module proportional to the square of the photocurrent. In practice, photocurrent is decreased by scribing the solar module into a large number (between 100 and 200) mini-modules and connecting them in series to create high-voltage, low-current devices (Booth, 2010). Since each layer in the solar module must be scribed after deposition, scribing is performed in 3 steps – Patterns 1, 2 and 3 (P1, P2 and P3) processes, which are also used in the commercial production of a-Si:H (hydrogenated amorphous silicon) and CI(G)S (copper indium gallium selenide) based thin film solar cell fabrications (Compaan and Matulionis, 2000; Murison et al., 2010; Bovatsek et al., 2010). Compared to mechanical scribing, key advantage of laser scribing is able to enable much smaller line width (50μm Vs. 500μm), so the "dead zone" can be much smaller with higher efficiency. Also, it is currently only industrial standard process for high speed mass production (scribing speed around 1 m/s Vs 0.05~0.1 m/s). However, laser scribing has been shown to leave a heat-affected zone around the scribe, which causes undesirably poor isolation between cells and low shunt resistance. Laser scribing has also been shown to leave high protruded ridges

along the edge of the scribe line, contributing to electrical shorts (Compaan and Matulionis, 2000). While scribing reduces resistive losses by decreasing photocurrent, it also forms dead zones between P1 and P3 slots, which contribute to reductions in module efficiency (Dunsky and Colville, 2008).

In order to decrease the thermal effect of laser irradiation during processing, the use of ultrashort pulsed lasers, such as picosecond and femtosecond lasers, are being investigation for scribing processes (Gecys and Raciukaitis, 2010; Wang et al., 2010). These lasers are complex and expensive, and regardless of pulse duration, material melting cannot be totally eliminated (Murison et al., 2010). Glass side laser processing (Beyer et al., 2003; Sano et al., 2002) has been shown to be more efficient than film side processing with reduced thermal effect. Film side laser scribing is governed by heating, melting and vaporizing of selective films, while glass side laser scribing is a thermal-mechanical process which involves stress induced material failure and removal rather than vaporization. The mechanical fracture and removal of film material during glass side scribing is commonly referred to as lift off or micro-explosion processing (Dunsky and Colville, 2008). During micro-explosion processing, the laser irradiates through the transparent substrate and is fully absorbed in a very thin layer of film at the interface. High pressure plasma is generated and expanded in the film. The plasma punches through the solid film above and the material is removed mechanically (Matylitsky et al., 2011). Micro-explosion processing is pronounced when the laser material penetration depth is much shallower than the film thickness, such as P2/P3 processes of CdTe and a-Si:H solar cells. Otherwise, films are removed through thermal ablation, such as P1 process for front contact films made by transparent conducting oxide (TCO) materials (Wang et al. 2013).

While glass-side laser scribing has led to improved scribe quality over competing methods, defects such as thermal effect, film delamination, scribe uncleanliness and micro cracks that lead to decreased module efficiency are still introduced (Shinohara et al., 2006; Kontgers et al., 2010). Although extensive work is carried out for optimizing the scribing qualities, the physical phenomena responsible for film removal during laser scribing and their effects on scribe quality are not well known. In addition, development of simulation capabilities will enable the fundamental understanding of the physical mechanisms and optimize the scribing processes instead of relying on trial-and-error experiments. To date, only rudimentary modeling efforts have been made, offering no predictive or optimization capabilities. Wang et al. 2003, developed two-dimensional thermal model to estimate the temperature distribution of CdTe-based thin film solar cells by ns laser pulses irradiated from the glass side, and simulated the film removal during micro-explosion process. However, the model does not consider the dynamic response of brittle materials during this high-velocity shock wave impact, and it also offers no experimental validations.

Based on the current thin-film solar cell technology, a 1% increase in efficiency from improved scribe quality equates to roughly a 10% reduction cost. Therefore, understanding the film removal mechanisms and characterizing the potential defects during laser scribing processes are important for the cost reduction of thin film solar cells. In the previous work (Wang et al. 2013), P1 scribing of TCO layer has been studied. P2 and P3 are similar processes, since both are under micro-explosion mechanism with the plasma occurs at the interface between absorber and TCO layers. In this study, P2 scribing of CdTe-based solar cells is carried out using a 532nm-wavelength 9ns-pulse-duration laser irradiated from glass side at different fluences and scribing

speeds, and the corresponding scribe geometry, induced defects and the sheet resistance of TCO layer after scribing are characterized. A two-dimensional numerical model, implemented with dynamic response of brittle material, is developed to simulate film removal via a micro-explosion process. The scribe geometry is studied by scanning electron microscopy (SEM) and optical profilometry, and removal cleanliness is estimated by energy-dispersive x-ray spectroscopy (EDX). The sheet resistance is measured through four-point probe method. Film microstructures and laser-induced defects are characterized by transmission electron microscopy (TEM).

6.2 Background

6.2.1 Laser Induced Defects and Their Effects on Solar Cells

Laser processing has been incorporated into many successful modifications of the properties of semiconductor materials in solar cells applications. For example, Tull et al. 2006 and Wang et al. 2012a, 2012b, have reported laser surface texturing induced optical property change of crystalline silicon and amorphous silicon. Compaan et al. 2000, has investigated laser scribing on different contact and absorber layers in order to change their electrical property. However, the quality of the laser treatment is often limited by the generation of defects which have adverse effects on solar cell performance through increased junction shunting or recombination centers. Due to the unique mechanical fracture caused by the micro-explosion process, defects as atomic structural change, micro cracks/voids and film delamination are induced resulting in poor photocurrent and inactive cells. Incomplete film removal is also observed causing an increase in contact resistance between the metal and TCO layers, which leads to less output power (Borrajo et al. 2009). Lauzurica et al. 2011, reported the formation of irregular scribe boundaries and

observed film peeling after ns-pulsed, P3 laser scribing of a-Si thin film solar cells. Tamaoki et al. 2010, showed the formation of micro-cracks and film delamination after scribing of a molybdenum film on a glass substrate using an ns-laser. Even the use of ultra-short pulse-duration lasers, has not shown the ability to eliminate defects such as film delamination (Gecys and Raciukaitis, 2010). Kontgers et al. 2010, have investigated the risk of power loss, up to 10%, in photovoltaic modules due to micro cracks induced inactive cells, and pointed out that the micro cracks can be continually opened up subjected to the mechanical and thermal stress. Acciani et al. 2010 have examined the abnormal heating in the restricted area of solar cells due to the presence of defects, such as voids, causes hot-spots, and the increased temperature will introduce dead cells in the solar panel.

Defects generation can also be introduced by laser-induced thermal effect. Golovan et al. 1996, investigate the defect formation in CdTe under laser-induced melting process and showed a decrease of photoreflectance due to the formation of electrically and recombination active defects. In addition, when the laser power density is high enough, the TCO layer underneath the absorber will be thermally damaged as well, which could lead to shunt resistance decrease and current leakage. Furthermore, when the laser photon energy is higher than the band gap of semiconductors, defect formation of recombination centers can be also introduced even at low laser fluences (less than the melting threshold). Emel'yanov et al. 1992, show that the fraction of the energy of the photo-excited electron-hole pairs is transferred in the process of electron-phonon relaxation and heat the lattice. The strong rise in temperature T (up to melting point) leads to the generation of defects by thermo-fluctuation, which are frozen in after the end of the

pulse due to the very rapid cooling process. The density of the thermo-fluctuation defects reaches its stationary value

$$N_d = const \cdot \exp\left[-\frac{E_A}{K(T_0 + \Delta T)} \right] \tag{6.1}$$

where T_0 is the initial temperature, ΔT is the temperature rise due to laser heating, E_A is the defect formation energy, K is Boltzmann constant. This equation describes the generation of vacancies (Schottky defects), the annihilation and the formation of defect complexes and other defects (Emel'yanov and Kashkarov, 1992). The lattice deformation caused by the heating reduces the value of the defect activation energy in Eq. (6.1). The defect formation energy can also be reduced due to the localization of the electronic energy in some point of the crystal, which will decrease the potential barrier of the defect transition to a new equilibrium position. Thus, the localization of the electronic excitation on some initial defect can introduce new centers due to the process of defect multiplication.

6.2.2 Dynamic Response of Brittle Materials

Due to the short duration of the laser pulse, film removal always occurs in nanosecond scales. This high-velocity pressure impact on CdTe will cause a high strain rate during laser scribing. Therefore, an assessment of the inelastic behavior including strain-rate phenomena, material degradation and pressure hardening needs to be considered. Micromechanical-based approach typically starts with the behavior of a single defect (crack or void) and the continuum level model is obtained by applying statistical averaging to an ensemble of defects (Addession and Johnson, 1990). Johnson and Holmquist (JH) (Holmquist and Johnson, 1994 and 2005) reported extensive work on brittle material response to high velocity impacts. The JH models use experimental data to determine constants that describe inelastic material behaviors in the

simulation, and they are more convenient to be implemented in finite-element models than the theoretical statistical calculation.

There are two variations of the JH models. Compared to the first version (JH-1), the second version (JH-2) incorporates a damage evolution rule by consideration of progressive damage with increasing deformation, which is more accurate for simulating the high-velocity impact performance of ceramics (Holmquist and Johnson, 1994). In JH-2 model, the strength of the material is expressed in terms of the normalized von Mises equivalent stress as

$$\sigma^* = \sigma_i^* - D(\sigma_i^* - \sigma_f^*) \tag{6.2}$$

where σ_i^* is the normalized intact equivalent stress, σ_f^* is the normalized fractured equivalent stress, and D is the damage variable. The normalized equivalent stresses (σ^* , σ_i^* , σ_f^*) have the general form $\sigma^* = \sigma / \sigma_{HEL}$,where σ is the actual von Mises equivalent stress and σ_{HEL} is the equivalent stress at the Hugoniot elastic limit (HEL). The model assumes that the normalized intact and fractured stress can be expressed as function of the pressure and strain rate as

$$\sigma_{\mathrm{i}}^* = A(p^* + T^*)^N \left[1 + C \ln \dot{\varepsilon}^*\right] \le \sigma_{\mathrm{i}}^{\max} \tag{6.3}$$

$$\sigma_f^* = B(p^*)^M \left[1 + C \ln \dot{\varepsilon}^*\right] \le \sigma_f^{\max} \tag{6.4}$$

where *A, B, C, M, N* are material constants, $\sigma_i^{\max}$ and $\sigma_f^{\max}$ are the optional limits. The normalized pressure, p^*, and normalized maximum tensile hydrostatic pressure, T^*, are defined as $p^* = p / p_{HEL}$ and $T^* = T / P_{HEL}$, where P, P_{HEL}, T are the actual pressure, pressure at the HEL and maximum tensile pressure that the material can withstand.

The damage initiation parameter, ω, accumulates with plastic strain according to

$$\omega = \sum \frac{\Delta \varepsilon^p}{\varepsilon_f^p(P)} \tag{6.5}$$

where $\Delta\varepsilon^p$ is the increment in equivalent plastic strain and $\varepsilon_f^p(P)$ is the equivalent plastic strain to fracture under constant pressure, defined as $\varepsilon_f^p = D_1(P^* + T^*)^{D_2}$, where D_1 and D_2 are constants. JH-2 model assumes that the damage variable increases gradually with plastic deformation by setting $D=\omega$.

The equations for the pressure-density is described as

$$p(\zeta) = k_1\zeta + k_2\zeta^2 + k_3\zeta^3 + \Delta p \text{ ; compression} \tag{6.6}$$

$$p(\zeta) = k_1\zeta \text{ ; tension} \tag{6.7}$$

where $\zeta=\rho/\rho_0-1$ and Δp is an increment in the pressure and k_1, k_2, k_3 are material constants. The increment in pressure arises from the conversion of energy loss due to damage into internal energy.

6.3 Experimental Setup

Polycrystalline TCO (SnO_2:F) films were deposited on a 3.2mm-thick soda lime substrate using chemical vapor deposition (CVD) at 600ºC. Stack layers of polycrystalline CdS and CdTe were then sequentially thermally evaporated at 350ºC substrate temperature. Film thicknesses of TCO, CdS and CdTe layers were about 400nm, 200nm and 2μm, respectively.

Experiments were carried out using a Nd:YAG laser. The system delivered 9-ns pulses at a 100Hz repetition rate and a wavelength of 532nm. The samples were cleaned with acetone in an

ultrasonic cleaner for 5 minutes and then rinsed with methanol and distilled water prior to processing. The sample was placed inside a metallic container sealed with quartz at both top and bottom to avoid hazardous plume during laser processing and collect the removed materials. This container was mounted on a three-axis translation stage and samples were irradiated by laser focused by a 20X objective lens. The focal plane was placed at the interface between TCO and CdS to create a circular beam spot with a diameter of around 50μm. The samples were irradiated from the glass side by single pulse with various fluences from 0.4 to 6 J/cm^2 at a stationary spot, and then scribed with the fluence values from 1 to 4 J/cm^2 at different speeds (1 to 4 mm/s). Regarding to the sheet resistance measurement, scribing areas of 5mm by 20mm were processed under different fluences (1 to 6 J/cm^2), a scribing speed of 2mm/s and 50% overlap between each scribing lines.

The treated samples were observed through SEM. Surface roughness and scribe profiles were measured by optical profilometry. The chemical components and cleanliness of laser processed samples were investigated by EDX. The sheet resistance was measured through four-point probe method. The generation of defects, such as material microstructure, micro cracks/voids and thermal effect after irradiation were analyzed by TEM.

6.4 Results and Discussion

Figure 6.1 shows the schematic of P2 laser scribing on CdTe-based solar cells from the glass side under micro-explosion mechanism. The removal mechanism can be divided into three steps: first, the laser has been absorbed by the entire and partial layers of CdS and CdTe, respectively. The absorption depths of CdS (film thickness of 200nm) and CdTe (film thickness of 2 μm) at

the wavelength of 532nm are ~1μm and 167nm, respectively. Second, as the pulse continues heating, the material in the absorption volume has been melted, vaporized and finally formed a plasma. Due to the confinement of substrate and solid CdTe, an intensive pressure induced by the plasma expansion will pull the solid CdTe material upwards and to delaminate from CdS layer. This is because the adhesion between CdS and CdTe layers is smaller than that between SnO_2:F and CdS layers due to the differences of their thermal expansion coefficients, i.e. thermal expansion of CdTe, CdS and SnO_2:F are 5.9×10^{-6}, 4×10^{-6} and 4×10^{-6}/K, respectively (Hodges et al. 2009). Third, the deformed solid CdTe layer has been removed due to brittle fracture and the ablated material is also ejected with the pressure release to the ambient. Some resolidified molten CdS and undamaged CdS materials remain after the removal process. Due to the weak adhesion between CdS and CdTe, there is no CdTe has been melted at the boundary. In contrast, CdS removal is dominant by ablation. Therefore, thermal effect only occurs at this layer.

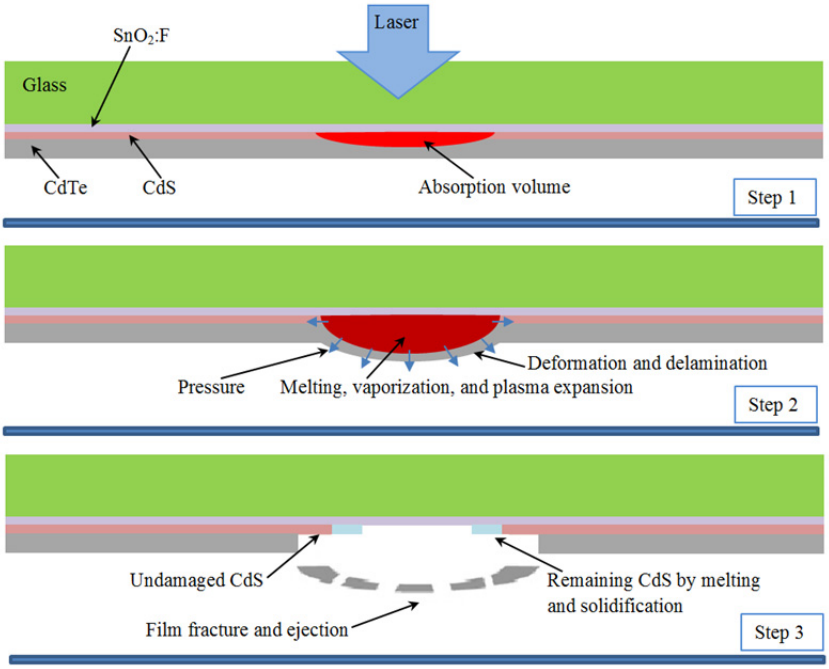

Figure 6.1 Schematic of film removal of P2 laser scribing on CdTe-based solar cells under micro-explosion mechanism

6.4.1 Film Removal by Single Pulse Irradiation

6.4.1.1 Scribe Geometry and Defect Characterization at a High Fluence

Figure 6.2 (a) shows the SEM image of film removal by single pulse irradiated at a fluence of 3 J/cm^2. It can be seen that a near-circular area with a diameter of around 75μm is scribed. A macro-crack occurs along the circumference of the scribed area. Magnified SEM image Fig. 6.2 (b) shows clearly that the macro-crack occurs at the boundary is partially broken, which may be due to the non-uniform beam energy distribution of the laser spot. The material at the central area with a high energy distribution has been removed faster than the surrounding area, and then the trapped pressure between the film and substrate is released quickly. Therefore, the significantly reduced pressure is not strong enough to facture the rest CdTe material, instead, the pressure makes CdTe delaminate from the CdS layer and form as a macro-crack after processing. It is also observed that some material remains, which may include the undamaged CdS material and solidification of a liquid flow driven to the boundary by plasma expansion. Since the molten CdS layer is much thinner than the thickness of removal films, and the pressure distribution at the boundary is almost parallel to the film surface due to the film deformation, thus, most of the molten CdS material can be pushed to the boundary. This is why from the optical profilometry measurement along line A shown in Fig. 6.2(c), the circle B area shows a gradual increase to the boundary and the highest point occurs at the interface of solid/liquid CdS. Circle A shows the appearance of the macro-crack of CdTe film, and the reason why no delamination can be seen is because the detecting optical beam is perpendicular to the samples, so that the gap at the CdS/CdTe interface cannot be measured. The depth of film removal is measured to be 2μm at the scribed center, and vertical sidewalls are formed after processing. EDX line profile scan along A is shown in Fig. 6.3. It can be seen that no other elements except Si and Sn in region B, which

indicates that CdS and CdTe are completed removed in this region and no inter-diffusion of S into the TCO layer. The co-existing of Si and Sn is due to the larger electron penetration depths of SnO_2:F compared to its thickness (Wang et al. 2013). In region A (~10μm) – macro-crack broken area, elements of Cd and S are detected besides Sn and Si. This demonstrates that the only CdS remains, which matches the mechanism described in Fig. 6.1 that higher adhesion occurs at the interface between CdS and TCO layers.

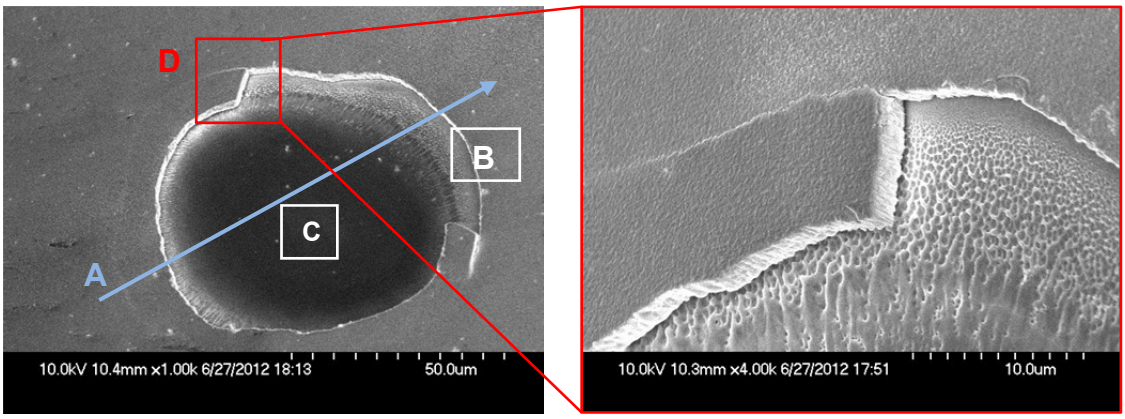

(a) (b)

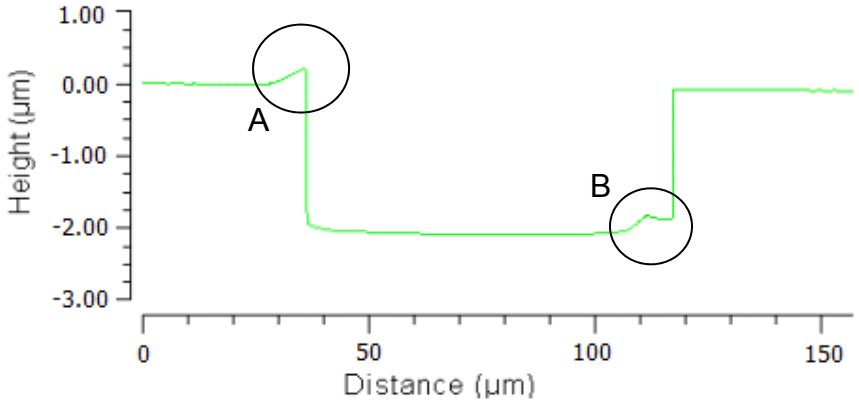

(c)

Figure 6.2 (a) SEM image of film removal by a pulse irradiated at a fluence of 3J/cm^2; (b) magnified SEM image at square D; (c) Optical profilometry measurement along A

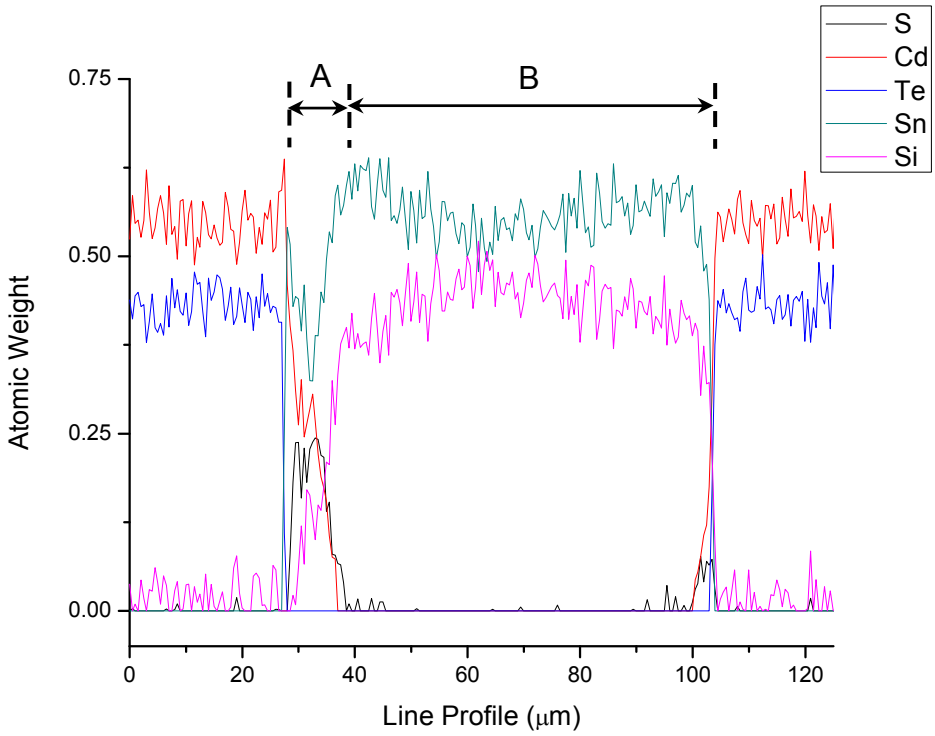

Figure 6.3 EDX line profile scanning along A in Fig. 6.2 (a), showing a clean removal at the center, and small amount of remaining material is CdS and no inter-diffusion occurs at the interface of TCO/CdS

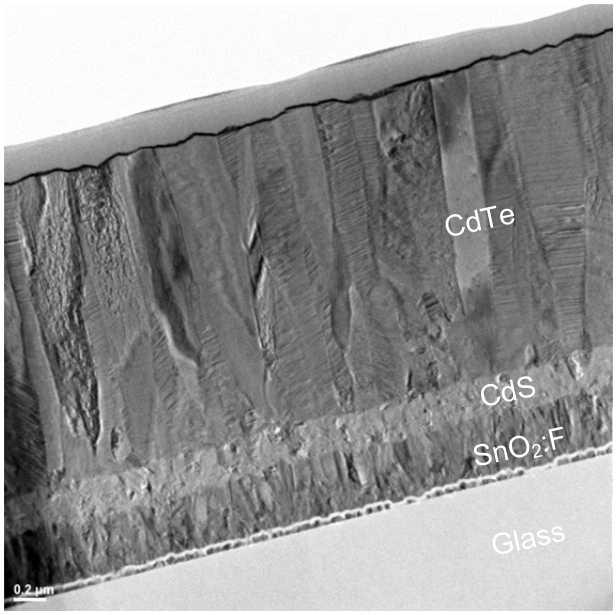

Figure 6.4 Cross-sectional TEM image of as-received CdTe/CdS/TCO/Glass samples

Figure 6.4 shows a cross-sectional TEM image of as-received samples. The thickness of CdTe, CdS and TCO layers are measured to be 1.85μm, 230nm and 430nm, respectively, which are close to the deposition estimation. CdTe grains grow epitaxially on CdS grains with a dominant orientation of (111) and the columnar CdTe grains with micro-twins results in a poor photocurrent and high series resistance (Luque and Hegedus, 2003). Vere et al. 1983, show that twinning is an intrinsic feature of the zincblende-structure materials with low stacking fault energy, such as II-V (CdTe) and III-V semiconductors. It originates on the liquid/solid interface during growth, where group of atoms deposited at a point or points on the interface are misorientated with respect to the reminder. Figure 6.5 depicts the cross-sectional TEM image at the scribe boundary B shown in Fig. 6.2 (a). It can be seen that CdTe is removed mechanically instead of thermal ablation. The pressure induced by plasma expansion causes the deformation of CdTe layer and delamination from the CdS layer. Brittle fracture sequentially occurs at high stress concentration points at the constraint boundary. Cracks initialize at the bottom of the CdTe layer and propagate to the top surface, since the deformed geometry of boundaries causes higher material strains at the bottom compared to the top surface. The crack propagates along the grain boundary (intergranular fracture) at the bottom, because impurities usually segregate at the CdS/CdTe interface in the beginning of deposition, which weaken and embrittle the grain boundaries. When crack propagates to the top surface, it passes through grains (transgranular fracture) by cutting across twins. This may be caused by the direction change of the applied stress due to the film deformation and grain geometries. The stress could lead to the secondary crack along the twin boundaries and form a zig-zag scribe boundary (Hughes et al. 2007). The atomic bonding energy becomes smaller for the atoms near the top surface, and a lateral nano-crack occurs at this point simultaneously. Figure 6.6 (a) shows that the remaining CdS layer near

the sidewall has the same microstructure and thickness compared to the undamaged CdS in Fig. 6.4. Likewise, the TEM image of Fig. 6.6 (b) taken at the scribe center (region C in Fig. 6.2 (a)) exhibits that only SnO_2:F layer remains. There is no SnO_2:F has been damaged after scribing by comparing the microstructure and the material thickness. Therefore, it can be concluded that CdS material has been ablated in the laser effected area. In the meanwhile, CdTe delaminates from CdS layer and is removed due to the brittle fracture caused by the plasma-induced pressure. The thermal effect only occurs at the layer of CdS and no damage of SnO_2:F or inter-diffusion of sulfur is observed after processing.

Figure 6.5 Cross-sectional TEM image of scribe boundary at square B shown in Fig. 6.2 (a), showing micro-crack is formed near the top surface at the scribe sidewalls

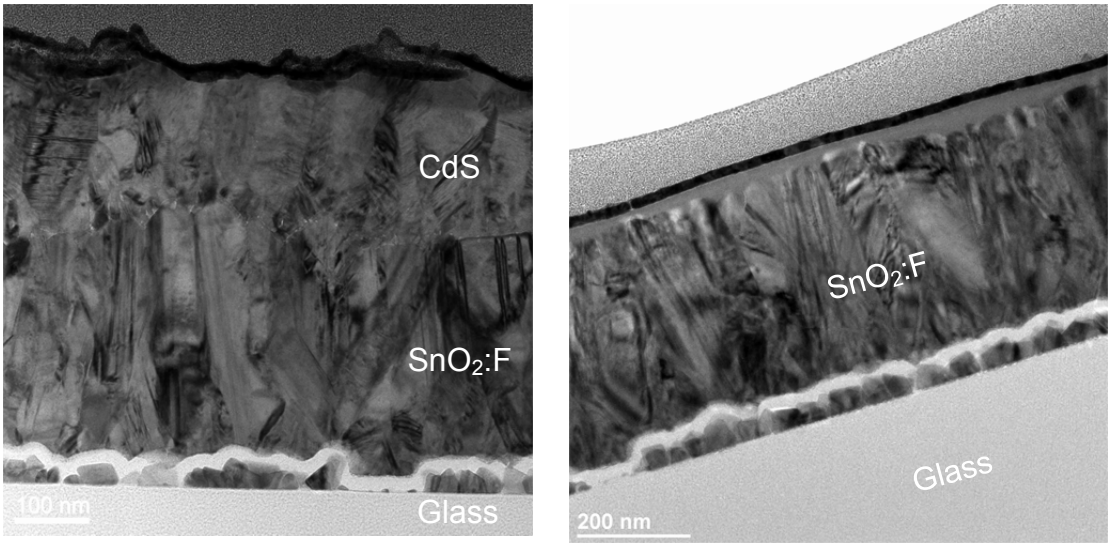

(a) near scribe boundary (b) scribe center

Figure 6.6 Cross-sectional TEM images of (a) near scribe boundary B and (b) scribe center region C in Fig. 6.2 (a)

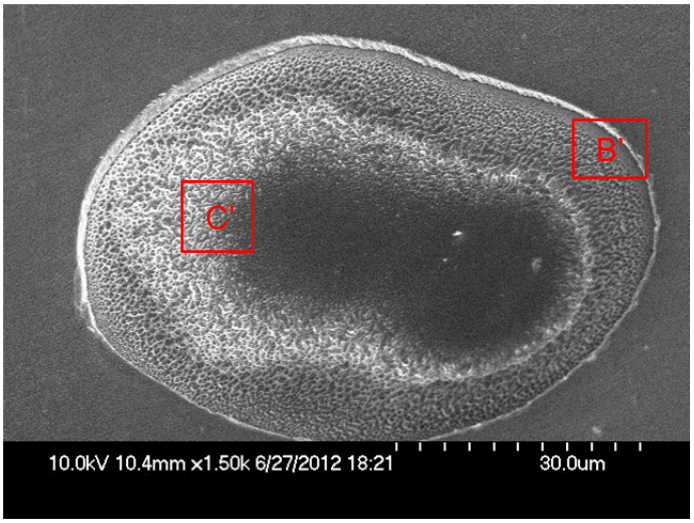

Figure 6.7 SEM image of film removal by a pulse irradiated at a fluence of 1J/cm^2, showing much more CdS remaining after processing compared to that processed at a fluence of 3J/cm^2

6.4.1.2 Scribe Geometry and Defect Characterization at a Low Fluence

Figure 6.7 shows the SEM image of film removal irradiated by one pulse at a fluence of 1J/cm^2. It can be seen that a circular scribed area with a diameter of around 60μm with much more remaining CdS material (determined by EDX, not shown) compared to that scribed under 3J/cm^2. In addition, no macro-crack is observed in this condition. This could be caused by a longer response time of CdTe film deformation at a lower fluence, and CdTe film will delaminate more from CdS substrate and the film at the boundary and center break at the same time. In order to understand the removal mechanism, cross-sectional TEM images at the scribe boundary B' are carried out as shown in Fig. 6.8 (a). It can be seen that a micro-crack and some nano-voids appear at the CdS/CdTe interface. The CdTe layer under a lower fluence needs more time to be completely fractured. Thus, when a crack initializes at the bottom and starts propagating to the top surface, there is enough time for the pressure to causes a lateral delamination and several nano-voids along the interface of CdS and CdTe due to the weak adhesion before the entire layer has been removed. Similarly to the film removal at 3J/cm^2, the remaining CdS is not thermal affected at the removal boundary and vertical sidewalls are formed. Figure 6.8 (b) shows the magnified TEM image near delamination tip. It can be observed that the high stress concentration at the tip causes change of atomic structures at both CdS and CdTe grain boundaries and interface. Moreover, nano-cracks are founded around the nano-voids (not shown). These phenomena suggest that those dislocation slips, caused by the atomic structure rearrangements, may play an important role on the further crack initiation and propagation (Hai and Tadmor, 2003) and then reduce the power output resulting in a long-term instability.

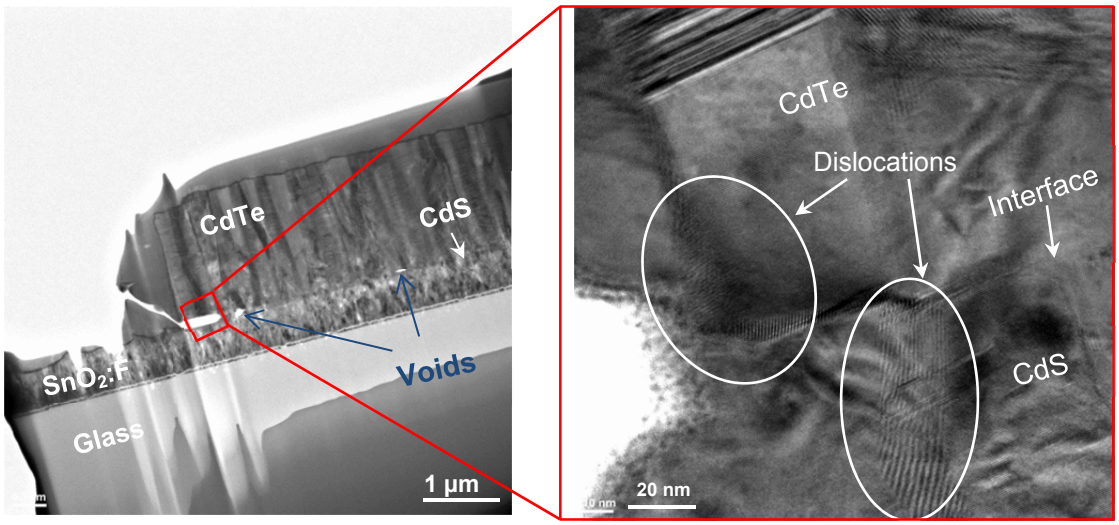

(a) (b)

Figure 6.8 Cross-sectional TEM images of (a) scribe boundary at square B' shown in Fig. 6.7 and (b) magnified image at the delamination tip, showing dislocations formed at both between the two layers and grains which may introduce further crack initiation

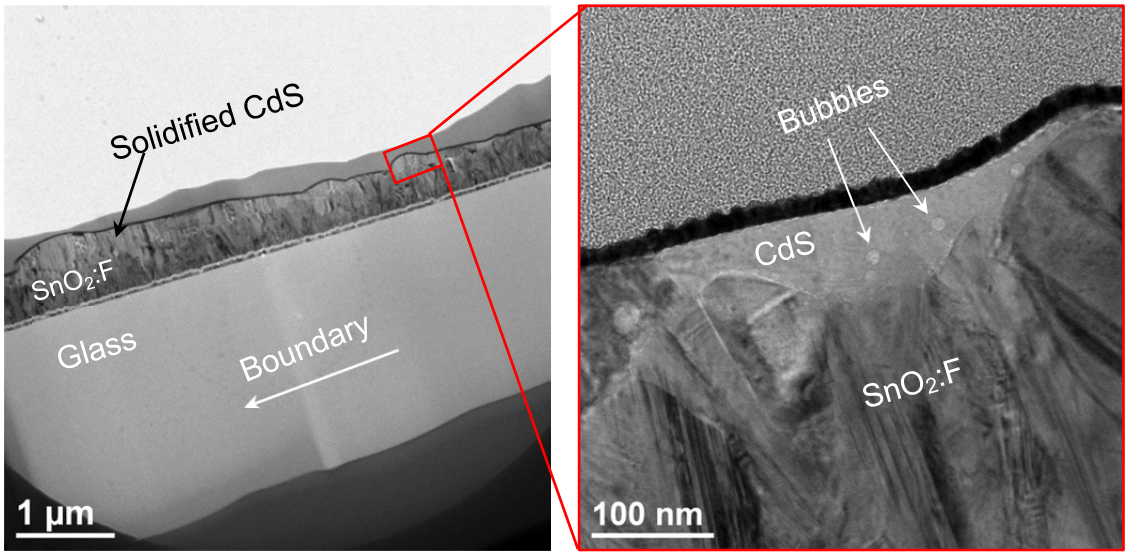

(a) (b)

Figure 6.9 (a) TEM images taken at region C' in Fig. 6.7 and (b) magnified TEM image at the interface between CdS and SnO_2:F layers, showing nano-bubbles formed due to the oxidation of sulfur during the laser processing

Cross-sectional TEM image taken at region C' in Fig. 6.7 is shown in Fig. 6.9 (a). It can be seen that both microstructures and thickness of CdS layer has been changed due to the thermal effect. The arrow shows the direction to the removal boundary. The molten CdS material solidifies and the grain grows vertically from SnO_2:F layers near the boundary, however, the grains close to the center shown in Fig. 6.9 (b) exhibit different microstructures and nano-bubbles near the interface. The grain size in this region is much smaller (a few nanometers) based on high-resolution TEM investigation (not shown). The thermal gradient in the molten pool drives the motion of liquid CdS provoking the deformation of the surface, and the pressure differences created at a curved interface support the evolution of the deformation on the liquid surface known as capillary waves (Wang et al. 2012a). However, due to the plasma expansion and micro-explosion process, the pressure propagated along horizontal direction pushes more liquid CdS to the boundary and forms the different amplitudes along the capillary wave. The liquid CdS close to the center under stronger pressure travels a longer distance, thus, there is no enough time for a similar recrystallization process to that happened near the boundary. Moreover, decomposition of CdS occurs due to the high temperature, and sulfur can be quickly oxidized and formed as gaseous phase. Sulfur oxide either evaporates to the environment or stay inside the CdS matrix to form as bubbles after solidification.

Overall, scribing under both two fluences can achieve a complete film removal and no damage of SnO_2:F or interdiffusion of sulfur occurs after processing. However, some CdS remains and partial of the material has been molted and recrystallized. This will affect the next-step contact layer deposition in the solar cell fabrication process. In addition, the ultra-fast heating process could introduce supercooling during recrystallization, which causes defects as recombination

centers and reduces the photocurrent density. Moreover, the bubbles formed by sulfur oxide will also introduce abnormal heating and eventually damage the cells (Acciania et al. 2010). Scribing under a high fluence can cause macro-cracks due to the pulse imperfection and micro-cracks near the top surface which may decrease the active area of absorber layers. However, scribing under a low fluence can lead to more remaining CdS material, which can cause a higher increase of contact resistances between TCO and metal layers. The film delamination will lead to an increase of inactive cells.

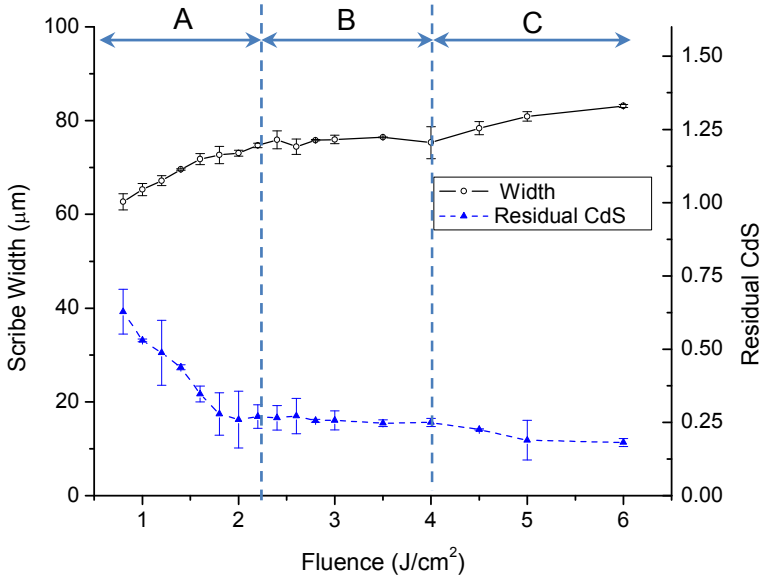

Figure 6.10 Dependence of scribe area and remaining CdS on laser irradiation conditions, error bars represents standard deviation

In order to understand the relationship between the induced defects and scribing conditions, a parametric study is carried out on the irradiation fluences (0.8J/cm^2 to 6J/cm^2) as shown in Fig. 6.10. Since the pulse shape is irregular, normalized diameters are calculated through the measurement of scribe areas. From the observation under SEM and optical profilometry, the threshold for complete removal is 0.8J/cm^2. The scribe diameter increases with the increasing fluence at range A (0.8 to 2.2J/cm^2) and keeps a constant around 75um at range B (2.2 to 4J/cm^2)

and then increase at fluence range C (4 to 6J/cm^2). This difference is because in the low fluence range, the film breaks at both boundary and center at a close time interval due to the longer removal time. In contrast, the center is removed much faster than the boundary when the fluence reaches a center threshold, and the reduced pressure cannot delaminate more CdTe material from CdS layer. The trend of scribe diameter increases again at fluence range C. This is due to absorption volumes become larger under higher fluences, therefore, the sequential plasma volume increase and more material will be removed. In addition, the increased pressure in lateral direction could cause solid CdS and CdTe material to fracture, which leads to an increase of scribe areas. The percentage of residual CdS area linearly decreases with increasing of fluences at the low fluence range A, and keeps a constant at fluence range B, and finally slightly decreases at the fluence range C. The laser-induced pressure becomes larger and larger with increasing fluences during micro-explosion processes, thus, more liquid CdS is driven to the boundary and less CdTe delaminates from the CdS layer due to faster brittle-fracture responses. Until the pressure reaches a threshold, all liquid CdS moves to the boundary and cannot flow out of the removal cavity by the prevention of CdTe layer.

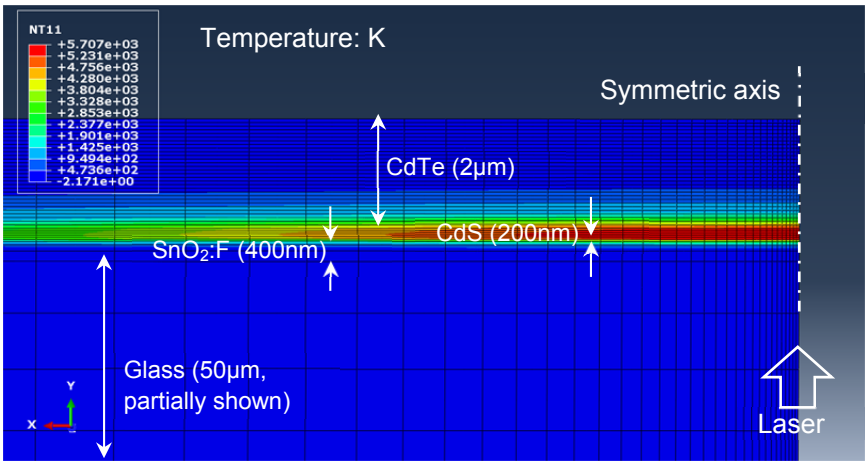

Figure 6.11 Simulation result of temperature distribution of CdTe/CdS/SnO_2:F/glass multilayer thermal model at a fluence of 1J/cm^2

6.4.2. Numerical Investigation on Film Removal and Defect Formation

Two-dimensional thermal and mechanical models are setup based on the previous study (Wang et al. 2013), except adding a CdS layer in the thermal model to determine the plasma volume and considering dynamic response in CdTe fracture criteria. Figure 6.11 shows the temperature distribution of CdTe/CdS/SnO_2:F stack layers on glass substrate as a result of the glass-side laser irradiation at a fluence of 1Jcm^2. The thicknesses of different layers are 2μm, 200nm, 400nm and 50μm, respectively. The laser pulse is 9ns in duration, Gaussian-distributed, 50μm in spot size and 532nm in wavelength. The thermal analysis is carried out with the consideration of energy loss due to the reflection at the interfaces of glass/air, glass/SnO_2:F and SnO_2:F/CdS, heat convection at the boundary, as well as the absorption by the glass substrate and SnO_2:F layer. Material properties can be found in ref. (Wang et al. 2013). It can be observed that the absorbing volume is confined between the CdTe and SnO_2:F layers, and the temperature is almost uniformly distributed in CdS layer due to its absorption depth and thickness as discussed before. This highly confined energy increases temperature up to 8000K at this condition, which is higher than the vaporization temperatures of both CdTe and CdS, therefore, plasma has been generated. The temporal and spatial distributions of plasma-expansion-induced pressure are then calculated based on ref. (Wang et al. 2013) and the constant fraction α is kept 0.04 to match the removal threshold compared to experimental results. Figure 6.12 shows the highest temperature of TCO layer at different conditions for estimating its thermal damage. The temperature is recorded when the film starts detaching from the TCO layer which is determined through the mechanical model, since there is no film deformation considered in the thermal model. It can be seen that the TCO temperature increases with the increasing of fluences and reaches the melting temperature at a fluence of 5.5J/cm^2.

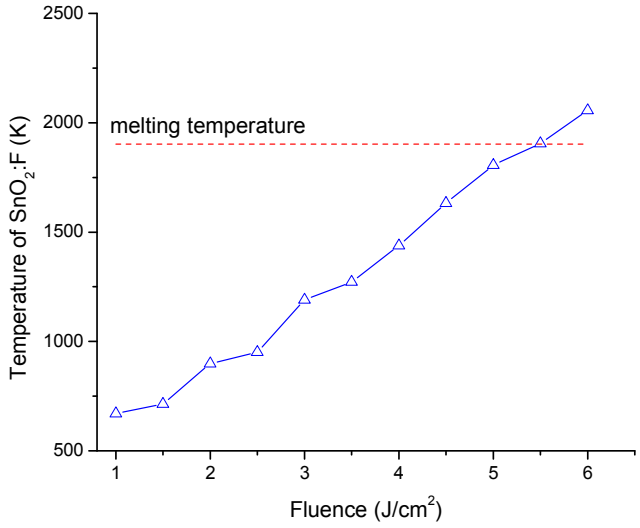

Figure 6.12 Simulation results of dependence of SnO_2:F (TCO) temperature on fluence, showing the TCO layer will be damaged when the fluence reaches 5.5J/cm^2

Film removal is presented in a mechanical model with the pressure incorporated on CdTe layer at the interface. A 10nm-thick layer of cohesive elements is implemented to consider the traction stresses at the interface. The cohesive layer is governed by the traction separation law described in (Wang et al. 2013), and serves the purpose of simulating the process in which the CdTe film lifts up and delaminates from the CdS layer caused by the plasma expansion. In order to simplify the problem, CdS is neglected from the mechanical model. Because CdS layer is dominantly removed by ablation based on experimental results, there is no effect of mechanical fracture on this layer during micro-explosion process. Since adhesion becomes zero at the plasma area, an open cavity at the center of the cohesive layer, representing plasma width, is implemented. The values of plasma width are extracted from the thermal model. The pressure is applied at the interface of CdTe and cohesive layer, and the pressure is set to be zero when the film is broken during the calculation and the boundaries are fixed.

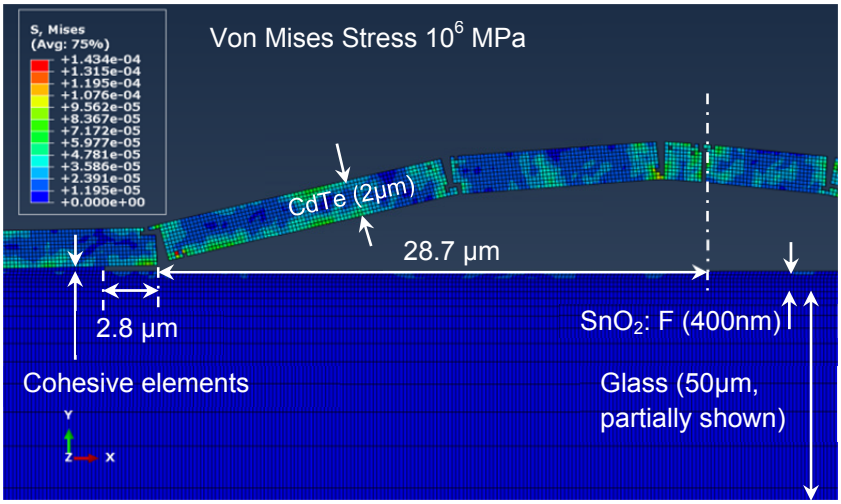

Figure 6.13 Complete film removal with a fluence of 1J/cm^2 at 97.9ns, the scribe radius is 28.7μm and delamination is 2.8μm through the interface

Figure 6.13 shows the complete film removal with a fluence of 1J/cm^2 at 97.9ns. It can be seen that a scribe area with a radius of 28.7μm and a delamination of 2.8μm at the interface. Therefore, film delamination occurs compared to the initial plasma width of 41.6μm. This matches the experimental result as shown in Fig. 6.8 (a). The simulation result shows that the strain rate of failed elements is up to $10^5 s^{-1}$. Therefore, the material dynamic response is necessary to be implemented. The film is removed mainly due to the tensile stress, and the strain-rate-dependent response has much less influence on the tensile yield stress than the compressive yield stress for brittle materials. However, the implemented criteria can still affect the compressive failure and lead to more accurate element deformations compared the static fracture laws. The film deformation causes tensile stress to the elements at the top center and bottom boundary. Therefore, the fracture occurs preferentially at these points. Since the pressure is not strong enough to break the entire layer immediately, a further delamination along the interface occurs due to its weak adhesion. The film still remains large pieces when the removal is completed and the breaks occur at both center and boundary. Figure 6.14 shows the complete

film removal at a fluence of 3J/cm^2. It can be seen that a scribe area with a radius of 34.8μm (plasma width is 58.8μm) and this removal takes 76.8ns, which occurs faster than that happened at 1J/cm^2. Similarly, initial fractures occur at the bottom boundary and top center. However, since the pressure is strong enough to cause further deformation, some elements between the boundary and center also achieve their fracture limit. Likewise, more and more elements between those "pre-fracture" points fail and finally, the film becomes many small pieces after removal. At the boundary, micro-cracks with a length of 1.4μm occur near the top surface rather than at the interface. During the crack propagates through the boundary from bottom to the top, the stress induced by the pressure and film deformation is strong enough to fracture their neighboring elements so that the micro-crack preferentially occurs at a relatively weak bonding area near the top surface, which has been presented in Fig. 6.5.

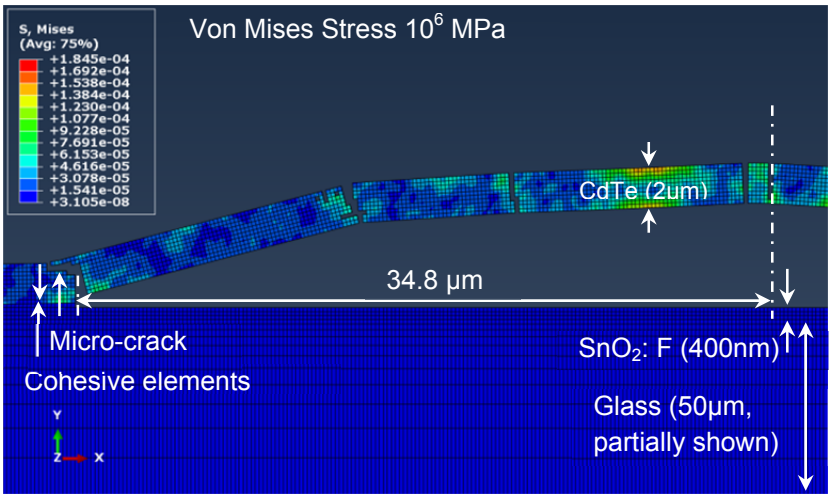

Figure 6.14 Complete film removal with a fluence of 3J/cm^2 at 76.8ns, the scribe radius is 34.8μm and micro-crack with a length of 1.4μm occurs near the top surface

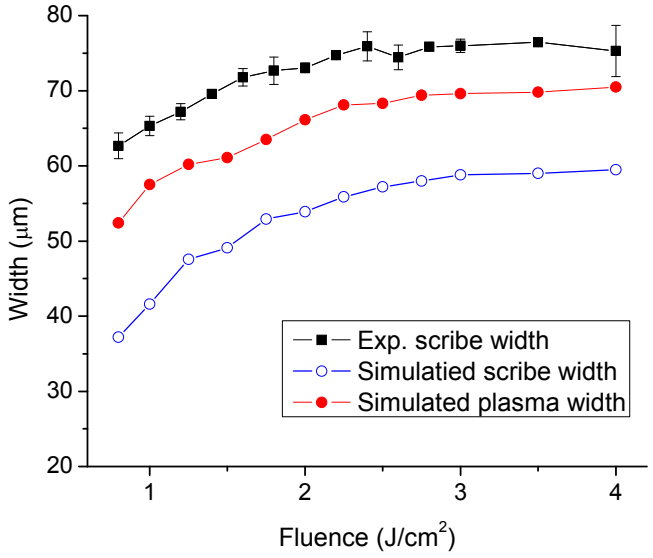

Figure 6.15 Comparison of experimental and simulation results on scribe width, error bars represents standard deviation

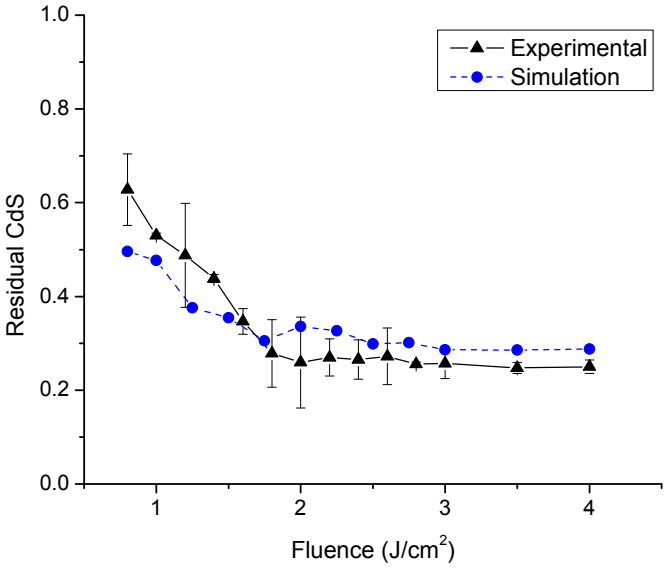

Figure 6.16 Comparison of experimental and simulation results on residual CdS, error bars represents standard deviation

Figure 6.15 and 6.16 show the simulation results of dependence of plasma width, scribe diameter and remaining CdS on laser irradiation fluences. Since the pressure is only applied vertically in the mechanical model, much less pressure in lateral direction in the simulation, thus, the model cannot well predict the lateral material fracture when the fluence is larger than 4J/cm^2 as shown in Fig. 6.10. In addition, these increased scribe widths at higher fluences enlarge the dead zone. Therefore, a narrower fluence range (0.8J/cm^2 to 4J/cm^2) is taken in the simulation. It can be seen that the plasma width increases to around 55μm at 2.5J/cm^2 and maintains almost a constant afterwards. Compared to the spot size (50μm), only 2.5μm-wide CdS material in lateral direction has reached the vaporization temperature beyond the laser irradiation area. This presents the laser-induced heat can only be transferred laterally close to CdTe film thickness (2μm), because it is dissipated quickly to the ambient at the top of CdTe layer. Therefore, the plasma width increases much slowly when it reaches the spot size. The simulation result shows the scribe diameter has a similar trend to that of plasma widths. At the low fluence range, more CdTe material delaminates from the layer underneath since it takes more time for the film to deform before entire layer is fractured. In contrast, at the high fluence range, the scribe width keeps a constant, because the pressure is strong enough to fracture the entire film immediately and there is no time to lead to further film deformation and delamination. The percentage of residual CdS material shows a similar trend to the experimental result, more CdS remains in the low fluence range and finally it keeps a constant in the high fluence range. The discrepancy of an underestimation at the low fluence range in the simulation could be caused by ignoring the thermal effect on the cohesive elements, since the adhesion decreases with the increasing of the temperature. The overestimation at the high fluence range could be due to the ignoring of the molten CdS movement by the lateral pressure. However, the overall fluence dependence on film

removal by micro-explosion is accurately captured by the simulation. Figure 6.17 shows the simulation results of crack and delamination lengths after laser scribing. It can be seen that the delamination exists when the fluence is lower than 2.5J/cm^2 and micro-cracks are remained at higher conditions. The delamination lengths are higher than that of the micro-cracks which shows the similar results of the cross-sectional TEM images. Those cracks and delamination will cause inactive cells and increase the dead zones. Therefore, a minimum crack length at a fluence of 3J/cm^2 is more desirable for the scribing conditions.

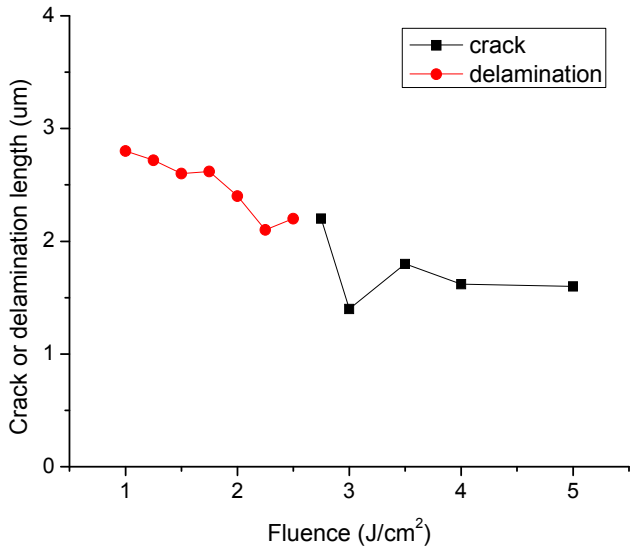

Figure 6.17 Simulation results of micro-crack and delamination lengths after laser scribing

6.4.3 Line Scribing and Sheet Resistance Measurement

In order to optimize the line scribing condition, samples are processed at the fluence values from 1 to 4 J/cm^2 with different speeds from 1 to 4 mm/s, which equivalent to the pulse overlapping from 80% to 20%. Among the complete removal conditions, the highest speed occurs at 2 mm/s under a fluence of 3 J/cm^2 as shown in Fig. 6.18 (a). It can be seen a clean line is formed in a width of ~75μm. Fig. 6.18 (b) shows that macro-cracks are removed by the next overlapped

pulse at the removal boundary. Although the scribing speed is not in the desirable range (m/s) due to the limitation of pulse repetition rate, the experimental results can still be referenced with different laser facilities based on the fluence and pulse overlapping.

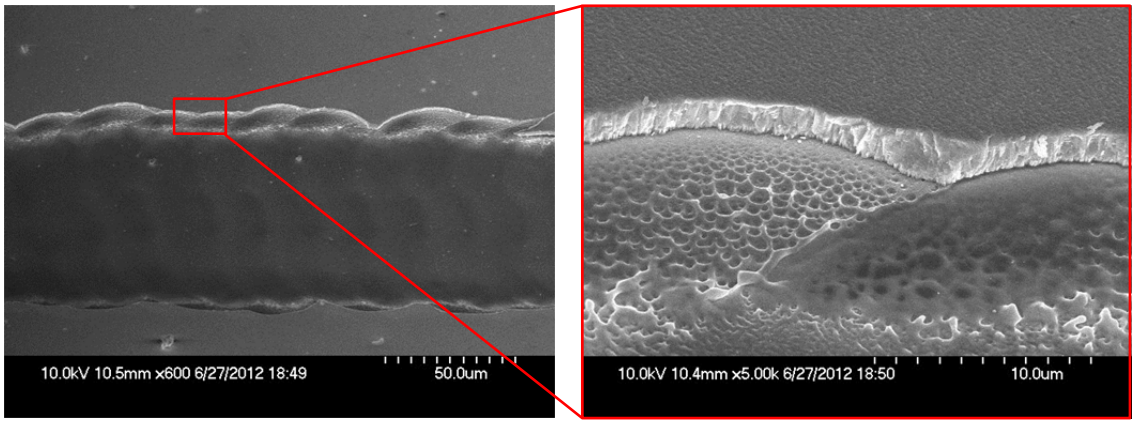

(a) (b)

Figure 6.18 SEM images of (a) line scribing at a fluence of 3J/cm^2 and a speed of 2mm/s, (b) magnified image at scribe boundary, showing macro-cracks are removed due to the pulse overlapping

Based on the line scribing results, an area of 5mm by 20mm is scribed with different fluences at a speed of 2mm/s and 50% line overlap. The sheet resistance measurement results are shown in Fig. 6.19. The sheet resistance measurement reflects the cleanliness of the laser scribing which will significantly affect the contact resistance between the further deposited metal layer and the TCO layer. Since contact resistance is partial of series resistance of a solar panel, the increased contact resistances in a large number of scribing lines will severely reduce the panel efficiency. Higher resistances can be caused by the residual material at lower fluences (1 J/cm^2 to 4J/cm^2) or the damage of TCO materials at higher fluences (5 J/cm^2 to 6J/cm^2). This TCO damage threshold is close to that of 5.5J/cm^2 predicted in the simulation shown in Fig. 6.12. The discrepancy could be caused by neglecting the heat conduction between the plasma and TCO layer after the film

detaching. It can be seen that the contact resistance achieves four orders of magnitude due to the damage of TCO materials compared to that at the lower fluence range. The contact resistance reaches the minimum value at 3J/cm^2, which is even a bit lower than that measured from TCO material only (samples of TCO deposited on glass substrate). Therefore, it can be concluded that the condition of 3 J/cm^2 with a scribing speed of 2mm/s is the optimal processing condition for P2 laser scribing of CdTe-based solar cells.

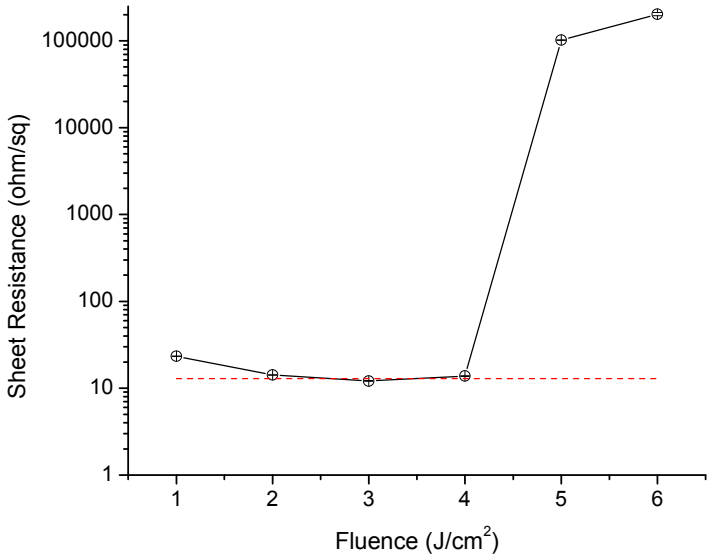

Figure 6.19 Dependence of sheet resistances on fluence. The high resistance at low energy range is due to the residual CdS, and high resistance at high energy range is caused by the TCO damage. Red dash line represents the sheet resistance of TCO material only and error bars represent standard deviations

6.5. Conclusion

In conclusion, it has been demonstrated that successfully selective film removal with well-defined sidewalls and little thermal effect is achieved by glass-side laser scribing of CdTe-based multilayer solar cells. The micro-explosion mechanism only leads melting and recrystallization on CdS layer, which could cause defect generation under the supercooling process. CdS material

is removed dominantly through ablation because its absorption depth is much larger than the thickness. In contrast, the rest of laser energy is fully absorbed by a shallow layer in the CdTe film. Due to the confinement of solid CdTe and the substrate, a shock wave is generated caused by the plasma expansion and CdTe material is removed through brittle fracture by the induced pressure. CdTe film delimitation from the CdS layer is also observed due to the weaker adhesion between these two layers compared to other interfaces, which will affect the next-step contact layer deposition in the solar cell fabrication process. Furthermore, other defects are characterized under both low and high fluence ranges. These defects, including nano-bubbles caused by sulfur oxidation, micro-cracks, dislocation formed at delamination tips due to the atomic structure rearrangement, could further induce abnormal heating and poor photocurrent. The optimal condition (with minimum defects at the scribe boundary and minimum sheet resistance in the scribe area) of glass-side laser scribing is determined to be at a fluence of $3J/cm^2$ with a speed of 2mm/s. The low scribing speed is limited by the pulse repetition rate; however, the experimental results are still valuable for the investigation on different required laser facilities. Finally, numerical finite element models are developed for P2 scribing based on micro-explosion mechanism. Good agreements with experimental results show that the simulation is capable of predicting the material removal dynamics and fracture behavior of CdTe.

Chapter 7: Conclusion

In this thesis, the state of knowledge of one-step laser surface texturing and crystallization of a-Si:H and laser scribing of CdTe thin films have been investigated. The understanding in the effects of pulse duration, processing medium and hydrogen on spike formation mechanisms, crystallinity and absorption capabilities on a-Si:H thin films has been considerably improved. In terms of laser scribing process, the selective film removal mechanisms of SnO_2:F and CdTe/Cds multilayers, as well as the laser induced-defect formation are analyzed through both experimental and numerical investigations, which is helpful to mitigate the defect formation and optimize the solar panel design. The major findings and contributions of each study are summarized below.

7.1 Laser Surface Texturing and Crystallization of a-Si:H Thin Films

7.1.1 Effect of Pulse Duration and Hydrogen on Spike Formation

Upon analysis of spike formation of laser surface texturing on a-Si:H thin films in air, femtosecond laser with a wavelength of 800nm and excimer nanosecond laser with a wavelength of 248nm are utilized. Since the band gap of a-Si:H is 1.7eV (730nm), the laser beam with a wavelength of 800nm cannot be directly absorbed by a-Si:H, thus, non-linear absorption occurs during the fs-laser-material interaction. A much narrower working window with lower fluences compared to crystalline bulk silicon is determined, in order to protect the damage and crystallization of the entire thin film. The micron-scale conical-shaped spikes are formed through ablation-dominant mechanism with their heights lower than the original surface. The average spike spacing and height are proportional to the laser fluence, and the spikes are taller, wider and

more sparsely distributed at the center than those at the exterior due to the spatial Gaussian distribution of the fs laser pulse.

In contrast to fs laser, excimer laser is directly interacted with a-Si:H. It is found that hydrogen molecules are formed due to the aggregation of H atoms through energy absorbing, and the sequential explosion will disturb the equilibrium of the molten pool. Capillary wave is then generated and periodic surface structure is formed after solidification. Afterwards, the conical-shaped spikes are grown by VLS (vapor-liquid-solid) mechanism until the height reaches a limit value (~2μm). The spikes are protruded from the original surface and the spike spacing keeps a constant since the laser pulse is spatially homogenized. Compared to the dehydrogenate a-Si samples, the spike achieved on a-Si:H film surface is two orders of magnitude higher. This indicates the importance of hydrogen on surface texturing behavior through melting and grown dominant spike formation mechanism by excimer ns laser.

7.1.2 Effect of Processing Medium and Pulse Duration on Crystallinity and Absorption

In order to understand the absorptance improvement based on the surface geometry changes, two processing mediums, air and water, are used for fs laser irradiation on a-Si:H samples. Compared to the conical-shaped spikes formed in air, the pillar-shaped spikes with lower height and higher density are formed in water. Although density can play a role on absorption, top angle of the spike, which can determine the number of multi-reflection in between spikes, is more important on absorptance enhancement. In the meanwhile, the air environment can also introduce more crystallinity due to its lower cooling rate and cause more impurities after processing. Crystallized silicon can broaden the absorption spectrum to 1100nm (band gap of crystalline silicon) and the

sub-band-gap induced by impurities can further absorb the light with longer wavelengths. Therefore, the samples treated in air have a better absorption capability over the entire solar spectrum than that treated in water.

Regarding to the pulse duration, the fs laser induces much less melting compared to that of excimer ns laser. Therefore, more crystallinity and bigger grains are formed during excimer laser irradiation. Due to the different spike formation mechanisms, large grains (~400nm) are grown on the spikes and fine grains are formed at the interface between spikes and the amorphous material during the excimer laser processing. In contrast, much smaller grains are attached on the amorphous spikes with a high density of defects for fs laser irradiations. The absorptance of these two laser irradiated samples in air are similar since conical spikes are formed in both processes, however, a better crystallization quality produced by excimer laser will lead to more stable solar cells. Overall, the laser surface texturing and crystallization of a-Si:H can improve its absorption and stability, which may be promising in solar cell applications.

7.2 Laser Scribing of CdTe-based Thin-Film Solar Cells

7.2.1 Film Removal and Defect Characterization of Glass-Side Laser Scribing

It has been demonstrated that successfully selective film removal with vertical sidewalls and little thermal effect is achieved by glass-side laser scribing of CdTe-based solar cells. Thin TCO (SnO_2:F) films (P1 process) are removed through laser ablation and thermal stress due to its larger absorption depth compared to its thickness at the wavelength of 1064nm. In terms of P2 scribing process, the micro-explosion removal mechanism leads to melting and recrystallization on partial of CdS materials, which could cause defects as recombination centers under the

supercooling process. In contrast, the rest of laser energy is fully absorbed by a shallow layer of CdTe materials. Due to the confinement of solid CdTe and the substrate, a shock wave is generated caused by the plasma expansion and CdTe material is completely removed through brittle fracture by the induced pressure.

Defect characterization is of critical importance in understanding the root causes of reduced output power and efficiency as a result of laser scribing. Cross-sectional TEM is employed for detection of both mechanical and thermal induced defects. Micro-cracks and CdTe film delimitation, which are due to the weaker adhesion at CdTe/CdS interface compared to other interfaces, are observed. These mechanical fracture-induced defects will cause inactive cells, and the residue material after delamination could also lead to an increase of contact resistances. Furthermore, nano-bubbles caused by sulfur oxidation through CdS decomposition under high temperature could further induce abnormal heating and affect the long-time cell stability. Finally, the relationship between partial of defects, such as thermal effect, TCO damage and residual material, and solar cell performance is estimated by the sheet resistance measurement of a scribed area. The optimal condition for P2 process is determined by the combined effects of defects formed at scribe boundaries (such as micro-cracks and delamination) and cleanliness of the scribe area (sheet resistances characterization), which leads to the optimization process in solar panel manufacturing.

7.2.2 Numerical Investigations

A fully-coupled thermal-mechanical model is implemented for P1 scribing process, showing that SnO_2:F film is removed at a laser fluence below the damage threshold due to thermal stresses.

The numerical simulation of P2 scribing process on scribe geometry and mechanical-induced defects, chiefly film delamination, micro-cracks and residue material, based on micro-explosion mechanism is also investigated. The pressure loading is estimated by the laser-induced plasma expansion and the CdTe material removal is determined through brittle fracture with a strain-rate dependent criterion since it is a highly dynamic process. Micro-cracks and delamination are identified with the damage but not yet completely fractured regions around the scribe slots and the interface. In the meanwhile, the models have been well validated by the experimental results including measurement of the scribe width and those defects formation. Good agreements with experimental results show that the simulation is capable of predicting the material removal dynamics and fracture behavior of CdTe materials.

7.3 Major Contributions

In this thesis, the understanding of the physical mechanisms on fs- and ns-laser-induced surface texturing of a-Si:H thin films is significantly improved. Especially, the effect of hydrogen on the texturing behavior during ns laser irradiation is well studied and explained. In addition, the understanding of the crystallization processes during these two laser irradiations with multiple pulses is further enhanced. A step-by-step processing method is successfully implemented in texturing processes in order to protect hydrogen from diffusion out of the film. Regarding to the laser scribing process, a fundamental understanding on the removal mechanism of CdTe/CdS multilayers is improved, and the link between laser processing parameters, defects formation and their effects on the electrical properties of solar cells is also investigated. Furthermore, a well-validated physics-based numerical model is developed for prediction of the scribe geometry and

major defects formation, which is promising to be applied on solar panel design against the trial-and-error experimental testing.

7.4 Further Work

The major findings and contributions in the laser scribing of CdTe-based solar cells detailed in the previous section were mostly in fundamental understanding of the different film removal mechanisms of thermal stress, ablation and micro-explosion. A continue work is to improve the predictive capabilities of the scribe geometry and defect formation during the micro-explosion process. In this way, the model needs to consider the laser-induced thermal effect during the scribing. There are three aspects related to the temperature: first, adhesion between CdTe and CdS layers; second, change of mechanical properties and brittle fracture criteria of CdTe material around the laser-induced plasma; third, the thermal damage of TCO layer. Therefore, the model could be designed to a fully-coupled thermo-mechanical finite-element model. The calculation at each time step of temperature distribution will be transferred to the stress analysis, and the mechanical deformation result is then passed back for the next-step thermal analysis. In addition, the pressure variation in both amplitude and direction during the micro-explosion process may also be implemented, because the plasma pressure in the current model is only applied in the vertical direction and simply set to be zero after film broken. Simulation capturing such effects can be performed by modeling of the response of structures to subsurface blasts by considering a multi-phase reaction domain. Regarding to the micro-explosion process, these domains include solid, gas and plasma. The variation of plasma pressure can be updated based on the volume geometry and temperature change calculated by equation of state, and calculation ends until the confined plasma flows out and mixes with the background gas after film breaking. Modification

on these two aspects may obtain more powerful numerical simulations on scribe geometry and defect formation of micro-crack, film delamination and residue materials.

In addition to the numerical prediction, investigation on the correlation between defects and electrical properties could be studied. In order to achieve this, a continue work of P3 scribing process of selective removal of CdS/CdTe/metal multilayer needs to be investigated. Subsequently, defects formation of different scribing processes (P1 to P3) and their effects on cell electrical properties can be categorized. Characterization of Electrical properties may start with small-scale modules (e.g. 2×2 cell array). Contact resistance between metallic and TCO layers at P2 slot could be measured through TLM (transmission line method), which can reflect the effects of residual material and TCO damage. In the meanwhile, the measurement of isolation resistances between P1 or P3 slots could determine P1 or P3 scribing cleanliness, where the poor scribing causes current leakages. Furthermore, measurements of current-power (I-V) curves of the solar module might determine the effects of micro-cracks and film delamination. The efficiency change can also verify the long-term stability affected by the defects, such as micro-bubbles and further crack propagation. These measurements of electrical property change are expected to significantly simplify and expedite studies of the influences of laser-induced defects on solar cells, in order to improve the defect mitigation process and the laser scribing optimization.

References

Chapter 1

Acciania, G., Falcone, O., Vergura, S., 2010, "Defects in Poly-Silicon and Amorphous Silicon Solar Cells", *Internacional Conference on Renewable Energy and Power Quality*, Spain.

Bejan, A., 1993, *Heat transfer*, J. Wiley and Sons, pp. 151.

Bian, Q., Shen, X., Chen, S., Chang, Z., Lei, S., 2010, "Femtosecond Laser Ablation of Indium Tin Oxide (ITO) Glass for Fabrication of Thin Film Solar Cells", *29th International Congress on Applications of Lasers & Electro-Optics*, pp.1190-1198.

Bohland, J., Kormanyos, K., Faykosh, G., Champion, V., Cox, S., McCarthur, M., Dapkus, T., Kamm, K., Flis, M., 2000, "Specific PVMaT R&D in CdTe Product Manufacturing: Phase I Annual Report", *National Renewable Energy Laboratory*, NERL/SR-27574.

Bohland, J., McMaster, A., Henson, S., Hanak, J., 2004, "Specific PVMaT R&D in CdTe Product Manufacturing: Final Subcontract Report", *National Renewable Energy Laboratory*, NERL/SR-520-35177.

Booth, H., 2010, "Laser Processing in Industrial Solar Module Manufacturing", Journal of Laser Micro/Nanoengineering, **5**(3), pp.183-191.

Bovatsek, J., Tamhankar, A., Patel, R.S., Bulgakova, N.M., Bonse, J., 2010, "Thin Film Removal Mechanisms in ns-Laser Processing of Photovoltaic Materials", *Thin Solid Films*, **518**, pp. 2897-2904.

Burger, A., 2011, "Colorado to be home to GE thin-film solar plant, largest in the US", http://cleantechnica.com/2011/10/14/colorado-to-be-home-to-ge-thin-film-solar-plant-largest-in-the-us/.

Callan, J.P., Kim, A, Roeser, C.A.D., Mazur, E., Solis, J., Siegel, J., Afonso, C.N., 2001, "Ultrafast Laser-induced Phase Transitions in Amorphous GeSb Films", *Physical Review Letters*, **86**(16), pp. 3650-3653.

Carey, J.E., 2004, "Femtosecond-Laser Microstructuring of Silicon for Novel Optoelectronic Devices", Ph.D. dissertation, Harvard University, Cambridge, MA.

Carslaw, H.S., Jaeger J.C., 1958, *Conduction of heat in solids*, 2nd Edition, Oxford Univ. Press, pp.10.

Choi, T.Y., Hwang, D.J., Grigoropoulos, C.P., 2003, "Ultrafast laser-induced crystallization of amorphous silicon films", *Opt. Eng.*, **42**(11), pp. 3383-3388.

Chopra, K.L., Paulson, P.D., Dutta, V., 2004, "Thin-Film Solar Cells: An Overview", *Prog. Photovolt: Res. Appl.*, **12**, pp. 69-92.

Compaan, A.D., Matulionis, S.N., 2000, "Laser Scribing of Polycrystalline Thin Films", *Opt. Lasers Eng*., **34**, pp. 15-45.

Crouch, C.H., Carey, J.E., Warrender, J.M., Aziz, M.J., Mazur, E., Genin, F.Y., 2004, "Comparison of structure and properties of femtosecond and nanosecond laser-structured silicon", *Applied Physics Letters*, **84**(11), pp. 1850-1852.

Dehghanpour, H., Parvin, P., Sajad, B., Nour-Azar, S., 2009, "Dose and Pressure Dependence of Silicon Microstructure in SF_6 Gas due to Excimer Laser Irradiation", *Applied Surface Science*, **255**, pp. 4664-4669.

Dunsky, C., 2007, "The Promise of Solar Energy: Applications and Opportunities for Laser Processing in the Manufacturing of Solar Cells", *Proc. of SPIE*, **6459**, pp. 64590M.

Dunsky, C.M., Colville, F., 2008, "Scribing Thin-Film Solar Panels", *Industrial Laser Solutions for Manufacturing*.

Etsion, I., 2008, "Laser Surface Texturing", *Innovation for Sustainable Production*, *Presentations Conference 1: Smart Materials for Sustainable Production*, Bruges, Belgium.

Emel'yanov, V.I., Kashkarov, P.K., 1992, "Laser-Induced Defect Formation in Semiconductors", *Applied Physics A*, **55**, PP. 161-166.

First Solar, 2012, "Innovative Cadmium Telluride Technology", from http://www.firstsolar.com/en/Innovation/CdTe-Technology

Frerichs, R., 1947, "Photo-Conductivity of Incomplete Phosphors", *Physical Review*, **72**(7), pp. 594-601.

Gattass, R., Mazur, E., 2008, "Femtosecond Laser Micromachining in Transparent Materials", *Nature Photonics*, **2**, pp. 219-225.

Gecys, P., Raciukaitis, G., 2010, "Scribing of a-Si Thin-Film Solar Cells with Picosecond Laser", *The European Physical Journal Applied Physics*, **51**, PP.33209.

Golovan, L., Kashkarov, P., Timoshenko, V., 1996, "Laser-Induced Melting and Defect Formation in Cadmium Telluride", *Laser Physics*, **6**(5), PP. 925-927.

Green, M., 1982, *Solar Cells: Operating Principles, Technology, and System Applications*, Prentice Hall, Englewood Cliffs, NJ, Chapter 1, pp. 1-12.

Hu, W., Shin, Y.C., 2010, "High Precision Scribing of Solar Cell Films by a Picosecond Laser", *International Congress on Applications of Lasers & Electro-Optics*, pp.1206-1209.

Hylton, J.D., Burgers A.R., Sinke, W.C., 2004, "Alkaline Etching for Reflectance Reduction in Multicrystalline Silicon Solar Cells", *Journal of the Electrochemical Society*, **151**(6), pp. G408-G427.

Im, J., Kim, H., Thompson, M., 1993, "Phase Transformation Mechanisms Involved in Excimer Laser Crystallization of Amorphous Silicon Films", *Applied Physics Letter*, **63**(14), pp. 1969-1971.

Jiang, L., Tsai, H.L., 2003, "Femtosecond Laser Ablation: Challenges and Opportunities", *Proceeding of NSF Workshop on Research Needs in Thermal*, *Aspects of Material Removal*, Stillwater, OK, pp. 163–177.

J.A. Woollam Co. Inc., 2008, *CompleteEASE Software Manual*, Version 3.60.

Kazmerski, L.L., 2006, "Solar Photovoltaics R&D at the Tipping Point: A 2005 Technology Overview", *Journal of Electron Spectroscopy and Related Phenomena*, **150**, pp. 105-135.

Kazmerski, L.L., 2012, "Conversion efficiencies of best research solar cells worldwide from 1976 through 2012 for various photovoltaic technologies", NREL.

Keldysh, L. V., 1965, "Ionization in the Field of a Strong Electromagnetic Wave", *Soviet Physics JETP*, **20**, pp. 1307-1314.

King, R. R., 2007, "40% Efficient Metamorphic GaInP/GaInAs/Ge Multijunction Solar Cells," *Appl. Phys. Lett*., **90**, pp. 183516.

Kontgers, M., Kunze, I., Kajari-Schroder, S., Breitenmoser, X., Bjorneklett, B., 2010, "Quantifying the Risk of Power Loss in PV Modules due to Micro Cracks", *25th European Photovoltaic Solar Energy Conference,* Valencia, Spain.

Kolodziej, A., 2004, "Staebler-Wronski Effect in Amorphous Silicon and its Alloys," *Opto-Electron. Rev.*, **12**(1), pp. 21–32.

Laskin, A., Laskin, V., 2010, "Improving Laser Technologies in Photovoltaics by Refractive Beam Shapers", *29th International Congress on Applications of Lasers & Electro-Optics*, PP.1235-1241.

Lauzurica, S., Garcia-Ballesteros, J.J., Colina, M., Sanchez-Aniorte, I., Molpeceres, C., 2011, "Selective Ablation with UV Lasers of a-Si:H Thin Film Solar Cells in Direct Scribing Configuration", *Applied Surface Science*, **257**, PP. 5230-5236.

Linde, D., Fabricius, N., 1982, "Observation of an Electronic Plasma in Picosecond Laser Annealing of Silicon", *Applied Physics Letter*, **41**(10), pp. 991-993.

Lorenzo, E., 1994, *Solar Electricity: Engineering of Photovoltaic System*, Progensa, Spain, Chapter 2.

Lowndes. D.H., Fowlkes, J.D., Pedraza, A.J., 2000, "Early stage of pulsed-laser growth of silicon microcolumns and microcones in air and SF6", *Applied Surface Science*, 154-155, pp. 647-658.

Luque, A., Hegedus, S., 2003, *Handbook of Photovoltaic Science and Engineering*, Wiley, UK.

Martirosyan, K.S., Hovhannisyan, A.S., Arouiounian, V.M., 2007, "Calculation of Reflectance of Porous Silicon Double-layer Antireflection Coating for Silicon Solar Cells", *Physica Status Solid (c)*, **4**(6), pp. 2103-2106.

Mathe, E., Naudon, A., Elliq, M., Fogarassy, E., Unamuno, S., 1992, "Influence of Hydrogen on the Structure and Surface Morphology of Pulsed ArF Excimer Laser Crystallized Amorphous Silicon Thin Films", *Applied Surface Science*, **54**, pp. 392-400.

Matylitsky, V.V., Huber, H., Kopf, D., 2011, "Selective Removal of Transparent Conductive Oxide Layers with Ultrashort Laser Pulses: Front- vs. Back-Side Ablation", *Int. Congr. App. Lasers Electro-Opt*., pp. 1022-1027.

Nayak, B.K., Gupta, M.C., 2007, "Femtosecond-laser-induced-crystallization and Simultaneous Formation of Light Trapping Microstructures in Thin a-Si:H Films", *Appl. Phys. A*, **89**, pp. 663-666.

Patel, R., 2010, "Beam Profile Effect for Thin Film Solar Cell Scribing", *Industrial Laser Solutions for Manufacturing*.

Polishchuk, A. Ya., Meyer-Ter-Vehn, J., 1994, "Electron-ion relaxation in a plasma interacting with an intense laser field", *Physical Review E*, 49, pp. 663-666.

Polman, A., Roorda, S., Stolk, P., Sinke, W., 1991, "Triggering Explosive Crystallization of Amorphous Silicon", *Journal of Crystal Growth*, **108**, pp. 114-120.

Prokhorov, A.M., Konov, V.I., Ursu, I., Mihailescu, N., 1990, *Laser heating of metals*, Taylor and Francis, pp. 43.

Roberts, H., Otterloo, B., 2001, "FIB-TEM Sample Preparation by in-situ Lift-Out Technique", *Philips Semiconductors Nijmegen PMO.*

Schulz-Ruhtenberg, M., 2009, "The SOLASYS Project - Laser Processes for Industrial Manufacturing of Solar Cells", *24th European Photovoltaic Solar Energy Conference*.

Schwarz-Selinger, T., Cahill, D.G., Chen, S., Moon, S., Griogoropoulos, C.P., 2001, "Micron-scale Modifications of Si Surface Morphology by Pulsed-laser Texturing", *Physical Review B*, **64**, pp. 155323-1-155323-7.

Shockley, W., Queisser, H., 1961, "Detailed Balance Limit of Efficiency of p-n Junction Solar Cells", *Journal of Applied Physics*, **32**, pp. 510-519.

Staebler, D.L., Wronski, C.R., 1980, "Optically Induced Conductivity Changes in Discharge-Produced Hydrogenated Amorphous Silicon", *Journal of Applied Physics*, **51**(6).

Sundaram, S.K., Mazur, E., 2002, "Inducing and Probing Non-Thermal Transitions in Semiconductors using Femtosecond Laser Pulses", *Nature Materials*, **1**(4), pp.217-224.

Tomaoki, S., Kaneuchi, Y., Kakui, M., Baird, B., Paudel, N., Wieland, K., 2010, "Development of Wide Operational Range Fiber Laser for Processing Thin Film Photovoltaic Panels", *29th International Congress on Applications of Laser & Electro-Optics*, Anaheim, CA.

Tull, B.R., Carey, J.E., Mazur, E., McDonald, J.P., Yalisove, S.M., 2006, "Silicon Surface Morphologies after Femtosecond Laser Irradiation", *MRS Bulletin*, **31**(8), pp. 626-633.

Vanecek, M., Poruba, A., Remes, Z., beck, N., Nesladek, M., 1998, "Optical Properties of Microcrystalline Materials", *Journal of Non-Crystalline Solids*, **227-230**, pp. 967-972.

Vechten, J.A., Tsu, R., Saris, F.W., 1979, "Nonthermal Pulsed Laser Annealing of Si; Plasma Annealing", *Physics Letters A*, **74**(6), pp. 422-426.

Wang, H., Yao, Y.L., Chen, H., 2013, "Removal Mechanism and Defect Characterization for Glass-Side Laser Scribing of CdTe/CdS Multilayer in Solar Cells", *41th North American Manufacturing Research Conference*, Madison, WI.

Wang, W., Jiang, G., Mei, X., Wang, K., Shao, J., Yang, C., 2010, "Damage Mechanism and Morphology Characteristics of Chromium Film in Femtosecond Laser Rear-Side Ablation", *Applied Surface Science*, **256**, pp. 3612-3617.

Yamamoto, K., Nakajima, A., Yoshimi, M., Sawada, T., Fukuda, S., Suezaki, T., Ichikawa, M., Koi, Y., Goto, M., Meguro, T., Matsuda, T., Kondo, M., Sasaki, T., Tawada, Y., 2004, "A High Efficiency Thin Film Silicon Solar Cell and Module," *Solar Energy*, **77**, pp. 939–949.

Chapter 2

Carey, J.E., 2004, "Femtosecond-laser Microstructuring of Silicon for Novel Optoelectronic Devices", Ph.D dissertation, Harvard University.

Chopra, K.L., Paulson, P.D., Dutta, V., 2004, "Thin-Film Solar Cells: An Overview", *Prog. Photovolt: Res. Appl.*, **12**, pp. 69-92.

Crouch, C.H., Carey, J.E., Warrender, J.M., Aziz, M.J., Mazur, E., Genin, F.Y., 2004, "Comparison of structure and properties of femtosecond and nanosecond laser-structured silicon", *Applied Physics Letters*, **84**(11), pp. 1850-1852.

Daminelli, G., Kruger, J., Kautek, W., 2004, "Femtosecond Laser Interaction with Silicon Under Water Confinement", *Thin Solid Films*, **467**, pp. 334-341.

Elliq, M., Fogarassy, E., Stoquert, J.P., Fuchs, C., Unamuno, S., Preot, B., 1990, "Pulsed Excimer and Nd:YAG Laser Crystallization of a-Si:H – The Specific Role of Hydrogen", *Applied Surface Science*, **46**, pp. 378-382.

Gattass, R., Mazur, E., 2008, "Femtosecond Laser Micromachining in Transparent Materials", *Nature Photonics*, **2**, pp. 219-225.

Goetzberger, A., Knobloch, J., Voss, B., 1998, *Crystalline Silicon Solar Cells*, Wiley, Chichester, Chap. 2

Her, T.H., Finlay, R.J., Wu, C., Mazur, E., 2000, "Femtosecond Laser-induced Formation of Spikes on Silicon", *Applied Physics A*, **70**, pp. 383-385.

Hylton, J.D., Burgers A.R., Sinke, W.C., 2004, "Alkaline Etching for Reflectance Reduction in Multicrystalline Silicon Solar Cells", *Journal of the Electrochemical Society*, **151**(6), pp. G408-G427.

Jiang, L., Tsai, H.L., 2003, "Femtosecond Laser Ablation: Challenges and Opportunities", Proceeding of NSF Workshop on Research Needs in Thermal, Aspects of Material Removal, Stillwater, OK, pp. 163–177.

Kautek, W., Rudolph, P., Daminelli, G., Kriger, J., 2005, "Physico-chemical Aspects of Femtosecond-pulse-laser-induced Surface nanostructures", *Applied Physics A*, **81**, pp. 65-70.

Kazmerski, L.L., 2006, "Solar Photovoltaics R&D at the Tipping Point: A 2005 Technology Overview", *Journal of Electron Spectroscopy and related Phenomena*, **150**, pp. 105-135.

Kruger, J., Kautek, W., 1995, "Femtosecond-pulse Laser Processing of Metallic and Semiconducting Thin Films", *SPIE*, **2403**, pp. 436-447.

Kuo C.C., Yeh, W.C., Chen, J.B., Jeng, J.Y., 2006, "Monitoring Explosive Crystallization Phenomenon of Amorphous Silicon Thin Films during Short Pulse Duration XeF Excimer Laser Annealing Using Real-time Optical Diagnostic Measurements", *Thin Solid Films*, **515**, pp. 1651-1657.

Luque, A., Hegedus, S., 2003, *Handbook of Photovoltaic Science and Engineering*, Wiley, UK, Chap. 7-8.

Martirosyan, Kh.S., Hovhannisyan, A.S., Arouiounian, V.M., 2007, "Calculation of Reflectance of Porous Silicon Double-layer Antireflection Coating for Silicon Solar Cells", *Physica Status Solidi (C)* , **4**(6), pp. 2103-2106.

Miles, R.W., Hynes, K.M., Forbes, I., 2005, "Photovoltaic Solar Cells: An Overview of State-of-the-art Cell Development and Environmental Issues", *Progress in Crystal Growth and Characterization of Materials*, **51**, pp. 1-42.

Nayak, B.K., Gupta, M.C., 2007, "Femtosecond-laser-induced-crystallization and Simultaneous Formation of Light Trapping Microstructures in Thin a-Si:H Films", *Appl. Phys. A*, **89**, pp. 663-666.

Shaaban, E.R., 2008, "Calculation of Optical Constant of Amorphous Germanium Arsenoselenide Wedge-Shaped Thin Films from Their Shrunk Transmittance and Reflectance Spectra", *Philosophical Magazine*, **88**(5), pp. 781-794.

Sheehy, M.A., Winston, L., Carey, J.E., Friend, C.M., Mazur, E., 2005, "Role of the Background Gas in the Morphology and Optical Properties of Laser-Microstructured Silicon", *Chem. Mater*, **17**, pp. 3582-3586.

Shen, M.Y., Crouch, C.H., Carey, J.E., Mazur, E., 2004, "Femtosecond Laser-induced Formation of Submicrometer Spikes on Silicon in Water", Applied Physics Letters, **85**(23), pp. 5694-5696.

Sipe, J.E., Young, J.F., Preston, J.S., Van Driel, H.M., 1983, "Laser-induced Periodic Surface Structure. I. Theory", *Physical Review B*, **27**(2), pp. 1141-1154.

Sundaram, S.K., Mazur, E., 2002, "Inducing and Probing Non-thermal Transitions in Semiconductors Using Femtosecond Laser Pulses", *Nature Materials*, **1**(4), pp. 217-224.

Staebler, D.L., Wronski, C.R., 1980, "Optically Induced Conductivity Changes in Discharge-produced Hydrogenated Amorphous Silicon", *Journal of Appl. Physics*, **51**(6).

Swanepoel, R., 1983, "Determination of the Thickness and Optical Constants of Amorphous Silicon", *J. Phys. E: Sci. Instrum.*, **16**, pp.1214-1222

Tan, B., Venkatakrishnan, K., 2006, "A Femtosecond Laser-induced Periodical Surface Structure on Crystalline Silicon", *J. of Micromechanics and Microengineering*, **16**, pp. 1080-1085.

Tull, B.R., Carey, J.E., Mazur, E., McDonald, J.P., Yalisove, S.M., 2006, "Silicon Surface Morphologies after Femtosecond Laser Irradiation", *MRS Bulletin*, **31**(8), pp. 626-633.

Wang, H., Kongsuwan, P., Satoh, G., Yao, Y.L., 2012, "Femtosecond Laser-Induced Simultaneous Surface Texturing and Crystallization of a-Si:H Thin Film: Absorption and Crystallinity", *Journal of Manufacturing Science and Engineering*, **134**(3), pp. 031006.

Wu, C., 2000, "Femtosecond Laser-gas-solid Interactions", Ph.D dissertation, Harvard University.

Yamamoto, K., Nakajima, A., Yoshimi, M., Sawada, T., Fukuda, S., Suezaki, T., Ichikawa, M., Koi, Y., Goto, M., Meguro, T., Matsuda, T., Kondo, M., Sasaki, T., Tawada, Y., 2004, "A High Efficiency Thin Film Silicon Solar Cell and Module," *Solar Energy*, **77**, pp. 939–949.

Younkin, R., Carey, J.E., Mazur, E., Levinson, J.A., Friend, C.M., 2003, "Infrared Absorption by Conical Silicon Microstructures Made in a Variety of Background Gases Using Femtosecond-laser Pulses", *J. of Applied Physics*, **93**(5), pp. 2626-2629.

Zheng, H.Y., Jiang, Z.W., 2010, "Femtosecond Laser Micromachining of Silicon with an External Electric Field", *Journal of Micromechanics and Microengineering*, **20**, pp. 017001.

Chapter 3

Callan, J.P., Kim, A, Roeser, C.A.D., Mazur, E., Solis, J., Siegel, J., Afonso, C.N., 2001, "Ultrafast Laser-induced Phase Transitions in Amorphous GeSb Films", *Physical Review Letters*, **86**(16), pp. 3650-3653.

Carey, J.E., 2004, "Femtosecond-laser Microstructuring of Silicon for Novel Optoelectronic Devices", Ph.D dissertation, Harvard University.

Choi, T.Y., Hwang, D.J., Grigoropoulos, C.P., 2003, "Ultrafast laser-induced crystallization of amorphous silicon films", *Opt. Eng*., **42**(11), pp. 3383-3388.

Chopra, K.L., Paulson, P.D., Dutta, V., 2004, "Thin-Film Solar Cells: An Overview", *Prog. Photovolt: Res. Appl.*, **12**, pp. 69-92.

Crouch, C.H., Carey, J.E., Shen, M., Mazur, E., Fenin, F.Y., 2004, "Infrared Absorption by Sulfur-doped Silicon Formed by Femtosecond Laser Irradiation", *Applied Physics A*, **79**, pp. 1635-1641.

Daminelli, G., Kruger, J., Kautek, W., 2004, "Femtosecond Laser Interaction with Silicon Under Water Confinement", *Thin Solid Films*, **467**, pp. 334-341.

Goetzberger, A., Knobloch, J., Voss, B., 1998, *Crystalline Silicon Solar Cells*, Wiley, Chichester, Chap. 2.

Gosain, D.P., Machida, A., Fujino, T., Hitsuda, Y., Nakano, K., Sato, J., 2003, "Formation of (100)-Textured Si Film Using an Excimer Laser on a Glass Substrate", *Jpn. J. Appl. Phys*., **42**, pp. L135-L137.

Halbwax, M., Sarnet, T., Delaporte, P., Sentis, M., Etienne, H., Torregrosa, F., Vervisch, V., Perichaud, I., Martinuzzi, S., 2008, "Micro and Nano-structure of Silicon by Femtosecond Laser: Application to Silicon Photovoltaic Cells Fabrication", *Thin Solid Films*, **516**, pp. 6791-6795.

Hua, X., Zhang, Y., Wang, H., 2010, "The Effect of Texture Unit Shape on Silicon Surface on the Absorption Properties", *Solar Energy Materials & Solar Cells*, **94**, pp. 258-262.

Kazmerski, L.L., 2006, "Solar Photovoltaics R&D at the Tipping Point: A 2005 Technology Overview", *Journal of Electron Spectroscopy and related Phenomena*, **150**, pp. 105-135.

Kolodziej, A., 2004, "Staebler-Wronski effect in amorphous silicon and its alloys", *Opto-electronics review*, **12**(1), pp. 21-32.

Linde, D., Fabricius, N., 1982, "Observation of an Electronic Plasma in Picosecond Laser Annealing of Silicon", *Applied Physics Letter*, **41**(10), pp. 991-993.

Luque, A., Hegedus, S., 2003, *Handbook of Photovoltaic Science and Engineering*, Wiley, UK, Chap. 7-8.

Meillaud, F., et al., 2009, "Limiting Factors in the Fabrication of Microcrystalline Silicon Solar Cells and Microcrystalline/Amorphous ('Micromorph') Tandems", *Philosophical Magazine*, **89**(28), pp. 2599-2621.

Miles, R.W., Hynes, K.M., Forbes, I., 2005, "Photovoltaic Solar Cells: An Overview of State-of-the-art Cell Development and Environmental Issues", *Progress in Crystal Growth and Characterization of Materials*, **51**, pp. 1-42.

Nayak, B.K., Gupta, M.C., 2007, "Femtosecond-laser-induced-crystallization and Simultaneous Formation of Light Trapping Microstructures in Thin a-Si:H Films", *Appl. Phys. A*, **89**, pp. 663-666.

Palani, I.A., Vasa, N.J., Singaperumal, M., 2008, "Crystallization and Ablation in Annealing of Amorphous-Si Thin Film on Glass and Crystalline-Si Substrates Irradiated by Third Harmonics of Nd^{3+}: YAG Laser", *Material Science in Semiconductor Processing*, **11**, pp. 107-116.

Sheehy, M.A., Winston, L., Carey, J.E., Friend, C.M., Mazur, E., 2005, "Role of the Background Gas in the Morphology and Optical Properties of Laser-Microstructured Silicon", *Chem. Mater*, **17**, pp. 3582-3586.

Shieh. J., Chen, Z., Dai, B., 2004, "Near-infrared Femtosecond Laser-induced Crystallization of Amorphous Silicon", *Applied physics letters*, **85**(7), pp. 1232-1234.

Spencer, C.H., Murty, M.V.R.K., 1962, "General Ray-tracing Procedure", *Optical Society of America*, **52**(6), pp. 672-678.

Staebler, D.L., Wronski, C.R., 1980, "Optically Induced Conductivity Changes in Discharge-produced Hydrogenated Amorphous Silicon", *Journals of Appl. Physics*, **51**(6).

Steen, W., 2003, *Laser Material Processing*, 3rd edition, Springer-Verkag, London, pp. 76-77.

Vechten, J.A., Tsu, R., Saris, F.W., 1979, "Nonthermal Pulsed Laser Annealing of Si; Plasma Annealing", *Physics Letters A*, **74**(6), pp. 422-426.

Wang, H., Kongsuwan, P., Satoh, G., Yao, Y.L., 2010, "Femtosecond Laser-induced Simultaneous Surface Texturing and Crystallization of a-Si:H Thin Film", *Proceedings of the 2010 International Manufacturing Science and Engineering Conference*, Erie, PA.

Wang, H., Kongsuwan, P., Satoh, G., Yao, Y.L., 2011, "Effect of Processing Medium and Condition on Absorption Enhancement of Femtosecond Laser Treated a-Si:H Thin Film", *Proceedings of the 2011 North American Manufacturing Research*, Corvallis, OR.

Wang, H., Kongsuwan, P., Satoh, G., Yao, Y.L., 2012, "Femtosecond Laser-induced Simultaneous Surface Texturing and Crystallization of a-Si:H Thin Film: Morphology Study", *The International Journal of Advanced Manufacturing Technology*, DOI: 10.1007/s00170-012-4291-0.

Yagi, T., Uraoka, Y., Fuyuki, T., 2006, "Ray-trace Simulation of Light Trapping in Silicon Solar Cell with Texture Structures", *Solar Energy Materials & Solar Cells*, **90**, pp. 2647-2656.

Yamamoto, K., et al., 2004, "A High Efficiency Thin Film Silicon Solar Cell and Module", *Solar Energy*, **77**, pp. 939-949.

Younkin, R., Carey, J.E., Mazur, E., Levinson, J.A., and Friend, C.M., 2003, "Infrared Absorption by Conical Silicon Microstructures Made in a Variety of Background Gases Using Femtosecond-laser Pulses", *J. of Applied Physics*, **93**(5), pp. 2626-2629.

Chapter 4

Bäuerle, D., 2000, *Laser processing and chemistry*, 3rd Edition, Springer, pp. 105.

Bejan, A., 1993, *Heat transfer*, J. Wiley and Sons, pp. 151.

Carslaw, H.S., Jaeger J.C., 1958, *Conduction of heat in solids*, 2nd Edition, Oxford Univ. Press, pp.10.

Chopra, K.L., Paulson, P.D., Dutta, V., 2004, "Thin-Film Solar Cells: An Overview", *Prog. Photovolt: Res. Appl*., **12**, pp. 69-92.

Crouch, C.H., Carey, J.E., Warrender, J.M., Aziz, M.J., Mazur, E., Genin, F.Y., 2004, "Comparison of structure and properties of femtosecond and nanosecond laser-structured silicon", *Applied Physics Letters*, **84**(11), pp. 1850-1852.

Dehghanpour, H., Parvin, P., Sajad, B., Nour-Azar, S., 2009, "Dose and Pressure Dependence of Silicon Microstructure in SF_6 Gas due to Excimer Laser Irradiation", *Applied Surface Science*, **255**, pp. 4664-4669.

Goetzberger, A., Knobloch, J., Voss, B., 1998, *Crystalline Silicon Solar Cells*, Wiley, Chichester, Chap. 2.

Heya, A., Serikawa, T., Kawamoto, N., Matsuo, N., 2008, "Behavior of Hydrogen in Excimer Laser Annealing of Hydrogen-Modulation-Doped Amorphous Silicon Layer", *Japanese Journal of Applied Physics*, **47**(3), pp. 1853-1857.

Hu, Q., 2010, "Dynamics of Melt-mediated Crystallization of Amorphous Silicon Films", Ph.D dissertation, Columbia University.

Hylton, J.D., Burgers A.R., Sinke, W.C., 2004, "Alkaline Etching for Reflectance Reduction in Multicrystalline Silicon Solar Cells", *Journal of the Electrochemical Society*, **151**(6), pp. G408-G427.

Im, J., Kim, H., Thompson, M., 1993, "Phase Transformation Mechanisms Involved in Excimer Laser Crystallization of Amorphous Silicon Films", *Applied Physics Letter*, **63**(14), pp. 1969-1971.

Martirosyan, Kh.S., Hovhannisyan, A.S., Arouiounian, V.M., 2007, "Calculation of Reflectance of Porous Silicon Double-layer Antireflection Coating for Silicon Solar Cells", *Physica Status Solidi (C)*, **4**(6), pp. 2103-2106.

Nayak, B.K., Gupta, M.C., 2007, "Femtosecond-laser-induced-crystallization and Simultaneous Formation of Light Trapping Microstructures in Thin a-Si:H Films", *Appl. Phys. A*, **89**, pp. 663-666.

Kazmerski, L.L., 2006, "Solar Photovoltaics R&D at the Tipping Point: A 2005 Technology Overview", *Journal of Electron Spectroscopy and related Phenomena*, **150**, pp. 105-135.

Kolasinski, K.W., 2007, "Solid Structure Formation during the Liquid/solid Phase Transition", *Current Opinion in Solid State and Materials Science*, **11**, pp. 76-85.

Lengsfeld, P., Nickel, N., Fuhs, W., 2000, "Step-by-step Excimer Laser Induced Crystallization of a-Si:H", *Applied Physics Letters*, **76**(13), pp. 1680-1682.

Lowndes. D.H., Fowlkes, J.D., Pedraza, A.J., 2000, "Early stage of pulsed-laser growth of silicon microcolumns and microcones in air and SF6", *Applied Surface Science*, 154-155, pp. 647-658.

Luque, A., Hegedus, S., 2003, *Handbook of Photovoltaic Science and Engineering*, Wiley, UK, Chap. 7-8

Mathe, E., Naudon, A., Elliq, M., Fogarassy, E., Unamuno, S., 1992, "Influence of Hydrogen on the Structure and Surface Morphology of Pulsed ArF Excimer Laser Crystallized Amorphous Silicon Thin Films", *Applied Surface Science*, **54**, pp. 392-400.

Miles, R.W., Hynes, K.M., Forbes, I., 2005, "Photovoltaic Solar Cells: An Overview of State-of-the-art Cell Development and Environmental Issues", *Progress in Crystal Growth and Characterization of Materials*, **51**, pp. 1-42.

Miyasaka, M., Stoemenos, J., 1999, "Excimer Laser Annealing of Amorphous and Solid-phase-crystallized Silicon Films", *Journal of Applied Physics*, **86**(10), pp. 5556-5565.

Ong, C.K., Sin, E.H., Tan, H.S., 1986a, "Heat-flow calculation of pulsed excimer ultraviolet laser's melting of amorphous and crystalline silicon surfaces", *J. Opt., Soc. Am. B*, **3**(5), pp. 812-814.

Ong, C.K., Tan, H.S., Sin, E.H., 1986b, "Calculations of melting threshold energies of crystalline and amorphous materials due to pulsed-laser irradiation", *Materials Science and Engineering*, **79**, pp. 79-85.

Polman, A., Roorda, S., Stolk, P., Sinke, W., 1991, "Triggering Explosive Crystallization of Amorphous Silicon", *Journal of Crystal Growth*, **108**, pp. 114-120.

Prokhorov, A.M., Konov, V.I., Ursu, I., Mihailescu, N., 1990, *Laser heating of metals*, Taylor and Francis, pp. 43.

Roorda, S., Sinke, W., 1989, "Rapid Nucleation in Pulsed Laser Heated Amorphous Si", *Applied Surface Science*, **36**, pp. 588-596.

Schwarz-Selinger, T., Cahill, D.G., Chen, S., Moon, S., Griogoropoulos, C.P., 2001, "Micron-scale Modifications of Si Surface Morphology by Pulsed-laser Texturing", *Physical Review B*, **64**, pp. 155323-1-155323-7.

Staebler, D.L., Wronski, C.R., 1980, "Optically Induced Conductivity Changes in Discharge-produced Hydrogenated Amorphous Silicon", *Journals of Appl. Physics*, **51**(6).

Tsao, J., Peercy, P., 1987, "Crystallization Instability at the Amorphous-Silicon/Liquid-Silicon Interface", *Physical Review Letters*, **58**(26), pp. 2782-2785.

Tull, B.R., Carey, J.E., Mazur, E., McDonald, J.P., Yalisove, S.M., 2006, "Silicon Surface Morphologies after Femtosecond Laser Irradiation", *MRS Bulletin*, **31**(8), pp. 626-633.

Unamuno, S., Fogarassy, E., 1989, "A thermal description of the melting of c- and a-Silicon under pulsed excimer lasers", *Applied Surface Science*, **36**, pp. 1-11.

Wang, H., Kongsuwan, P., Satoh, G., Yao, Y.L., 2012a, "Femtosecond Laser-induced Simultaneous Surface Texturing and Crystallization of a-Si:H Thin Film: Morphology Study", *The International Journal of Advanced Manufacturing Technology*, DOI: 10.1007/s00170-012-4291-0.

Wang, H., Kongsuwan, P., Satoh, G., Yao, Y.L., 2012b, "Femtosecond Laser-Induced Simultaneous Surface Texturing and Crystallization of a-Si:H Thin Film: Absorption and Crystallinity", *Journal of Manufacturing Science and Engineering*, **134**(3), pp. 031006.

Yamamoto, K., et al., 2004, "A High Efficiency Thin Film Silicon Solar Cell and Module", Solar Energy, **77**, pp. 939-949.

Chapter 5

Assay, J.R., Shahipoor, M., 1992, *High-Pressure Shock Compression of Solids*, Springer-Verlag, New York.

Beyer, S., Tonrnari, V., Gornicki, D., 2003, "Comparison of Laser Induced Front- and Rear Side Ablation", *Proc. SPIE*, **5063**, pp. 202-207.

Booth, H., 2010, "Laser Processing in Industrial Solar Module Manufacturing", *Journal of Laser Micro/Nanoengineering*, **5**, pp. 183-191.

Bovatsek, J., Tamhankar, A., Patel, R.S., Bulgakova, N.M., Bonse, J., 2010, "Thin Film Removal Mechanisms in ns-Laser Processing of Photovoltaic Materials", *Thin Solid Films*, **518**, pp. 2897-2904.

Camanho, P.P., Dávila, C.G., 2002, "Mixed-Mode Decohesion Finite Elements for the Simulation of Delamination in Composite Materials", *NASA Langley Res. Cent*., TM-2002-211737, pp. 1-37.

Carlomagno, G.M., Brebbia, C.A., 2011, *Computational Methods and Experimental Measurements XV*, WIT Press, Southampton.

Compaan, A.D., Matulionis, S.N., 2000, "Laser Scribing of Polycrystalline Thin Films", *Opt. Lasers Eng*., **34**, pp. 15-45.

Dhere, R.G., Bonnet-Eymard, M., Charlet, E., Peter, E., Duenow, J.N., Li, J.V., Kuciauskas, D., Gessert, T.A., 2011, "CdTe Solar Cell with Industrial Al:ZnO on Soda-lime Glass", *Thin Solid Films*, **519**, pp. 7142-7145.

Dunsky, C.M., Colville, F., 2008, "Scribing Thin-Film Solar Panels", *Industrial Laser Solutions for Manufacturing*.

Fabbro, R., Fournier, J., Ballard, P., Devaux, D., Virmont, J., 1990, "Physical Study of Laser-Produced Plasma in Confined Geometry", *J. Appl. Phys*., **68**, pp. 775-784.

Gecys, P., Raciukaitis, G., 2010, "Scribing of a-Si Thin Film Solar Cells with Picoseconds Laser", *Eur. Phys. J. Appl. Phys*., **51**, pp. 33209.

Kontgers, M., Kunze, I., Kajari-Schroder, S., Breitenmoser, X., Bjorneklett, B., 2010, "Quantifying the Risk of Power Loss in PV Modules due to Micro Cracks", *25th European Photovoltaic Solar Energy Conference*, Valencia, Spain.

Lowndes, D.H., Fowlkes, J.D., Pedraza, A.J., 2000, "Early Stage of Pulsed-Laser Growth of Silicon Microcolumns and Microcones in Air and SF_6", *Appl. Surf. Sci*., **154-155**, pp. 647-658.

Luque, A., Hegedus, S., 2003, *Handbook of Photovoltaic Science and Engineering*, Wiley, UK.

Luque, A., Hegedus, S., 2011, *Handbook of Photovoltaic Science and Engineering*, second ed., John Wiley & Sons, UK.

Matylitsky, V.V., Huber, H., Kopf, D., 2011, "Selective Removal of Transparent Conductive Oxide Layers with Ultrashort Laser Pulses: Front- vs. Back-Side Ablation", *Int. Congr. App. Lasers Electro-Opt*., pp. 1022-1027.

Murison, R., Dunsky, C., Rekow, M., Dinkel, C., Pern, J., Mansfield, L., Panarello, T., Nikumb, S., 2010, "CIGS P1, P2 and P3 Laser Scribing with an Innovative Fiber Laser", *35th IEEE Photovoltaic Specialists Conf.*, pp. 179-184.

Peter, C., 1994, *Properties of Narrow Gap Cadmium-Based Compounds*, the Institution of Electrical Engineers, UK.

Potts, P.J., 1987, *A Handbook of Silicate Rock Analysis*, Chapman and Hall, London, UK.

Rubin, M., 1985, "Optical Constants and Bulk Optical Properties of Soda Lime Silica Glasses for Windows", *Sol. Energy Mater*., **12**, pp. 275-288.

Sano, T., Yamada, H., Nakayama, T., Miyamoto, I., 2002, "Laser Induced Rear Ablation of Metal Thin Films", *Proc. SPIE*, **4426**, pp. 70-73.

Seica, M.V., Packer, J.A., 2004, "Mechanical Properties and Strength of Aged Cast Iron Water Pipes", *Journal of Materials in Civil Engineering*, **16**, pp. 69-77.

Shinohara, W., Shima, M., Taira, S., Uchihashi, K., Terakawa, A., 2006, "Applications of Laser Patterning to Fabricate Innovative Thin-Film Silicon Solar Cells", *Proceedings of SPIE*, pp. 6107.

Wang, W., Wang, K.D., Jiang, G.D., Mei, X.S., Yang, C.J., 2010, "Comparison of Femtosecond Laser-Induced Front- and Rear-Side Ablation of Films", *Proc. Inst. Mech. Eng., Part B: J. Eng. Manuf*., **225**, pp. 520-527.

Zhang, W., Yao, Y.L., 2002, "Micro-Scale Laser Shock Processing of Metallic Components", *ASME Trans. J. Manuf. Sci. Eng*., **124**, pp. 369-378.

Chapter 6

Acciania, G., Falcone, O., Vergura, S., 2010, "Defects in Poly-Silicon and Amorphous Silicon Solar Cells", *Intl. Conf. on Renewable Energy and Power Quality, Spain*.

Addession, F.L., Johnson, J.N., 1990, "A Constitutive Model for the Dynamic Response of Brittle Materials", *Journal of Applied Physics*, **67**(7), pp. 3275-3286.

Beyer, S., Tonrnari, V., Gornicki, D., 2003, "Comparison of Laser Induced Front- and Rear Side Ablation", *Proc. SPIE*, **5063**, pp. 202-207.

Booth, H., 2010, "Laser Processing in Industrial Solar Module Manufacturing", *Journal of Laser Micro/Nanoengineering*, **5**, pp. 183-191.

Borrajo, J., Vetter, M., Andreu, J., 2009, "Laser Scribing of Very Large 2.6m × 2.2m a-Si:H Thin Film Photovoltaic Modules", *Proceedings of the 2009 Spanish Conference on Electron Devices,* Santiago de Compostela, Spain.

Bovatsek, J., Tamhankar, A., Patel, R.S., Bulgakova, N.M., Bonse, J., 2010, "Thin Film Removal Mechanisms in ns-Laser Processing of Photovoltaic Materials", *Thin Solid Films*, **518**, pp. 2897-2904.

Compaan, A.D., Matulionis, S.N., 2000, "Laser Scribing of Polycrystalline Thin Films", *Opt. Lasers Eng*., **34**, pp. 15-45.

Dhere, R.G., Bonnet-Eymard, M., Charlet, E., Peter, E., Duenow, J.N., Li, J.V., Kuciauskas, D., Gessert, T.A., 2011, "CdTe Solar Cell with Industrial Al:ZnO on Soda-lime Glass", *Thin Solid Films*, **519**, pp. 7142-7145.

Dunsky, C.M., Colville, F., 2008, "Scribing Thin-Film Solar Panels", *Industrial Laser Solutions for Manufacturing*.

Emel'yanov, V.I., Kashkarov, P.K., 1992, "Laser-Induced Defect Formation in Semiconductors", *Applied Physics A*, **55**, pp. 161-166.

Gecys, P., Raciukaitis, G., 2010, "Scribing of a-Si Thin Film Solar Cells with Picoseconds Laser", *Eur. Phys. J. Appl. Phys*., **51**, pp. 33209.

Golovan, L., Kashkarov, P., Timoshenko, V., 1996, "Laser-Induced Melting and Defect Formation in Cadmium Telluride", *Laser Physics*, **6**(5), PP. 925-927.

Hai, S., Tadmor, E.B., 2003, "Deformation Twinning at Aluminum Crack Tips", *Acta Materialia*, **51**, pp. 117-131.

Hodges, D.R., Palekis, V., Bhandaru, S., Singh, K., Morel, D., Stefanakos, E.K., Ferekides, C.S.., 2009, "Mechanical Properties and Adhesion of CdTe/CdS Thin Film Solar Cells Deposited on Flexible Foil Substrates", *Material Research Society Symposium Proceedings*, **1165**, pp. 1165-M02-09.

Holmquist, T.J., Johnson, G.R., 1994, "An Improved Computational Constitutive Model for Brittle Materials", *AIP Conf. Proc*. **309**, pp. 981-984.

Holmquist, T.J., Johnson, G.R., 2005, "Characterization and Evaluation of Silicon Carbide for High-Velocity Impact", *Journal of Applied Physics*, **97**, pp. 093502.

Hughes, G.M., Smith, G.E., Flewitt, P.E.J., Crocker, A.G., 2007, "The Brittle Fracture of Polycrystalline Zinc", *Proceedings of the Royal Society A*, **463**, pp. 2129-2151.

Kontgers, M., Kunze, I., Kajari-Schroder, S., Breitenmoser, X., Bjorneklett, B., 2010, "Quantifying the Risk of Power Loss in PV Modules due to Micro Cracks", *25th European Photovoltaic Solar Energy Conference*, Valencia, Spain.

Lauzurica, S., Garcia-Ballesteros, J.J., Colina, M., Sanchez-Aniorte, I., Molpeceres, C., 2011, "Selective Ablation with UV Lasers of a-Si:H Thin Film Solar Cells in Direct Scribing Configuration", *Applied Surface Science*, **257**, pp. 5230-5236.

Luque, A., Hegedus, S., 2003, *Handbook of Photovoltaic Science and Engineering*, Wiley, UK.

Matylitsky, V.V., Huber, H., Kopf, D., 2011, "Selective Removal of Transparent Conductive Oxide Layers with Ultrashort Laser Pulses: Front- vs. Back-Side Ablation", *Int. Congr. App. Lasers Electro-Opt*., pp. 1022-1027.

Murison, R., Dunsky, C., Rekow, M., Dinkel, C., Pern, J., Mansfield, L., Panarello, T., Nikumb, S., 2010, "CIGS P1, P2 and P3 Laser Scribing with an Innovative Fiber Laser", *35th IEEE Photovoltaic Specialists Conf.*, pp. 179-184.

Sano, T., Yamada, H., Nakayama, T., Miyamoto, I., 2002, "Laser Induced Rear Ablation of Metal Thin Films", *Proc. SPIE*, **4426**, pp. 70-73.

Shinohara, W., Shima, M., Taira, S., Uchihashi, K., Terakawa, A., 2006, "Applications of Laser Patterning to Fabricate Innovative Thin-Film Silicon Solar Cells", *Proceedings of SPIE*, pp. 6107.

Tomaoki, S., Kaneuchi, Y., Kakui, M., Baird, B., Paudel, N., Wieland, K., 2010, "Development of Wide Operational Range Fiber Laser for Processing Thin Film Photovoltaic Panels", *29th International Congress on Applications of Laser & Electro-Optics*, Anaheim, CA.

Tull, B.R., Carey, J.E., Mazur, E., McDonald, J.P., Yalisove, S.M., 2006, "Silicon Surface Morphologies after Femtosecond Laser Irradiation", *MRS Bulletin*, **31**(8), pp. 626-633.

Vere, A.W., Cole, S., Williams, D.J., 1983, "The Origins of Twinning in CdTe", *J. of Elec. Mat*, **12**(3), pp. 551-561.

Wang, H., Lusquiños, F., Yao, Y.L., 2012a, "Effect of Hydrogen on Surface Texturing and Crystallization of a-Si:H Thin Film Irradiated by Excimer Laser", *Applied Physics A*, **107**(2), pp. 307-320.

Wang, H., Kongsuwan, P., Satoh, G., Yao, Y.L., 2012a, "Femtosecond Laser-Induced Simultaneous Surface Texturing and Crystallization of a-Si:H Thin Film: Absorption and Crystallinity", *ASME Trans., Journal of Manu. Science and Engineering*, **134**(3), pp. 031006.

Wang, H., Hsu, S., Tan, H., Yao, Y.L., Chen, H., Azer, M., 2013, "Predictive Modeling for Glass-Side Laser Scribing of Thin Film Photovoltaic Cells", *Journal of Manufacturing Science and Engineering, accepted.*

Wang, W., Wang, K.D., Jiang, G.D., Mei, X.S., Yang, C.J., 2010, "Comparison of Femtosecond Laser-Induced Front- and Rear-Side Ablation of Films", *Proc. Inst. Mech. Eng., Part B: J. Eng. Manuf*., **225**, pp. 520-527.

Appendix

This appendix provides the details of numerical models, data processing and hardware control programs associated with the work achieved in this thesis. The appendix is separated into three sections. The first section explains the numerical models developed in this thesis. The second part describes the peak identification of extraction data from AFM measurement of laser textured a-Si:H sample surface. The third section shows the hardware control programs of both femtosecond laser and excimer laser.

A1 Numerical Models

A1.1 Simulation of Light Absorption of As-Received a-Si:H Thin Film

This model (*Absorption Program.m*) is based on Eq. (2.5) to Eq. (2.7) to simulate both transmission and reflection of as-received a-Si:H thin films using *Matlab*. The first step of the simulation is to determine the optical constants based on the experimental measurement of transmission as shown in Fig. 2.4. The optical constant is calculated using Eq. (2.6) at the corresponding wavelengths that cause peaks and valleys, and a polynomial curve fitting of those values gives the optical constants over the solar spectrum. The raw data of transmission measurement and simulation program are included in (*Numerical Models and Programs\A1.1 Light absorption of as-received a-Si:H thin film*). The next step is using the calculated refractive index to compute the transmission based on Eq. (2.5) and reflection based on Eq. (2.7). Finally, absorption can be calculated using $A = 100\% - T - R$.

A1.2 Simulation of Light Absorption of Laser Textured a-Si:H Thin Film

This model uses a ray tracing method to simulate the sunlight as a group of discrete rays. The path of the waves through a system with regions of varying propagation velocity and absorption characteristics is based on geometrical optics. The model is set up using software of *TracePro*. The first step is to build up the surface geometry of the material using Rep Tile Surface. The conical and pillar spike geometries generated in air and water are saved in *Conical spike.txt* and *Pillar spike.txt* files in (*Numerical Models and Programs\A1.2*). Every time, you can import this surface geometry into TracePro model (*Air_conical.oml* and *Water_pillar.oml* files) in the menu of *Tools-> Database -> Import* and browse to the location of the file. The surface geometry can be modified by going to *Define-> Edit Property Data -> Rep Tiles Properties*. Next step is to define the material property by *right click -> Properties -> Material*. The calculated optical constants in *A1.1* will be added here. The final step is to define a light source. In this model, a *Grid Source* is used to specify the spatial and angular distribution of rays in a certain area which covers the entire surface of a-Si:H thin film. The solar radiation is defined by setting up the wavelengths range (250nm to 2500nm), a set of 60,000 rays with a total intensity of 1 watt.

A1.3 Models for Ellipsometry Measurement

Ellipsometry is a powerful tool for measuring the thickness of thin film with resolution in angstrom scale. The method for determining the film thickness and optical constants of the material is using a numerical model to fit the experimental measurements. The models of a-Si:H and CdTe solar cell samples are included in (*Numerical Models and Programs\A1.3*). The model is set up by using software of *CompleteEASE*. In a-Si:H model, the optical constants of glass substrate is simulated using Cauchy's equation, and a layer of a-Si:H is then added by clicking

"*Layer Commands: Add*". The material property of a-Si can be selected from the material database of the software by clicking *material->semiconductor*, and the film thickness is set to "*fit*". After setting up the model, click "*Fit*" button on the top left, the software will calculate the fitting curve of the model. If the curves of model and experiment are fitting well, the thickness is accurately calculated.

Regarding to SnO_2:F thin film on glass substrate, the model creates 4 layers on glass which is better representation of this complex TCO material. The film thickness can be estimated by adding these four layers together. For the multilayer of CdTe/CdS/SnO_2:F on glass substrate samples, the model consists of 7 layers on glass to better fit the measurement. The discrepancy between model and measurement is due to the roughness of CdTe film which can be improved by tuning CdTe material parameters.

A1.4 Simulation of Spike Spacing during Excimer Laser Irradiation

The dispersion relation of capillary waves formed during excimer laser irradiation is express in Eq. (4.7). The relaxation time of the capillary wave is due to the damping coefficient, can be expressed as $\tau = \frac{1}{2\upsilon k^2} = \frac{\lambda^2}{8\upsilon\pi^2}$. The relaxation time for some wavelengths is much smaller than the melting duration, indicating that some wavelengths damped out before freezing. This model seeks to find the minimal wavelengths after solidification at each condition. The first step is to calculate the melting duration and temperature via a thermal model using Abaqus (Thermal_a-Si.cae). The heat source of the thermal model is defined in the subroutine file (*248nm-excimer.for*) located in (*Numerical Models and Programs\A1.4*). The second step is to calculate the relaxation time using a *Matlab program (Relaxation Time.m)*. The viscosity is estimated by

$v=0.75-1.22/1000\cdot(T-T_m)$. The minimal wavelength is determined when this relaxation time equals to the melting duration. A detailed description is in a *PDF* file in the same directory.

A1.5 Simulation of P1 Laser Scribing of CdTe Solar Cell

This two-dimensional model is used to simulate SnO_2:F material removal during P1 laser scribing of CdTe solar cells. This fully-coupled thermal/mechanical finite element model is built using Abaqus and included in (*Numerical Models and Programs\A1.5*). The material fracture criterion is implemented in a user defined material subroutine of *VUMAT.for*. A detailed explanation of this subroutine is in *VUMAT_comments.txt*. The file of *P1 scribing.inp* is the simulation program at a fluence of 3J/cm^2, and it can be opened in Abaqus by going to *File-> Import-> Model*. The thermal load caused by the laser irradiation is implemented in *Field-> Analytical Field* and *Amplitudes*, and the percentage of energy after passing through the glass substrate is estimated using Eq. (5.10). An *.inp* file will be generated after creating a job in Abaqus. The command for calculation is "*abaqus job=job name.inp user=subroutine name.for interactive*". Visualization of the material removal profile may be performed through *Abaqus CAE*. The unit used in model is micro-meter and nano-second. The detail unit (*Unit of Abaqus Model. xlsx*) is included in the same directory.

A1.6 Simulation of P2 Laser Scribing of CdTe Solar Cell

This two-dimensional model is used to simulate the film fracture during P2 laser scribing of CdTe layer based on micro-explosion mechanism. The first step is calculating the pressure caused by plasma expansion based on Eq. (5.4) and Eq. (5.5). The *Matlab* program (*LSP_CdTe.m*) and detailed explanation is included in (*Numerical Models and*

Programs\A1.6\Pressure Calculation). The next step is simulating the film fracture using Abaqus. The *mechanical.inp* file in (*Numerical Models and Programs\A1.6*) is the simulation program of pressure induced CdTe film fracture at a fluence of 3J/cm^2. This program can be opened in Abaqus by going to *File-> Import-> Model*. The fracture criterion of CdTe film is applied in *Material Property* on the left model tree. The calculated temporal distribution of pressure is applied in "*Amplitudes*", and its spatial distribution (Gaussian) is added in *Field-> Analytical Field*. The three-dimensional thermal model (*thermal.inp*) is also included in the same directory and used to estimate the temperature distribution of CdTe solar cell. The laser source is written in the subroutine of *532nm_laser.for*. The percentage of energy absorbed by CdTe and CdS multilayer is estimated by Eq. (5.12). The command for running the program with the subroutine is similar to the one shown in A1.5. Visualization of the thermal and material removal profiles may be performed through *Abaqus CAE*. The unit used in model is micro-meter and nano-second. The detail unit (*Unit of Abaqus Model. xlsx*) is included in the same directory.

A2 Peak Identification of Laser Textured a-Si:H Thin Film

This algorithm is used to identify the peaks of laser textured a-Si:H samples. The raw data measured by AFM at a condition of 1.2J/cm^2 and 20 pulses can be found in (*Numerical Models and Programs\A2*). First step is applying a smoothing filter, $Z(x,y)=\frac{1}{25}\sum_{i=-2}^{2}\sum_{j=-2}^{2}Z(x+i,y+j)$, to eliminate the labeling of the small height fluctuations as peaks. The next step is determine the peak positions by finding where the first-order derivative is zero, $\frac{\partial Z(x,y)}{\partial x}=\frac{\partial Z(x,y)}{\partial y}=0$, and the second-order derivative is less than zero, $\frac{\partial^2 Z(x,y)}{\partial x^2}<0$. The average spacing of one spike is

calculated by the average value of the distances with its five closest neighbors. A detailed description is in a *PDF* file in the same directory.

A3 Programs for Laser Hardware Control

A3.1 Program of Femtosecond Laser Control

The program is used to control the number of pulses and repetition rate of the femtosecond laser. The communication between the hardware and software is realized through a serial port. The programs (*SingleShot.vi* and *MultipleShot.vi*) are written by software of Labview. The programs are included in (*Numerical Models and Programs\A3.1*). For multiple pulse irradiation, the repetition rate can be set up by setting the delay time between pulses.

A3.2 Program of Excimer Laser Control

This program is used to control *Newport ESP 301* motion stage which is synchronized with excimer laser through a serial port, resulting in a laser irradiated area with different number of pulses. The programs (*Area_10x12_1pulse.vi* and *Area_5x5_100pulses.vi*) are written by software of Labview and are included in (*Numerical Models and Programs\A3.2*). For single pulse irradiation, the program will send laser firing command one at a time by setting the triggering mode of excimer laser to "*EXT*". Regarding to multiple pulses, the program will fire the laser in a certain time coordinated with the preselected repetition rate by setting the triggering mode of excimer laser to "*INTG*".

A4 Publications Under Candidature

- **Wang, H.,** Yao, Y.L., Chen, H., "Removal Mechanism and Defect Characterization for Glass-Side Laser Scribing of CdTe/CdS Multilayer in Solar Cells", *Solar Energy Materials and Solar Cells, to be submitted*.

  Also, *41th North American Manufacturing Research Conference*, Madison, WI, June, 2013

- **Wang, H.**, Hsu, S., Tan, H., Yao, Y.L., Chen, H., Azer, M., 2012, "Predictive Modeling for Glass-Side Laser Scribing of Thin Film Photovoltaic Cells", *Journal of Manufacturing Science and Engineering*, accepted.

  Also, *40th North American Manufacturing Research Conference*, Notre Dame, IN, June, 2012.

- **Wang, H.**, Lusquiños, F., Yao, Y.L., 2012, "Effect of Hydrogen on Surface Texturing and Crystallization of a-Si:H Thin Film Irradiated by Excimer Laser", *Applied Physics A,* **107**(2), pp. 307-320.

  Also, *Proceedings of 30th International Congress on Application of Lasers & Electro-Optics*, Orlando, FL, Oct., 2011.

- **Wang, H.**, Kongsuwan, P., Satoh, G., Yao, Y.L., 2012, "Femtosecond Laser-induced Simultaneous Surface Texturing and Crystallization of a-Si:H Thin Film: Absorption and Crystallinity", *Journal of Manufacturing Science and Engineering*, **134**(3), pp. 031006.

  Also, *Proceedings of the 2011 North American Manufacturing Research Conference*, Corvallis OR, June, 2011.

- **Wang, H.**, Kongsuwan, P., Satoh, G., Yao, Y.L., 2013, "Femtosecond Laser-induced Simultaneous Surface Texturing and Crystallization of a-Si:H Thin Film: Morphology Study", *The International Journal of Advanced Manufacturing Technology,* **65**(9), pp. 1691-1703.

  Also, *Proceedings of the 2010 International Manufacturing Science and Engineering Conference*, Erie, PA, Oct. 2010.

- Kongsuwan, P., **Wang, H.**, Yao, Y.L., 2012, "Single Step Channeling in Glass Interior by Femtosecond Laser", *Journal of Applied Physics,* **112**(2), pp.023114.

  Also, *40th North American Manufacturing Research Conference*, Notre Dame, IN, June, 2012.

- Chen, Y., **Wang, H.**, Zhang, J., Garty, G., Simaan, N., Yao, Y.L., Brenner, D.J. 2012, "Automatic Recognition of Primary Robotic Manipulation Failure Modes in High-throughput Biodosimetry Tool", *Expert Systems with Applications,* **39**, pp.9602-9611.

- Garty, G., Chen, Y., Turner, H., Zhang, J, Lyulko, O., Bertucci, A., Xu, Y., **Wang, H.**, Simaan, N., Randers-Pehrson, G., Yao, Y.L., Brenner, D.J., 2011, "The RABIT: A Rapid Automated BIodosimetry Tool For Radiological Triage. II. Technological Developments", *International Journal of Radiation Biology*, **87**(8), pp.776-790.

- Turner, H.C., Brenner, D.J., Chen, Y., Bertucci, A., Zhang, J., **Wang, H.**, Lyulko, O., Xu, Y., Shuryak, I., Schaefer, J., Simaan, N., Randers-Pehrson, G., Yao, Y.L., Amundson, S., and Garty, G., 2011, "Adapting the γ-H2AX Assay for Automated Processing in Human Lymphocytes. 1. Technological Aspects", *Radiation Research*, **175**, pp.282-290.

- Hsu, S., **Wang, H.,** Satoh, G., Yao, Y.L., 2011, "Application of Surface Structuring with Lasers", *Invited Paper, Proceedings of 30th International Congress on Applications of Lasers and Electro-Optics*, Orlando, FL.

- Kongsuwan, P, **Wang, H.**, Vukelic, S., Yao, Y.L., 2010, "Characterization of Morphology and Mechanical Properties of Glass Irradiated by Femtosecond Laser," *Journal of Manufacturing Science and Engineering,* **132**(4), pp. 041009.

  Also, *Proceedings of 28th International Congress on Applications of Lasers and Electro-Optics*, Orlando, FL, Nov. 2009.

- Chen, Y., Zhang, J., **Wang, H.**, Garty, G., Xu, Y., Lyulko, O.V., Turner, H.C., Randers-Pehrson, G., Simaan, N., Yao, Y.L. and Brenner, D.J., 2010, "Development of a Robotically-based Automated Biodosimetry Tool for High-throughput Radiological Triage", *International Journal of Biomechatronics and Biomedical Robotics,* **1**(2), pp.115-125.

  Also, *Proceedings of 2009 ASME/IEEE International Conference on Mechatronic and Embedded Systems and Applications,* **3**, pp. 61-67.

- Garty, G., Chen, Y., Salerno, A., Turner, H., Zhang, J., Lyulko, O.V., Bertucci, A., Xu, Y., **Wang, H.**, Simaan, N., Randers-Pehrson, G., Yao, Y.L., Amundson, S. A. and Brenner D.J. 2010, "The RABIT: A Rapid Automated Biodosimetry Tool for radiological triage", *Health Phys.* **98**(2), pp.209-217.